STRUCTURE, FUNCTION, AND IMMUNOGENIC APPLICATIONS OF AB$_5$-TYPE

ADP-RIBOSYLATING BACTERIAL TOXINS

by

Elise Marie Overgaard

A dissertation

submitted in partial fulfillment

of the requirements for the degree of

Doctor of Philosophy in Biomolecular Sciences

Boise State University

December 2022

BOISE STATE UNIVERSITY GRADUATE COLLEGE

DEFENSE COMMITTEE AND FINAL READING APPROVALS

of the dissertation submitted by

Elise Marie Overgaard

Dissertation Title: Structure, Function, and Immunogenic Applications of AB_5-type ADP-Ribosylating Bacterial Toxins

Date of Final Oral Examination: 12 September 2022

The following individuals read and discussed the dissertation submitted by student Elise Marie Overgaard, and they evaluated the student's presentation and response to questions during the final oral examination. They found that the student passed the final oral examination.

Juliette K. Tinker, Ph.D.	Chair, Supervisory Committee
Allan R. Albig, Ph.D.	Member, Supervisory Committee
Richard S. Beard Jr., Ph.D.	Member, Supervisory Committee
Daniel Fologea, Ph.D.	Member, Supervisory Committee

The final reading approval of the dissertation was granted by Juliette K. Tinker, Ph.D., Chair of the Supervisory Committee. The dissertation was approved by the Graduate College.

DEDICATION

This dissertation is dedicated to:

- my nieces and nephews, Addy, Wally, Christian, Willie, Sylvie, Georgie, Vinny, and Esti – stay curious.

- the love of my life, Johnny, and our cat Pounce de León – stay wild.

- my parents, Meg and Wil, and the Weiser Science Club – there's a great big world out there to explore but it's always a great day to be a Wolverine.

- and Dr. Anthony Fauci – thank you for your expertise and leadership through a turbulent time.

ACKNOWLEDGMENTS

Every day for the past 4 years I envisioned working in lab as equally stressful as working in space. Saturday Night Live did a sketch in 2019 called Space Mistakes. It's a fake trailer that pokes fun at all the tropes of a good space movie where things go wrong. It opens with an astronaut dad promising his son and wife that he'll be safe in space (but he won't). The astronaut must reassure his wife, who worries that he might crack his helmet. Spin too fast! Push the wrong thing and the top comes off! And then the astronauts make it to space, but because they're in space, every mistake is tremendously more consequential than it would be on Earth. This is how I felt in lab. Every time I dropped an important piece of equipment or spilled an expensive reagent or pipetted the wrong clear liquid into the other clear liquid, I muttered under my breath, "ugh, space mistake!". I literally pushed the wrong button and the top came off. Multiple times.

My first acknowledgement is to my soul mate, the love of my life, and my partner in everything, Johnny Boyd. The one who was there to clean up the mess when I crumbled after the space mistakes. In August of 2018 Johnny and I retired from the Oinkari Basque Dancers, a group we'd been with for over a decade and were heartbroken to leave, bought a four-plex "fixer upper" and started renovations on it, started a property management LLC, and I turned 31 and started this program. It was quite a month. Johnny held us together through so many journeys. He and I exist within multiple large, layered, and tightly knit communities. Between friends, family, and all the activities and groups we are a part of, we had a lot of ups and downs over the past four years. Weddings,

funerals, nieces and nephews being born, celebrations, illnesses...sometimes it was tough to manage all the demands. Johnny gave me space to feel my feelings, support when I asked for it, time for deep and nerdy conversations, and continuously brought joy (and so much triki music!) into our home. I am so excited to spend the rest of my life with him.

My next acknowledgement is to Dr. Tinker for her eternal patience and calm problem solving in seemingly dire situations that seemed insurmountable at the time. My learning curve in lab was steep, but Dr. Tinker was always willing to talk things through, help me duct tape the air lock back together, and support me in carrying on. Her positive attitude about research and insistence that we can learn something from every space mistake is something I will try to carry with me forever. I also want to thank Dr. Tinker for all the time she allocated to having long discussions about the big pictures of the world and where we as scientists and researchers fit in. We had a lot happen in the last four years. Multiple events that demanded that we stop whatever we were doing and tune in because of the gravity of the situation. Climate change indicators continually broke records. #MeToo broke the dam for thousands of women who had remained silent for years. Brett Kavanaugh and Amy Coney Barrett took seats as Associate Justices of the Supreme Court. The most diverse class of lawmakers in history was sworn into Congress. Black Lives Matter pushed the world to act on social justice issues. Repeated horrific school shootings captured the news cycles. The U.S. women's soccer team won the world cup (again) and achieved a groundbreaking deal for equal pay. A global pandemic swept the Earth. Incredible and unprecedented global scientific teamwork led to groundbreaking mRNA vaccines and an explosion of research and public interest in vaccine development. AlphaFold revolutionized protein biology. A mob overran the U.S. Capitol seeking to

keep a president in power. Women in towns across the Basque Country performed dances that only men had ever been allowed to dance. Simone Biles became one of the greatest gymnasts of all time, drew the world's focus to the topic of mental health, and courageously testified against USA Gymnastics and the U.S. Olympic Committee for failing to protect gymnasts from sexual abuse to the Senate Judiciary Committee, all within 2 years. Civilians went to space. Roe v. Wade was overturned. The James Webb Space Telescope captured pictures that represented both time AND space. And I'm only listing the things that made my cry! I am deeply appreciative of the space that Dr. Tinker always created for digesting current events and for situating our work among the events of the world in a way that motivated and inspired me. Maybe we didn't personally solve all the problems of the world, but we gave it a good shot, and we accomplished a few things here and there.

I need to thank Omid Mohammad Mousa, my first partner in space mistakes. He taught me the protein purification skills that would become the foundation of my work with limitless patience. He printed out and posted a picture of my first successful SDS-PAGE gels for the entire lab to see, what a great cheerleader! I always appreciated his kindness, his relentless perseverance on difficult technical problems, and his sense of humor when we made the space mistakes. I am certain I wouldn't have made it through my first two years of the program without him. Omid also laid the initial groundwork that enabled me to learn cryo-EM at the Pacific Northwest Cryo-EM Center, an incredible opportunity for which I will eternally be grateful.

I also have to thank Haley Bridgewater and Leslie Kendrick, my right-hand women for our adventures in science communication, troubleshooting, and dragging each

other's exhausted brains and bodies over finish lines. I am so grateful to these women for believing in me and for answering the phone at two o'clock a.m. when things weren't working and I was breaking down. Haley and I also made some strides in science communication and in community organization and I think we both agree that we learned…a lot. I hope we will continue our educations and our friendships long into the future!

To my mentors and role models for life - Dr. Eric Hayden, Dr. Allan Albig, Dr. Daniel Fologea, and Dr. Henry Picklestein-Charlier – thank you for continually making time and space for your students! Each of you impacted my life and provided lessons, for both science and life, that will stick with me forever. I came to this program with no idea what I was doing. You opened up the wondrous world of ribozymes, G-quadruplexes, phase-separated membrane-less organelles, beta sheet propellers, and amino acid ionizations. I'm leaving inspired, motivated, and certain of the difference between a rate and a rate constant.

And finally, last but certainly not least, thank you to all of my tribes. Thank you to my parents, Meg and Wil, who have bent over backwards to make my explorations possible, listened to bad run-throughs of presentations, read and edited drafts, and generally tolerated my nonstop science chatter for, not just the last four years, but the last 35. Thank you to my sister Ana, who constantly inspires me with her fearless adventuring and relentless curiosity, and who forced me out of my cave and provided some of my best grad school escape memories over the past four years. The pandemic stuck her in Boise but it did mean we got to spend more time together! Thank you to my cousin Molly, who was always ready with a coffee or a hiking plan or a therapy dog visit. Thank you to my

insistent cheerleaders, my brother Willie and his wife Jess, and my brother Mikel and his wife Caroline, who have been there for every failure, every overwhelmed phone call, and every celebration in between. Mikel brings the calm (and the fish), Caroline brings the dance party, Willie brings the silliness (and the baked goods), and Jess brings coffee, counseling, and so many on-point memes. My life is so much richer because all of you are in it!

Thank you to my second family, John, Sharon, Kristin, Jordan, and Booey, plus all of Johnny's aunts, uncles, cousins, and in-laws, for believing in me, for feeding me, for playing with me when I wasn't in lab, and, most of all, for creating space for me! Special thank-yous go out to Phyllis and Janice for reading drafts of things, making delicious cookies, and always being ready to help clean or paint or whatever else we needed with house renovations.

To all the Garmendias, Bieters, Overgaards, Boyds, Roystons, Juli at the Basque Center and the rest of the Basque community, the Weiser Wolverines, my chosen families from Boston University, my rugby families, and especially to the other students of the BMOL program, I wouldn't have finished this thing without you. I love you all and it's a joy to be a part of your tribe.

ABSTRACT

Bacterial mono-ADP-ribosyltransferases (ARTs) catalyze the singular transfer of an ADP-ribose moiety from an NAD+ molecule onto a target molecule. ARTs contain an ancient and highly conserved tertiary structure and have a wide variety of intracellular targets and effects. Some, but not all, bacterial ARTs have an AB_5-type multimeric structure consisting of an enzymatically active subunit non-covalently situated atop of a non-toxic pentamer. The active, or A, subunit of AB_5-type toxins has a catalytic action that contributes to bacterial pathogenicity, and it is sometimes, but not always, an ART. ArtAB is an ART with AB_5-type structure from the virulent and highly antibiotic resistant *Salmonella* Typhimurium DT104. In the studies described here, we tested the hypothesis that the active subunit of ArtAB is structurally and enzymatically homologous to that of the well-characterized AB_5-type ART pertussis toxin. ArtAB was purified from *E. coli* and was used to characterize ArtAB's cellular effects, predicted structure, and biophysical properties. In addition, a set of single-residue mutants was constructed and purified to probe ArtAB's active site. AB_5-type toxins have long been studied for their immunogenic properties, and some of these bacterial munitions have been harnessed and repurposed as vaccines or vaccine adjuvants to prevent infectious disease. Their receptor-binding pentamer, abbreviated as B_5, binds to, and facilitates entry into, host cells. In additional work presented here, we tested the hypothesis that the B_5 subunit of cholera toxin (CTB) from *Vibrio cholerae* could be used to construct a safe and effective mucosal vaccine against *Staphylococcus aureus*-caused mastitis. We constructed a bovine vaccine

x

by conjugating *Staphylococcus aureus* antigens to the CTB-based adjuvant platform, and the immunogenicity of the vaccine was characterized in a bovine clinical trial. Finally, clinical isolates of caprine *S. aureus* were screened for the presence of surface antigens that could be use in a caprine version of the vaccine against mastitis. The work on bacterial AB$_5$-type ARTs presented here contributes to a growing global understanding of the bacterial ART family, lays a foundation for the potential incorporation of ArtAB in a vaccine against *Salmonella,* and advances the development of bovine and caprine vaccines against *S. aureus*-caused mastitis.

TABLE OF CONTENTS

xiii

LIST OF TABLES

LIST OF FIGURES

LIST OF ABBREVIATIONS

AB$_5$ protein structure - active (A) and pentameric binding (B) subunits

AC   adenylyl cyclase

ADP   adenosine diphosphate

ADP   adenosine diphosphate-ribose

AF2   AlphaFold 2

ART   ADP-ribosyltransferase

ArtA   ArtAB active subunit

ArtAB   *Salmonella* Typhimurium DT104 AB$_5$-type ADP-ribosylating native holotoxin

ArtAB-HIS   histidine-tagged *Salmonella* Typhimurium DT104 AB$_5$-type ADP-ribosylating toxin

ArtB   ArtAB binding subunit

AUC   analytical ultracentrifuge

BA   blood agar

bp   base pair

BCA   bicinchoninic acid

BGS   bovine growth serum

BRV   Biomedical Research Vivarium

BSA   bovine serum albumin

BSU   Boise State University

cAMP   cyclic adenosine monophosphate

Caco-2   human colorectal adenocarcinoma cell line

ccRMSD	common core root mean squared deviation
CD	circular dichroism
CFU	colony-forming units
CHO	Chinese hamster ovary cell line
ClfA	clumping factor A
CM	chloramphenicol
CT	cholera toxin
CTA	cholera toxin active subunit
CTA_1	enzymatically active domain of CTA
CTA_2	linking domain of CTA
CTB	cholera toxin binding subunit
CTA_2/B	cholera toxin A_2 and B subunit
Da	dalton
DAPI	4′,6-diamidino-2-phenylindole
DMEM	Dulbecco's modified Eagle's medium
DMSO	dimethyl sulfoxide
DpnI	restriction enzyme
*Ec*PltA	*E. coli* pertussis-like toxin
EDTA	ethylenediaminetetraacetic acid
ELISA	enzyme-linked immunosorbent assay
ER	endoplasmic reticulum
FITC	fluorescein isothiocyanate
FITC-OVA	fluorescein isothiocyanate-conjugated ovalbumin

FBS	fetal bovine serum
GAPDH	glyceraldehyde 3-phosphate dehydrogenase
GC	Graduate College
GDT	global distance test
GM1	monosialotetrahexosylganglioside
HBMEC	human brain microvascular endothelial cells
HRP	horseradish peroxidase
IACUC	institutional animal care and use committee
IFN-γ	interferon gamma
IgA	immunoglobulin A
IgG	immunoglobulin G
IL-4	interleukin-4
IL-6	interleukin-6
IL-10	interleukin-10
IL-12	interleukin-12
IS	inhibitor solution
IsdA	iron-regulated surface determinant A
IsdA + ClfA-CTA$_2$/B	CTA$_2$/B-based vaccine containing IsdA and ClfA antigens
kDa	kilodaltons
LB	Luria Broth
LC–MS	liquid chromatography-mass spectrometry
LDDT	local distance difference test
LF	left front

LR	left rear
LTI	*E. coli* type I heat-labile enterotoxin
LTIIaA	*E. coli* type IIa heat-labile enterotoxin
MSA	mannitol salt agar
MW	molecular weight
MWCO	molecular-weight cutoff
nRMSD	normalized root mean squared deviation
NT	nucleotide
NTS	non-typhoidal serovars of *Salmonella*
O.D.	optical density
PBMC	peripheral blood mononuclear cell
PBS	phosphate-buffered saline
PCR	polymerase chain reaction
PKA	protein kinase A
PKC	protein kinase C
pLDDT	predicted local distance different test
Plt	pertussis-like toxin
PMSF	phenylmethylsulfonyl fluoride
PT	pertussis toxin
PTA	pertussis toxin active subunit
PtxB S1, S1, S3, S4	pertussis toxin binding subunits
qRT-PCR	quantitative reverse transcription polymerase chain reaction
RF	right front

RMSD	root mean squared deviation
RR	right rear
RT	room temperature
RT-PCR	reverse transcription polymerase chain reaction
SAgs	superantigens
SalB	likely AB$_5$ toxin from *S. arizonae*
SCC	somatic cell count
SDS-PAGE	sodium dodecyl sulphate-polyacrylamide gel electrophoresis
SNF	solids-not-fat
SubB	*E. coli* subtilase cytotoxin B
SubB2	uncharacterized *E. coli* subtilase cytotoxin-like binding subunit
T84	human colorectal carcinoma cell line
TB	Terrific Broth
TER/TEER	transmembrane epithelial electrical resistance
THP-1	monocyte cell line isolated from acute monocytic leukemia patient
TM-score	template modeling score
TNF-α	tumor necrosis factor alpha
TT	typhoid toxin
UCSF	University of California San Francisco
USD	United States Dollar
WB	Western blot
YrpB	likely AB$_5$ toxin from *Yersinia pestis*
YtxA	uncharacterized *Yersinia* AB$_5$ toxin

CHAPTER ONE: INTRODUCTORY MATERIAL

Bacteria have been engaging in molecular warfare for billions of years. They are true experts at producing molecules of death and destruction. Bacterial weapons are often made of proteins that poke holes in cells, commandeer signaling pathways, and lock critical ion channels or protein synthesis complexes in positions that assure cellular chaos. The work contained within these chapters focuses on bacterial weapons of the Trojan horse variety, AB_5 toxins.

The Trojan horse activity of these toxins is a direct result of their protein structures. Bacterial AB_5 protein toxins are composed of two individual subunits. The binding (B_5) subunit is formed by a set of five monomers, identical in some cases and distinct in others, which non-covalently self-assemble into a pentameric doughnut-like structure with a central pore. The B subunit binds to host cell receptors and mediates uptake of the toxin into the host cell. The active (A) subunit is an enzyme that catalyzes reactions within the host cell. It is non-covalently bound to the B_5 subunit, often through a C-terminal domain that acts as a linker by inserting itself into the central pore of the pentamer. In many AB_5 toxins, the linking, or A_2, domain is separated from the main active, or A_1, domain by proteolytic cleavage during post-translational processing or upon entry into the host cell. The A_1 domain remains secured to the holotoxin through a disulfide bond at the interface of the pentamer, linking it to the A_2 domain under normal physiological conditions. In many AB_5 toxins, the A_2 domain physically obstructs the

substrate binding pocket so that no substrates can interact with the active site of the A_1 subunit until the conditions are favorable. Favorable conditions occur once the toxin has moved into the host cell where the disulfide bond is reduced, freeing the A_1 subunit in its activated state. The generalized structure of an AB_5 toxin is shown in the graphical abstract (Figure 1.1a) below. To orient the reader, throughout this dissertation these toxins are referred to with abbreviated names, and individual subunits are referred to with the nomenclature of toxinID-subunit. For example, in discussions of pertussis toxin, abbreviated as PT, the A subunit is PTA, and the B_5 pentameric subunit is PTB.
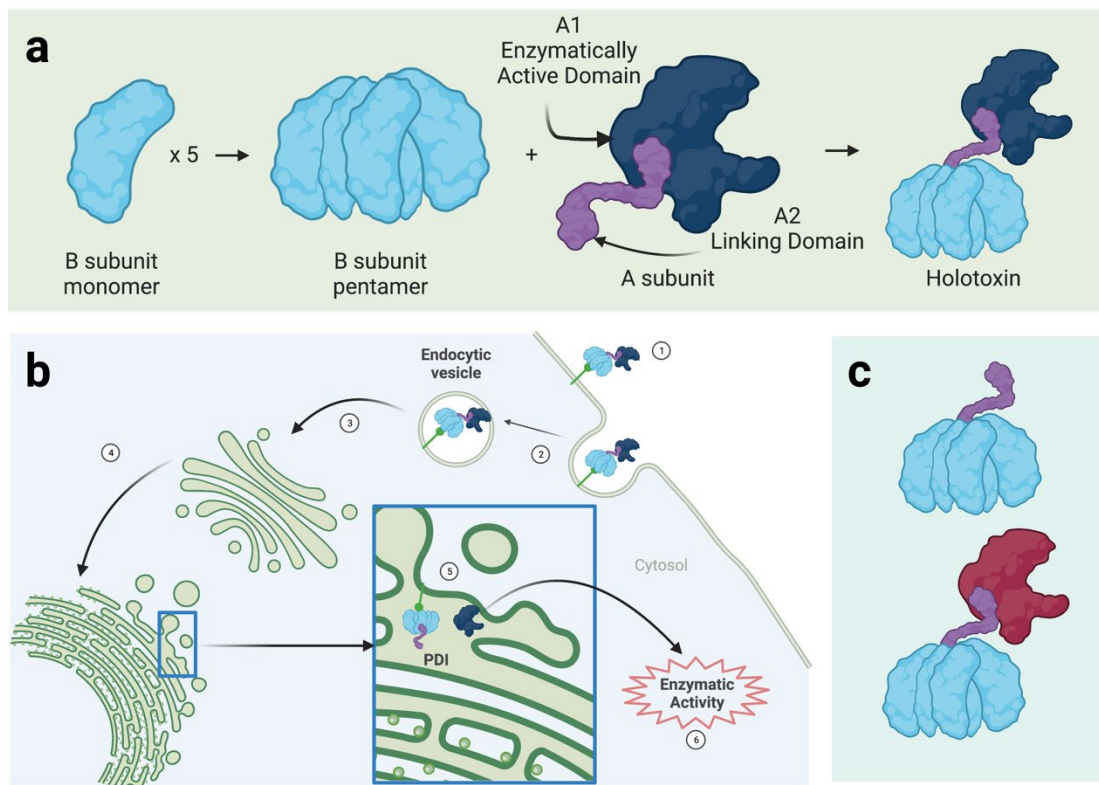
Figure 1.1.   Graphical Abstract

Diagrams showing (a) conserved AB5 toxin subunit multimerization to form holotoxin; (b) the trafficking pathway of an AB_5 toxin from binding (1), through internalization (2), retrograde transport through the trans-Golgi network (3) to the endoplasmic reticulum (4), separation and retrotranslocation of the active A subunit into the cytosol (5) and enzymatic activity (6); and (c) utility of A2/B5 linking domain/pentamer platform as a "Trojan horse tool" or vaccine adjuvant with the toxic A1 subunit removed (top) and replaced with an antigen from another source (bottom). Graphical abstract was created with biorender.com.

The intracellular activities of AB_5 toxins vary from increasing intracellular cAMP levels to inhibiting protein synthesis, but they all use the B_5 pentamer as the Trojan horse that grants them entry and carries them into the host cell. The pentamer binds to specific cellular receptors, allowing the toxin to be endocytosed, retrograde transported through the trans-Golgi network, and eventually released in the endoplasmic reticulum (ER). There, the A_1 and A_2/B_5 subunits are separated. The A_1 subunit unfolds and exits the ER via retrotranslocation by slinking through the cell's ER-associated degradation pathway for misfolded proteins. In the cytosol, the A_1 subunit rapidly refolds, avoiding proteolytic cleavage, and moves on to carry out its enzymatic battle assignment. Toxin entry is shown in the graphical abstract (Figure 1.1b).

In the 1990s and early 2000s, a surge of research on AB_5 toxins produced crystal structures, information about cellular receptors and trafficking pathways, and confirmation of enzymatic activities of some of the better-known toxins like *Vibrio cholerae*'s cholera toxin (CT), *Bordetella* pertussis's pertussis toxin (PT), and *Escherichia coli*'s heat-labile enterotoxins (LT and LTIIa). These studies have produced a robust literature collection which has been reviewed.[1–5] In more recent years, global efforts at genomic and proteomic sequencing and protein structural determinations have resulted in large amounts of searchable data. Combined with the rapid development of computational algorithms and artificial intelligence-based bioinformatics tools (with increasingly accessible user interfaces), new AB_5 toxins are being discovered on a regular basis. The first part of my work focuses on one such toxin called ADP-ribosylating toxin (ArtAB), which was discovered on the genome of *Salmonella* Typhimurium phage type DT104 in 2005.[6] Studies since its discovery have confirmed its membership in the AB_5

toxin family, but it has not yet been vigorously characterized. ArtAB is of interest due to its presence on an important and highly antibiotic resistant human and animal pathogen and for its close relationships to CT and PT.

CT is the toxin responsible for the profuse watery diarrhea that is characteristic of the disease cholera, caused by the bacterium *Vibrio cholerae*. The *Escherichia coli* heat-labile enterotoxins LT and LTIIa are closely related structurally and enzymatically to CT. PT is produced by *Bordetella pertussis*, the causative agent of pertussis, or whooping cough. All of these toxins, along with ArtAB, have A subunits that are ADP-ribosyltransferases, or ARTs. ARTs catalyze the singular transfer of one ADP-ribose moiety from one NAD+ molecule to a residue on a target protein. The ADP-ribosylation post-translational modification affects varied intracellular processes, many of which are discussed later. ARTs are found in all domains of life and have varying nomenclatures throughout the literature.[7–9] For the purpose of this dissertation, the abbreviation ART is consistently used in discussions of bacterial ADP-ribosyltransferases. For clarity, ArtAB was named for its ART activity (**ADP-r**ibosyl**t**ransferase with **AB** structure), but will only be referred to here as ArtAB, ArtA, or ArtB. Capital letters (ART) refer to the general class of ADP-ribosyltransferases.

The AB_5-type ARTs CT, PT, LT, and others have long been known to have adjuvant, or immunostimulatory and delivery, activity that is separate from their antigen capacity. These toxins can trigger immune responses to co-delivered antigens, even when delivered to surfaces like the skin or mucosa, which makes them very valuable components of vaccines for a variety of diseases.[10] CT and PT in particular are of interest because they are bacterial munitions that have been successfully repurposed by scientists

as weapons against the bacteria themselves. CT and PT have both been utilized in commercial vaccines that have been shown to be safe for humans and effective at preventing cholera and whooping cough, respectively.[11,12] LT and Shiga toxin B (STB) have also shown promise in a vaccine to prevent traveler's diarrhea caused by *E. coli*, although this vaccine has not yet made its way into an FDA-approved product.[13]

I have worked for the past four years in the lab of Dr. Juliette Tinker. The research in this lab focuses on the study of bacterial AB_5 toxins as both important virulence factors and as key components of vaccines. *Salmonella* produces a number of AB_5-type toxins that have only recently been discovered, including ArtAB. No human vaccine for non-typhoidal *Salmonella* has been licensed, and there is a great need to design improved *Salmonella* vaccines for animals. Dr. Tinker's lab has focused on AB_5 toxins from *Salmonella* with the idea that CT and PT made successful vaccines, so ArtAB may show promise as a *Salmonella* vaccine candidate. My work to characterize ArtAB provides foundational knowledge for future vaccine design.

For many years, the Tinker lab has also worked on the development of a vaccine platform based on the CTB pentamer. This platform requires using molecular cloning techniques to remove the toxic A_1 subunit from the holotoxin, thereby detoxifying the protein. The A_2/B_5 complex can then be used as a non-toxic Trojan horse to send any antigen of choice into a host cell where it can be processed by and interact with their immune system (Figure 1.1c). An antigen interacting with the immune system to produce a short- or long-term immune response is the definition of a vaccine. It sounds simple enough, but there are, of course, a multitude of steps that can go wrong in trying to attach an antigen to the A_2/B_5 complex. Even if an antigen is successfully attached via the

linking domain, proteins may not fold correctly or may encounter steric hindrance with the pentamer that prevents the vaccine from being useful. Work has been done to address these challenges.[14,15] The second part of my work focuses on a vaccine that Dr. Tinker and her previous students developed using *Staphylococcus aureus* antigens. *S. aureus* is a main causative agent of mastitis in dairy animals. I joined her lab just as they were finishing a bovine clinical trial and just in time to process milk and blood samples and perform assays for the immunogenicity portion of the study.

Before we dive into the chapters of this dissertation, I want to iterate that there are many facets to the subjects of bacterial AB_5 toxins and bacterial ARTs. One critical concept to remember is that not all AB_5 toxins have A subunits with ART activity, and not all ARTs have an AB_5 structure. This makes the work of investigating both AB_5 toxins and bacterial ARTs interesting! There are boundless questions that can be asked about A subunits, B_5 subunits, and holotoxins, and each answer affects our understanding of the others.

There are a few additional "answers" about AB_5 toxins and ARTs that I'd like to highlight. From an evolutionary standpoint, most of these bacterial toxins, including ArtAB[16–18], are phage-derived[19–23]. The mechanisms for selecting or carrying different A and B_5 subunits is still poorly understood, but likely involve phage host specificity. Interesting recent evidence shows that the B_5 subunits are somewhat interchangeable; different bacteria may carry similar B_5 subunits but unique A subunits, and some B_5 subunits can form complexes with alternate A subunits.[24] This flexibility apparently extends to the overall structure of the holotoxins as well; some toxins may even have "stackable" A subunits, as in the case of Typhoid toxin, which carries two distinct A

subunits with its pentamer.[16,25] Finally, despite a lack of defined catalytic roles, the

Trojan horse B$_5$ subunits have their own distinct effects on host cells and are known to

strongly stimulate the immune system.[26] While their distinct effects on host cells are

poorly defined, we have taken advantage of the immune response and can now repurpose

those pentamers as tools to send cargo into cells. My work has weaved in and out of each

of these overarching themes, tugging at the threads of many questions. Below is a brief

orientation to the work that follows this introduction. Each chapter involves a distinct

facet of the AB$_5$/ART toxins theme, and, as such, has its own fairly comprehensive

introductory section to orient the reader to the current state of knowledge on each topic.

Chapter two includes our most recent publication. The introduction provides a

deeper orientation to *Salmonella* Typhimurium DT104 and to the ArtAB toxin. As part of

this study, we developed a method for purifying large amounts of recombinant ArtAB

from *E. coli*. We then used our purified toxin to explore the effects the toxin has on

mammalian cells, which had not previously been done. We defined a morphological

phenotype for cells treated with ArtAB and characterized its effects on cellular metabolic

activity and proliferation, and we obtained preliminary data on the B subunit's distinct

cellular effects.

Chapter three comprises my most independent chapter. It begins with a much

deeper review of the ancient and conserved ART tertiary structure. Since no crystal

structure of ArtAB exists yet, I established a predicted model for ArtAB and used the

model to define ArtAB's relationship to other related toxins as well as to investigate the

potential active site. I used biophysical techniques to gather preliminary structural

information about our purified ArtAB, and I created a set of mutants with mutations in

critical residues as determined with the modeling work. I then tested the mutants to determine the mutations' effects on ArtAB's catalytic activity. This chapter concludes with an outline of next steps for a future graduate student to continue characterizing the structure of ArtAB and a consideration of its utility in a *Salmonella* vaccine.

Chapter four addresses the effects of ArtAB on paracellular barrier and adhesion molecule function. AB_5 toxins are known to affect cellular barriers, however, the mechanisms are still poorly understood. The literature on this topic is sparse and presents more questions than answers. This is a discussion-heavy chapter with a small amount of data presented. We designed and executed many experiments hoping to tie some of these threads together, however, we encountered many roadblocks that were insurmountable with our time and resource limitations. I include this chapter mainly because the work to review the literature and to design experiments will be useful to someone in the future, and the challenges are not intractable given time (and funding). I have included complete methods sections outlining what has been done and what issues we encountered so that the next student may address and, hopefully, avoid these same pitfalls.

Chapter five moves away from the ArtAB investigations and describes the design, execution, and outcomes of a bovine trial with a vaccine to prevent mastitis, or infection of the udder, which is caused by the bacterium *Staphylococcus aureus*. This study uses the A_2/B_5 platform to promote intranasal delivery of a vaccine containing *S. aureus* antigens. The introduction includes a summary of the current state of bovine mastitis and the implications this vaccine could have in the dairy industry. We tested the vaccine in six cows. Though the sample size was low, we obtained valuable data about the immunogenicity of the vaccine and laid the groundwork for future, larger studies.

Finally, I conducted a short preliminary project to investigate the potential of constructing a caprine vaccine in the same way that we did the bovine vaccine for the mastitis trial. The study was small, using only three clinical isolates, so I have included this study as an Appendix (Appendix A). Each isolate was screened for the presence of surface antigens that are known to be conserved and/or immunogenic. This chapter should provide a foundation for future studies on B_5 pentamer-based caprine vaccine development.

The studies that focus on the *Salmonella* toxin, ArtAB, will add to the expanding body of knowledge about ADP-ribosylating AB_5 toxins. In particular, this work consolidates some of the many resources in the literature regarding these toxins and will be useful as a foundation for future researchers in the field. Understanding the catalytic activity of a superfamily of toxins permits future work on how to harness that activity and use it as either a therapeutic tool or target.

The work on the *S. aureus* vaccine highlights the specific utility of AB_5 toxins as vaccine adjuvants. Having vaccines against infectious diseases in the animal food production industry improves the lives of the animals, reduces the bulk amount of antibiotics required for treatment, and saves producers both time and money. The contributions here will push the bovine mastitis vaccine's development forward and facilitate the future design of a caprine version of the vaccine.

And, finally, as Dr. Tinker frequently reminds me – there is no end product in science. Each answer leads to more questions. I certainly have more questions. I have attempted to be as thorough as possible in my methods sections so that this work will be

useful to someone else in the future and so that someday some of these questions may be

answered.

CHAPTER TWO: CELLULAR ACTIVITY OF *SALMONELLA* TYPHIMURIUM

ARTAB TOXIN AND ITS RECEPTOR-BINDING SUBUNIT

Elise Overgaard[1], Brad Morris[2], Omid Mohammad Mousa[2], Emily Price[3], Adriana Rodriguez[2],Leyla Cufurovic[2], Richard S. Beard[4] and Juliette K. Tinker[1,2,*]

[1]   Biomolecular Sciences Graduate Program, Boise State University, Boise, ID
[2]   Department of Biological Sciences, Boise State University, Boise, ID
[3]   Idaho Veterans Research and Education Foundation, Infectious Disease Section, Boise, ID
[4]   Biomolecular Research Center, Boise State University, Boise, ID
*   Correspondence: juliettetinker@boisestate.edu

Authorship statement: My direct contributions to this manuscript included conceptualization and methodology of the experiments; investigation, including performing the work of expression and purification of ArtAB-His, ArtAB, and ArtB from *E. coli*, binding and internalization slides, binding ELISAs, cellular morphology and metabolic/cytotoxicity studies, and cell length measurements; data curation, visualization, and formal analysis; writing the manuscript, and preparing it for submission with Dr. Tinker's help.

Abstract

Salmonellosis is among the most reported foodborne illnesses in the United States. The *Salmonella enterica* Typhimurium DT104 phage type, which is associated with multidrug-resistant disease in humans and animals, possesses an ADP-ribosylating toxin called ArtAB. Full-length *art*AB has been found on a number of broad-host-range non-typhoidal *Salmonella* species and serovars. ArtAB is also homologous to many AB_5 toxins from diverse Gram-negative pathogens, including cholera toxin (CT) and pertussis toxin (PT), and may be involved in *Salmonella* pathogenesis, however, in vitro cellular toxicity of ArtAB has not been characterized. *art*AB was cloned into *E. coli* and initially isolated using a histidine tag (ArtAB-HIS) and nickel chromatography. ArtAB-HIS was found to bind to African green monkey kidney epithelial (Vero) cells using confocal microscopy and to interact with glycans present on fetuin and monosialotetrahexosylganglioside (GM1) using ELISA. Untagged, or native, holotoxin (ArtAB), and the pentameric receptor-binding subunit (ArtB) were purified from *E. coli* using fetuin and D-galactose affinity chromatography. ArtAB and ArtB metabolic and cytotoxic activities were determined using Vero and Chinese hamster ovary (CHO) epithelial cells. Vero cells were more sensitive to ArtAB, however, incubation with both cell types revealed only partial cytotoxicity over 72 hours, similar to that induced by CT. ArtAB induced a distinctive clustering phenotype on CHO cells over 72 hours, similar to PT, and an elongated phenotype on Vero cells, similar to CT. The ArtB binding subunit alone also had a cytotoxic effect on CHO cells and induced morphological rounding. Results indicate that this toxin induces distinctive cellular outcomes. Continued

biological characterization of ArtAB will advance efforts to prevent disease caused by non-typhoidal *Salmonella*.

Introduction

Salmonellosis, caused by the Gram-negative bacteria *Salmonella*, is one of the most common foodborne diseases in the world.[27,28] Non-typhoidal serovars of *Salmonella* (NTS) generally cause self-limiting gastroenteritis. However, they can cause systemic infections and are increasingly antibiotic resistant, resulting in an estimated 1.35 million illnesses and 420 deaths per year in the U.S.[29] *Salmonella* has a complex taxonomy and is a diverse human and animal pathogen. *Salmonella enterica*, one of two overall species, has six subspecies. One subspecies, *enterica* (*Salmonella enterica*, subsp. *enterica*), contains over 2500 serovars. The NTS within this subspecies are pathogenic to a broad range of vertebrate species, including humans and human food sources such as cattle, swine, and poultry.[30,31] This is in contrast to the narrow host range of the human typhoidal serovars *S.* Typhi and *S.* Paratyphi, which cause severe invasive disease with a high mortality rate but with lower numbers of cases globally.

The virulence factors contributing to *Salmonella enterica* pathogenicity are numerous and include well-characterized secretion systems, adhesins, and capsular polysaccharides.[32] In the mid-1990s, the NTS phage-type *S.* Typhimurium DT104 became the predominant strain infecting livestock and was commonly associated with human hospitalization.[33] DT104 is highly antibiotic resistant and virulent, however, studies have failed to fully identify the mechanism of increased virulence.[34,35] In 2005, DT104 was found to contain an enterotoxin, with homology to AB_5-type toxins, called artAB.[6] AB_5-type toxins are potent virulence factors produced by many pathogenic Gram-negative bacteria. They are composed of a pentameric B subunit (B_5), which binds to host cell-surface receptors, and an A subunit, which becomes catalytically active inside

the host cell. AB_5-type toxins contribute to the development of infectious diseases associated with altered ion flow across membranes and disruption of epithelial barrier function.[36,37] *art*AB has since been identified on a number of additional *S. enterica* serotypes, and on *S. bongori*, and has been determined to be a secreted ADP-ribosylating toxin with homology to the AB_5-type toxins cholera toxin (CT) and pertussis toxin (PT).[16,38,39]

CT and PT are two of the most well-characterized bacterial toxins. CT, produced by *Vibrio cholerae*, is folded into a holotoxin in the bacterial periplasmic space prior to secretion and interaction with the host cell. CT becomes activated when the active subunit (CTA) is proteolytically cleaved, or nicked, by a host serine protease.[40] After secretion, the binding subunit (CTB) binds to monosialotetrahexosylganglioside (GM1), which is expressed on the surface of intestinal epithelial cells. This interaction triggers retrograde endocytosis of the CT holotoxin to the endoplasmic reticulum (ER). In the ER, CTA becomes separated from CTB and moves into the host cell cytoplasm where it binds to, and constitutively activates, the $G_{\alpha s}$ protein through ADP ribosylation. $G_{\alpha s}$ activates adenylyl cyclase (AC), causing an increase in cyclic adenosine monophosphate (cAMP), which leads to dysregulation of cellular ion channels and, ultimately, secretory diarrhea. PT, produced by *Bordetella pertussis*, is a homologous AB_5 toxin with mechanistic similarities. However, the B subunit is structurally distinct and binds to a broader range of sialylated and non-sialylated N-linked glycans.[41] PT's active subunit (PTA) has a distinct ADP-ribosylation target; it inactivates $G_{\alpha i}$. Despite having different ADP-ribosylation targets, the outcome is similar; AC is activated, and cellular cAMP is increased. CT and PT are also both components of licensed safe and effective

vaccines.[12,42] The ability to chemically or genetically detoxify CT, PT, and other AB_5 toxins while retaining antigenicity and immunomodulatory characteristics has supported their use as vaccine adjuvants and molecular tools for cellular delivery.[43–46] Thus, in addition to improving the understanding of *Salmonella* pathogenesis, the study of the cellular activities of ArtAB and ArtB is relevant to vaccine design and development.

While the ADP-ribosylation activity and in vivo lethality of ArtAB have been reported, the cellular activity, including the cytotoxicity and morphologic activities, of ArtAB and its receptor-binding subunit, ArtB, have not been previously described.[38,39] In addition, despite numerous studies on various AB_5-type toxins, few studies have directly compared the cellular effects of these toxins. The goals of this study were to develop a rapid method of purification of ArtAB and ArtB from *E. coli* and to use the purified proteins to identify a reproducible and consistent cellular phenotype *in vitro*. Results indicate that ArtAB induces a slow cytotoxic response and characteristic changes in cellular morphology, similar to the responses induced by CT and PT. ArtB alone may also be cytotoxic, and it induces a distinct morphologic response. These studies will promote further structural and functional characterization of ArtAB and improve our understanding of its role in *Salmonella* pathogenesis.

Materials and Methods

<u>Bacterial Strains and Growth Conditions</u>

Salmonella enterica Typhimurium phage-type DT104, isolates SC09039, SC09068, SC09073, SC09074, are human gastroenteritis clinical isolates obtained from the Idaho Bureau of Laboratories (Boise, ID) and used for genomic DNA preparation, *art*AB PCR, and sequencing. The isolate SC09039 was used for *art*AB and *art*B cloning and purification. Human clinical *S.* Typhi, *S.* Paratyphi A and *S.* Choleraesuis genomic DNA was supplied by the Idaho Bureau of Laboratories for PCR. *E. coli* TE1[47] was used for cloning, and *E. coli* ClearColi® BL21(DE3) (Lucigen) was used for protein expression and toxin isolation. For genomic DNA preparation, bacterial cells were grown overnight in Luria Broth (LB) at 37 °C. For plasmid preparation, cells were grown in LB plus 25 μg/mL chloramphenicol (CM) and 0.02% glucose overnight at 37 °C.

<u>Phylogenetic Analysis and Predicted Tertiary Structure of AB$_5$ Toxin Subunits</u>

Sequence alignments and evolutionary analysis were completed using MEGA 7.[48] A rooted dendrogram of exhaustive pairwise AB$_5$ toxin alignments of 20 sequences (A subunits) or 19 sequences (B subunits) was constructed using the maximum-likelihood method based on the JTT matrix-based model.[49] Protein sequences were retrieved from the National Center for Biotechnology Information NCBI. Available online: https://www.ncbi.nlm.nih.gov/ (accessed online on 22 May 2020) and accession numbers are provided in Supplementary Table 2.S1. The I-TASSER server was used to visualize predicted tertiary structures of ArtA and ArtB using the model templates: *E. coli* SubB[50] for ArtB and *E. coli* PltA[51] for ArtA.[52,53]

Construction of ArtAB-HIS, ArtAB, and ArtB Expression Plasmids

The *art*AB gene was amplified from *S.* Typhimurium DT104 SC09039 by polymerase chain reaction (PCR) from isolated genomic DNA using the 070pr forward primer (GATCCTCGCTAGCGTTTCTGTAGGAGGGTGTATG) and the 071pr reverse primer (GTACCAGAAGCTTTTAGTGATGGTGATGGTGATGGTTTGGCAACGTAGGTCCC), that introduces a 6XHIS. The amplified product was cloned into the pBAD18CM vector (ATCC, Manassas, VA) and transformed into *E. coli* TE1 for confirmation prior to introduction into the endotoxin-free *E. coli* strain ClearColi® (Lucigen, Madison, WI) for protein production. The resulting plasmid (Supplementary Figure 2.S2A) was designated pBM003. For pBM006 construction (Figure 2.3A), the *art*AB gene was amplified from DT104 SC09039 using the forward primer 070pr and the reverse primer 099pr (GCGCCAGAAGCTTGAAATATTTAGTTTGGCAACGTAG). The amplified product was similarly cloned into pBAD18CM and transformed into *E. coli* TE1 and ClearColi®. To clone artB alone into pLC001 (Figure 2.3D), the forward primer, 198pr (GCCTAGGGCTAGCGGTAAATATTTTAGGAGTGG), which contains a modified ribosome-binding site, and the reverse primer, 099pr, were used to amplify *art*B from *S.* Typhimurium SC09039, and the resulting product was cloned into pBAD18CM and purified from ClearColi®. The sequences of pBM003, pBM006, and pLC001 were confirmed by sequencing through forward and reverse junctions (Idaho State University Molecular Research Core Facility, Pocatello, ID).

Expression and Purification of ArtAB-HIS, ArtAB, and ArtB from *E. coli*

ClearColi® transformed with plasmid pBM003 was cultured in LB containing 25

µg/mL CM and 0.02% glucose overnight at 37 °C. Overnight cultures were then

transferred to Terrific Broth (TB) with 25 µg/mL CM and shaken at 37 °C. When the

culture reached an optical density between 0.6 and 0.9, protein expression was induced

with 0.2% l-arabinose. Induced cultures were shaken overnight at 37 °C. After

centrifugation, the harvested cells were resuspended and protein was extracted from the

periplasmic space by the addition of 1 mg/mL polymyxin B. The cell extract was

collected by centrifugation and phenylmethylsulfonyl fluoride (PMSF) was added at 100

µM. The extract was purified using cobalt affinity column chromatography (HisPur™

Cobalt Resin, Thermo Fisher Scientific, Waltham, MA, USA) per the manufacturer's

instructions. Fractions were collected in 1.5 mL aliquots and confirmed using SDS-

PAGE. Fractions containing ArtAB-HIS were pooled and dialyzed using 12,000 Da-

molecular-weight cutoff (MWCO) dialysis cassettes (Slide-A-Lyzer™, Thermo Fisher

Scientific) against 1× PBS + 5% glycerol at 4 °C overnight with one buffer change after 6

hours. Dialyzed sample was further concentrated using a 50,000 Da MWCO

concentration filter (Amicon Ultra-15, Merck Millipore Ltd., Thermo Fisher Scientific).

Molecular weight and purity were confirmed using SDS-PAGE and Western blot with α-

HIS6 primary (1:2500 Abcam, Cambridge, MA, USA) and HRP-conjugated goat α-rabbit

IgG secondary (1:5000, Promega, Madison, WI, USA) antibodies. Protein concentration

was determined by bicinchoninic acid (BCA) protein assay (Pierce™ BCA Protein Assay

Kit, Thermo Fisher Scientific) using bovine serum albumin (BSA) as a standard.

For purification of native ArtAB and native ArtB, *E. coli* ClearColi® was transformed with plasmid pBM006 or pLC001and induced protein isolated from the *E. coli* periplasmic space as above for pBM003. The extract was purified using immobilized D-galactose affinity column chromatography (Pierce™ D-galactose Agarose, Thermo Fisher Scientific), as described.[54] Column equilibration and washing were performed using 1× PBS, and elution was performed using 1 M D-galactose (ACROS Organics™). Fractions were collected in 1.5 mL aliquots and confirmed with SDS-PAGE. Fractions containing ArtAB or ArtB were pooled and dialyzed in 12,000 Da MWCO dialysis cassettes (Slide-A-Lyzer™, Thermo Fisher Scientific) against 1× PBS + 5% glycerol at 4 °C overnight with one buffer change after 6 hours. Dialyzed samples were concentrated using a 50,000 Da MWCO disposable filter (Amicon Ultra-15, Merck Millipore Ltd., Thermo Fisher Scientific). Molecular weight and purity were confirmed with SDS-PAGE, and protein concentration was determined by BCA protein assay (Pierce ™ BCA Protein Assay Kit, Thermo Fisher Scientific) using BSA as a standard. Protein sequences were confirmed by LC–MS (Supplementary Figure 2.S2, Table 2.S3).

ELISA Binding Assays

Flat-bottomed 96-well plates (Nunc MaxiSorp™, Invitrogen, Thermo Fisher Scientific) were coated with either 10 µg/mL fetuin in 1× PBS or 0.15 µM GM1 in DMSO + 1× PBS. Plates were incubated overnight at room temperature. After washing and blocking plates for 1 hour in blocking buffer (1% skim milk powder + 0.05% Tween-20), the toxins CT (List Biological Labs, Inc., Campbell, CA, USA) or ArtAB-HIS were added to the first well at a concentration of 20 µg/mL or 10 µg/mL. Serial two-fold dilutions into blocking buffer were performed and plates were incubated for 2 hours at 37

°C. After washing, rabbit anti-6XHIS antibodies (Bethyl Laboratories, Inc., Montgomery, TX, USA) or rabbit anti-CT antibodies (Sigma-Aldrich, St. Louis, MO, USA) were added at 1:5000 dilution and incubated at 37 °C for 1 hour. After washing, goat anti-rabbit HRP-conjugated antibodies (Pierce®, Thermo Fisher Scientific) were added and incubated at 37 °C for 1 hour. Plates were developed with tetramethylbenzidine (TMB) (PromegaTM TMB One, Thermo Fisher Scientific) and read at 370 nm per TMB manufacturer's instructions using a BioTek Cytation 3 imager. ArtAB ELISAs were compared to the average of a no-toxin negative control coated with fetuin or GM1 and using anti-6XHIS antibody. Titers were defined as the reciprocal of the highest dilution at a 370 nm absorbance cut off of 0.2. Titers represent the averages of four independent assays performed in triplicate for ArtAB, or the average of four independent assays for CT.

Cell Culture

African green monkey kidney (Vero; ATCC, Manassas, VA, USA) cells were cultured in Dulbecco's modified Eagle's medium (DMEM) (Corning®, Thermo Fisher Scientific) supplemented with 10% fetal bovine serum (FBS; HyClone™, Thermo Fisher Scientific), or bovine growth serum (BGS; HyClone™, Thermo Fisher Scientific) and 1% penicillin/streptomycin (Thermo Fisher Scientific). CHO-K1 cells (CHO; ATCC®) were cultured in Ham's F-12 medium (Corning®, Thermo Fisher Scientific) supplemented with 10% FBS and 1% penicillin/streptomycin. Cells were maintained in T-flasks at 37 °C in a humidified 5% CO_2 incubator and were passaged at 80% confluency using 0.05% trypsin/EDTA. Serum-free cell starvation procedures were

completed with media (DMEM for Vero cells, Ham's F-12 for CHO-K1 cells)

supplemented with 1% penicillin/streptomycin but without FBS/BGS.

Cellular Activity and Morphology Assays

      Cellular activity was assessed using alamarBlue™ and crystal violet assays. 96-

well plates were seeded with Vero or CHO-K1 cells at a density of 5000 cells per well in

200 μL of complete culture media and incubated overnight. Cells were starved in serum-

free media for 4 hours prior to treatment. ArtAB, or ArtB, in a buffer of 1× PBS + 5%

glycerol at a concentration of 10 μg/mL (2 μg total in 200 μL), 25 μg/mL (5 μg total in

200 μL), or 50 μg/mL (10 μg total in 200 μL); or CT (List Biological Labs, Inc) in a

buffer of 1× PBS at a concentration of 10 μg/mL (2 μg total in 200 μL); or PT (List

Biological Labs, Inc.) in a buffer of 1× PBS at a concentration of 10 μg/mL (2 μg total in

200 μL); or respective buffer alone (vehicle) in complete culture media was added to the

cells. Each treatment was added to 6 wells per plate. One replicate included an individual

plate for each of four post-dose time points. Plates for one replicate were treated at the

same time, incubated, and removed from the incubator at the appropriate time point (4-,

24-, 48-, or 72-hours post-treatment) for analysis. Three replicates each were completed

on Vero cells and CHO-K1 cells. Statistical analysis was completed on one representative

replicate (plate) for each cell line (n = 6).

      After 4, 24, 48, or 72 hours of incubation with treatment, brightfield microscopy

images at 20× magnification were collected using a BioTek Cytation 3 imager. Images

were collected randomly from varied locations within wells and from multiple wells for

each treatment dose. Immediately after imaging, 200 μL of 10% (v/v) alamarBlue™

(Invitrogen™) in complete culture media was added to each well and plates were

incubated for 4 h. Fluorescence was read on the BioTek Cytation 3 imager using excitation wavelength of 560 nm and emission wavelength of 590 nm per alamarBlue™ manufacturer's instructions. Light microscopy image files were analyzed using ImageJ Download for Mac OS X. Available online: https://imagej.nih.gov/ij/download.html (Accessed on 22 July 2021). For each image, scale was set according to the pixel:length relationship of the scale bar. Cell length was measured on adherent cells only with a line drawn between the two most distant edges and centered through the middle of the cell body. Dendrites were followed as long as the line could be kept centered in the cell body. Measurements were collected for ten cells in each of three or four frames where each frame represented an independent well for a total of 30 measurements per treatment group.

After collection of fluorescence data, alamarBlue™ and media were removed and cells were rinsed 3 times with 200 μL 1× PBS. Crystal violet assays were performed per Cold Spring Harbor Protocols.[55] Briefly, 50 μL of crystal violet solution was added to each well and the plates were incubated for 20 minutes at room temperature with agitation on an orbital shaker. Crystal violet solution was removed and the cells were rinsed 3 times with deionized water with care given not to lift cells from the plates. Plates were air dried overnight. The next day, 100 μL methanol was added to each well and the plate was incubated for 20 minutes at room temperature with agitation on an orbital shaker. Absorbance at 570 nm was read on the BioTek Cytation 3 imager.

Results

<u>Phylogenetic Analysis of AB$_5$ Toxin Subunits</u>

      Phylogenetic trees were constructed with MEGA using the maximum-likelihood method to align the amino acid sequences of *S.* Typhimurium DT104 ArtA and ArtB to those of AB$_5$ toxin subunits from other Gram-negative bacteria.[48] As shown in Figure 2.1A, the enzymatically active ArtA subunit is most closely related to ArtA from *S.* Worthington and *S. bongori*, as described.[38] *S.* Typhimurium DT104 ArtA is also related to the active subunit of an AB$_5$ toxin from *E. coli* (68% identity), which has been named previously as both pertussis-like toxin (*Ec*PltA) and ArtA.[51,56] *S.* Typhimurium DT104 ArtA also has homology (58% identity) to *S.* Typhi PltA, an active subunit of the *S.* Typhi pertussis-like toxin (Plt). Plt is also commonly referred to as typhoid toxin (TT). Plt/TT is a unique A$_2$B$_5$ toxin that utilizes two active subunits: PltA and CdtB. CdtB has nuclease activity and low homology (18% identity) to *S.* Typhimurium DT104 ArtA.[57] ArtA also shows significant relatedness to a pseudogene found in both *S.* Typhi and *S.* Montevideo (90% identity over a 99 amino acid central region), that is unlikely to be expressed.[58] Lastly, ArtA is distantly related to the active subunits of PT (PTA S1; 28% identity), an uncharacterized AB$_5$ toxin from *Yersinia* (YtxA; 26% identity), *E. coli* type IIa heat-labile enterotoxin (LTIIaA; 24% identity), and CT (CTA; 23% identity).
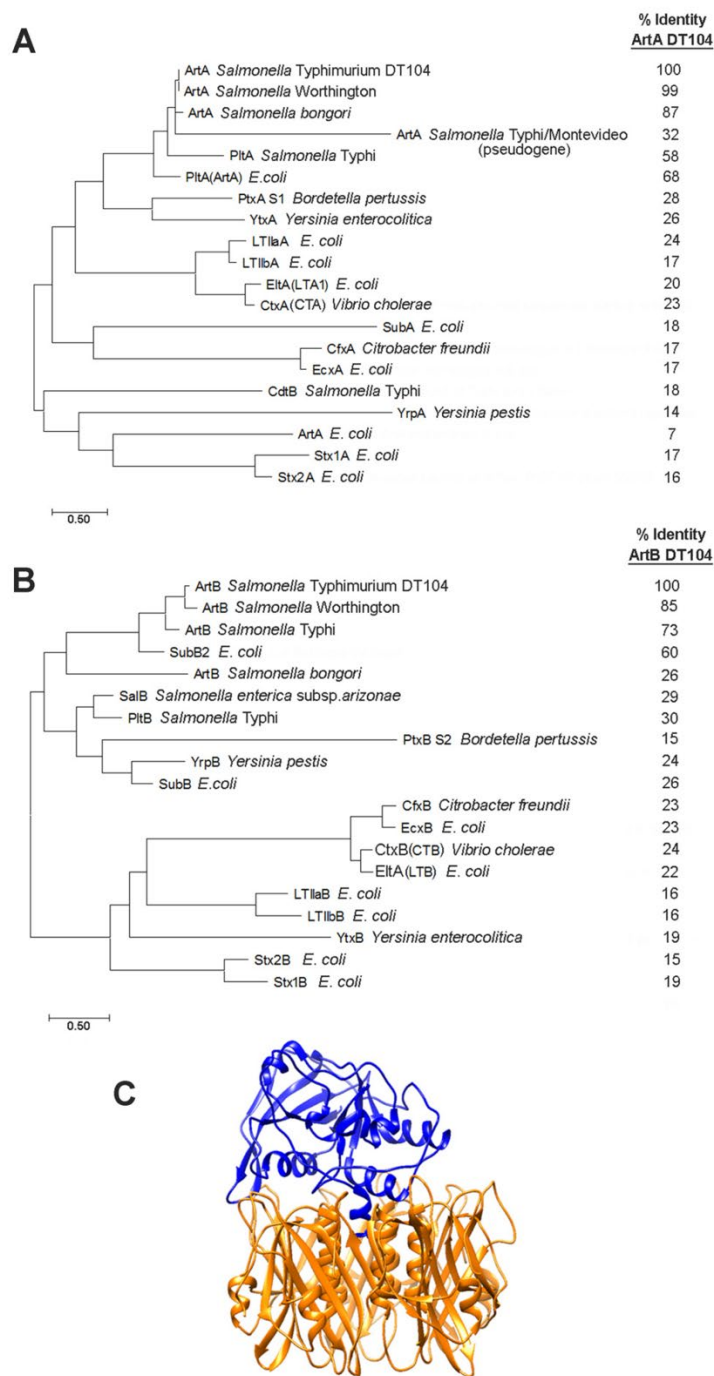
Figure 2.1. **Phylogeny and predicted tertiary structure of ArtAB and closely related AB$_5$ toxins**

(A) phylogenetic analysis of enzymatically active (A) subunits of AB$_5$ toxins, and (B) binding (B) subunits of AB$_5$ toxins, as constructed with MEGA7 software using a maximum-likelihood method based on the JTT matrix-based model.[48] (C) I-TASSER Salmonella DT104 ArtAB tertiary structure prediction based on E. coli SubB and S. Typhi PltA subunit crystal structures showing the pentameric B subunit (gold) and the active A subunit (blue).[59]

Figure 2.1B shows the phylogenetic relationships of *S.* Typhimurium DT104 ArtB, which is most closely related to the B subunits from *S.* Worthington and *S.* Typhi (85 and 73% identity, respectfully). An uncharacterized subtilase cytotoxin-like binding subunit (SubB2) from *E. coli* shows 60% identity to *S.* Typhimurium DT104 ArtB, while the more well characterized *E. coli* subtilase cytotoxin B (SubB), which has been shown to promote the binding to sialylated glycans, has only limited homology (26% identity).[50] *S.* Typhimurium DT104 ArtB has low homology to the binding subunit of Plt/TT (PltB; 30% identity), supporting previous glycan array studies that revealed ArtB's specificity for sialylated glycans that are distinct from those that bind with PltB.[24,52] *S.* Typhimurium ArtB has more limited homology to the well-characterized binding subunit of CT (CTB; 24% identity), as well as to the likely AB$_5$ toxins from *S. arizonae* (SalB; 29% identity), *S. bongori* (ArtB; 26% identity), and *Yersinia pestis* (YrpB; 24% identity). PT has four distinct binding subunits, and ArtB has some limited homology to the second (PtxB S2; 15% identity). A ribbon diagram of the predicted structure of ArtAB was constructed using I-TASSER and is shown in Figure 2.1C.[53,59]

The *art*AB-like operons from a non-DT104 *S.* Typhimurium isolate, as well as *S.* Typhi, *S.* Paratyphi, and *S.* Choleraesuis were analyzed by PCR and compared to four human clinical *S.* Typhimurium DT104 isolates using flanking primers of the *art*AB region (Supplementary Figure 2.S1A). The smaller amplicons of 957 and 954 bp, respectively, support the presence of the homologous *art*B gene and a truncated pseudogene which contains a deletion within *art*A (Supplementary Figure 2.S1B).

Purification and Binding of ArtAB-HIS

       S. Typhimurium DT104 *art*AB was cloned into the pBAD18 expression vector with a hexa-histidine tag (6XHIS) introduced at the C-terminus of the B subunit to construct pBM003 (Supplementary Figure 2.S2A). Holotoxin was purified using cobalt affinity chromatography. Purified toxin with the expected molecular weights of processed (signal sequence removed) ArtA (~25.6 kDa) and ArtB-HIS (~14.2 kDa) were confirmed using SDS-PAGE, western blotting (Supplementary Figure 2.S2B), and protein sequencing by mass spectrometry (Supplementary Table S2). A consistently co-purified, but unexpected, second small peptide (~13 kDa) was also confirmed to be ArtB by protein sequencing (Supplementary Figure 2.S2C, Supplementary Table S2). This peptide was not HIS-tagged, as determined by anti-6XHIS western blot (Supplementary Figure 2.S2B).

       We assessed the binding of ArtAB-HIS to epithelial cells in vitro using fluorescence microscopy. After 1 hour at 4 °C to block endocytosis, ArtAB-HIS was found to be surface-associated on African green monkey kidney epithelial (Vero) cells. After 1 hour at 37 °C, the toxin was no longer visible on the cell surface, but microscopy revealed potential punctate staining within the cell that was above background levels (Figure 2.2A).
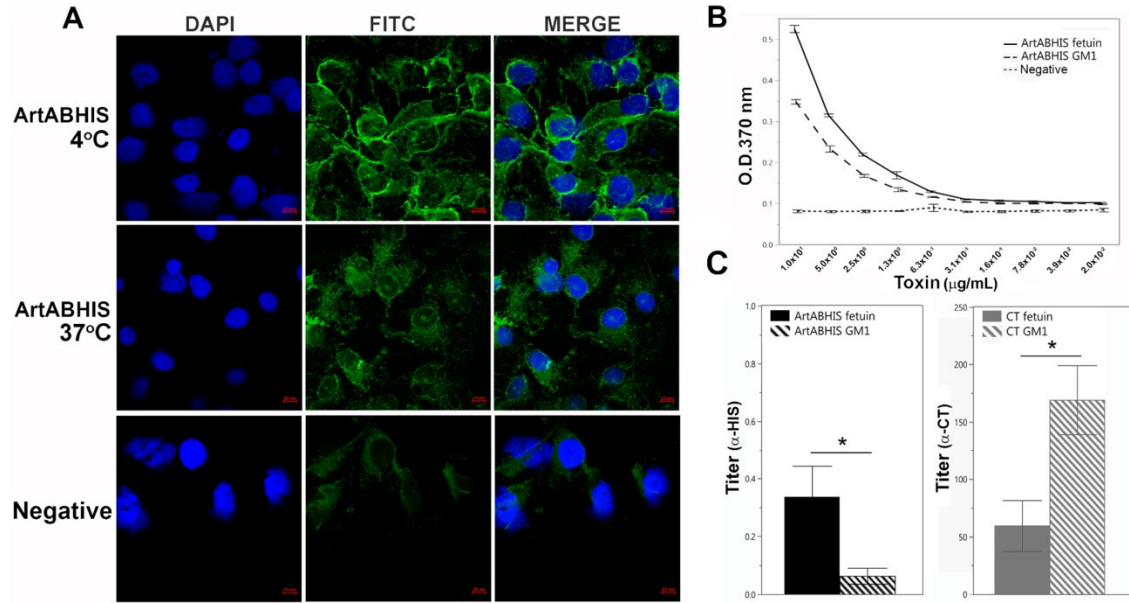
Figure 2.2. **Characterization of ArtAB-HIS purified from *E. coli***

(A) binding (at 4 °C) and uptake (at 37 °C) of 50 μg/mL ArtAB-HIS after 1 hour on Vero cells using anti-6XHIS (α-HIS) and FITC-conjugated secondary antibodies (negative = no toxin control, scale bar = 10 μm), (B) representative ELISA dilution series of ArtAB-HIS on ganglioside GM1 and fetuin (negative = no toxin control), and (C) average titers of fetuin and GM1 ELISAs of ArtAB-HIS using α-HIS and CT using anti-CT (α-CT) antibody. Results show the mean +/− SE (n = 4). A two-tailed, unpaired t-test was performed for comparison within each toxin group (ArtAB-HIS fetuin to GM1 * p = 0.0487; CT fetuin to GM1 * p = 0.0262).

To begin to assess the binding specificity of ArtAB-HIS, we performed ELISA-based binding assays with purified ArtAB-HIS. Since CT is known to have a strong binding affinity for GM1 and some affinity for the sialylated glycans found on the blood protein fetuin, we performed a comparative assay with these two receptor molecules using anti-6XHIS (for ArtAB) or anti-CT (for CT) antibodies.[60,61] ArtAB-HIS bound to fetuin with consistently higher titers than to GM1 (Figure 2.2B,C), while CT bound to GM1 with higher average titers (Figure 2.2C).

Cloning and Glycan Affinity Purification of ArtAB and ArtB

To eliminate potential interference of the affinity tag with toxin assembly and receptor binding, native (untagged) ArtAB was purified using glycan affinity chromatography. This approach was based on methods of purification of other AB$_5$

toxins and the observed binding of ArtAB-HIS to fetuin and GM1. The plasmid pBM006 (Figure 2.3A) was constructed to express untagged *S.* Typhimurium DT104 ArtAB, and the toxin was purified using fetuin affinity chromatography with increasing salt concentrations based on reported protocols for PT.[62] Purified holotoxin with the expected subunit molecular weights of ArtA ($\cong$ 25.6 kDa) and ArtB ($\cong$ 13.3 kDa) was confirmed using SDS-PAGE (Figure 2.3B) and mass spectrometry (Supplementary Table 2.S2).
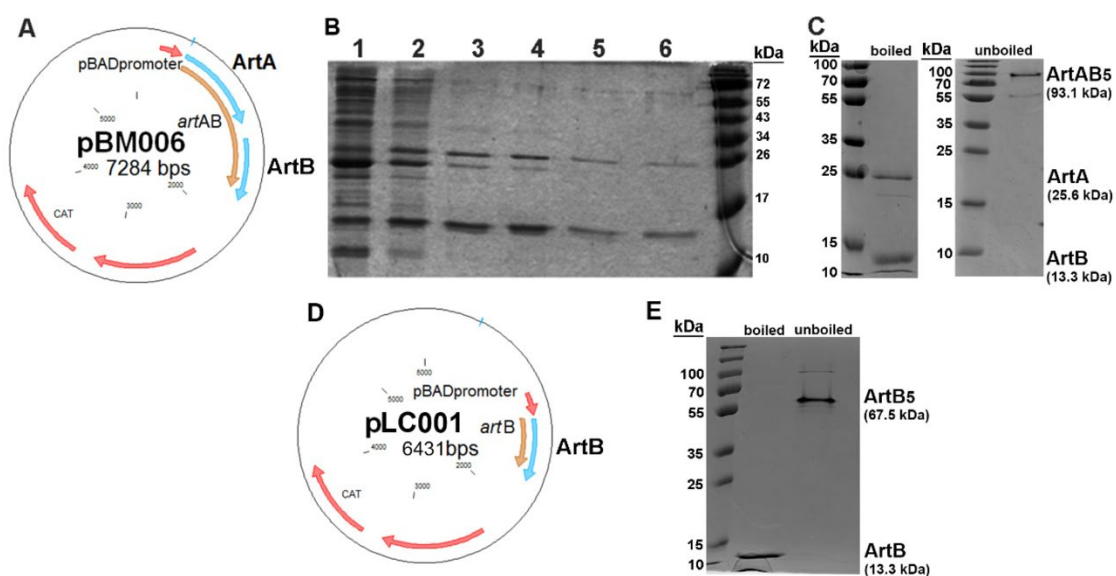
Figure 2.3.   Purification of ArtAB and ArtB from *E. coli*

(A) plasmid pBM006 for expression of ArtAB, (B) SDS-PAGE of ArtAB purified with fetuin, showing increasing salt fractions (1: flow through, 2: 0.1 M NaCl, 3: 0.1 M MgCl2, 4: 0.5M NaCl, 5: 0.5M MgCl2, 6: 1 M NaCl). (C) SDS-PAGE of the ArtAB elution purified with D-galactose, and boiled/unboiled samples, (D) plasmid pLC001 for expression of ArtB and (E) SDS-PAGE of the ArtB elution purified on D-galactose, boiled and unboiled samples.

As determined from ArtAB-HIS binding assays, ArtAB also binds to ganglioside GM1. GM1 contains D-galactose moieties, thus ArtAB holotoxin was also purified using D-galactose affinity chromatography. Purified ArtAB was confirmed with SDS-PAGE (Figure 2.3C), and unboiled samples supported an AB5 composition of approximately 93 kDa. Despite evidence that ArtAB binds less well to GM1, native ArtAB isolated using immobilized D-galactose was of markedly higher purity than native ArtAB isolated on

fetuin, and had higher purification efficiency, with close to 6 mg of protein purified from one liter of culture (versus 2–4 mg/liter using fetuin). SDS-PAGE of fetuin-purified ArtAB, and sometimes D-galactose-purified ArtAB, revealed a third peptide that was similar in molecular weight to ArtA (Figure 2.3B, lanes 3–4). All peptide bands, including the two ArtA bands that purified near 25 kDa, were sequenced by LC–MS mass spectrometry to confirm identity (Supplementary Figure 2.S2D, Supplementary Table S2). The larger (~26 kDa) and smaller (~23 kDa) peptides were both confirmed to be ArtA, indicating that the A subunit may also be proteolytically cleaved, or nicked, similar to that observed for PT.[63]

Purification of the ArtB binding subunit alone was also completed using D-galactose affinity chromatography. The plasmid pLC001 (Figure 2.3D), was constructed to express *S.* Typhimurium DT104 ArtB alone from *E. coli*. D-galactose-isolated ArtB was observed using SDS-PAGE and unboiled samples were consistent with a pentameric structure of approximately 67 kDa (Figure 2.3E). Purified ArtB was also confirmed by mass spectrometry (Supplementary Table 2.S2).

Cellular Activity of ArtAB

The cellular activity of purified ArtAB was determined using two epithelial cell lines. Vero and Chinese hamster ovary (CHO) epithelial cells have long been used to characterize the effects of AB_5-type toxins such as CT and PT.[64,65] The cellular activity of three concentrations of purified ArtAB on Vero and CHO cells over 72 hours of incubation was assessed (Figure 2.4). Metabolic activity was determined using resazurin dye (alamarBlue™), and cytotoxicity was determined using crystal violet, as described.[55]

The effect of each concentration of toxin is expressed as a percent of the effect of vehicle alone.

On CHO cells, metabolic assays at early time points indicated that ArtAB had no effect, or potentially increased the metabolic activity (Figure 2.4A). At later time points, metabolic activity dropped to an average of 90% of vehicle control (lowest activity was 85.8% of control with 2 μg at 48 hours). Cytotoxicity assays on CHO cells treated with holotoxins were consistent with these results, with significant differences between holotoxin-treated and vehicle-treated cells at all time points (Figure 2.4B). Vero cells revealed a higher sensitivity to ArtAB with metabolic activity dropping to an average of 80% of vehicle control (lowest activity was 77% of control with 10 μg at 72 hours), and significant differences between holotoxin-treated and untreated cells at 48 and 72 hours (Figure 2.4C). Vero cell cytotoxicity reached greater than 50% at later time points, with significant differences between holotoxin-treated and untreated cells at 24, 48 and 72 hours (Figure 2.4D). There was no significant dose-dependent effect of ArtAB for either cell type in the range used (2 μg to 10 μg of toxin) in these assays. The metabolic and cytotoxic activity of 2 μg of ArtAB was similar to that of 2 μg of CT on both cell types (Figure 2.4A–D). The cytotoxicity of ArtAB on Vero cells was significantly greater than that of 2 μg of CT at 5 μg ($p = 0.0030$) and 10 μg ($p = 0.0025$). PT was consistently more active on CHO cells than ArtAB, reaching below 80% of untreated cells for metabolic and cytotoxic activity with 2 μg of protein (Supplementary Figure 2.S3).
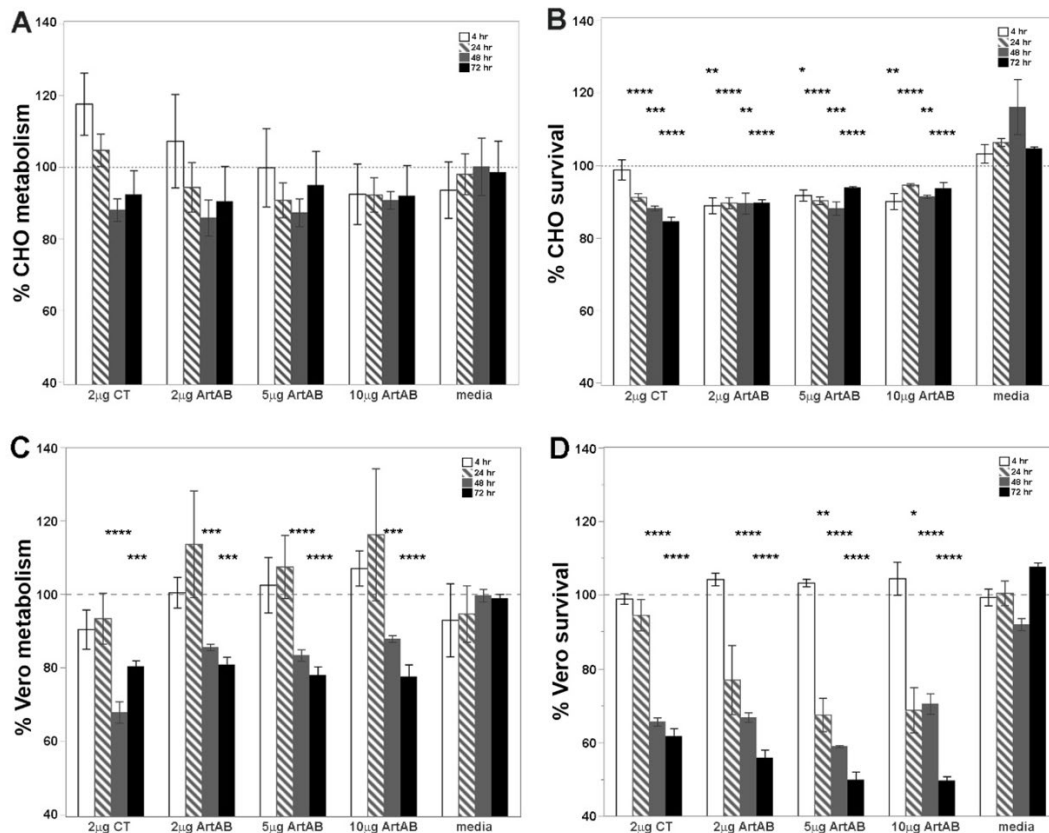
Figure 2.4.   Metabolic and cytotoxic activity of ArtAB and CT on epithelial cells in vitro

(A) Resazurin metabolic assays and (B) crystal violet cytotoxicity assays on CHO cells, and (C) resazurin and (D) crystal violet assays on Vero cells. Purified ArtAB was incubated with cells at 2, 5, or 10 μg per 200 μL well for 4, 24, 48, or 72 hours at 37 °C. Results are reported as the percent of vehicle control activity, and toxin groups at each time point are compared to media alone (also reported as the percent of vehicle control activity) using a one-way analysis of variance (ANOVA) and Tukey's HSD. Stars above the bar indicate a significant difference from media alone at that time point (* p ≤ 0.05, ** p ≤ 0.01, *** p ≤ 0.001, **** p ≤ 0.0001).

Cellular morphological changes in response to treatment with ArtAB were examined using light microscopy. Treatment with ArtAB caused CHO cells to exhibit some elongation and a definitive clustering morphological phenotype compared to vehicle-treated cells beginning at 24 hours. This response was similar to that induced by 2 μg of PT (Figure 2.5). By 72 hours, CHO cell clusters were larger and less distinct for both toxins. In contrast, CT induced a distinctive elongated phenotype on CHO cells that was observable through 72 hours. Cell length was quantified from representative images

and, while significant CHO cell clustering effects by ArtAB were not identified using this method, CT elongation was highly consistent and easily quantified (Supplementary Figure 2.S4A).
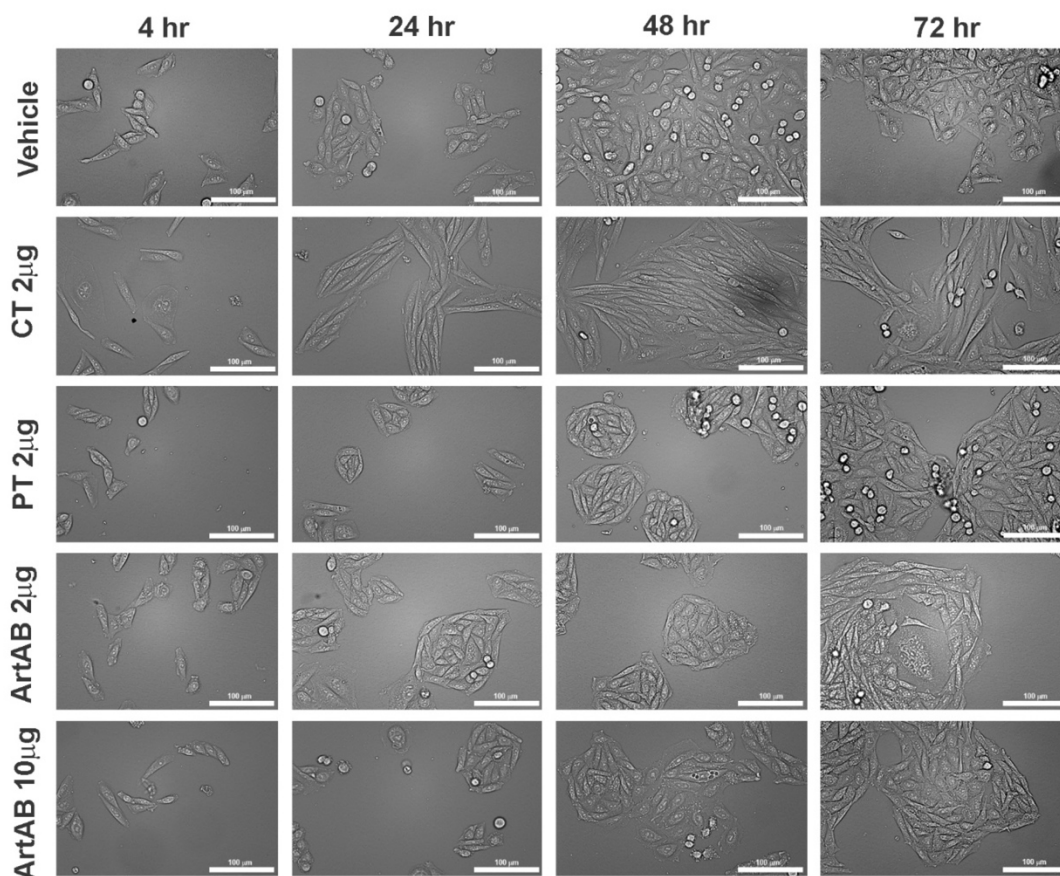
Figure 2.5.   Cellular aggregate and morphology of CHO cells incubated with AB₅ toxins

CHO cells were incubated with ArtAB (2 μg and 10 μg), CT (2 μg) and PT (2 μg) at 4, 24, 48 and 72 hours. Images were collected using brightfield microscopy (20×, scale bar = 100 μm).

On Vero cells, all ArtAB treatments triggered varying levels of destruction of the cells with a less distinct phenotype. However, Vero cells treated with ArtAB demonstrated elongation and potential dendrite formation at early time points and throughout the 72-hour incubation (Figure 2.6). This result was similar to that observed with CT at 2 μg. In contrast, PT treatment of Vero cells at 2 μg caused a very high

amount of cellular destruction, even at early time points, with some cell populations able to recover by 72 hours. Quantification of images verified a significant elongation effect of ArtAB treatment on these cells (Supplementary Figure 2.S4B).
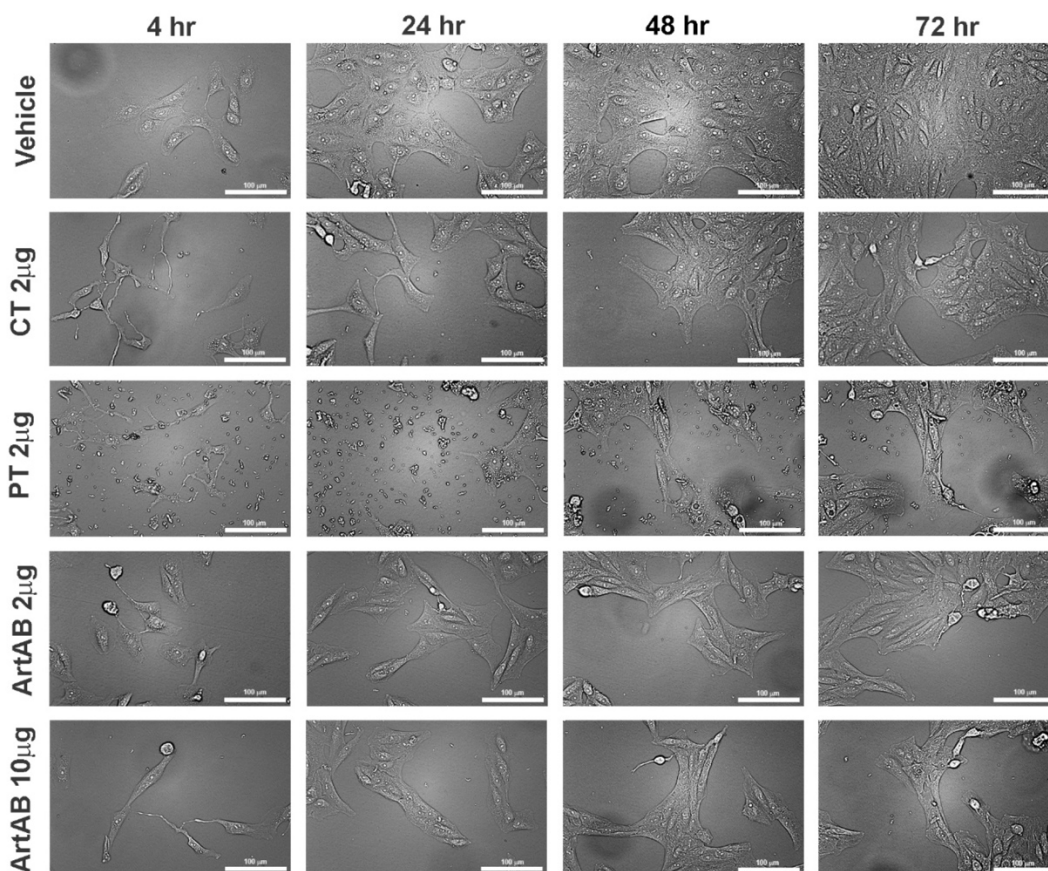
Figure 2.6.   Cellular aggregate and morphology of Vero cells incubated with AB$_5$ toxins

Vero cells incubated with ArtAB (2 μg and 10 μg), CT (2 μg) and PT (2 μg) at 4, 24, 48 and 72 hours. Images were collected using brightfield microscopy (20×, scale bar = 100 μm).

Cellular Activity of ArtB

The metabolic and cytotoxic activity of ArtB was determined using the same epithelial cell lines. Similar to holotoxin, ArtB induced an increase in metabolic activity at early time points that was significant over media alone for the lower 2 μg concentration (Figure 2.7A). At higher concentrations and later time points, ArtB significantly slowed

metabolic activity and induced cell death, with percent survival below 40% at higher

concentrations after 72 hours (Figure 2.7B). ArtB also induced a significant

concentration-dependent effect on both metabolism and cell survival at all time points.

Visual assessment of cells by microscopy indicated that ArtB alone induces morphologic

changes on CHO cells that are distinct from those induced by holotoxin. Treatment with

ArtB may have prevented adherent CHO cells from forming paracellular junctions,

resulting in the consistent rounding of adherent cells (Figure 2.8). The quantification of

cell length also supported the consistent rounding of CHO cells as a result of incubation

with ArtB (Supplementary Figure 2.S4C). Incubation of Vero cells with ArtB alone did

not result in significant metabolic, cytotoxic, or morphologic cellular changes that were

distinct from vehicle-treated cells alone (data not shown).
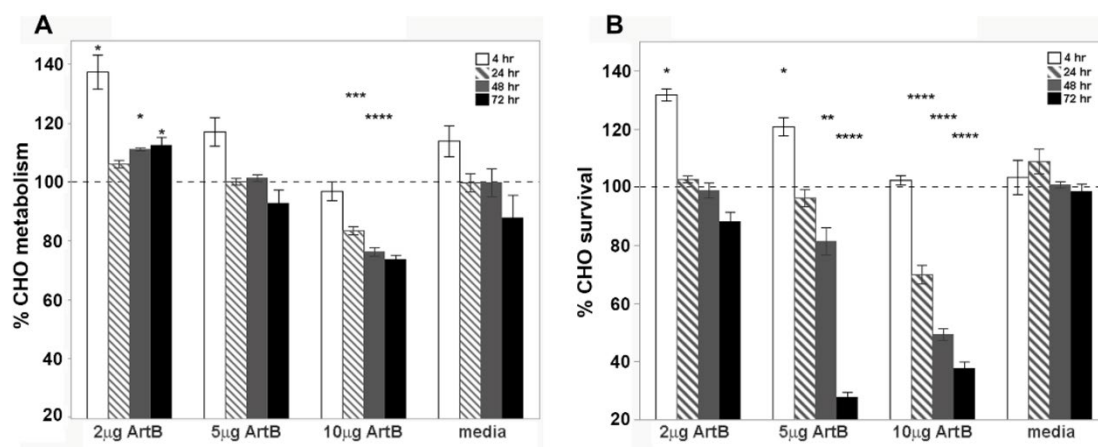
Figure 2.7.   **Metabolic and cytotoxic activity of the ArtB subunit on epithelial cells in vitro**

(A) Resazurin metabolic assays and (B) crystal violet cytotoxicity assays on CHO cells. Purified ArtB was incubated with cells at 2, 5, or 10 μg per 200 μL well for 4, 24, 48, or 72 hours at 37 °C. Results are reported as the percent of vehicle control activity, and toxin groups are compared to media alone at each time point (also reported as the percent of vehicle control activity) using a one-way analysis of variance (ANOVA) and Tukey's HSD. Stars above the bar indicate a significant difference from media alone at that time point (* $p \leq 0.05$, ** $p \leq 0.01$, *** $p \leq 0.001$, **** $p \leq 0.0001$).
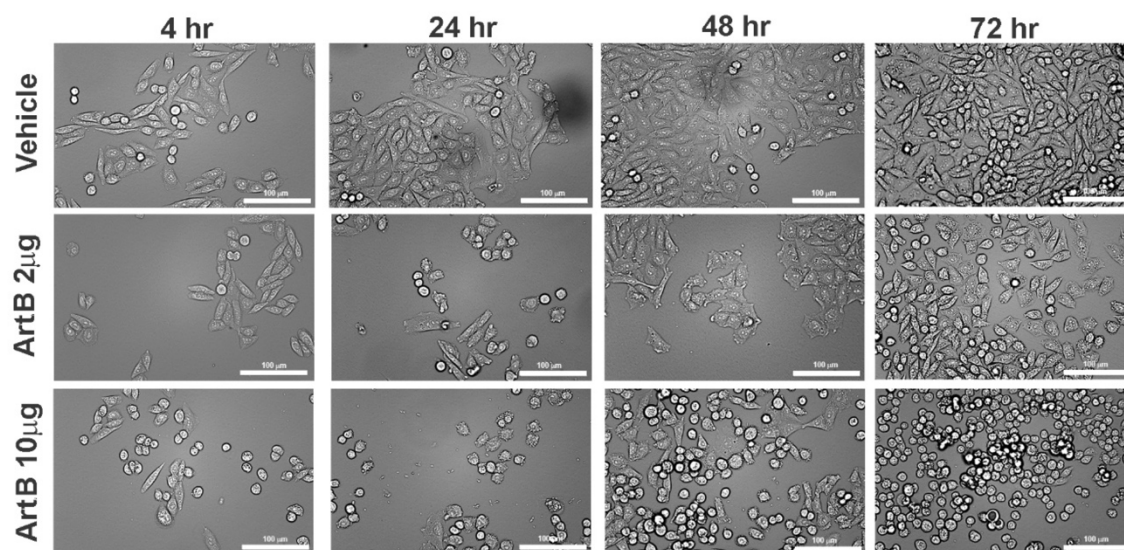
Figure 2.8.   Cellular aggregate and morphology of CHO cells incubated with the ArtB subunit

CHO cells incubated with ArtB (2 μg and 10 μg) at 4, 24, 48 and 72 hours. All images collected using brightfield microscopy (20×, scale bar = 100 μm).

Discussion

We report the glycan affinity purification and cellular activity of *S.* Typhimurium ArtAB toxin as well as that of the ArtB binding subunit alone. The method of using D-galactose affinity for purification was found to be rapid and efficient and was used to purify native (untagged) ArtAB and ArtB to high concentrations. The cellular metabolic, cytotoxic, and morphologic effects were identified on two epithelial cell lines that have been commonly used to characterize bacterial toxins.

Native toxin purified from *E. coli* is consistent with the expected size and sequence of toxin purified directly from *S. enterica* Typhimurium DT104, enabling large scale protein purification to be performed in lower biohazard laboratory conditions. Unidentified differences in purification conditions resulted in the occasional production of a lower-molecular-weight peptide that was confirmed by LC–MS to also be ArtA (Supplementary Figure 2.S2D), providing evidence that ArtA contains a proteolytic cleavage site. An A1 subunit of 22–23 kDa indicates that ArtA may contain a proteolytic processing site, similar to that reported for PT and CT.[66,67] The cleavage of CT is required for maximal activation and cellular activity. The enzyme for CT cleavage is a host-derived serine protease that generates a 22 kDa A1 subunit which remains connected to the A2 subunit via a disulfide bond.[40] Similar to CT, processing of PT is predicted to occur within a protease-sensitive loop of the S1 subunit near the C-terminus. The PT S1 subunit is thought to remain connected to the holotoxin through a disulfide bond; located between residues C41 and C201.[68] In vitro, PT S1 cleavage results in a 22 kDa S1 subunit (from the 26 kDa full-length S1) and enhances ADP ribosylation.[66] While reduction of the disulfide bond and ATP-binding are both required for PT activity, proteolytic

processing has not been found to be essential for cellular activity.[69,70] Our results indicate that the A subunit of ArtAB may be cleaved. However, current efforts have not identified a specific cleaving enzyme or determined if cleavage is required for activation. ArtA does contain cysteine residues (C38 and C198) in primary structure locations similar to those of PT, which may hold the cleaved strands of the A subunit together into the holotoxin structure.

Purification of hexa-histidine-tagged ArtAB resulted in the consistent production of two lower-molecular-weight bands under 15 kDa (Supplementary Figure 2.S2C). Both peptides were confirmed by LC–MS to be ArtB, and the smaller band was untagged as determined by Western blot. We hypothesize that the location of the HIS-tag results in steric hindrance and may prevent pentamer formation with fully tagged monomers. While this toxin could be purified to high concentration, the location of the tag may reduce normal receptor binding and/or prevent glycan binding at a second site, which has been determined to be located on the outside of the pentamer.[24] Cell trafficking and receptor-binding assays reported here with the ArtAB-HIS protein are preliminary, and there is a possibility of non-specific interactions using α-HIS. Thus, future studies will focus on the use of native toxin for these assays.

Cellular assays indicated that purified ArtAB induced a slow and limited cytotoxicity that is similar to that of CT. These studies revealed an approximate 15% (CHO) to 50% (Vero) decline in cell viability compared to vehicle-treated cells over 72 hours. In dividing cells, alamarBlue™, or resazurin dye, is reduced to resorufin by aerobic respiration, so this assay is an indicator of metabolic activity rather than a comparison of live-versus-dead cells. Resazurin assays confirmed the decline in cell

viability at later time points. Notably, we did not observe concentration-dependent cellular activity using a limited range of concentrations (2, 5, or 10 μg per 200 μL treatment). In addition, by 72 hours, some cells in all cultures were able to recover from, or were initially resistant to, toxin treatment such that a detectable recovery of individual cells, as well as the population as a whole, could be observed. This is consistent with a bi-modal response to toxins that are able to bind to more than one cellular receptor, as has been described.[71,72] Binding to a sub-optimal host glycan may promote a lower concentration of toxin reaching the host cytosol and thus a population of cells that are not fully intoxicated. This effect may also explain why concentration-dependent responses cannot be detected unless concentrations cover a larger range. Future studies can assess a broader range and use assays to detect individual cell responses within a population.

The cellular aggregation and morphological changes observed in this study are consistent with a previous assay of the *Salmonella* supernatant activity on CHO cells and the identification of ADP-ribosylation activity.[39] These studies indicate that the observed cellular changes are induced by active toxin-stimulated increases in cAMP and that they are dependent upon specific active subunit–receptor interactions.[73,74] CT is well known to induce elongation in CHO cells and rounding in Y1 adrenal gland cells and has been reported to cause increased cellular adherence.[75–77] It has also been reported that adhesion molecules such as Thrombospondin-1 and Integrin-β1 are upregulated when monocytes are treated with CT.[78] In contrast, when treated with PT, CHO cells, which normally grow in uniform monolayers, exhibit a distinct clustering phenotype.[79] This is similar to our observations with ArtAB and supports the hypothesis that this toxin also induces a receptor-specific cellular activity that involves cytoskeletal rearrangement and changes in

expression of adhesion molecules.[80] Two novel pertussis-toxin-like toxins from *E. coli* have been reported to induce both elongation and clustering of CHO cells.[22] These studies further utilize CHO morphology as a sensitive bioassay to determine toxin titer and identify potential receptors. The cellular phenotypes identified for ArtAB could similarly be used to assay toxin concentrations and identify receptors using mutant cell lines.

Somewhat surprisingly, the ArtB subunit alone also had cytotoxic activity on CHO cells, killing up to 60% of cells after 72 hours at higher concentrations, as determined by crystal violet assay. The morphology of CHO cells was also affected by ArtB. We observed a distinct rounding of individual adherent cells, possibly indicating that ArtB is preventing the formation of paracellular junctions. These results indicate that receptor-binding and/or internalization of the B subunit alone induces significant cellular activity and may be relevant in bacterial pathogenicity. This has not been described for CTB but has been described for Shiga toxin B subunit.[81] *art*B is also present on typhoidal *Salmonella* serovars and is associated with an *art*A pseudogene that is likely not expressed. Recently *S.* Typhi *art*B has been found to be present on many additional *Salmonella* serovars and may provide an alternative binding subunit for Typhi Toxin (TT).[58] *art*B of *S.* Typhi was also determined to be expressed, especially under conditions that may occur inside of host cells. While ArtB of *S.* Typhi has only 74% identity to ArtB of *S.* Typhimurium DT104 (Figure 2.1), these studies support the important role that the binding subunit alone may play in *Salmonella* pathogenesis. The crystal structure and glycan binding array of *S.* Typhimurium ArtB has been determined using a purified 6XHIS subunit from *E. coli*.[24] These studies indicated that ArtB likely binds to terminal

Neu5Ac and Neu5Gc sialylated glycans, both of which can be found on bovine fetuin. GM1 is a monosialylated glycosphingolipid with an internal Neu5Ac, and a terminal D-galactose. D-galactose agarose affinity purification has long been established as a rapid and efficient method of purifying CT.[82] The ability of ArtAB to be efficiently purified using D-galactose indicates that this toxin also binds well to this terminal glycan and likely has a broad receptor specificity, similar to that of PT.[41] The binding to Neu5Gc also supports the importance of this toxin in animal disease, as humans do not synthesize this glycan. In these studies, we identified the binding and internalization of ArtAB-HIS into Vero cells, and activity on Vero and CHO cells. Future studies will assess the activity of ArtAB on additional cell types, as well as the binding to other glycoproteins/glycolipids, to help narrow potential cellular receptors, define target host cells and explore the utility of this toxin or receptor as a potential animal or human vaccine.

Both cell types incubated with ArtAB, and CHO cells incubated with ArtB, showed a potential increase in metabolic activity at early time points. This response was significant for ArtB on CHO cells and corresponded to an increase in cell number. The metabolic increase is consistent with the use of CT as an adjuvant that enhances the activation and proliferation of immune cells, as well as other cell types, at low concentrations.[83–85] This burst may also reflect the initiation of programmed cell death and the production of extracellular membrane vesicles, or exosomes, in response to intoxication. CT has been found to induce apoptosis in different cell types.[86,87] Vero cells in these studies were more sensitive to toxin and also produced a large number of exosomes in response to both CT and ArtAB. Exosomes can be induced as a survival

mechanism to rapidly rid the cell of toxin or B subunit, as has been shown for *S. aureus* α-toxin.[88] We hypothesize that the mechanisms behind cell death and cellular defenses to ArtAB are similar to that of CT, and this toxin may induce apoptosis in some cell types. These activities will continue to be explored.

Conclusions

We report a method of rapid native ArtAB and ArtB purification based on glycan affinity and identify toxin binding and cellular activity in vitro. The availability of ArtAB and ArtB in native form will promote a varied set of downstream applications for the continued biological characterization of this toxin. Cellular assays can be used to further assess the expression of ArtAB from pathogenic *Salmonella* and the extent of ArtAB's contribution to virulence and clinical outcomes in a broad host range. The structure and functionality of ArtAB can also be further defined, which will advance our understanding of bacterial AB5 toxins, as well as support efforts to prevent or treat salmonellosis in humans and animals. The identification of methods to reduce or eliminate *Salmonella* in agriculturally important animals is a priority, and will help to reduce animal mortality, increase production, and prevent transmission to humans.

Supplementary Materials
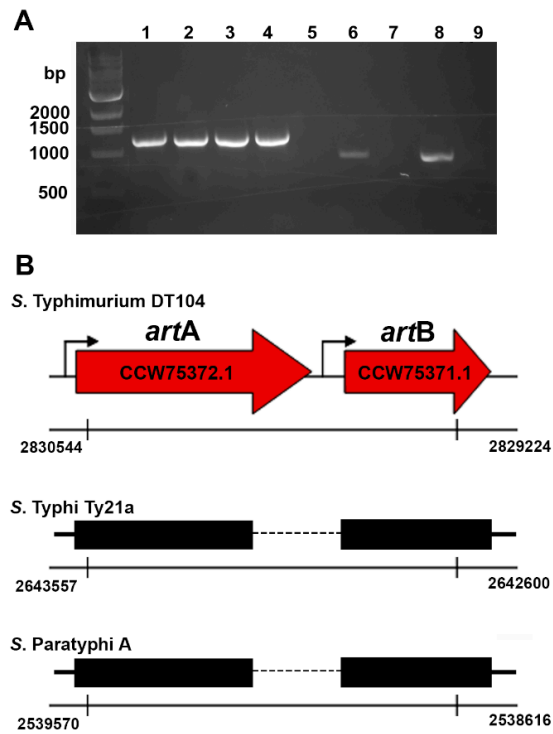
Figure 2.S1.   Full length and truncated *art*AB on different *Salmonella* serovars

(A) PCR of S. enterica serovars Typhimurium DT104 (lanes 1–4; 1320 bps), and Typhimurium non-DT104 (lane 5; no amplification), Typhi (lane 6; 957 bps), Choleraesuis (lane 7; no amplification), and Paratyphi A (lane 8; 954 bps). Lane 9, negative control. (B) Diagram of the artA – _artB region in S. Typhimurium DT104 (NCBI HF937208), S. Typhi Ty21a (NCBI CP023975), and S. Paratyphi A (NCBI CP019185). Serovars Paratyphi, Typhi and Montevideo are positive for artB and a truncated version of artA (pseudogene) respectively.
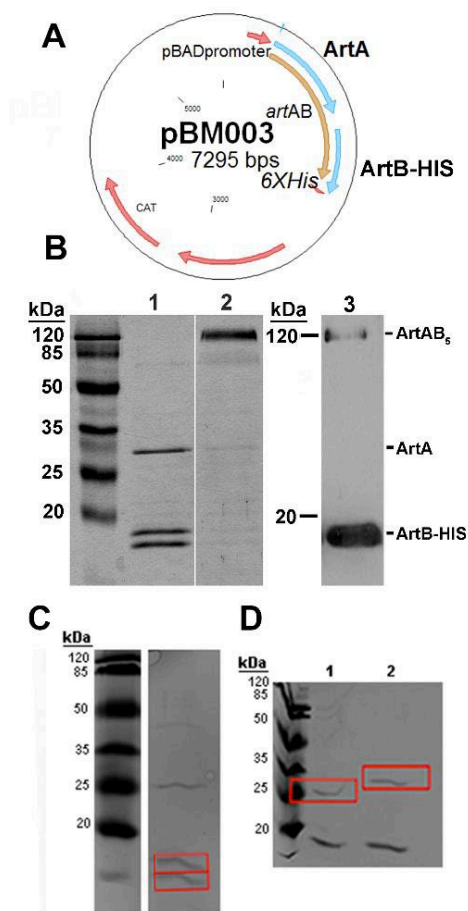
Figure 2.S2. Purification of ArtAB-HIS from *E. coli,* and sequencing of ArtB-HIS and native ArtA

(A) plasmid pBM003 for the expression of ArtAB-HIS; (B) SDS-PAGE of: 1) purified ArtAB-HIS boiled and 2) purified ArtAB-HIS unboiled, and 3) anti-6XHIS western blot of boiled ArtAB-HIS (ArtA $\cong$ 25.6 kDa, ArtB-HIS $\cong$ 14.2 kDa, ArtAB5-HIS $\cong$ 96.5 kDa). Bands collected for protein sequencing by mass spectrometry (LC-MS, Supplementary Table S2) included (C) ArtB-HIS (from pBM003; top band = pBM003 1, bottom band = pBM003 2) and (D) native ArtA (from pBM006; right band = pBM006 1, left band = pBM006 2).
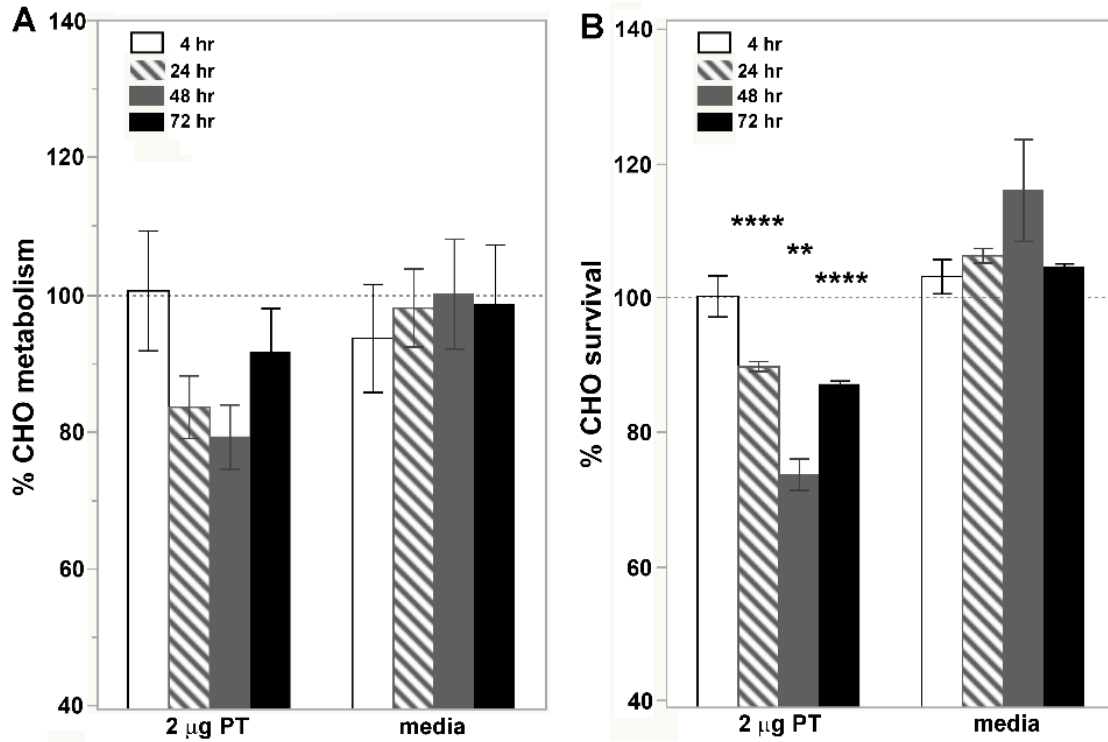
Figure 2.S3.   Cellular effects of PT on CHO cells

alamarBlue™ metabolic assays (A) and crystal violet cytotoxic assays (B). PT was incubated with cells at 2 μg per 200 μL well for 4, 24, 48, or 72 hours at 37 °C. Results are reported as the percent of vehicle control and the toxin group is compared to media alone at each time point using a one-way analysis of variance (ANOVA) and Tukey-HSD. Stars above the bar indicate a significant difference from media alone at that time point (*p ≤ 0.05, **p ≤ 0.01, ***p ≤ 0.001, ****p ≤ 0.0001).
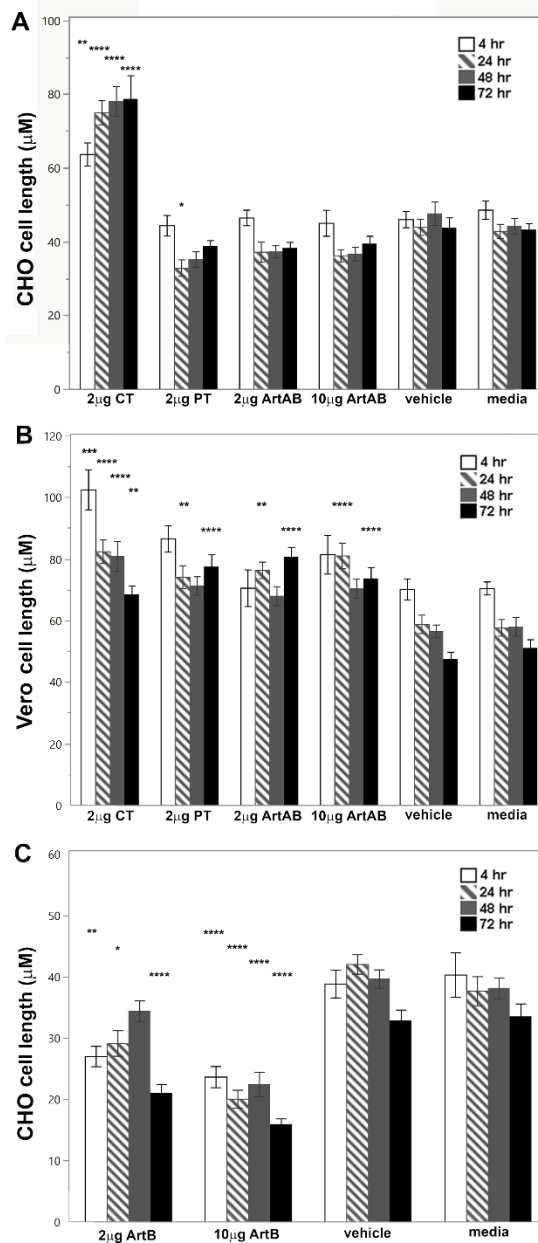
Figure 2.S4. Cell length measurements

(A) cell length for CHO cells treated with ArtAB, CT and PT holotoxin, (B) cell length for Vero cells treated with ArtAB, CT and PT holotoxin and (C) cell length for CHO cells treated with ArtB subunit. Results are reported as average cell length in μm, and toxin groups and vehicle-treated groups are compared to media alone at each time point using a one-way analysis of variance (ANOVA) and Tukey-HSD. Stars above the bar indicate a significant difference from media alone at that time point (*p ≤ 0.05, **p ≤ 0.01, ***p ≤ 0.001, ****p ≤ 0.0001).

Table 2.S1.   Protein accession numbers for phylogenetic analysis

Toxin A subunits	NCBI Accession #	Toxin B subunits	NCBI Accession#
ArtA *S.* Typhimurium DT104	WP_156015302	ArtB *S.* Typhimurium DT104	5WHU_A
ArtA *S.* Worthington	BAX76679.1	ArtB *S.* Worthington	BAX76680
ArtA *S. bongori*	ASG55211.1	ArtB *S.* Typhi	AE014613.1
ArtA *S.* Typhi/Montevideo pseudogene	AAMFER010000002	SubB2 *E. coli*	WP_169004307
PltA *S.* Typhi	AE014613.1	ArtB *S. bongori*	BAX76684
PltA/ArtA *E. coli*	WP_001355271	SalB *S. arizonae*	ABX22253.1
PtxA S1 *B. pertussis*	WP_019248344	PltB *S.* Typhi	AE014613.1
YtxA *Y. enterocolitica*	WP_023161032	PtxB S2 *B. pertussis*	WP_050830703
LtIIa *E. coli*	TFY48810	YrpB *Y. pestis*	WP_002209112
LTIIb *E. coli*	1TII_A	SubB *E. coli*	Q6EZC3
EltA (LTA1) *E. coli*	WP_001398470	CfxB *C. freundii*	BAC16522
CtxA *V. cholerae*	1001196A	EcxB *E.coli*	EEU4199622
SubA *E. coli*	WP_000912970	CtxB *V. cholerae*	WP_000593522
CfxA *C. freundii*	BAC16521.1	EltB *E. coli*	WP_024167713
EcxA *E. coli*	WP_071999469	LTIIaB *E. coli*	KDA69244
CdtB *S.* Typhi	NC_003198	LTIIbB *E. coli*	WP_096985491
YrpA *Y. pestis*	WP_064516147	YtxB *Y. enterocolitica*	WP_050137877
ArtA *E. coli*	WP_077887430	Stx2B *E. coli*	EEV2598235
Stx1A *E. coli*	WP_000691354	Stx1B *E. coli*	WP_097586066
Stx2A *E. coli*	EEV2155635.1		

Table 2.S2. LC-MS sequencing of purified proteins

Protein	Accession	Description	Coverage [%]	# Peptides	# PSMs	# Unique Peptides	# Protein Groups	# AAs	MW [kDa]	calc. pI	Score Sequest HT: Sequest HT	# Peptides (by Search Engine): Sequest HT
pBM003 1	Q404H3	ArtB protein OS=Salmonella enterica subsp. enterica serovar Typhimurium str. DT104	48	12	318	12	1	141	15.8	8.05	1047.44	12
pBM003 2	Q404H3	ArtB protein OS=Salmonella enterica subsp. enterica serovar Typhimurium str. DT104	48	10	236	10	1	141	15.8	8.05	812.33	10
pBM006 1	Q404H4	ArtA protein OS=Salmonella enterica subsp. enterica serovar Typhimurium str. DT104	59	13	317	13	1	241	27.6	8.7	1488.67	13
pBM006 2	Q404H4	ArtA protein OS=Salmonella enterica subsp. enterica serovar Typhimurium str. DT104	58	13	496	13	1	241	27.6	8.7	2323.94	13
pLC001	Q404H3	ArtB protein OS=Salmonella enterica subsp. enterica serovar Typhimurium str. DT104 OX=85569 GN=ArtB PE=1 SV=1	40	7	60	7	1	141	15.8	8.05	184.77	7

Funding, Acknowledgements, and Conflicts of Interest

CHAPTER THREE: STRUCTURAL ANALYSIS OF THE ADP-RIBOSYLATING A SUBUNIT OF THE *SALMONELLA* TYPHIMURIUM ARTAB TOXIN

Authorship statement: My direct contributions to the work in this chapter included conceptualization and methodology of the experiments; project administration; investigation and data curation for every experiment except for the mass spectrometry and analytical ultracentrifuge work which were performed by BRC staff; validation; data curation; visualization; formal analysis; and writing this original chapter, which can be used as a manuscript draft and submitted for publication in the future.

This work has not yet been submitted for publication. Upon submission for publication, additional authors will be included with authorship contributions as follows, according to CRediT (Contributor Roles Taxonomy) definitions:

Elise Overgaard[1]   Conceptualization, methodology, validation, formal analysis, investigation, data curation, writing – original draft, writing – review and editing, visualization, project administration

Haley Bridgewater[1]   Investigation, writing – review and editing,

Luke Woodbury[1,2]   Validation, formal analysis, writing – review and editing

Juliette K. Tinker[3]   Conceptualization, methodology, validation, formal analysis, resources, writing – review and editing, visualization, supervision, funding acquisition

[1]   Biomolecular Sciences Graduate Program, Boise State University, Boise, ID
[2]   Biomolecular Research Center, Boise State University, Boise, ID
[3]   Department of Biological Sciences, Boise State University, Boise, ID
*   Correspondence: juliettetinker@boisestate.edu

Abstract

ADP-ribosyltransferases (ARTs) are found throughout all domains of life and have a highly conserved NAD+-binding tertiary fold. ArtAB, an ART from the virulent and highly antibiotic resistant *Salmonella* Typhimurium DT104, has some homology to ARTs in the cholera toxin-like ART subfamily. In this study, a 3D predicted structural model was established using AlphaFold 2 and Phyre2 protein prediction algorithms. Studies with the model showed that ArtAB is most closely related to pertussis toxin (PT) from *Bordetella pertussis*, and this homology was used to predict catalytic and other important residues in the expected NAD+-binding pocket. The biophysical properties and stability of ArtAB were probed with analytical ultracentrifugation and circular dichroism (CD). Based on these experiments, ArtAB has a molecular weight close to that of the sequence-based prediction, it exists as a singular homogenous non-aggregated holotoxin species in solution, and it is stable at physiologically relevant temperatures. It is composed of approximately 32% β strands, 14% α helices, 24% turns, and 29% unordered domains. A set of mutants with single residue point mutations was created to probe the structure of the catalytic core. The mutants were tested using CD, cAMP and cellular morphology and metabolic activity assays. The H32A mutant had little effect on the secondary structure and did not affect the toxin's cAMP activity, however, it did abolish ArtAB's characteristic clustering and elongation effects on CHO cells. The R6A mutant also had little effect on the secondary structure, but it increased cellular cAMP and abolished the clustering and elongation effects on CHO cells. It also caused some CHO cells to round up. The T50A mutant showed increased baseline holotoxin stability, potentially due to an increase in β strand content, lowered cellular cAMP levels, and

introduced a separation of clustering and elongation effects on CHO cells where

clustering was present but elongation was not. In sum, a foundational understanding of

ArtAB's structure and catalytic pocket was achieved. The 3D predicted model will be

useful for future studies in determination of a high-resolution atomic structure of ArtAB,

and the mutants will be useful for probing its active site.

Introduction

ADP-ribosylation is an ancient and highly conserved post-translational modification involving the transfer of an ADP-ribose (ADPr) moiety from a molecule of NAD+ onto a target, which is often a single residue of a target protein, but can also be a nucleic acid or small molecule.[89] The reaction is catalyzed by ADP-ribosyltransferases (ARTs), a superfamily of enzymes that have been identified in all domains of life. ARTs have been extensively reviewed over the past two decades.[89–97] ADP-ribosylation is a reversible PTM, with ADPr "erasers" existing in viruses, bacteria, and eukaryotes alike.[98] With the current and ever-increasing availability of genomic sequences, ARTs are being discovered regularly. *In silico* bioinformatics approaches involving the mining of protein and genetic sequencing databases have been used successfully to discover functional ARTs in plant, animal, and insect pathogens.[91,96,99–104] While recognizing that there is much crossover and great value in collaborating with researchers of viral and eukaryotic ARTs, for the purpose of this study we remain focused on bacterial ARTs.

While traditional bacterial ART studies have focused on toxins that affect mammalian host species, some of the more recent ART discoveries include Plx1, Plx2, and C3larvin from *Paenibacillus larvae*, which causes American foulbrood in honey bees,[105] scabin from *Streptomyces scabies*, which causes scab disease in potatoes and other root vegetables, and vorin from *Erwinia amylovora,* which causes fire blight in fruit trees. A summary of several known bacterial ARTs is provided in Table 1.

As demonstrated in Chapter 2, ARTs have very limited genetic homology. It is well established, though, that, despite this limited genetic homology, ADP-ribosylating toxins contain highly conserved tertiary structures and specific catalytic residues. Crystal

structures have been obtained for many ARTs (Table 3.1) and these have been used to demonstrate the presence of a conserved ART fold. The ART fold bears some resemblance to the well-studied Rossmann fold, though the ART fold is specific to NAD+ and catalyzes ADPr transfer. The Rossman fold is not specific to NAD+, it can bind other molecules like NADP+ and FAD, and it holds NAD+ in an orientation that is favorable for redox chemistry but cannot catalyze the glycosidic bond cleavage that is required for ADPr transfer.[89] The structure and chemistry of the ART fold is characterized in great detail in reviews by Domenighini et. al. (1994), Han and Tainer (2002), and, most recently, Cohen and Chang (2018).[8,92,106] A summary in a single paragraph cannot do justice to what these authors have artfully reviewed over dozens of comprehensive pages, but here is a rudimentary attempt at briefly characterizing the ART fold: the ART fold is defined by a split β sheet. As opposed to the Rossmann fold, which is defined by a series of sequential β strands and α helices that form a "β sheet sandwich" with a central parallel β sheet flanked by α helices,[107] the ART fold has a distinct center marked by an α helix and the protein chain weaves across this central line several times to form the split β sheet with non-sequential antiparallel β strands. A glutamic acid residue and a nucleophilic residue that is either a histidine (DT, PAETA) or an arginine (CT, LT, LT2, PT, exoS, and MTX) are conserved throughout all ARTs and are positioned on β-strands that flank the NAD+-binding cavity (glutamic acid on β2, histidine/arginine on β1). The nucleophilic residue is usually preceded by a tyrosine or phenylalanine.

ARTs have a wide range of targets and cellular activities, including modulation of the cytoskeleton, activation and inhibition of cAMP pathways, and promotion of host cell

death through apoptosis (Table 1). ADP-ribosylation targets are diverse and include (but are not limited to) the heterotrimeric $G_i/G_o/G_t$ protein subfamily ($G_{\alpha i1}$, $G_{\alpha i2}$, $G_{\alpha i3}$, and $G_{\alpha io}$), the $G_s/G_{olf}/G_t$ subfamily ($G_{s\alpha}$), elongation factor 2 (EF-2), Rho-GTPases, and actin (Table 3.1). Though bacterial ARTs contain protein domains outside the catalytic region, target selection is not usually mediated by these regions. Rather, it is thought that target selection is mediated by interactions of the target within the ART fold and catalytic domain. This contrasts the selection process of eukaryotic ARTs, which do rely on the domains outside the catalytic region. Cohen and Chang (2018) provide an excellent and detailed review of this topic.[89]

Some ARTs are single chain monomers with distinctive active (A) and receptor-binding (B) domains, and some are monomeric ARTs with no binding domain at all. Many ADP-ribosylating toxins are structured as an AB or AB_5 multimer with the active ART, or A, subunit non-covalently bound to a distinct receptor-binding, or B, subunit. AB_5 multimers are more well known to have homopentamers, but can also have heteropentamers, as in the case of pertussis toxin (PT), which has four distinct, and one repeated, binding subunits. Because they were discovered and well-characterized early on, AB_5 toxins have received much attention and it is easy to be misled into thinking that all AB_5 toxins are ARTs. However, there are AB5 toxins that without ART activity, such as the subtilase cytotoxin from Shiga toxigenic *Escherichia coli*, a serine protease[108] that cleaves the endoplasmic reticulum chaperone BiP, and EcxAB from *Escherichia coli,* a metzincin-type metalloprotease.[109] The idea that bacterial toxins can utilize binding subunits to send cargo into host cells and the details surrounding the binding subunits that

carry ARTs into cells are fascinating, but they are outside the scope of this study. We will remain focused on the active ART subunits.

ARTs are divided into distinct categories based on their structural homologies and catalytic activities. These categories have changed over time as more information is discovered about ART structure and function, but these are the common currently used subdivisions[110]:

- DT/ExoS-like toxins: Most of these toxins have an AB structure with a single chain that is organized in distinct active (A) and binding (B) domains. They contain a conserved HYE motif within the NAD+ binding pocket. Toxins in this group target elongation factor 2 (EF-2) and inhibit protein synthesis.
- CT-like toxins: These toxins are defined by a conserved R-STS-E motif in the NAD+ binding pocket. CT-like toxins encompass all toxins with this conserved motif, including the known AB_5-type toxins. The AB_5 toxins largely target the α subunits of G-protein coupled receptors. Besides the AB_5 group, the CT-like group with the conserved R-STS-E motif also includes the following subgroups:
  - C2-like toxins: These toxins have distinct A and B subunits which, AB_5-type toxins, are expressed and synthesized separately. The B subunit in this case is a monomer. The toxins directly target actin and prevent actin polymerization.
  - C3-like toxins: These toxins contain a single A-domain subunit. They largely target Rho GTPases and have a wide range of intracellular effects.

A final note, Pierisin-1 is an ART from the cabbage butterfly, *Pieris rapae,* which specifically targets 2'-deoxyguanosine residues in DNA and induces apoptosis in mammalian cell lines. Pierisin-1 also contains a C-terminal domain that normally blocks the active site.[111,112] We mention this eukaryotic ART only because several of the newly discovered bacterial ARTS such as the mosquitocidal toxin (MTX) from *Bacillus sphaericus*, scabin from *Streptomyces scabies,* and Plx1 from *Paenibacillus larvae*

exhibit closer homology to this eukaryotic ART than they do to other bacterial ARTs, which is interesting as we consider the structural relatedness of these proteins. A summary of several known bacterial ARTs (and also Pierisin-1, for comparison) is included in Table 3.1.

Table 3.1.   Table of ADP-ribosylating toxins

Toxin Name	Abbr.	Species	ADP-ribosylation Target	Role in Pathogenesis	Uniprot Accession Number	Structure
DT-like group						
diphtheria toxin	DT	*Corynebacterium diphtheriae*	elongation factor 2	Inhibition of protein synthesis	P00588	AB (single strand)
Pseudomonas exotoxin A	PAETA	*Pseudomonas aeruginosa*			P11439	
cholix toxin	chxA	*Vibrio cholerae*			Q5EK40	
CT-like group						
ADP-ribosylating toxin	ArtAB	*Salmonella* Typhimurium DT104	*unknown,* similar to PT targets (Gα$_i$/Gα$_o$/Gα$_t$)[38]	*unknown*	Q404H4	AB5 homo-pentamer
cholera toxin	CT	*Vibrio cholerae*	membrane-associated G proteins,[106] Gα$_s$/Gα$_t$	Inhibition of Gα-mediated signal transduction	P01555	
heat-labile enterotoxin 1	LT	*Escherichia coli*			P06717	
heat-labile enterotoxin 2a	LTIIa				P13810	
E. coli pertussis-like toxin	*Ec*PltAB		membrane-associated G proteins, Gα$_i$[51]		A0A0B1 KWV6	
pertussis toxin	PT	*Bordetella pertussis*	membrane-associated G proteins[106], Gα$_i$/Gα$_o$/Gα$_t$		P04977	AB5 hetero-pentamer
typhoid toxin pertussis-like toxin subunit	PltA[113]	*Salmonella enterica typhi*	*unknown*		Q8Z6A4	A2B5 homopentamer
putative pertussis-like toxin subunit	N/A	*Salmonella enterica paratyphi A*	*unknown*		A0A6C7I 185	*unknown*
pierisin-like group*						
Pierisin-1	N/A	*Pieris rapae*	deoxyguanosine residues	*unknown*	Q9U8Q4	
mosquitocidal toxin	MTX	*Bacillus sphaericus*	elongation factor 2 in *E. coli*[114] *eukaryotic target unknown*[115]		Q03988	AB (single strand)
toxin 1	Plx1	*Paenibacillus larvae*	DNA (suspected, not experimentally proven)[116]		M9V7X5	
putative secreted protein	scabin	*Streptomyces scabiei*	deoxyguanosine residues[101,117,118]		C9Z6T8	A

*Note: the eukaryotic *Pieris rapae* toxin is included in this table as it is the founding member of the class of pierisin-like bacterial toxins.

Toxin Name	Abbr.	Species	ADP-ribosylation Target	Role in Pathogenesis	Uniprot Accession Number	Structure
C3-like group						
C3 exoenzyme	C3 bot[119,120]	*Clostridium botulinum*	Rho GTPase inactivation	depolymerization of actin cytoskeleton	P15879	A
C3-like	C3 lim[121]	*Clostridium limosum*			Q46134	
C3 exoenzyme	C3 cer	*Bacillus cereus*			Q8KNY0	
C3 exoenzyme	C3 stau1	*Staphylococcus aureus*			Q9ADS9	
C3 exoenzyme	C3 stau2					
C3 exoenzyme	C3 stau3					
epidermal cell differentiation inhibitor	EDIN				P24121	
vegetative insecticidal protein 2	VIP2	*Bacillus cereus*			Q844J9	AB (single strand)
C3larvinA	C3lA[104]	*Paenibacillus larvae*			A0A4Y5 UTI8	AB
toxin 2A	Plx2A				M9V3B7	
exoenzyme S	exoS	*Pseudomonas aeruginosa*	Ras[122]		G3XDA1	
C2-like/binary group						
C2 toxin	C2[123]	*Clostridium botulinum*	actin	Prevents actin polymerization	C4B698	AB
C. difficile binary toxin	CDT	*Clostridioides difficile*			Q7WUH3	
iota toxin	none[124]	*Clostridium perfringens*			A2IA70	
C. spiroforme toxin	CST[125]	*Clostridium spiroforme*			O06497	
N/A	SpvB	*Salmonella enterica*			P21454	AB (single strand)

The ART referred to as ADP-ribosylating toxin (ArtAB) was found on the genome of *Salmonella* Typhimurium DT104 in 2005.[6] While the role of this toxin in pathogenicity has not been determined, DT104 is an epidemic strain of highly resistant *S.* Typhimurium that has contributed to significant human and animal disease.[126] ArtAB is an AB_5-type toxin with binding subunits similar to CT, and ART activity similar to PT.[38,39] It is believed to be phage-derived, with expression induced during cellular SOS responses,[39,127] and it is known to target the same type of G-proteins, $G_{\alpha i}$, as PT.[39] In recent studies we determined ArtAB's cytotoxicity and effects on cellular morphology and metabolic activation. ArtAB has limited cytotoxicity on multiple cell lines and produces a mixed cellular phenotype that is similar to that of both CT- and PT-treated cells.[128]

In this study we sought to examine the structure and biophysical properties of ArtAB using predictive protein modelling and biophysical techniques, to compare it to bacterial ARTs with known structures, and to investigate ArtAB's potential NAD+ binding pocket through mutational studies. We hypothesize that ArtA will be structurally similar to PT and that selected mutants will alter the activity of ArtAB. The results of our work will provide insight into ArtAB's mechanism of enzymatic activity and add to the growing body of work on bacterial ARTs.

Materials and Methods

Structural Predictions and Model Comparisons Using Matchmaker in ChimeraX

To obtain the AlphaFold 2 models, sequences were input into the UCSF
ChimeraX version 1.4 (2022-06-03) AlphaFold 2 (AF2) tool. Structures were predicted
by running an AlphaFold version 2.2.0 calculation using Google Colab[129]. A multimeric
structure of ArtAB holotoxin was produced by entering the sequence of ArtA and the
sequence of ArtB in quintuplicate, all without signal sequence included, as a comma
separated list of sequences. A monomeric structure of ArtA was produced by entering the
sequence of ArtA without signal sequence included. In comparison to the full version of
AF2, this version of AF2 used 245 gigabytes of sequence data from sequence databases
(versus 2 terabytes used by full AlphaFold 2) to find multiple sequence alignments and
does not use structure templates from the individual monomers. Five separately trained
neural networks returned 5 predicted structures, each with an individual confidence score.
The structure with the best confidence score was energy minimized and loaded into
ChimeraX.

To obtain the Phyre2 model, the sequence of ArtA without signal sequence
included was input into the Phyre2 web portal.

In ChimeraX, structures were directly compared using the Matchmaker tool
which superimposes two structures and returns an alignment score and RMSD in the log.
The align tool shows conserved residues and percent identity.

Table 3.2.   Sequences used for structural predictions

Toxin	UniProt Accession Number	Residues	Signal Sequence Residues	Structures Available (PDB ID)
ArtA	Q404H4[6]	241	1-18	none
ArtB	Q404H3[6,24]	141	1-23	5WHU, 5WHV

Multiple structure alignment was performed using the mTM-align server[130,131] for protein structure comparisons. First, the ArtA monomeric model from AlphaFold 2 was input and a database search was conducted to find similar structures. The algorithm for the database search first compares the input sequence to sequences in the GenBank Non-Redundant Protein Sequence Database, which contains entries from contains entries from GenPept, Swissprot, PIR, PDF, PDB and NCBI RefSeq, by PSI-BLAST,[132] then performs iterative methods to identify additional candidates. The output was a list of 51 structures with a template modeling score[133] (TM-score) > 0.5 to the input sequence (a TM score of 1 is a perfect match). From that list, we selected nine protein structures to include in the multiple structure alignment.

Recombinant ArtAB, CT, and ArtAB Mutant Expression and Purification

ArtAB, CT, and ArtAB mutants were expressed and purified as previously described.[128] Briefly, ClearColi® (Lucigen, Madison, WI, USA) transformed with appropriate plasmid (Table 3.3) was grown in Terrific Broth containing chloramphenicol (Fisher Bioreagents Ref. No. BP904-100) at 37°C to O.D. 0.6-0.9 followed by induction with 20% L-arabinose. Overnight induction broth was centrifuged, cells were resuspended, and protein was extracted from the periplasmic space by treatment with Polymyxin B. The cell extract was collected by centrifugation, filter sterilized with a 0.2

μm vacuum filter (Millipore, Cat. No. SCGP00525), and purified using immobilized D-galactose affinity column chromatography (Pierce™ D-galactose Agarose, Thermo Scientific™, Ref. No. 20372). The column was equilibrated and washed with 1X PBS and eluted with 1M D-galactose (ACROS Organics™). Fractions were collected in 1.5 mL aliquots and confirmed with SDS-PAGE. Fractions containing ArtAB were pooled and dialyzed in 12,000 Da MWCO tubing (Fisher Scientific, Cat. No. 21-152-14) against 1X PBS + 5% glycerol at 4°C overnight with one buffer change after 6 hrs. Dialyzed samples were concentrated using a 50,000 MWCO disposable regenerated cellulose filter (Amicon Ultra-15, Merck Millipore Ltd, Ref. No. ACS505024, or 5-20 mL Pierce Protein Concentrators with 30 kDa (Cat No. 88529) or 50 kDa (Cat No. 88540) MWCO with PES membranes, or 2-6 mL Pierce Protein Concentrators with 30 kDa MWCO with PES membranes, Cat. No. 88521) Note: we had many issues with protein concentrators, likely due to their ability to bind our toxin. We lost a great deal of product each time we had to concentrate purified protein. This is an issue that must be addressed in the future for higher production efficiency. Molecular weight and purity were confirmed with SDS-PAGE. Protein concentration was determined by BCA protein assay (Pierce ™ BCA Protein Assay Kit, Thermo Scientific™, Ref. No. 23227) using BSA as a standard.

Table 3.3. **Plasmids used for protein purification**

Protein	Plasmid	Gene	Vector	Source
ArtAB	pBM006	*artA* (*S.* Typhimurium DT104) *artB* (*S.* Typhimurium DT104)	pBAD18	[128]
CT	pJKT46	*ctxA* (*V. cholerae*) *ctxB* (*V. cholerae*)	pARCT5	[134]
ArtAB R6A	pBM006-R6A(4)	*artA* (*S.* Typhimurium DT104) with R6A point mutation *artB* (*S.* Typhimurium DT104)	pBAD18	This study
ArtAB H32A	pBM006-H32A(4)	*artA* (*S.* Typhimurium DT104) with H32A point mutation *artB* (*S.* Typhimurium DT104)	pBAD18	This study
ArtAB T50A	pBM006-T50A(1)	*artA* (*S.* Typhimurium DT104) with T50A point mutation *artB* (*S.* Typhimurium DT104)	pBAD18	This study

Analytical Ultracentrifugation

All measurements were performed with ArtAB at a concentration of 0.560 ug/mL measured by BCA and dialyzed into 1X PBS at 4°C using a Beckman Coulter Proteomelab XL-I Analytical Ultracentrifuge with an An-60 Ti 4-cell titanium rotor rated for 60,000 rpm maximum speed. Sedimentation velocity experiments were run at 30,000 rpm for 6.5 hours with continuous scans measuring absorbance at 280 nm from 5.8 - 7.3 cm at 0.003 intervals. Two biological replicates were collected. Data were analyzed using both SedFit and DCDT+ by John Philo.[135,136]

Far-Ultraviolet Circular Dichroism

Far-UV CD measurements were carried out on 400 μL protein samples with a target concentration of 0.1 mg/mL (0.050-0.154 mg/mL actual, Table 3.4) as determined on the day of experiment by bicinchoninic acid assay (BCA, Pierce ™ BCA Protein Assay Kit, Thermo Scientific™) using BSA as a standard. Proteins were dialyzed into a CD buffer of 50 nM sodium phosphate, 140 mM sodium fluoride at pH 7.5. Chlorine

anions absorb strongly in the wavelength region of interest so NaF was used instead of NaCl.[137] CD spectra were obtained with Jasco J-810 Circular Dichroic Spectropolarimeter and a Peltier cell holder using a 0.1 cm path length cell. Raw data was collected from 270 nm to 170 nm with a 1 nm step size at temperatures ranging from 20C to 80C, increasing in either 10- or 20-degree increments, in continuous scan mode, scan speed 100. For each run, three scans were accumulated and averaged. Blank (CD buffer from dialysis steps containing everything except protein) measurements were collected at each temperature in triplicate, averaged, and subtracted from averaged sample measurements prior to data analysis. Three (ArtAB, H32A, CT) or four (T50A, R6A) biological replicates were collected and the averaged scans for each biological replicate were included in data analysis (total of 3 averaged scans per biological replicate, 3 or 4 biological replicates). A single biological replicate was collected for CT scans from 30-70 °C.

Protein secondary structures and normalized root mean squared deviation (NRMSD) values were estimated by singular value deconvolution of CD spectra using the DichroWeb[138–140] analysis server with the CDSSTR algorithm[141,142] and reference data set 4[142,143], which is suitable for soluble, globular proteins in the 190-240 nm range[140]. Data (collected in millidegrees) were converted into mean residue ellipticity by Dichroweb using the equation:

$$\Delta\varepsilon = \theta * \frac{0.1 * MRW}{(C \; x \; l) * 3298}$$

where θ is the ellipticity in millidegrees, MRW is the mean residue weight in daltons, C is the concentration of the protein in mg/mL, and l is the path length in

centimeters. Mean residue weight was calculated based on the predicted molecular weights of processed subunits (estimated with ProtParam[144]) as follows:

ArtB Pentamer

ArtB Processed (without signal sequence, runs here on SDS gel): 118 residues, MW: 13342.82

Residues: (5*118 residues) = 590 residues

Molecular Weight (MW): (5*13342.82) = 66714.1

Mean Residue Weight (MRW) = 66714.1 Da/590 residues = **113.07 Da/residue**

ArtAB Holotoxin

ArtA Processed (without signal sequence, runs here on SDS gel): 160 residues, MW: 21614.96

Res: ArtA processed + (5*ArtB processed) = 160 residues + (5*118 residues) = 750 residues

MW: ArtA processed + (5*ArtB processed) = 216154.96 + (5*13342.82) = 88329.03

MRW = 88329.03 Da/750 residues = **117.77 Da/residue**

Cholera Toxin

CTA Processed (runs here on SDS): 240 residues, MW: 27193.97

CTB Processed (runs here on SDS): 103 residues, MW: 11645.36

Res: CTA Processed + (5*CTB processed) = 240 residues + (5 * 103 residues) = 755 residues

MW: CTA processed + (5*CTB processed) = 27193.97 + (5 * 11645.36) = 85420.77

MRW = 88329.03 Da/750 residues = **113.14 Da/residue**

Spectra with backgrounds subtracted were further processed using CDToolX.[145] The Jasco spectropolarimeter collects data in millidegrees. Background-subtracted experimental spectra were opened in CDToolX and converted to delta epsilon units using the same parameters described above. Biological replicates were averaged and zeroed at 265-270 nm where protein absorbance is expected to be zero. All experimental spectra were scaled at 195 nm to allow for comparison of similarities and to correct for magnitude errors. Data shown are the zeroed, scaled, and smoothed averages of all biological replicates.

Predicted CD spectra for CT and PT were calculated using PDBMD2CD[146] using PDB files 1S5E[147] (CT, PDB DOI: 10.2210/pdb1S5E/pdb) and 1PRT[148] (PT, PDB DOI: 10.2210/pdb1PRT/pdb).

Table 3.4. **CD protein preparation and conditions**

Experiment Date	Protein	Temperatures Collected	Conc (ug/mL)
30Nov2021	ArtAB	20, 30, 40, 50, 60, 70	154
	CT		92
17Dec2021	T50A (1)		44
	R6A (4)		32
	H32A (4)		34
	ArtB		8
25Mar2022	T50A (1)	20, 40, 60, 80	100
	R6A (4)		100
	H32A (4)		100
	ArtAB	20, 30, 40, 50, 60, 70, 80	70
	ArtAB		47
02May2022	T50A (1)	20, 40, 60, 80	100
	T50A (1)		100
	H32A (4)		95
	H32A (4)		100
	R6A (4)		100

Mutagenesis

Primers (Integrated DNA Technologies) were reconstituted to 100 μM in

nuclease-free water (Promega, Ref. No. P119C) Annealing temperatures for primer pairs

were calculated using ThermoFisher's Tm calculator. Template DNA was prepared by

purifying plasmid pBM006 from ClearColi® (freezer stock Box 6 H1) using a GeneJet

Plasmid Miniprep kit (K0502). Concentration of purified plasmid was confirmed using

NanoDrop equipment. Mutagenesis reactions were performed using a Phusion Site-

Directed Mutagenesis Kit (ThermoScientific, Ref. No. F-541) per manufacturer's

protocol with PCR cycling parameters as indicated below. Mutagenesis PCR was

confirmed using agarose gel electrophoresis with positive identification of a band near

7200 bp (plasmid pBM006 contains 7284 bp). Parental DNA was digested using DpnI

digestion per manufacturer's protocol. 5 µL of DpnI-digested PCR product was used for ligation, and ligation was performed per manufacturer's protocol.

Ligated PCR product was transformed into competent ClearColi® cells by thawing 200 µL aliquots of competent cells on ice, incubating them with 10 µL ligation mix on ice for 45 minutes, heat shocking the cells for 2 min at 42 °C using a heat block, incubating on ice again for 4 minutes, then adding to 3 mL LB broth and incubating for 2 hours at 37 °C. After incubation, cells were centrifuged at 6000 rpm for 10 minutes. Supernatant was discarded except for a few drops. Cells were resuspended in drops, then 10 µL or 100 µL were incubated on antibiotic (chloramphenicol) LB plates and incubated overnight at 37 °C. Individual colonies were streaked onto a new CM/LB plate and confirmed by colony PCR using primers for the ArtAB insert containing the mutated nucleotide and primers for the insert + the pBAD18 promoter. Attempts were made to confirm the transformation by single and double restriction enzyme digests, however these were largely inconclusive.

Successfully transformed bacteria were collected from colony streak plates and stocked down in 1 mL LB + 20% glycerol + 0.5% glucose for long-term storage at -80 °C. pBM006 mutant plasmids were purified from successfully transformed bacteria using a GeneJet Plasmid Miniprep kit (K0502). Concentration of purified plasmid was confirmed using NanoDrop equipment. Plasmids and PCR products were prepared for Sanger sequencing at the Idaho State Molecular Research Core Facility (Pocatello, ID) with 100-250 ng total DNA for plasmids (2 µL of mini prep plasmid product + 8 µL nuclease-free H20) or 30 ng total DNA for PCR products (0.5 µL + 9.5 µL nuclease-free H20) with 2 µL primer at 3.2 µM for a total volume of 12 µL. Note: sequencing was

never successful using the pBAD18 or pBADecoli forward primers – all successful

sequencing was performed with reverse primer 200pr.

Mutant ArtAB was purified from successfully transformed bacteria with mutation

confirmed by plasmid sequencing. Purifications were performed as described above.

Table 3.5.   Mutagenesis primer pairs and annealing temps

ID	Sequence	# of NTs	MW g/mol	Ext Coeff l/(mol*cm)	Tm °C	Calc. Anneal. Temp °C	Anneal. Temp Used °C
H32AFW	GAATCTTCAGCAAGCTATTAG AGGTGACTCGTG	33	10192.7	325200	70.5	59.8*	63***
H32ARV	CTGTTATTACCATGAGAATTA AAACC	26	7937.3	259700	59.8		
R6AFW	GATTTTGTATATGCTGTTGACT CGAGACC	29	8913.9	276700	66.6	61.8	60
R6ARV	AACAGCACTTGCATAACCAG	20	6079	198900	61.8		
T50AFW	GACAGTAACTACATTGCGGCT ACCTCAGATATTAATG	37	11356.5	366100	70.2	70.2**	70
T50ARV	CCGACTACCGGCGGAACACGA G	22	6739.4	212700	71.5		
E115AFW	CGCTTGCAAAGTGCTTATGTA GCCGTAAATTC	32	9814.5	303900	70.8	63.0*	66***
E115ARV	CATCATCACTCGCTCAAAATG AC	23	6936.6	218700	63.0		
E115AFW #2	CGGTTGCAAAGTGCCTATGTA GCCGTAAATTC	32	9839.5	307700	71.8	68.6	70
E115ARV #2	CATCATCACTCGCTCAAAATG ACTAAACTGG	31	9432.2	299200	68.6		

* Tm difference ≥ 5 °C is not recommended
** Combined annealing/extension recommended when Tm values are >69 °C, using 72 °C for annealing step
*** Per kit – annealing temp should be +3 °C from calculator value if primers are ≥ 20 nucleotides.
Tried H32A at 60 °C at first but didn't work. Reactions at 63 °C did work.

Table 3.6.   Mutagenesis PCR cycling parameters

Primer Pairs (Date Used)	Initial Denaturation		Denaturation		Annealing		Extension		# of Cycles	Final Extension	
	T (°C)	t (s)	T (°C)	t (s)	T (°C)	t (s)	T (°C)	t (s)		T (°C)	t (m)
R6A, H32A (Feb 21)	98	30	98	10	60	30	72	210	25	72	10
T50A (Mar 21)					70						
E115A (Aug 21)					66						
T50A (Aug 21)											
E115A #2 (Oct 21)					70						

Table 3.7.   Colony PCR confirmation primers for mutants

Primer Name	Sequence	Expected Product	Amplicon (bp)
070pr	GATCCTCGCTAGCGTTTCTGTAGGAGGGTGTATG	Insert Containing ArtAB/Mutated ArtAB	1335
099pr	GCGCCAGAAGCTTGAAATATTTAGTTTGGCAACGTAGG		
pBAD18	CTGACGCTTTTTATCGCAACTCTC	Insert + pBAD18 Promoter	1400
099pr	GCGCCAGAAGCTTGAAATATTTAGTTTGGCAACGTAGG		
pBAD18	CTGACGCTTTTTATCGCAACTCTC	Insert + pBAD18 Promoter*	656
200pr	GGGTACTTACCTGTGGTACTG		

*Note: 200pr is closer to the promoter than 099pr, making it better for sequencing

Table 3.8.   Sequencing primers used to confirm mutants

Primer Name	Sequence	Notes
pBAD18 (FW)	CTGACGCTTTTTATCGCAACTCTC	Never worked for sequencing, worked for PCR
pBADecoli (FW)	GCGATCCTACCTGACGC	Never worked for sequencing, worked for PCR
099pr (RV)	GCGCCAGAAGCTTGAAATATTTAGTT TGGCAACGTAGG	Not long enough to see mutation
200pr (RV)	GGGTACTTACCTGTGGTACTG	Worked each time

Competent Cells

100 mL LB broth was inoculated with 0.5 mL of O/N broth culture. Broth was shaken at 37 °C until OD600 reached 0.3-0.5, then incubated on ice for 5 minutes. Broth was centrifuged for 10 minutes at 6000 rpm at 4 °C and supernatant was discarded. Cell pellet was resuspended in 50 mL sterile, chilled 0.1 M $MgCl_2$ and incubated on ice for 30 minutes. Cells were centrifuged for 10 min at 6000 rpm at 4 °C and supernatant was discarded. Pellet was resuspended in 5 mL sterile 0.1 M CaCl2 + 15% glycerol. Suspension was dispensed in 200 μL aliquots into sterile 1.5 mL microcentrifuge tubes and stored at -80 °C.

Mass Spectrometry Confirmation of Mutants

Samples of purified T50A, R6A, and H32A mutants were submitted to Boise State University's Biomolecular Research Center for mass spectroscopy analysis to confirm that the purified proteins contained the expected mutated residue. Mutant proteins in a 1X PBS + 5% glycerol buffer were preciptated by acetone precipitation.

Protein pellets were resuspended in 8 M urea solution, reduced by dithiothreitol, and alkylated by iodoacetamide. Samples were diluted to 1M urea concentration and incubated with trypsin overnight at 30 °C. Digested samples were desalted using a reverse-phase C18 spin column. Resulting peptides were separated on a reverse-phase C18 column (10cm x 75µm, 3 µm, 120 Å) and analyzed on a Velos Pro Dual-Pressure Linear Ion Trap mass spectrometer (Thermo Fisher Scientific) as described previously.[149] Peptide spectral matching were achieved by database search using Sequest HT algorithms in a Proteome Discoverer 2.2 (Thermo Fisher Scientific).

Cell Culture

CHO-K1 cells (CHO; ATCC®) were cultured in Ham's F-12 medium (Corning®, Thermo Fisher Scientific) supplemented with 10% FBS and 1% penicillin/streptomycin. Cells were maintained in T-flasks at 37◦C in a humidified 5% CO2 incubator and were passaged at 80% confluency using 0.05% trypsin/EDTA. Serum-free cell starvation procedures were completed with media (Ham's F-12for CHO-K1 cells) supplemented with 1% penicillin/streptomycin but without FBS.

ADP-Ribosylation Assays

ADP ribosylation assays were adapted from previously reported protocols (Tamamura et al., 2017[38], Xu/Barbieri, 1996[150], Uchida et al., 2009[39]).

In Experiment 1: the reaction mixture (120 uL) contained 0.1 mM ATP, 20 mM DTT, 3 mM thymidine, 10 µM biotinylated NAD+, 10 µM PT, ArtAB, or *E. coli* control, and 0.5 uL G-proteins in a buffer of 1X PBS, pH 7.4. G-proteins were isolated by another lab member per the Tamamura protocol were used. Briefly, cell membranes were prepared from mammalian cells grown in T75 flasks. Cells were washed twice with 1X

PBS, scraped from flasks, then centrifuged for 5 min at 600 × g. Pellets were resuspended in a solution of 0.25 M sucrose, 25 mM Tris-HCl (pH 7.5), and 5 mM $MgCl_2$, homogenized using a sample-grinding kit, and centrifuged at 600 × g for 10 min (to remove nuclei and unbroken cells). Supernatant was centrifuged at 40,000 × g for 20 min, then sediment was resuspended in a solution of 20 mM Tris-HCl (pH 7.5) and 5 mM $MgCl_2$ and stored at −80 °C.

The reaction proceeded for 3 hours at room temperature then was stopped by adding 2X SDS-PAGE sample buffer. Samples were resolved on a 12.5% SDS-PAGE gel, then transferred onto nitrocellulose membranes (Invitrogen Ref. No. IB23001) using the iBlot2 dry blotting system with the P0 setting. Membranes were incubated overnight in blocking buffer consisting of 10% BCS, then washed 3 times for 10 minutes with PBS-T, incubated with streptavidin-HRP diluted 1:10,000 for 3 hours at 4 °C, and washed again as above. 2 mL each of luminol enhancer solution and stable peroxide solution from the SuperSignal West Pico Plus Chemiluminescent Substate kit (ThermoScientific Cat. No. 34577) were combined in a 50 mL conical, and 2 mL of the mixed substrate was added directly to each membrane. Boxes were wrapped in foil and incubated at RT for 5 min, then removed from boxes, covered in plastic wrap and smoothed using the iBlot roller, and imaged on the BioRad imager in the shared equipment room.

In Experiment 2: Experiment 1 was repeated but was done with proteins isolated with Mem-PER kit. Both cytosolic and membrane fractions were used (in separate reaction). Membrane proteins were separated from cytosolic proteins in Vero cells using Mem-PER Plus membrane protein extraction kit (ThermoScientific, Cat. No. 89842) per manufacturer's protocol. Briefly, adherent Vero cells were scraped from T75 flask and

resuspended into growth media, counted, and washed with centrifuge steps to remove

supernatant. Cells were permabilized and cytosolic proteins were collected by

centrifugation and stored at -20 °C. Pellet was resuspended in solubilization buffer and

membrane proteins were collected by final centrifugation step and stored at -20 °C.

In Experiment 3: the reaction mixture (20 uL) contained 0.1 mM ATP, 20 mM

DTT, 5 mM thymidine, 10 μM biotinylated NAD+, 100 ng PT, ArtAB, or *E. coli* control,

and 0.1 μg recombinant human $G_{\alpha s}$ (abcam Prod. No. ab268602) or recombinant $G_{\alpha i}$

(abcam Prod. No. ab268599) in a buffer of 0.1 M Tris-HCl, pH 7.6. Reactions were set

up so that each toxin/control was tested against each G_α protein. All proteins to be used in

assay, including the G_α proteins, were confirmed on an SDS-PAGE gel prior to setting up

the reactions.

Reactions proceeded for one hour at 37 °C and were stopped by adding 2X SDS-

PAGE sample buffer. Samples were loaded and run on SDS-PAGE gels and transferred

to nitrocellulose membranes as described above. Membranes were stained with Ponceau

stain to confirm presence of protein. Membranes were blocked in 5% BCS in 1X PBS for

40 minutes at RT, then washed twice with PBS-T. Membranes were then incubated in

PBS-T on a rocker at RT for 10 minutes with a rinse step after incubation. This step was

repeated twice. 5 mL of streptavidin-HRP at 1:1000 in 2.5% BCS in 1X PBS was added

to the membranes and they were incubated for one hour at 37 °C, then washed twice with

PBS-T. Membranes were then incubated in PBS-T on a rocker at RT for 10 minutes with

a rinse step after incubation. This step was repeated three times. Chemiluminescence was

detected and membranes were imaged as described above.

In Experiment 4: The reactants that were leftover from the Experiment 3 reactions were used in a dot blot experiment. PVDF membrane was soaked in methanol then rinsed in nanopure water and, finally, transfer buffer, then arranged on top of a filter paper stack. 5 μL of each reaction mixture was blotted onto the membrane. G_α proteins were blotted as negative controls, and a biotinylated goat anti-rabbit antibody was blotted as a positive control. Presence of protein was confirmed by incubating membrane with Revert™ autofluorescent stain (Cat. No. 926-11011) and imaging on a LiCor imager. Membrane was then rinsed and streptavidin blocking solution in Odyssey blocking buffer for ten minutes at RT. Membrane was rinsed, then incubated with Streptavidin-IR800 dye (Cat. No. 926-32230) diluted to 1:4000 in blocking buffer for 30 minutes at RT. Membrane was rinsed twice in WB wash buffer for 5 minutes, then once in TBS. Membrane was imaged on the LiCor equipment. Fluorescence at blotted locations was detectable, unfortunately, the signal from the positive control was too bright and it obstructed the other controls and some of the experimental blots. This experiment was repeated but had the same issue with the positive control.

In Experiment 5: Reactions were set up as described for Experiment 3 using all of the same materials. Reactions were stopped using 4X sample buffer (Li-Cor, Prod. No. 928-40004) supplemented with 10% β-mercaptoethanol at a ratio of 3 μL sample to 1 μL buffer. Samples of each reaction, as well as G_α negative controls and a positive control of a biotinylated-hyaluronin binding protein (biotin-HBP), were run on mini-protean TGX precast 4-20% SDS-PAGE gels (Cat. No. 456-1094) supplied by the Beard lab. Gels were transferred to nitrocellulose membranes using the BioRad transfer kit materials, including 5X transfer buffer (Cat. No. 10026938) diluted to 1X and TransBlot Turbo mini stacks

(Cat. No. BR20180319), using the Power Blotter semi-dry transfer system in the Jorcyk lab. The pre-programmed method for mixed range proteins with molecular weight 25-150 kDa was run for 7 minutes. Membranes were air dried for 30 minutes at RT. After drying, membranes were stained with Revert™ (Cat. No. 926-11011) and imaged to confirm presence of protein. Membranes were rinsed and blocked in Intercept TBS blocking buffer (Cat. No. 927-60001) for 30 minutes at RT, then incubated with Streptavidin-IR800 dye (Cat. No. 926-32230) diluted to 1:1000 in Intercept antibody diluent (Cat. No. 927-65001) in a heat-sealed pouch overnight at 4 °C on a rocker. The next day, the membranes were rinsed five times wtin TBS-T for 10 minutes at RT, then once with TBS for 10 minutes at RT, then imaged on Li-Cor equipment. The biotin-HBP positive control was clearly present, but no other bands could be detected.

In Experiment 6: Experiment 5 was repeated using sample buffer without β-mercaptoethanol. Samples were also used to prepare a dot blot as described above. The biotin-HBP positive control was detected on both the nitrocellulose membrane and the dot blot, but no other samples were detected.

MacroGreen Expression and Purification

Plasmid pNIC28-MacroGreen containing the gene for MacroGreen (modified macro domain protein called Af1521 that binds both free ADP-ribose and ADP-ribosylated proteins conjugated to GFP and containing mutations to improve ADP-ribose binding and reduce ADP-ribosyl glucohydrolase activity) was purchased from AddGene and received as a bacterial stab (Prod. No. 160655). Bacteria from stab was expanded by streaking onto Luria Broth (LB) plates supplemented with kanamycin (Acros, Ref. No.

61129.0050) antibiotic, and bacteria from streaked plates was stocked down for long-term storage at -80 °C in LB + 20% glycerol + 0.5% glucose.

MacroGreen was expressed and purified as close to the originally described protocol as possible (Figure 3.1).[151] Bacteria containing the MacroGreen plasmid were grown in Terrific Broth containing kanamycin at 37°C to O.D. 0.35, then induced with 0.5 mM IPTG. Overnight induction broth was centrifuged and cells were resuspended in B-PER (ThermoScientific Ref. No. 78260) at 4 mL/1 g cell pellet supplemented with 10 uL/mL EDTA-free Halt protease inhibitor cocktail (Thermo Scientific Cat No. 78439) and 2 uL/mL DNAseI (Fisher Bioreagents BP81071). The soluble lysate was collected by centrifugation, filter sterilized with a 0.2 μm vacuum filter (Millipore, Cat. No. SCGP00525), and purified over His-Pur cobalt resin (Thermo Scientific Cat No. 89964). The column was equilibrated and washed with equilibration/wash buffer (50 mM sodium phosphate, 300 mM sodium chloride, 10 mM imidazole; pH 7.4) and eluted with elution buffer (50 mM sodium phosphate, 300 mM sodium chloride, 300 mM imidazole; pH 7.4). Fractions were collected in 1.5 mL aliquots and confirmed with SDS-PAGE (Figure 3.1a).

Fractions containing MacroGreen were pooled and dialyzed in a 30 mL dialysis cassette with 20 kDa MWCO (ThermoScientific Cat No. 66030) against 1X PBS + 5% glycerol at 4°C overnight with one buffer change after 6 hrs. Molecular weight and purity were confirmed with SDS-PAGE. Protein concentration was determined by BCA protein assay (Pierce ™ BCA Protein Assay Kit, Thermo Scientific™) using BSA as a standard. GFP activity was confirmed by loading sample onto black-walled clear-bottomed plate

96-well plate (Costar Ref. No. 3603) and reading fluorescence (excitation 395 nm, emission 509 nm) on a BioTek Cytation 3 plate reader (Figure 3.1b).

Figure 3.1.   Purification and GFP activity of MacroGreen

*Histidine-tagged MacroGreen was purified over cobalt. **(a)** Washes (W) and elutions (E) from initial cobalt purification step. Fractions with minimal junk were pooled, dialyzed, and concentrated; **(b)** Final purified product exhibited GFP activity with absorbance at 395 nm and emission at 509 nm. A single replicate was performed so no statistics were performed on this figure.*

MacroGreen Experiments

Western blot: CHO cells were seeded at 50,000 cells/well on a 12-well cell culture plate and incubated overnight. Cells were then treated with 2 mL of CT or ArtAB at 25 ug/mL in complete media or media control. Cells were incubated for 24 hours, after which brightfield images were collected to assess cell structures and confirm toxin activity. Cells were then rinsed four times with 1 mL 1X PBS, 300 uL of 1X SDS sample buffer (BioRad Prod. No. 1610737) was added to each well, and cells were harvested by scraping the bottom of the plate with a cell scraper and aspirating the product with a pipette. Cells were collected into a 1.5 mL centrifuge tube, boiled for 5 minutes, and stored at 4C. The next day, 100 uL of each sample were aliquoted for sonication (two times with 2 second pulses).

100 uL of sonicated and unsonicated samples were run on 15% SDS-PAGE gels, then transferred to nitrocellulose membranes using the iBlot 2 transfer stack system (Prod

#1323001) using program P0. Membranes were stained with Ponceau stain and imaged to confirm presence of protein. Membranes were rinsed with water to remove Ponceau stain, then 2 mL of purified MacroGreen at 25 ug/mL in 1X PBS was added and membranes were incubated on a rocker at room temperature for 30 minutes. Membranes were rinsed by incubating in 10 mL 1X PBS + 0.05% Tween-20 (PBS-T) on a rocker at room temperature for 5 minutes, then incubating in 10 mL 1X PBS on a rocker at room temperature for 5 minutes, then rinsed with 10 mL 1X PBS. Membranes were imaged on a BioRad imager (shared equipment room) using the settings for detecting green fluorescent dyes. No bands were detected on the membranes. There may be a better way to detect GFP on a membrane, but we ran out of time to troubleshoot this assay.

ELISA: The remaining 100 uL of sonicated/unsonicated samples from the WB experiment were added to the first column of a black-walled, clear-bottomed 96-well plate and serial dilutions into 1X PBS were performed with the last column filled with only 1X PBS. Plate was incubated overnight at room temperature. Lysates were removed by decanting and plate was rinsed one time with 200 uL PBS-T. Plate was blocked in 5% bovine serum albumin in 1X PBS for 45 minutes at 37C, then rinsed three times in 200 uL PBS-T. 50 uL of purified MacroGreen at 50 ug/mL in 1X PBS was added to each well and plate was incubated at 4C for 10 minutes. Plate was rinsed 3 times in 200 uL PBS-T and one time in 1X PBS, with a final application of 100 uL 1X PBS to keep the proteins hydrated, and plate was read on BioTek Cytation3 plate reader with fluorescent settings of 470 nm excitation/515 nm emission. Issues with the plate reader resulted in inconclusive results, and we ran out of time to troubleshoot this assay.

Fixed cell staining: CHO cells were grown for 24 hours to subconfluence on uncoated coverslips at 37C with 5% CO2. Cells were washed twice with 1X PBS, then treated with toxins at 125 ug/mL in complete media and incubated for 2 hours at 37C. Cells were then fixed in 4% formaldehyde (incubation for 15 minutes at room temperature) and permeabilized in 0.05% Triton X-100 in PBS (incubation for 15 minutes at room temperature). Quenching was performed by incubating fixed/permeabilized cells with 100 mM glycine in 1X MBS for 10 minutes at room temperature, then cells were blocked in wash buffer of 1X PBS + 0.05% Tween-20 + 0.5% bovine serum albumin for 30 minutes at room temperature. Cells were washed twice in wash buffer, then incubated with 5 μM MacroGreen in wash buffer for 20 minutes at room temperature. After incubation cells were washed three times in wash buffer, then once in PBS, and, finally, coverslips were mounted onto slides using DAPI mounting medium (Southern Biotech, Cat. No. 0100-20). Slides were visualized using an EVOS with a GFP filter. No GFP signal could be detected on the slides.

Cellular Activity and Morphology Assays

Cellular activity was assessed using alamarBlue™ as previously described.[128] 96-wellplates were seeded with Vero or CHO-K1 cells at a density of 5000 cells per well in 200μL of complete culture media and incubated overnight. Cells were starved in serum-free media for 4 hours prior to treatment. ArtAB, ArtAB mutants, or CT in a buffer of 1×PBS + 5% glycerol at a concentration of 25μg/mL (5μg total in 200μL, or PT (List Biological Labs, Inc, Prod. No. 180) in a buffer of 1×PBS at a concentration of 5μg/mL (1μg total in 200μL); or a vehicle control consisting of growth of the empty pBAD18 vector in *E. coli* induced and purified the same way as the toxins; or complete culture

media was added to the cells. Each treatment was added to 3 wells per plate. One biological replicate included three treated wells for each of four post-dose time points, and three biological replicates were collected. Plates were treated at the same time, incubated, and removed from the incubator at the appropriate time point (4-, 24-, 48-, or 72-hours post-treatment) for analysis.

After 4, 24, 48, or 72 hours of incubation with treatment, brightfield microscopy images at 10× and 20× magnification were collected using a BioTek Cytation 3 imager. Images were collected randomly from varied locations within wells and from multiple wells for each treatment dose. Immediately after imaging, 200 μL of 10% (v/v) alamarBlue™(Invitrogen™) in complete culture media was added to each well and plates were incubated for 4 hours. Fluorescence was read on the BioTek Cytation 3 imager using excitation wavelength of 560 nm and emission wavelength of 590 nm per alamarBlue™ manufacturer's instructions.

For fluorescence images, after 4, 24, 48, or 72 hours of incubation with treatment, media/treatment was aspirated using a multichannel pipette. Cells were rinsed 2 times with 150 μL 1X PBS, then fixed in 150. μL 4% formaldehyde (incubation for 15 minutes at room temperature (RT)) and permeabilized in 150 μL 0.5% Triton X-100 in 1X PBS (incubation for 15 minutes at RT), and rinsed three times in 150 μL 1X PBS. Cells were incubated with 50 μL 1X Hoescht stain in 1X PBS and 50 μL orange CellMask actin tracking stain (Invitrogen, Prod. No. A57244) for 15 minutes at RT. Note: actin tracking stain was purchased as a three-color sample pack. Preliminary studies showed that the green stain (Prod. No. A57243) also produced satisfactory images. Another note: this Hoescht stain was obtained from the Biomolecular Research Center and it photobleached

very quickly. It was difficult to obtain clear images with defined nuclei. Another nuclear stain, or freshly diluted stain from the same parent stock, should be pursued for future experiments. After incubation with stains, cells were rinsed 3 times in 150 μL 1X PBS, and 50 μL 1X PBS was added to prevent cells from dehydrating during imaging. Cells were imaged with an EVOS microscope.

Results

<u>Establishment of a Predicted Structural Model of ArtAB</u>

The practice of identifying proteins with limited genetic or protein sequence homology but close structural homology is not novel. Countless proteins have been found to contain conserved structural cores even as genetic and protein sequences differ. Recently, in response to a rapid increase in the number of available protein structures, tools have been developed to help researchers account for and investigate structural homologies. These tools utilize structural models, rather than protein sequences, and compare the spatial alignments of residues of multiple proteins. A crystal structure of ArtAB has not yet been obtained, however, current bioinformatics and artificial intelligence (AI) technologies allow for powerful predictive protein structural modelling.

AlphaFold 2 (AF2) is a powerful AI-based deep learning tool from DeepMind for predicting protein structures with open source software that was released in July of 2021 alongside a Nature publication.[152–155] AF2 and AlphaFold Multimer, released in November 2021, both allow for modelling and predictions of multimeric complexes, but AF2 is easily accessible through ChimeraX Version 1.4.[156] We generated a multimeric structure for ArtAB holotoxin by running an AlphaFold version 2.2.0 calculation using Google Colab[129] (Figure 3.2a). Outputs are colored according to the predicted Local Distance Difference Test (pLDDT) score, a measure of the confidence of the prediction of the location of each residue on a scale from 0-100. To summarize, LDDT was developed as a quantitative method of assessing predicted models. While many quantitative model assessments, including root mean square deviation (RMSD) and global distance test (GDT), involve superposing predicted and experimental structures

and measuring the differences between backbone Cα atoms, there are limitations with this method. Flexible proteins can result in experimental structures that don't line up exactly with predicted models, missing parts of models cause issues, and the method depends wholly on the superposition of the model and reference structure. The LDDT is a superposition-free method that takes into account the local interactions of each atom, including non- Cα atoms, the distances between all pairs of atoms in the reference structure within tolerance thresholds of 0.5, 1, 2, and 4 Å, and the stereochemical plausibility of the model.[157] Each residue receives a score, and AlphaFold stores the scores in the metadata of the PDB file so the model can be colored according to the pLDDT scores. Regions of a predicted model with pLDDT 90 (light blue) to 100 (dark blue) are expected to have high accuracy, and regions with pLDDT 70 (colored yellow) to 90 (light blue) are expected to at least have a well-modeled backbone.[158] In the multimeric predicted model, the residues at the interface where the A subunit interacts with the B subunit have lower pLDDT scores as indicated by the red to yellow coloring and may not be relied upon for structural accuracy (Figure 3.2a,b).

The purpose of this study was to specifically probe the structure of the active subunit, so we established a model of the ArtA subunit alone (without the pentamer) that could be used for further study. We separated the A chain from the multimeric holotoxin structure for further direct analysis (Figure 3.2b). We also generated a monomeric ArtA structure using AF2 (Figure 3.2c). In both models, the regions of the A subunit distal to the pentamer interface contain residues with extremely high expected accuracy, and the secondary structures appear to align closely with the expected conserved ART fold (Figure 3.2a,b,c). In the monomeric AF2 model, with the ArtA sequence input alone, the

pLDDT scores are even higher across more of the model (Figure 3.2c). Additional views of the models are available in Supplementary Figure 3.S1 and movies of the models are available (see Supplementary Materials section for link).

To investigate whether the ArtA chain of the multimeric predicted model and the individual ArtA monomeric predicted model are similar, we used the Matchmaker tool in ChimeraX to superimpose and compare the two (Supplementary Figure 3.S2a-c). The models are nearly identical except for the 53 residues at the C terminus and a short section of five residues within the flexible loop region, which, upon visual inspection, do not appear to affect the catalytic pocket (Supplementary Figure 3.S2d). The RMSD over all residue pairs is 6.427, however, after pruning long atom pairs (pairs that exceed 2 Å) which mainly includes the C-terminus after residue 171, the RMSD is 0.541. More research is required to confirm whether the differences between predicted models are significant and obtaining a high-resolution 3D structure would provide essential confirmation of these issues. We chose to use the monomeric AF2 model since it had higher overall pLDDT scores but aligned closely in the ART fold region with the multimer model.

We had previously constructed a model for ArtA using the Protein Homology/analogY Recognition Engine V 2.0 (Phyre2)[159] protein modelling system (data unpublished). We used the same ArtA protein sequence (without the signal sequence) to produce the model (Figure 3.2d, additional views in Supplementary Figure 3.S1 and movies available in Supplementary Material). We compared this model to the AlphaFold monomeric model in the same way, by superimposing the structures with the Matchmaker tool in ChimeraX (Figure 3.2e,f) and calculating RMSD values for the

backbone Cα molecules (Figure 3.2g). The AF2 and Phyre2 models are closely aligned in the ART fold region. The RMSD over all residue pairs is 5.464, however, after pruning long atom pairs (pairs that exceed 2 Å), the RMSD is 1.030. A visual examination of the structures indicates that the two predicted models contain nearly identical secondary structures throughout, with the major differences occurring after residue 171 and continuing through the C terminus. While a few smaller sections of 5 to 7 residues do not align perfectly and have higher Cα RMSD values (residues 39-43, 63-71 and 135-141), visual inspection reveals that these sections contain the same secondary structures and features and differ mainly in their three-dimensional location within the molecule (Supplementary Figure 3.S3). These models will support analysis of a high-resolution experimental structure, such as that obtained from cryo-electron microscopy (cryo-EM). In addition, since both algorithms had differences in predicting residues 39-43 and the C-terminal residues from around P171 to the end of the sequence, it will be important to define these regions with a high-resolution experimental structure.
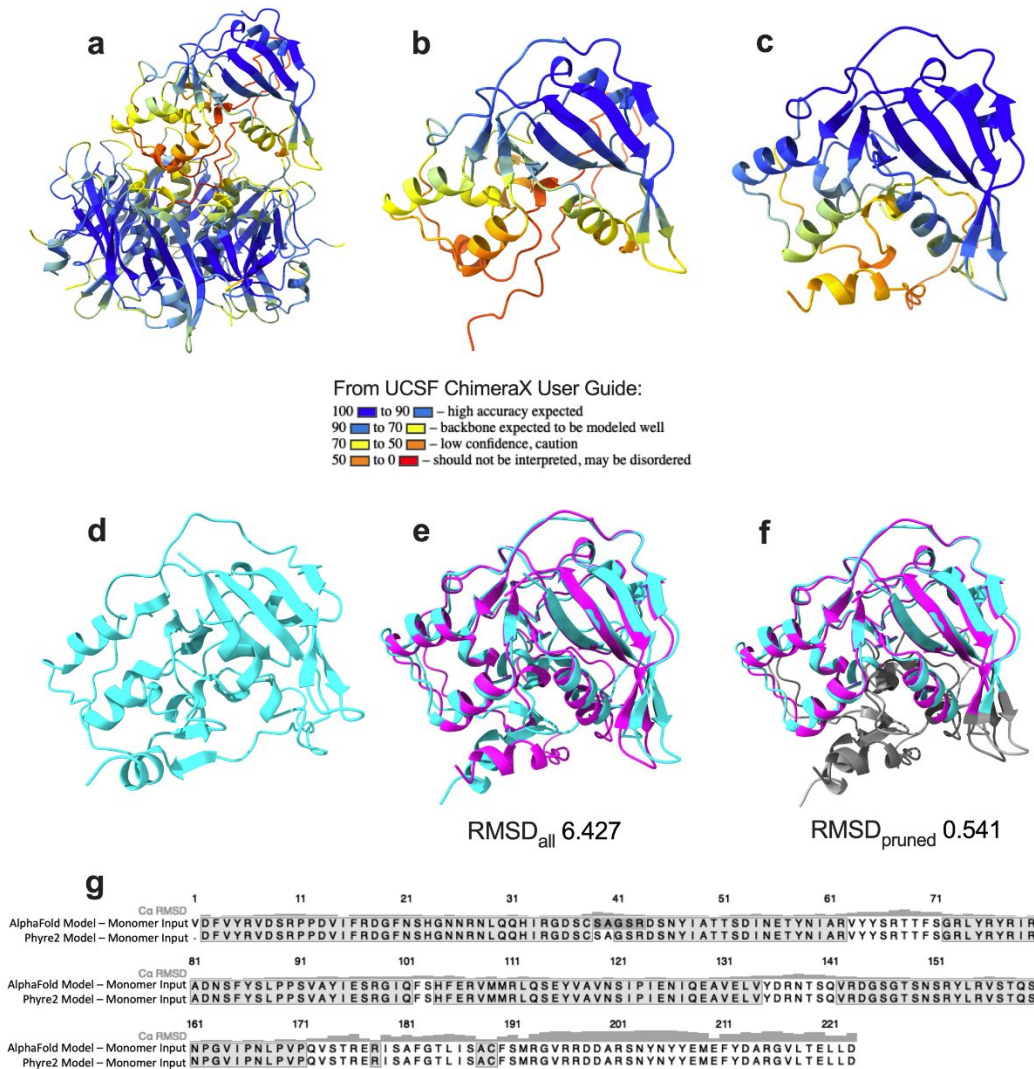
Figure 3.2.   Establishment of a predicted structure for ArtA

(a) Structural model of ArtAB holotoxin predicted using AlphaFold 2 (AF2); (b) ArtA chain isolated from the holotoxin multimeric complex model; (c) structural model of ArtA individual monomer predicted using AF2; (d) structural model of ArtA individual monomer predicted using Phyre2; (e) Phyre2 (cyan) and AF2 (magenta) models superimposed; (f) superimposed models shown with poorly fit residues shaded in gray; and (g) a pairwise sequence alignment was completed using the Matchmaker tool in ChimeraX. AF2 models are colored according to the predicted Local Distance Difference Test scores. RMSD values for Cα molecules are indicated in gray above the sequence alignment.

Structural Comparison to Other ADP-Ribosylating Toxins

Since both models aligned closely in the critical ART fold region, and the

monomeric model has higher overall pLDDT scores, we chose to use the AF2 monomeric

model for further analysis. We used mTM-align,[130,131] a robust algorithm for pairwise

structural alignments, to examine the structural homology of ArtA to the other ADP-ribosylating toxins. mTM-align performs a database search to identify proteins with structural homology to the input query sequence, in this case, the monomeric ArtA model from AF2. The output is a list of related sequences with a TM-score > 0.5, where a TM-score of 1 is a perfect match. From the list of 51 results, we selected 9 structures to use for a multiple structure alignment (Figure 3.3). We chose models that contained only holotoxins; models with small molecules or binding substrates were excluded. For some proteins multiple models existed, as in CTA and LTA, and we included both. mTM-align produces a phylogenetic structure-based tree (Figure 3.3a) showing the relationship of each input to the query sequence. The closest structural match to ArtA is the *E. coli* pertussis-like toxin A (*Ec*PltA) subunit, with a closely related branch on the phylogenetic tree being the putative pertussis-like toxin subunit of Typhoid Toxin. Each of these falls under the main branch of pertussis toxin A (PTA), which is surprisingly removed from cholera toxin A (CTA) and the *E. coli* heat-labile enterotoxins (LTA and LTIIBA).

mTM-align also provides the TM-score, RMSD, sequence identity, length of protein, and length of the protein that is aligned with the query protein (Figure 3.3b). None of the sequences share more than 70% sequence identity with ArtA. The TM-scores and RMSD values are largely reflected in the phylogenetic tree.

The multiple structure alignment is colored so that columns in magenta are common core regions, which are composed of columns that have no gaps and meet the maximum pairwise residue distance parameter of < 4 Å (Figure 3.3c). Figure 3.3d presents the calculated metrics for the alignment, including the length of the common core (L_{core}, 124 residues), the average pairwise RMSD within the common core

(ccRMSD, 1.11), the average pairwise TM-score within the common core (ccTM-score, 0.778), the average pairwise length (L_{ali}, 135), the average pairwise RMSD (RMSD, 1.18), and the average pairwise TM-score (TM-score, 0.843). All of these metrics indicate a good fit model that provides coverage of related proteins. The regions that are not included in the common core are mainly in flexible loops and turns and in the C-terminal residues after residue 260 in the multiple structure alignment, which have been cut off to save space (Figure 3.3c). mTM-align compiles the common core residues into an aligned structure in a downloadable PDB file. Multiple views of the common core are provided in Figure 3.3e. Findings that come from these studies will promote comparisons with other ARTs and the identification of new toxins. Our results will be further investigated with wet lab experiments, and future studies will provide further analysis of the common core structure.

a — phylogenetic tree:
- query - *S.* Typhimurium DT104 ArtA
- 4z9dC - EcPltA
- 4z9cA - EcPltA Oxidized
- 4k6IG - Putative pertussis-like toxin subunit of Typhoid Toxin
- 1prtA - PTA
- 4tlwA - CARDS Toxin
- 1s5eA - CTA
- 1ltbA - LTA
- 1xtcA - CTA
- 1tiiA - LTIIBA

b

Protein Name	PDB ID	TM-score	RMSD	Sequence Identity	Length (Residues)	Aligned Length (Residues)
EcPltA	4z9dC	0.7427	1.25	0.674	175	172
EcPltA Oxidized	4z9cA	0.8200	2.74	0.654	223	208
Putative pertussis-like toxin subunit of Typhoid Toxin	4k6IG	0.8296	2.73	0.587	224	208
PTA	1prtA	0.7654	3.43	0.271	224	203
CARDS Toxin	4tlwA	0.7766	3.02	0.240	567	204
CTA	1s5eA	0.5785	2.73	0.245	232	151
LTA	1ltbA	0.5731	2.81	0.240	185	150
CTA	1xtcA	0.5797	2.85	0.237	192	152
LTIIBA	1tiiA	0.5768	2.67	0.208	186	

c — multiple structure alignment

d

Metrics	Value
L_{core}	111
ccRMSD	1.25
ccTM-score	0.538
L_{ali}	151
RMSD	1.56
TM-score	0.714

Figure 3.3. **Multiple structure alignment of ArtA with other ADP-ribosylating toxin subunits**

*Analysis was performed with mTM-align web portal. **(a)** A phylogenetic tree showing structural relationships between ArtA and 9 selected related toxins; **(b)** alignment metrics for pairwise comparisons to ArtA; **(c)** multiple structure alignment with common core regions highlighted in magenta; **(d)** metrics of the common core calculation from multiple pairwise structural alignments; **(e)** multiple views of the common core structure produced by mTM-align.*

The phylogenetic tree shows that ArtA is closely related to PTA. Since PT is readily available as a commercial product and can be purchased and used for wet lab studies, and since we have conducted studies with PT in the past, we chose to move forward by comparing the structures of PTA and ArtA. Figure 3.4a shows a cartoon diagram of ArtA's fold pattern. As described in the introduction, it bears overall three-dimensional resemblance to the Rossmann fold, but its specific folding pattern is unique. Figure 3.4b shows a snapshot of the ArtA model with the secondary structures labelled according to the cartoon diagram. Comparing this diagram to PTA reveals a nearly identical structure, although a beta sheet composed of ArtA β7 and β8 are not present in

PTA; β6 leads directly to β7, which exits the core structure (Figure 3.4c,d). Using the

Matchmaker alignment tool again, as described above, we compared the experimental

structure of PTA and the AlphaFold monomeric predicted model. The alignment is close;

the RMSD over all residue pairs is 6.989, however, after pruning long atom pairs, the

RMSD is 0.890 (Figure 3.4e). A visual examination of the structures reveals a very close

alignment with the only major differences being that PTA has a longer α3 helix than

ArtA, and PTA's β6 and β7 are actually just longer and more aligned, whereas ArtA's

same section is seemingly divided into four separate β sheets that are "bent" out of the

plane that PTA's β6 and β7 run in (Figure 3.4f). The differences are easily identifiable on

the movies, which are included in the supplementary materials. The differences could be

an artifact of the modelling process and could be confirmed with a high resolution atomic

structure. Figure 3.4g shows the multiple sequence alignment.
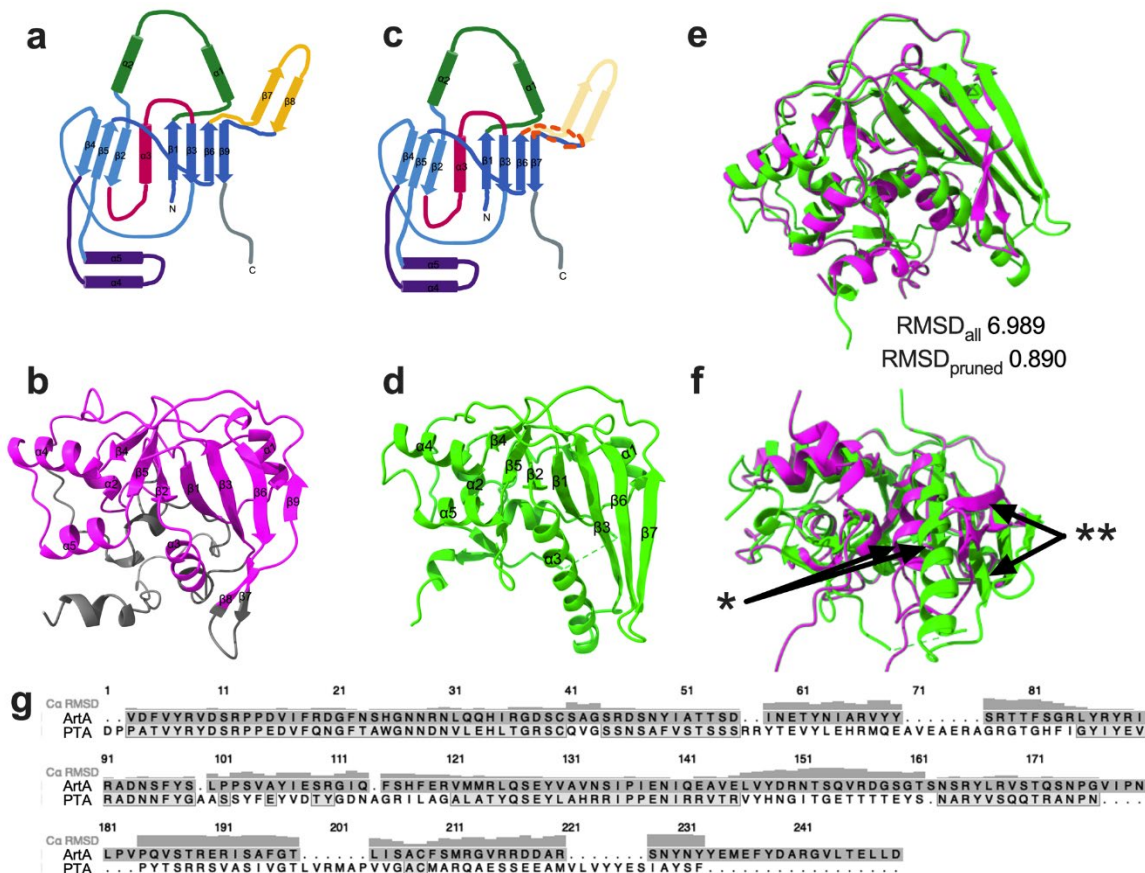
Figure 3.4.   Comparison of ArtA and PTA

(a) Cartoon depiction of the folding structure for ArtA; (b) snapshot from ChimeraX of the ArtA structure with labels corresponding to the cartoon diagrams in panel (a); (c) cartoon depiction of the folding structure for PTA; (d) snapshot from ChimeraX of the PTA structure with labels corresponding to the cartoon diagrams in panel (c); (e) structures of ArtA and PTA superimposed using ChimeraX Matchmaker tool; (f) alternate view of the superimposed structures showing the major differences; (g) a pairwise sequence alignment was completed using the Matchmaker tool in ChimeraX. RMSD values for Cα molecules are indicated in gray above the multiple sequence alignment.* the α3 helix of PTA is longer than that of ArtA. ** PTA's β6 and β7 are long and continuous, whereas ArtA's same section is divided into β6, β7, β8, and β9, and the middle pair juts out discontinuously.

Biophysical Characterization of Purified ArtAB

In addition to predictive modelling, biophysical techniques can be used to investigate the structure and biophysical properties of a protein. According to our modeling work, ArtAB is expected to be structurally similar to PT. Because it has four distinct subunits that make up its pentamer (one is present in two copies), PT has proven difficult to clone and purify in our lab. It is available commercially but the quantity needed for experiments exceeds our current budget. CT, on the other hand, has been

cloned and successfully purified in our lab and we can produce it as needed. We have shown that our purified CT is active and behaves similarly to commercially purchased CT (see study in Chapter 4, Figure 4.1). For these reasons, we chose to use CT as a comparator for the biophysical studies presented below.

As a solution-state method, analytical ultracentrifugation (AUC) allows for examination of a protein in its native environment without requiring comparison to standard curves, chemical modifications, or use of physical matrices. In addition, AUC experiments directly provide information on the size, sedimentation, gross shape, and homogeneity of a protein sample. We performed sedimentation velocity experiments to investigate these parameters for ArtAB and analyzed the results using both SedFit (for a c(s) analysis) and DCDT+ (for g(s) and -dc/dt analyses). Results are presented in Figure 3.5.

Size: The experimental molecular weight of ArtAB was calculated to be 83.4 ± 4 kDa. This is close to the molecular weight predicted by ProtParam[144] of 88.3 kDa. For comparison, a previous AUC study of CT showed that CT had an experimental molecular weight of around 79 kDa,[160] which is also close to, but lower than, the predicted MW of 85.4 kDa. This could be evidence of proteolytic cleavage at the A_1/A_2 cut site occurring at some point during purification, although further investigation is required to confirm.

Sedimentation: A sedimentation coefficient of 3.7 ± 0.1 S was calculated for ArtAB from sedimentation velocity experiment data. This is lower than the reported sedimentation coefficient of 5.25 ± 0.05 S for CT.[160] The sedimentation coefficient can be defined by the equation: $s = \frac{m}{6\pi\eta r_0}$ where m is the mass of the particle, η is the viscosity of the medium, and r_0 is the Stokes radius of the particle. A higher

sedimentation coefficient indicates that the particle sediments faster. Since CT and ArtAB have very similar masses, the difference in sedimentation coefficients indicates that ArtAB likely has a larger Stokes radius than CT. Sedimentation coefficients have been reported for the CTB pentamer (3.6 S,[161] 4.4 S,[162] 6.3 S for a heterodimer[163]) and the LTB pentamer (4.4 $\pm$ 0.1 S)[163] but we did not identify any additional reported sedimentation coefficients for similar AB_5-type holotoxins determined by AUC that we could use for direct comparison.

Gross Shape: In the first experiment the spheroid parameters returned were 15.00 for a/b oblate and 13.21 for a/b prolate. In the second experiment the result was 15.87 for a/b oblate = 15.87 and 13.96 for a/b prolate. These results indicate that ArtAB exists as a globular but asymmetric protein. The exact shape of the molecule could be verified by obtaining a high-resolution atomic structure through X-ray crystallography or cryo-EM.

Homogeneity/aggregation: Each sedimenting boundary is created by an individual species in solution, so the presence of a single sedimenting boundary, indicated by a single peak accounting for > 90% of the material as identified in both the Sedfit and DCDT+ data analysis (Figure 3.5c-e), is evidence of homogeneity of the solution and of a lack of either aggregation or separation into A monomers and B pentamers or monomers.

Model quality: Model quality, as assessed by the residuals (Figure 3.5c-e), appears to be good for each model. Residuals show randomness, indicating a lack of systemic issues, and are contained within an acceptable range.

Table 3.9.   Predicted and experimental molecular weights of ArtAB and CT subunits and holotoxins

Toxin/Subunit	Expected MW per ProtParam (Da)	Previously Reported Results (kDa)
CTA	27193.97	SDS-PAGE: 28[164], 24[165], 28[166]
CTB	11645.36	SDS-PAGE: 11[164], 9.7[165], 8[166]
CTB Pentamer	58226.8	SDS-PAGE: 68[164], 50[161] AUC: 50[161], 58[162]
CT	85420.77	AUC: 79[160],
ArtAB Holotoxin	88329.03	
ArtA	216154.96	SDS-PAGE: 27[38] Mass Spec: 27.6[128]
ArtB	13342.82	SDS-PAGE: 13.8[38] Mass Spec: 15.8[128]
ArtB Pentamer	66714.1	
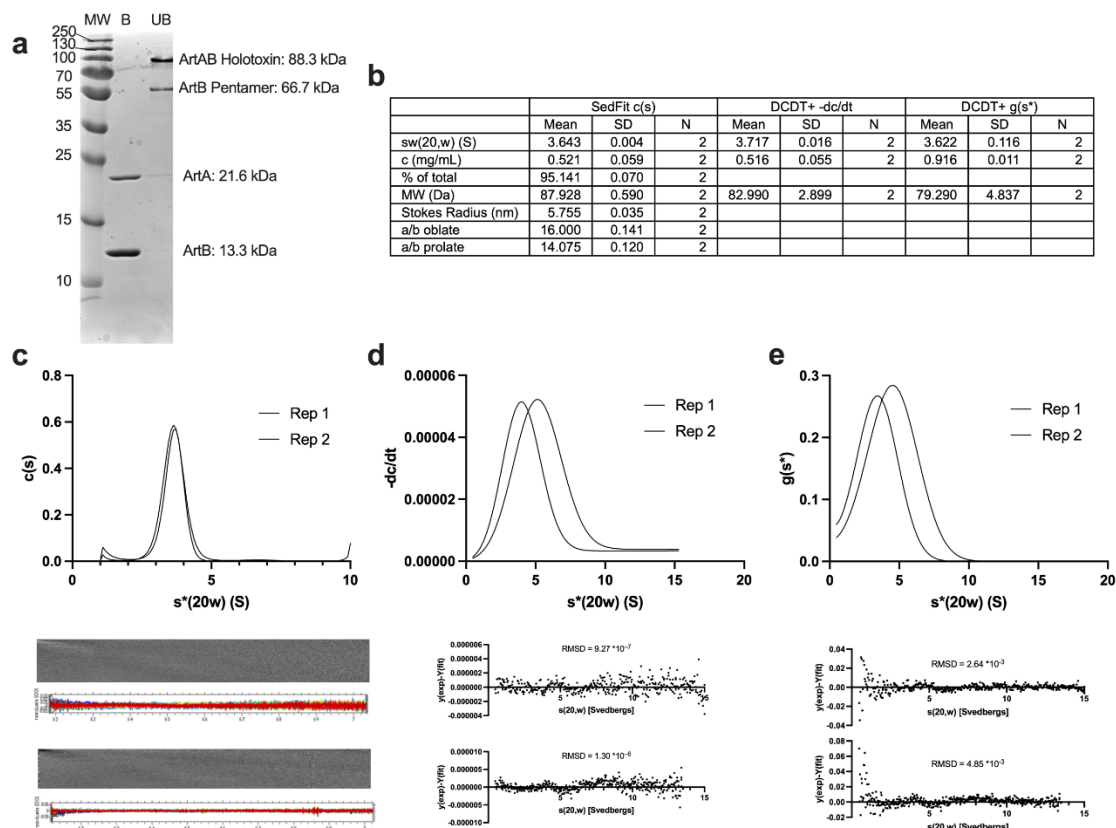
Figure 3.5.   **Analytical ultracentrifugation sedimentation velocity study of ArtAB**

(a) SDS-PAGE gel with non-heat-denatured/unboiled (UB) and heat-denatured/boiled (B) samples of ArtAB used for AUC experiments. Per ProtParam predictions (Table 3.9), ArtAB holotoxin is expected to run at 88.3 kDa, ArtB pentamer at 66.7 kDa, ArtA at 21.6 kDa, and ArtB at 13.3 kDa; (b) Results of two biological replicates of a sedimentation velocity study analyzed with a c(s) distribution using SedFit, a -dc/dt distribution using DCDT+, and a g(s*) distribution using DCDT+; and Graphical representations of the fitted curves for (c) the c(s) distribution (SedFit),(d) -dc/dt distribution (DCDT+), and (e) g(s*) distribution (DCDT+). Residuals for each individual experiment are included below the corresponding graphical representation

We next sought to explore the secondary structure of ArtAB in comparison to CT and to investigate the toxin's thermal stability using far-UV circular dichroism (Figure 3.6). The ArtAB CD spectrum at 20°C contains a wide negative minimum between 210-220 nm and a positive maximum around 195 nm which is characteristic of proteins containing large amounts of β strand structures (Figure 3.6a). Deconvolution of the CD spectra using CDSSTR deconvolution algorithm (via DichroWeb[138,139]) shows that ArtAB at 20°C has a large percentage of β strands (21% β1, 11% β2) and a low percentage of α helices (5% α 1, 9% α 2). 24% of the protein is made up of turns, and

29% is unordered (Figure 3.6b). A thermal denaturation experiment showed that ArtAB was stable at temperatures from 20°C to 70°C with changes in secondary structure appearing to occur at 70°C as evidenced by a change in the spectrum at 70°C (Figure 3.6c). This is a somewhat unexpected change as the shape of the curve with a deeper minimum appears to represent formation rather than a loss of secondary structure. Deconvolution solutions, however, do not show a significant loss of either α or β secondary structures (Figure 3.6d).

To confirm the quality of the DichroWeb results, DichroWeb back-calculates CD spectra based on the secondary structures determined and overlays the back-calculated spectrum on the experimental spectrum. The program reports the normalized root mean squared deviation (NRMSD), a goodness-of-fit parameter, which indicates the correspondence of the experimental and back-calculated spectra. NRMSD values > 0.1 indicates a poor fit and suggests that the protein of interest contains features that are not present in the proteins that comprise the reference set. All NRMSD values for these experiments were < 0.1 (Figure 3.6g).

As discussed above, ArtAB is expected to be structurally homologous to the CT pentamer and the PT active subunit, so we expected to find some similarities in the CD spectra. We were not able to produce an experimental PT spectrum for comparison, however, the web server PDBMD2CD is an *in silico* molecular dynamics-based resource for generating predicted CD spectra from PDB protein structural files.[146] With a PDB file uploaded as the input, PDBMD2CD first produces a predicted spectra based on a reference of seven different types of secondary structures derived from CD studies on a reference set of proteins. Next, it uses proteins in the reference set that have close

secondary structural content to that of the input protein to eventually produce a prediction spectra. Finally, the two predicted spectra from each approach are averaged and a single spectrum output is produced. We generated predicted CD spectra for both CT and PT using the web server PDBMD2CD and compared them to the experimental spectra for ArtAB and CT at 20 °C (Figure 3.6e). Note: we chose to compare at 20 °C because that was the only temperature at which we were able to collect three replicates of CD data for CT due to time constraints.

While the CT and PT experimental spectra are visually quite similar, and the two predicted spectra are visually quite similar, the experimental and predicted spectra have some major differences. The predicted spectra have a shape characteristic of proteins that contain a large amount of α helices as indicated by the negative minima with similar magnitude at 208 and 222 nm and the positive maximum at 190 nm. Running the predicted spectra through DichroWeb as above allowed for comparison of predicted and experimental secondary structure comparisons (Figure 3.6f). Predicted CT is composed of more alpha helices (22% α1, 15% α2) than beta strands (9% β1, 8% β2). This is markedly different from the experimental CT composition of a lower percentage of alpha helices (6% α1, 7% α2) than beta strands (21% β1, 14% β2). The experimental CT secondary structure composition closely matches that of ArtAB. Pertussis toxin's predicted secondary structure composition (10% α1, 11% α2 α-helices, 18% β1, 10% β2 β-strands) is closer to the experimental secondary structure compositions of both ArtAB and CT, however, it is different enough as to raise questions about the usefulness of the model.

The direct comparison in PDBMD2CD showed poor fits. The 1S5E (CT) structure compared to the experimental ArtAB and CT CD spectra had RMSDs of 15.008 and 11.000, respectively, and the 1PRT (PT) structure compared to the experimental ArtAB and CT CD spectra had RMSDs of 15.699 and 11.835 respectively. The high RMSD values indicate a poor fit. Neither CT (Uniprot ID P01555 (CTA) and P01556 (CTB), PDB ID 1S5E) nor PT (Uniprot ID P04977 (PTA), P04978 (PTB), P04979 (PTC), P0A3R5 (PTD), P04981 (PTE), PDB ID 1PRT) have depositions in the Protein Circular Dichroism Data Bank[167] (PCDDB) so it was not possible to directly compare experimental spectra, and searches of the PCDDB for related spectra using the DichroMatch[168] website resulted only in poorly fitted spectra of proteins with no obvious relationship to ADP ribosylating AB5 toxins. The normalized root mean squared deviation (NRMSD) of the top five matches were > 0.45 for the ArtAB input and > 0.32 for CT input.

It is possible that the poor fits of the models are due to a lack of similar structures in the reference set. Future experiments could be performed to collect experimental PT CD data and to further investigate the root causes of these discrepancies. Our own experimental CD data could potentially be cleaned and entered into the PCDDB. This would be the first representative of any ARTs or AB_5-type toxins that we know of in the database and would support future CD studies of ART and AB_5 toxin structure and characterization of new ARTs.
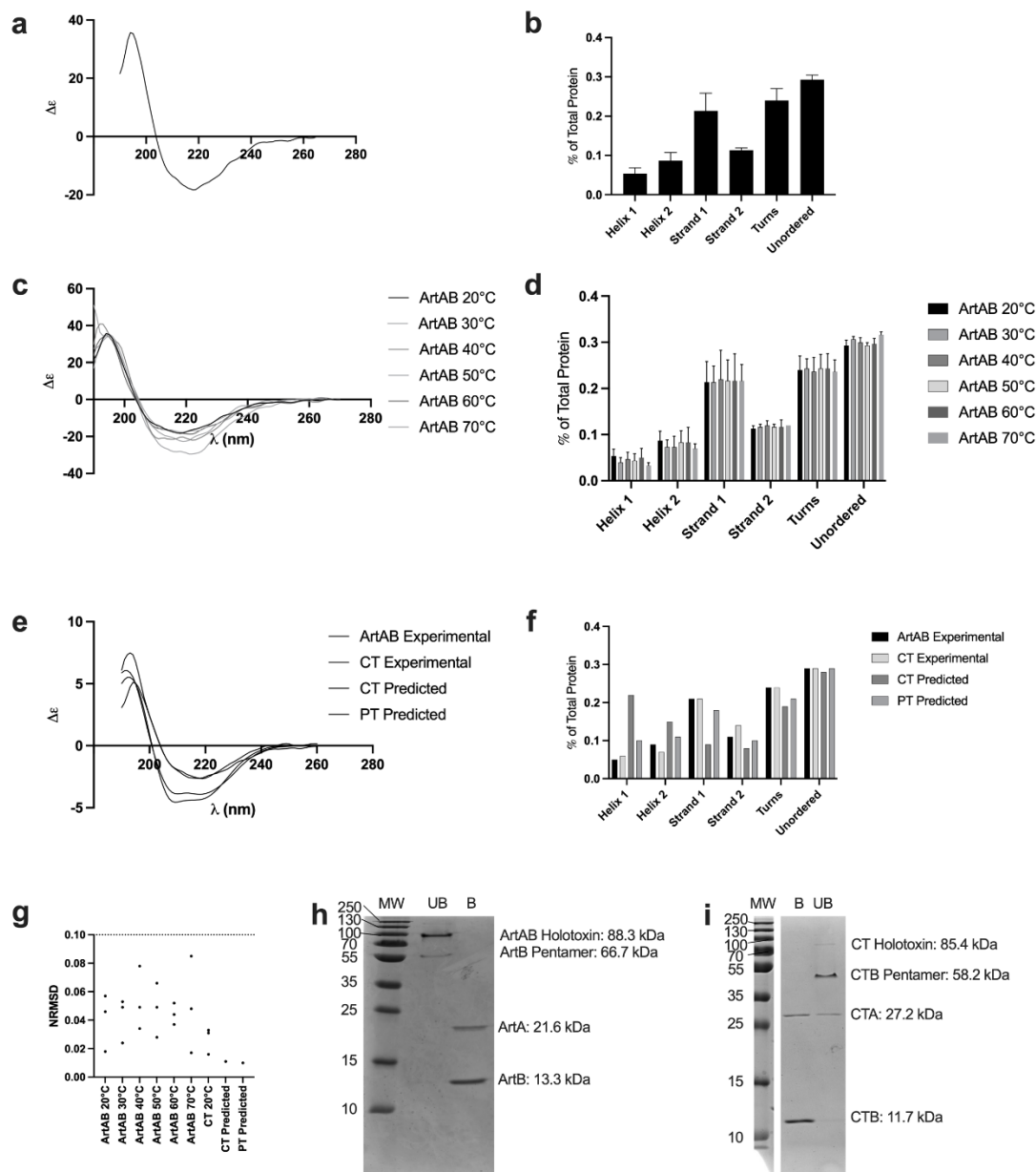
Figure 3.6.   Far-UV circular dichroism studies on *S.* Typhimurium DT104 ArtAB

(a) experimental spectrum for ArtAB at 20 °C; (b) secondary structures for ArtAB at 20 °C; (c) experimental spectra for ArtAB at different temperatures; (d) secondary structures for ArtAB at different temperatures; (e) experimental CT and ArtAB spectra at 20 °C overlayed with predicted CT and PT structures (based on PDB files); (f) secondary structures for CT and ArtAB at 20 °C from experimental data spectra and for CT and PT from predicted spectra; (g) NRMSD for individual secondary structure calculations; (h) SDS-PAGE gel with non-heat-denatured/unboiled (UB) and heat-denatured/boiled (B) samples of ArtAB used for CD experiments; (i) SDS-PAGE gel with non-heat-denatured/unboiled (UB) and heat-denatured/boiled (B) samples of CT used for CD experiments. Per ProtParam predictions (Table 3.9), CT holotoxin is expected to run at 85.4 kDa, CTB pentamer at 58.2 kDa, CTA at 27.2 kDa, and CTB at 11.7 kDa. A note on our purified CT: There is consistently a band between 35 and 55 kDa in both CT and CTB purifications. The band does not fall where the expected pentamer is, however it is recognized by both our anti-CT and anti-CTB antibodies (see Western blot section in Chapter 4, Figure 4.1). This band is present only in unboiled samples. Since the boiled/unboiled samples are always taken from the same parent sample, and when the band is present the CTB band is clearly lighter, we assume this to be an aggregate of four CTB subunits, which would be expected to run at 46.6 kDa. This is consistent with commercially purchased CT and CTB as well.

ArtAB Mutagenesis

Since the crystal structure of ArtAB has not yet been solved, we sought to investigate the predicted catalytic/NAD+ binding pocket of ArtAB using mutational studies. Mutational studies with the ArtA R6 and E115 residue have been done previously,[39] however, no models were available at the time to provide visual support for the chosen mutational sites so they were chosen solely based on a multiple sequence alignment and knowledge of PTA's structure. In addition, the group that performed this study only tested the mutants in *in vitro* ADP-ribosylation assays and not for cellular activity.

PT's active site was originally explored using simple deletion studies. Recent advances have allowed for the construction of high-resolution crystal structures which have been used to, not only confirm, but also to define the specific biochemistry of these catalytic residues and to characterize their interactions with each other and with NAD+ substrates within the active site.[148,169–171] The referred literature contains detailed descriptions of the biochemistry of PT's active site.

Briefly, the NAD+ molecule is nestled between the conserved split β-sheets, where it interacts with residues projecting into the space between the β-sheets. H35 is within hydrogen bonding distance of E129, and it hydrogen bonds with the NAD+ substrate, helping to stabilize it within the catalytic pocket. Mutation of this residue reduces, but does not abolish, PT's ART activity.[170,172] T53 is the central residue of the highly conserved STS motif ([52]STS[54] in PT) of ADP-ribosylating toxins in the CT-like subgroup. While it does not interact directly with the NAD+ substrate, it is critical to stabilizing the NAD+ binding pocket. R9 also interacts with the NAD+ molecule.

Mutations here have severely reduced enzymatic activity without affecting the protein's structure.[173,174] E129 is PTA's catalytic residue, which is essential for enzymatic activity. A proposed mechanism is described in detail in a recent publication of the crystal structure of PT with NAD+.[175]

We used the multiple structure alignment between PT and our monomeric AF2 ArtA model (Figure 3.4) to predict residues in the active site of ArtA. In our model, ArtA R6 aligns with PT R9 (Figure 3.7a). ArtA H32 aligns with PT H35 (Figure 3.7b). ArtA T50 aligns with PT T53 (Figure 3.7c). Finally, ArtA E115 aligns with PT E129 (Figure 3.7d). The alignments are quite close upon visual inspection, with only slight differences in orientation. Figure 3.7e and 3.7f present two views of the active site with superimposed residues shown.

We next created a set of mutants, each with a single point mutation in the gene for ArtAB at locations that were suspected to be important to the toxin's ADP-ribosylating activity. Each point mutation coded for an alanine residue. We designed the primers so that each point mutation coded for an alanine residue. We successfully created mutants for H32A, R6A, and T50A. We attempted to create an E115A mutant as E115 is suspected to be the primary catalytic residue based on alignments and structural prediction models (Table 3.1, Figure 3.4), however we were unable to complete a successful mutagenesis reaction with the primers we designed. Potential alternate primers have been designed and could be used for future attempts, or a commercial plasmid containing the desired mutation could be purchased.

We transformed each of the three successful mutant plasmids into ClearColi® (Lucigen) and confirmed the presence of the desired genetic mutations by sequencing.

Mutant ArtAB was expressed and purified from successful transformants. Mutant holotoxins were confirmed by SDS-PAGE (Figure 3.7g). The T50A mutant was the only mutant that appeared to readily form holotoxin. We know that the R6A and H32A mutants must form holotoxin because we depend on the holotoxin form for purification. We purify the toxins by pulling them out of solution with a binding interaction between the pentamer and a D-galactose column. If ArtA were not associating with the pentamer it would not be present in the sample. Even though the samples are unboiled, the A and B subunits sometimes separate due to the conditions of the SDS gels. Even the native ArtAB holotoxin separates on SDS gels and the presence of the holotoxin is not always clearly present. It is possible that the T50A mutation has somehow increased the stability of the holotoxin so that it remains intact on the SDS gel. The Mutant holotoxins were also confirmed by mass spectrometry (Figure 3.7h-j). All three mutants were confirmed to contain the expected alanine residue at the site of mutation.
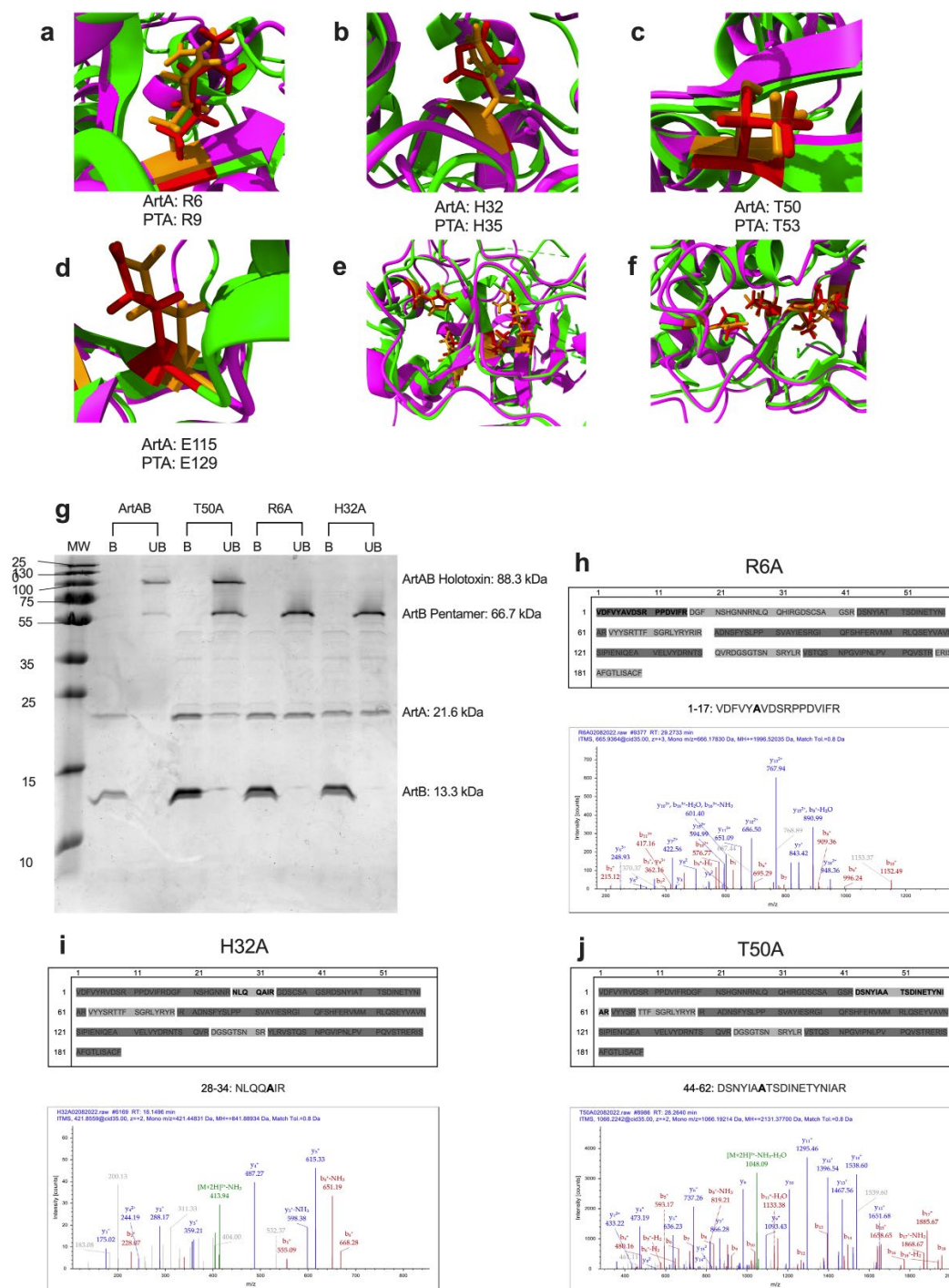
Figure 3.7. Site-directed mutagenesis of ArtAB based on alignment with PT

(a-d) Snapshots from ChimeraX of the overlaid residues to be targeted for mutational studies with ArtA in magenta and ArtA residues highlighted orange, and PT in green with PT residues highlighted red; (e,f) two views of the NAD+ binding pocket and catalytic site of the two ADP-ribosylating toxins, coloring as in a-d; (g) 15% SDS-PAGE gel of purified ArtAB and ArtAB mutants. Samples were heat denatured (B, boiled) or not heat denatured (UB, unboiled), prior to running the gel; (h-j) mass spectrometry confirmation of mutations in purified protein. Fragments produced by trypsin digestion are indicated by alternating gray highlights. Fragment of interest is indicated with bold lettering and is also written out below the table with the residue of interest in bold. All three mutants contain the expected alanine residue at the site of interest.

To investigate the effects of the mutations on the structure of the holotoxin, we performed thermal denaturation circular dichroism studies on ArtAB mutants containing the single point mutations of H32A, R6A, or T50A (Figure 3.8). Investigation of the individual mutants' spectra at temperatures from 20 to 80 °C show minimal changes upon heating (Figure 3.8a-c). Deconvolution solutions similarly show minimal changes upon heating (Figure 3.8d-f). A comparison of the ArtAB and ArtAB mutants' spectra at 20°C (Figure 3.8g) shows that the single point mutations do not affect the structure of holotoxin. The corresponding deconvolution solutions (Figure 3.8h), however, show that the mutants contain slightly lower $\alpha2$ and turns content and slightly higher $\beta1$ content. Examining the CD signal at 220 nm (Figure 3.8i) at different temperatures shows a slight loss in signal as temperature increases, indicating a change in the secondary structure. The trend is similar to ArtAB's, indicating that the mutations did not cause a significant change in thermal stability. All NRMSD values for these experiments were < 0.1. except one biological replicate of R6A at 80 °C (Figure 3.8j). From these data we conclude that the point mutations do not significantly affect the secondary structural makeup of the holotoxin and that further use of the mutants within physiological ranges of temperatures should not affect the stability of the holotoxins. In the future, cryo-EM studies could be performed to confirm the effects of the point mutations on holotoxin structure.
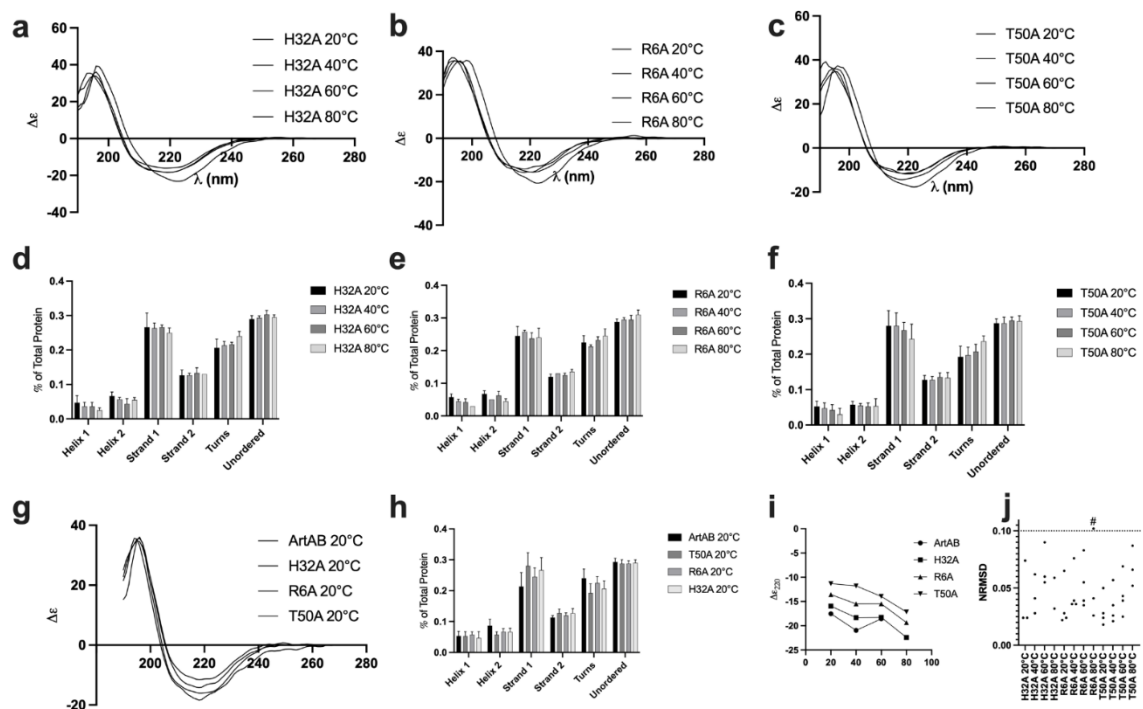
Figure 3.8.   Far-UV circular dichroism studies on *S*. Typhimurium DT104 ArtAB mutants

(a-c) experimental spectra for H32A, R6A, and T50A mutants at different temperatures; (d-f) secondary structures for H32A, R6A, and T50A mutants at different temperatures; (g) experimental spectra of ArtAB, H32A, R6A, and T50A at 20 ℃; (h) secondary structures of ArtAB, H32A, R6A, and T50A at 20C; (i) CD signal (in units of delta epsilon) at single wavelength of 222 nm over different temperatures; (j) NRMSD for individual secondary structure calculations.

Active Site Exploration with Mutants

The next step was to determine whether the mutations affected the catalytic

activity of ArtAB. ADP-ribosylation assays are the gold standard for testing ADP-

ribosylation activity. Thus far, however, these assays have not been successful. Attempts

using biotinylated NAD+, purified Gα proteins, purified toxins, and other standard ADP-

ribosylation assay materials (Appendix 3A) did not provide conclusive results.

The recently reported MacroGreen tool was also used.[151] MacroGreen is based on

a modified macro domain protein called Af1521 that binds both free ADP-ribose and

ADP-ribosylated proteins. Af1521 is conjugated to GFP and contains mutations to

improve ADP-ribose binding and reduce ADP-ribosyl glycohydrolase activity, an off-

target effect of removing an ADP-ribose moiety.[91] The final product is a 51.7 kDa protein

with GFP activity. MacroGreen was transformed into *E. coli*, purified using nickel

chromotography, and confirmed to absorb/emit light (excitation 395 nm, emission 509

nm, Figure 3.1). The protein was then used in Western blot and ELISA assays with

treated cell lysates and also in fixed and permeabilized treated cells to detect ADP-

ribosylations. Unforunately, these assays have not yet provided conclusive results. With

further troubleshooting, though, MacroGreen may still be a novel method to rapidly

determine ADP-ribosylation in future studies.

ART toxic activity can also be detected using a luminescence-based cAMP assay.

To review, G-protein coupled receptors that interact with adenylyl cyclase affect

intracellular cAMP levels. cAMP stimulates PKA, which utilizes ATP to phosphorylate

various substrates. The cAMP assay uses the ATP-dependent luciferin/luciferase reaction

to produce a luminescent signal that is dependent on the amount of ATP present. If a cell

is producing more cAMP, PKA becomes more active and uses more ATP, leaving it

unavailable for the luciferin/luciferase reaction, so a lower luminescent signal will be

produced, and vice versa. A high luminescent signal represents a lower level of PKA

stimulation by cAMP. This is an indirect measurement of GPCR activity, but can reveal

the expected toxic activity of adenylyl cyclase regulation via G_α proteins.

CT and PT were used as controls. CT's ADP-ribosylation target is $G_{\alpha s}$, which

results in cAMP stimulation, and this is well documented, making it a reliable control for

cAMP activity. In the cAMP assay it is expected to produce a low luminescent signal. PT

was used as a control because of its structural homology and expected similar activity to

ArtAB. PT's ADP-ribosylation target is $G_{\alpha i}$, which normally inhibits adenylyl cyclase.

The modification is expected to interfere with the inhibitory action of $G_{\alpha i}$, resulting in increased cAMP production, however, previous studies have documented PT's failure to stimulate basal cAMP levels in CHO cells treated with similar conditions to ours.[176] cAMP activity can be detected on PT-treated cells as an enhancement of the effect of other treatments like isoprenaline and forskolin.[177,178] ArtAB was previously shown to increase cAMP when co-administered with isoprenaline.[38] Thus, we did not expect a change in basal cAMP in this assay, we simply used PT and ArtAB as controls to investigate the mutants' activities. Since we did not achieve high quality results, in the future we could include isoprenaline or forskolin treatments to elicit responses from PT and ArtAB, and use this to evaluate the activity of the mutants.

The assay was conducted in triplicate with a single biological replicate and qualitative comparisons between groups are shown (Figure 3.9). As expected, CT had a very low signal compared to the *E. coli* and media controls. In contrast, but as expected, PT had seemingly little effect. ArtAB's response in this cAMP assay is similar to that of PT and may be further evidence that its activity is more like that of PT than CT. The response of the mutants is more variable and may indicate some activity. The H32A mutant appeared to have a response similar to that of ArtAB and PT. The R6A mutant had a response more like CT, where intracellular cAMP was increased. The T50A mutant had the opposite effect, where a much lower amount of cAMP was present. The cAMP assay is thus far evidence that activity can be detected using purified toxins and CHO cells, but will be repeated using isoprenaline and the mutant responses will be evaluated further before any conclusions are drawn. In addition, despite efforts to develop a

standard curve for quantitative analysis of this assay, results are not currently satistactory

and will be resolved prior to repeating for publication in the future.
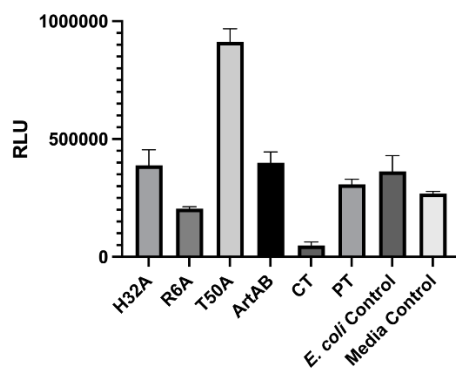
Figure 3.9.   cAMP assay on CHO cells

cAMP assays were performed on treated cells using a commercial luciferin/luciferase reaction-based assay. The assay detects free ATP. If cAMP is present in large amounts, as is the case for CT-treated cells, cAMP stimulates PKA (added as part of the assay) and ATP is consumed, leaving little ATP available for a luciferin/luciferase reaction and resulting in a low signal. If cAMP is not present, or if ATP levels are high, a higher signal is expected. PT is known to have little-to-no effect on basal cAMP levels in mammalian cells.

cAMP is still only an indirect measure of toxin activity. Additional, direct cellular

measurements are required. We previously reported that ArtAB has a clustering effect on

CHO cells, like PT, and has some elongation effect on CHO cells, like CT. Thus, CHO

cell assays were conducted, as previously described,[128] to investigate the activity of the

mutants in comparison to the holotoxin. In addition to collecting brightfield images,

fluorescent images of treated cells stained with an actin stain were collected to show the

changes in the F-actin structure. In addition to 20× images, as previously reported, 10×

views, which included larger populations of cells but were still close enough to detect

individual cell morphology patterns, were collected (EVOS). This allowed for a better

analysis of the cell populations across individual wells.

Images were assessed and compared by visual examination. Results are

representative of the experiment performed idependently three times in triplicate

(brightfield images) or one time in triplicate (fluorescent). Both CT and PT elicited the

expected morphological responses of elongation (CT) and clustering (PT), and ArtAB

elicited a mixed response with both elongation and clustering (Figure 3.10a-c). The 10×

brightfield images reinforced the finding that ArtAB does, in fact, exhibit both

morphologies (Figure 3.10a). The H32A mutant-treated cells closely resemble those of

the *E. coli* and media controls, with a large, even carpet of cells and few individual

clusters, and the clusters that are present are not tightly packed or rounded. The R6A

mutant-treated cells have a similar appearance, with more individual cell rounding, but a

lack of defined clusters or clear elongation. The rounding could possibly indicate cell

death, although this was not evident in the corresponding alamarBlue™ assay (discussed

below). Rounding does involve a change in the adhesion molecules at the paracellular

barrier and this could be further investigated in the future. The T50A mutant-treated cells

have clear, tightly packed clusters, however, the elongation that is visible in ArtAB-

treated cells is not detectable. The separation of clustering and elongation effects is

interesting and the mechanism should be investigated in future studies.

112
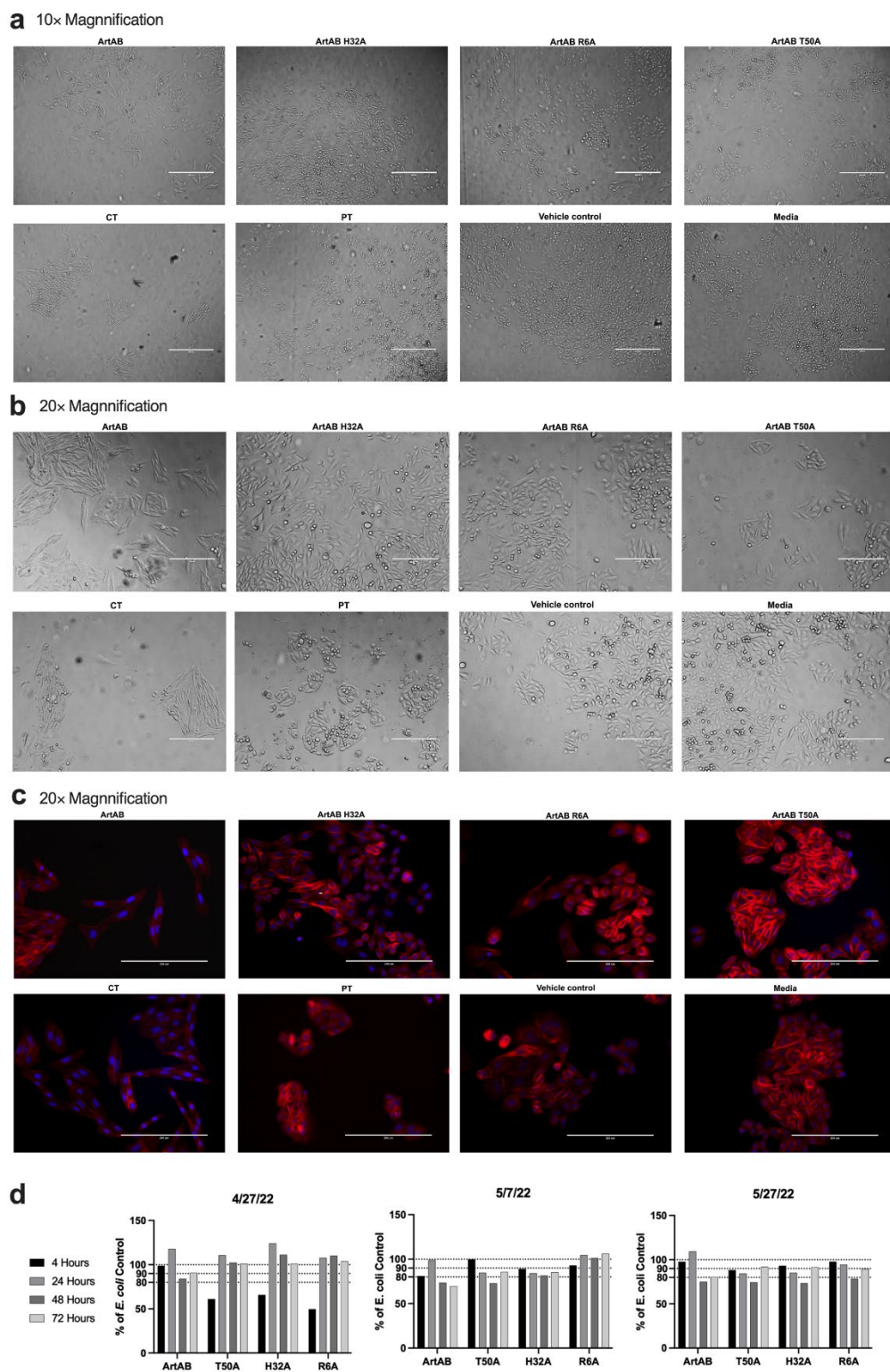
Figure 3.10. Morphology and alamarBlue™ cellular activity assays

(a) Brightfield images of treated CHO cells at 10× magnification; (b) brightfield images of treated CHO cells at 20× magnification; (c) fluorescent images of treated, fixed, permeabilized, and stained CHO cells at 20× magnification; and (d) results of three separate biological replicates of alamarBlue™ assays on treated CHO cells.

Quantitative analysis of the images could be performed using a standardized CHO cell clustering assay as reported.[179,180] We have reported elongation as measured by the distance from one cell border to the other across the nucleus using the longest diameter as the final measurement. This clearly showed the CT elongation but failed to characterize the PT clustering effect. Quantitative assays will be used to continue analyzing this data and for future assays with these and other mutants.

As reported previously,[128] we also performed alamarBlue™ assays to determine toxin and toxin-mutant effects on CHO cells. ArtAB acted as expected, or as previously demonstrated, by causing an increase in metabolic activity at the 24-hour timepoint followed by a decrease and an eventual small rebound, and this pattern was consistent across all three biological replicates. Unfortunately, the mutants showed very little consistency between replicates, making interpretation of the results difficult. Additional replicates may show more consistent trends, or another cellular proliferation or metabolic activity assay could be used to further qualify this parameter.

Discussion

In this study we created three distinct 3-dimensional structural models for ArtA, evaluated each of them, and established a model that could be used for further study. The structural homology analysis showed that ArtAB is structurally quite similar to PT. Future studies could be done with the recently published PT model, PDB ID: TSKY, which contains the structure of NAD+ within the NAD+ binding site.[175] Molecular docking studies could be done to show interactions between the residues of interest and possible NAD+ binding, and NAD+ binding in experimental PT and predicted ArtAB active sites could be compared.

According to the pLDDT scoring, AlphaFold 2 (AF2) assigned low confidence in the accuracy of the C-terminal residues of ArtA in both AF2 models of ArtA. The Phyre2 model obviously differed in the same region as well. Previous deletion studies in PT showed that mutations within the CTD do not affect the enzymatic activity of PT,[174] and it is accepted that the active site is confined to the N-terminal portion of ARTs, so it is not surprising that the C-terminal residues of ArtA are less conserved and more difficult to model. The C-terminus of bacterial ARTs remains of interest, however, as it is used as a linking domain at the interface of the A and B_5 subunits of AB_5-type toxins, linking the catalytic subunit to its receptor-binding B subunit. The interaction at the interface of the pentamer of AB_5-type toxins has been explored, and there is great value in understanding these interactions and in considering how these multimers non-covalently self-assemble.[181,182] Our model could be used to investigate this interface, or, even better, a high-resolution 3D structure could be obtained through X-ray crystallography or cryo-electron microscopy.

The C-terminus is also interesting for its role as a protective domain that physically blocks the NAD+ binding site in the A subunit's active site until activation, providing some amount of regulation and ensuring that the enzymatic activity occurs inside a host cell. As previously discussed, residues at the C-terminus are tethered to the NAD+ binding site by an intramolecular disulfide bond. Recent studies on PT and *Ec*Plt have shown that activation of the ART by disulfide bond reduction results in physical structural rearrangements within the NAD+ binding pocket and the active site loop that ultimately make the NAD+ binding site available. [51,171] CT's CTD has been shown to be allosterically activated by interactions with GTP-bound ADP-ribosylation factors that allow NAD+ access to the binding pocket.[183] Regardless of the specific mechanism that triggers rearrangement, the presence of C-terminal residues that block the active site is conserved. Future studies could further define the C-terminal structure and identify possible linking domains, residues that interact at the interface of the pentamer, and/or residues that act to obstruct the active site until the conditions are favorable for activation. Understanding these parameters will add to our understanding of the AB_5-type bacterial toxin family. Along these same lines, future studies could investigate disulfide bond linkages and mechanisms for activation of ArtA. ArtA has increased activity in the presence of thiol agents like DTT, indicating that it contains a disulfide bond (potentially between C38 and C189) and a proteolytic cleavage site, similar to PT, which must be reduced inside the host cell.[39] Other ARTs have a defined cut site for proteolytic cleavage, which activates the toxin.[184] This cut site remains undefined for ArtA and is an area for future study.

In our biophysical characterization studies, we showed that ArtAB has an experimental molecular weight (MW) close to, but lower than, that of its predicted MW. We determined that it is an asymmetrical, globular protein and that it exists in solution as a stable holotoxin that neither aggregates nor separates into individual subunits, even under the intense conditions of ultracentrifugation. It remains fairly stable over a range of temperatures with secondary structures that do not show changes until 70 °C, a temperature that is not biologically relevant. The biophysical experiments showed that ArtAB is quite different from CT. It would be interesting to collect the same data on PT for comparison.

A summary of the activity of the mutants is provided in Table 3.10. The H32A mutant had little effect on the secondary structure and did not affect the toxin's cAMP activity, however it did abolish ArtAB's characteristic clustering and elongation effects on CHO cells. The R6A mutant also had little effect on the secondary structure, but it increased cellular cAMP and abolished the clustering and elongation effects on CHO cells. This is evidence for the importance of the R6A residue in ArtA-catalyzed ADP-ribose transfer, and it supports previous findings; the group that previously conducted mutational studies on ArtAB created R6A and E115A mutants and showed that both of these mutants markedly reduced the activity of ArtAB through ADP-ribosylation studies.[39] In contrast to the H32A mutant, the R6A mutant also caused CHO cells to round up; an effect which should be further investigated. The T50A mutant showed increased stability based on the stronger holotoxin band in the SDS gel, potentially due to an increase in beta strand content as measured by CD. It also lowered cellular cAMP levels and introduced a separation of clustering and elongation effects on CHO cells

where clustering was present, but elongation was not. T50A's decrease in cellular cAMP is interesting because it represents a decrease in the basal cellular cAMP. We could consider that this indirect cAMP assay is actually measuring the availability of ATP. It's possible that the mutant could have increased the production of ATP. A future assay could investigate whether T50A is stimulating ATP production in the cells. Producing predicted models or, better yet, obtaining high-resolution X-ray crystallography or cryo-electron microscopy structures of each mutant could confirm the structural changes associated with each mutation and may provide insight into the mechanisms of these results.

Table 3.10.   Summary of findings in mutant assays

Mutant	SDS Gel	Stability/Secondary Structure (CD Analysis)	cAMP Assay	Clustering/Elongation	Cellular Activity
H32A	No holotoxin identified	Possibly more beta strands Possibly fewer alpha helices Possibly fewer turns Same thermal stability as native	(same as ArtAB) No effect on cAMP	No clustering, no elongation	Indeterminate
R6A	No holotoxin identified	Possibly more beta strands Possibly fewer alpha helices Possibly fewer turns Same thermal stability as native	(more like CT) Higher cAMP levels than controls	Individual rounding but no clusters or elongation	Indeterminate
T50A	Strong holotoxin band	More beta strand content Possibly fewer alpha helices Possibly fewer turns Same thermal stability as native	Much lower cAMP levels than controls	Clustering but no elongation	Indeterminate

The mutational studies aid in elucidating the activity within ArtAB's active site, but they could also present opportunities for vaccine development. Many AB_5-type ARTs and have been successfully used in vaccines. The CT and LT pentamers are known to stimulate the immune system and are well studied as vaccine adjuvants. PT and DT

holotoxins detoxified with chemical (formaldehyde, glutaraldehyde, or formalin treatment) methods are components of vaccines currently licensed in the U.S. that protect against diphtheria, tetanus, and pertussis disease. These vaccines are commonly referred to as DT, Td, DTaP or Tdap vaccines, where the letters D/d, T/t, and aP/ap refer to diphtheria, tetanus, and acellular pertussis components of the combination vaccines, upper-case letters indicate a full-strength dosage of that vaccine component, and lower-case letters indicate smaller doses. Licensed vaccines include the seven pediatric vaccines Daptacel (DTaP), Infanrix (DTaP), Quadracel (DTaP + polio), Kinrix (DTaP + polio), Pentacel (DTaP + polio and Haemophilus b), Pediarix (DTaP + polio and Hepatitis B), and Vaxelis (DTaP + polio, Haemophilus b, and Hepatitis B) as well as the five adult vaccines TDVAX (Td), TENIVAC (Td), a generic DT vaccine from Sanofi Pasteur, Inc, with no tradename, Adacel (Tdap), and Boostrix (Tdap).[185] All of the licensed vaccines listed incorporate chemically detoxified DT and/or PT holotoxins. More relevant to the work presented here, though, are the vaccines that have been developed based on genetic mutations in the ART catalytic pockets.[186] A CT mutant with alterations that disable the nicking and separation of the two subunits has recently been tested in preclinical studies.[187] An LT double mutant with the same mechanism has been in development for years and has recently been investigated in clinical trials.[188] An especially relevant example is a pertussis toxin vaccine candidate that was genetically detoxified by altering the same R9 and E129 residues we have discussed here. The vaccine did not affect the structure of the protein, therefore its immunogenic epitopes were retained, and it produced robust immune responses in assays with a novel human model system.[189] Based

on our results we can hypothesize that the double mutant would diminish the ability of NAD+ to bind properly in the active site as well as abolish the catalytic activity.

We have demonstrated ArtAB's striking homology to PT and have shown that mutations in the R6 residue does alter the activity of ArtAB, and previous work showed that E115 mutations abolished ArtAB's activity. With further work it could be feasible to produce a genetically detoxified ArtAB mutant for consideration as a *Salmonella* vaccine candidate. While interesting, this strategy is unlikely to be immediately impactful. The importance of the presence of ArtAB on the *S.* Typhimurium genome is still undefined. ArtAB's contributions to pathogenicity are unclear, and, unlike pathogens that cause toxin-mediated diseases (e.g. *V. cholerae* is only pathogenic if it contains the *ctxAB* operon[190]), non-typhoidal salmonellosis is usually mediated by inflammatory responses within the host's gut and interactions with the immune system that create environments that are favorable to *Salmonella* survival[16], so the use of genetically detoxified ArtAB as a single antigen *Salmonella* vaccine to prevent salmonellosis is unlikely to be successful. It could potentially be incorporated into a multivalent vaccine, though, and is worth pursuing. Future studies could evaluate the immunogenicity of a genetically detoxified mutant. If it is shown to be highly immunogenic, it could potentially be used as an adjuvant.

Finally, in our previous work we showed that the clustering and elongation effects are unique to the A subunit of ArtAB; the pentamer alone had completely distinct effects which were not observed upon treatment with the holotoxin. The B_5 subunit alone did not cause any clustering or elongation. This suggests that morphological changes are linked to the ADP-ribosylation activity of the A subunit. We have been considering both cAMP

activity and morphological changes to be indicative of toxic activity, however, it has also been proposed that PT's characteristic clustering response is independent of cAMP activity. In a recent (2021) review article of PT's enzymatic activity, Hewlett et al.[180] wrote, "at present state of knowledge, it is not appropriate to describe PT as increasing cAMP levels, as its primary mechanism of action or at all, without consideration of the other variables in play."[180] If the cAMP response is independent of the morphological changes, then there must be a distinct cAMP-independent molecular interaction occurring after ADP-ribosylation and leading to morphological changes. Additional downstream interactions should be investigated in future studies.

Conclusions

We provided supporting evidence for the hypothesis that ArtA is structurally and enzymatically similar to PT. The predicted model we established will guide future studies of ArtAB, and the set of mutants will be immediately useful for continuing to characterize ArtAB's ART activity. Combined with the biophysical studies we presented, these studies provide robust preliminary data for advancing efforts to obtain a crystal or cryo-EM structure of ArtAB.

A critical next step for developing this research is to establish an assay to measure ADP-ribosylation activity. ADP-ribosylation assays are common in the literature, but even our contacts who work with them daily have admitted to their difficulty. With further troubleshooting the MacroGreen tool may be a promising avenue for detection of ART activity, and we have established contact with the lab that produced the tool and the original publication. In addition, cAMP assays including isoprenaline or forskolin as described above can and should be pursued, although it will be important to establish a repeatable standard curve for quantitative analysis. These assays will be indispensible as novel AB_5-type ARTs are discovered and the need to characterize them arises.

Interesting questions for future research include further characterizing the intracellular signaling mechanisms and interactions that occur downstream of the ADP-ribosylation event and elucidating the mechanisms of morphological changes. The separation of the clustering and elongation response is interesting. ArtAB clearly produces both morphologies and the T50A mutant produced a separation of the two. ArtAB and the T50A mutant are, therefore, excellent models to work with in elucidating this mechanism. Work in this area will aid in investigating the proposal by Hewlett et. al.,

122

described earlier in this chapter, that cAMP production is not the main effect of ADP-ribosylation by PT.

Finally, it is important to remember that, though this work focuses on bacterial ARTs, researchers across the globe are conducting similar studies on mammalian, insect, and plant ARTs.[191–195] Keeping apprised of the literature and networking with other scientists in the field will remain essential to advancing our global understanding of ART biochemistry and cell biology.

Supplementary Materials

Supplementary videos can be viewed by following this link (or going to

https://docsend.com/view/s/rfa6qtrmf664rtuu) and using the passcode 24601. Email

eliseovergaard@u.boisestate.edu with any issues accessing the videos.
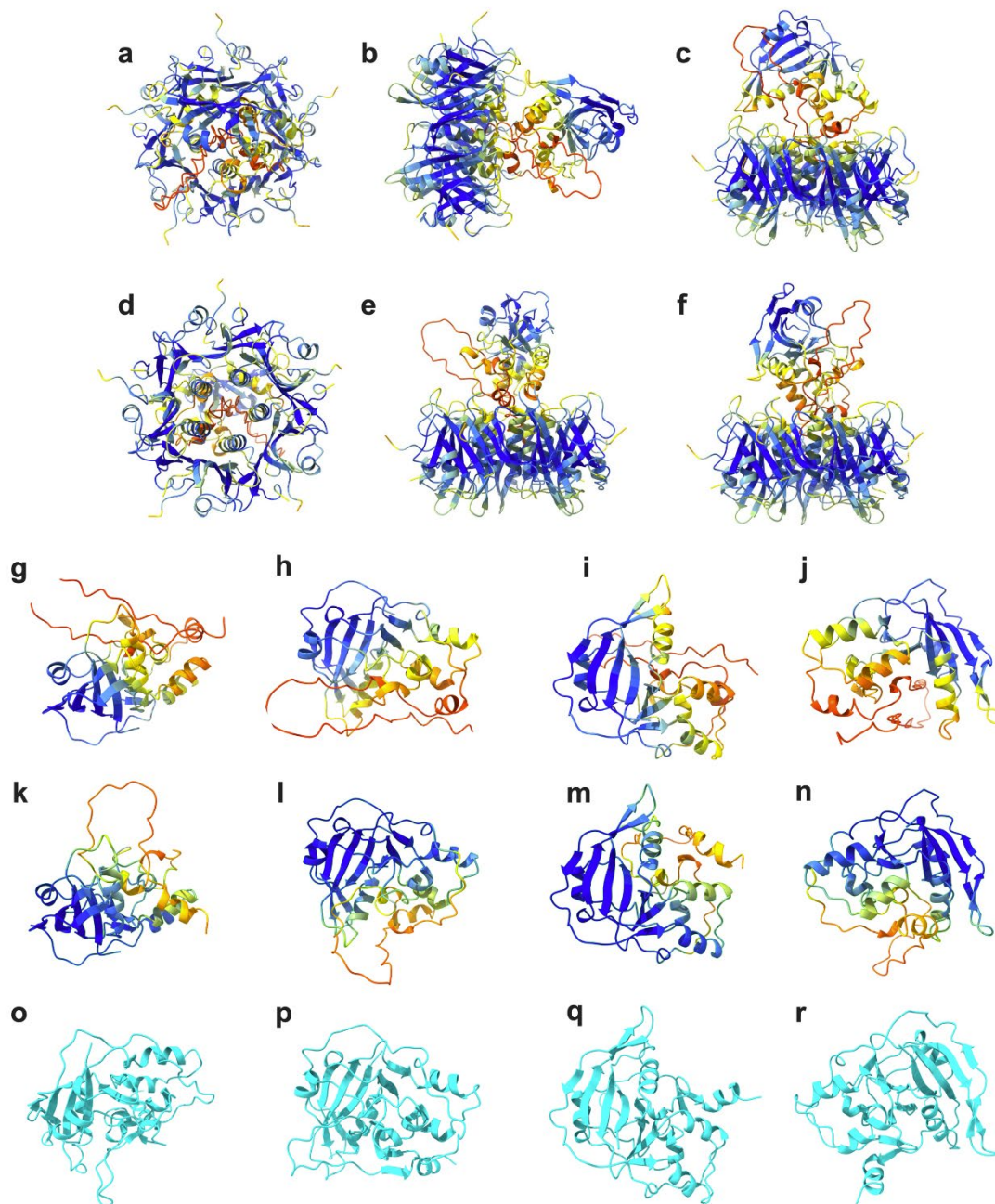
Figure 3.S1.   Alternative views of models predicted with AlphaFold

(a-f) *Top (a), bottom (d), tilted (b), and multiple side (c, e, f) views of the ArtAB holotoxin multimeric model predicted with AlphaFold 2;* *(g-j)* *alternative views of ArtA chain isolated from the ArtAB holotoxin multimeric model predicted with AlphaFold 2;* *(k-n)* *Alternative views of the ArtA subunit monomeric model predicted with Alphafold 2; and* *(o-r)* *views of the ArtA subunit monomeric model predicted with Phyre2.*
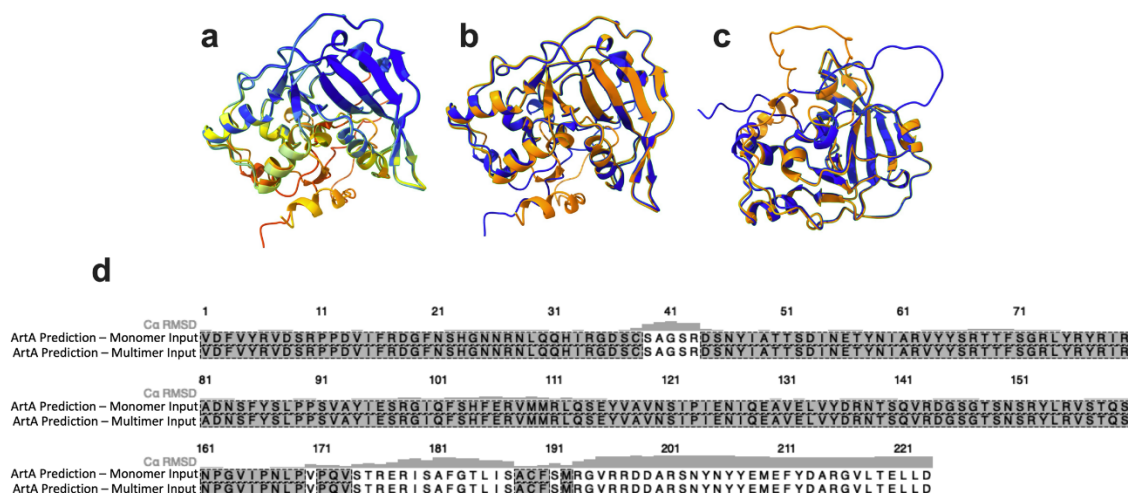
Figure 3.S2. Comparison of ArtA predicted model as chain of holotoxin multimeric model or as monomer

*The Matchmaker tool in ChimeraX was used to superimpose the ArtA structural models from the A chain of the multimeric model and the individual monomeric model. **(a)** Superimposed models are shown with the pLDDT coloring scheme. **(b)** Same view as panel a, but with the multimeric model in blue and the monomeric model in orange. **(c)** An alternate view with the blue multimeric model and orange monomeric model coloring scheme. **(d)** A pairwise sequence alignment and structural alignment were completed using the Matchmaker tool in ChimeraX. RMSD values for Cα molecules are indicated in gray above the sequence alignment.*
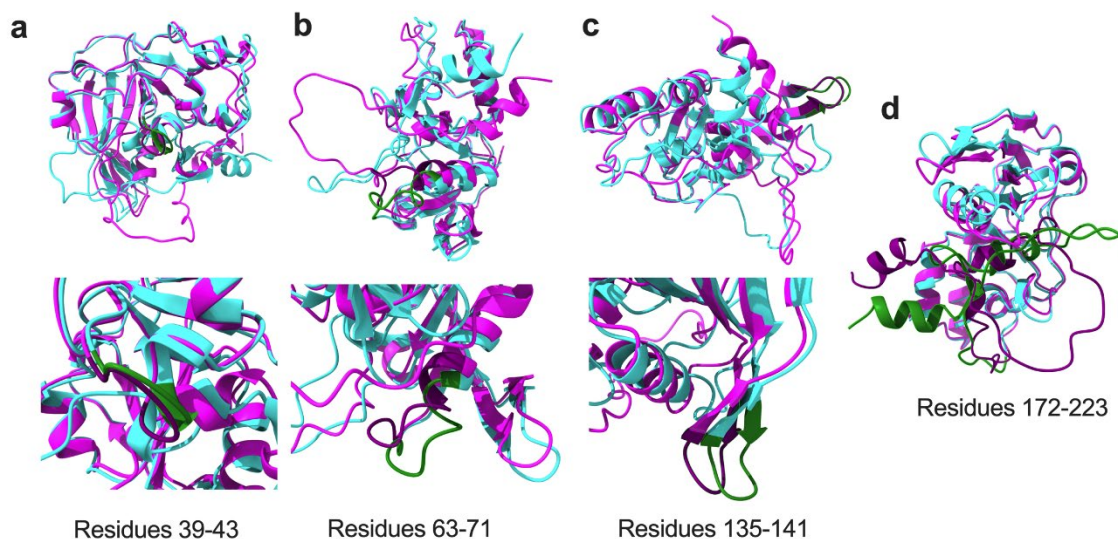
Figure 3.S3. Comparison of AlphaFold and Phyre2 predictions for monomeric ArtA

*A structural alignment of AlphaFold model (magenta) and Phyre2 model (cyan) was completed using the Matchmaker tool in ChimeraX. Regions with high RMSD values are highlighted in dark purple (AlphaFold model) or forest green (Phyre2 model). Alignments of **(a)** residues 39-43, **(b)** residues 63-71, **(c)** residues 135-141, and **(d)** residues 172-223 show areas of discrepancy between models.*

Funding, Acknowledgements, and Conflicts of Interest

CHAPTER FOUR: EFFECTS OF ARTAB ON PARACELLULAR BARRIER

FUNCTION AND ADHESION MOLECULE REGULATION

Elise Overgaard[1], Haley Bridgewater[1], and Juliette K. Tinker[3]

[1]   Biomolecular Sciences Graduate Program, Boise State University, Boise, ID
[2]   Department of Biological Sciences, Boise State University, Boise, ID
*   Correspondence: juliettetinker@boisestate.edu

Authorship statement: My direct contributions to this chapter included conceptualization and methodology of the experiments; investigation (including performing the work for every experiment); data curation, visualization, and formal analysis; writing this chapter, which could be used for submitting grant applications or for future manuscripts if more work is completed.

This work has not yet been submitted for publication. As explained in the introduction, the main purpose of including this chapter is to provide a foundation on the literature and a complete set of methods for experiments that have already been designed but not fully executed. The aim is for a future student to be able to pick up where I left off.

Abstract

ADP-ribosylating AB_5-type toxins have effects on intestinal barriers, however the mechanisms of these effects are unclear. Intestinal barriers are defined by tight junctions and adherens junctions. Junctional proteins are up- or down-regulated in response to many external and internal stimuli, and they are not solely up/down-regulated at the genetic level. Intracellular trafficking, including delivery of junctional proteins to plasma membranes and removal/recycling of junctional proteins from plasma membranes, also accounts for junctional protein turnover, and these processes are tightly regulated. Rab/Rap GTPases are regulators of this turnover. Rab proteins themselves can be regulated by phosphorylation post-translational modifications by Ser/Thr protein kinases, one of which, PKA, is regulated by intracellular cAMP levels. Rap GTPases can be regulated by Epacs, a family of GEFs that are also regulated by intracellular cAMP levels. ADP-ribosylating AB_5-type toxins in the CT-like family specifically target G-proteins that regulate intracellular cAMP levels, therefore it is possible that the effects of these toxins on paracellular barriers is mediated by PKA-phosphorylated Rab GTPases and/or Epac-regulated Rap GTPases. We sought to investigate this hypothesis. Unfortunately, we encountered many obstacles that could not be overcome by the time this dissertation was written. We considered it worthwhile, though, to document the literature review, conceptualization of experiments, justification for methods chosen, and methods for attempted experiments so that the next graduate student to pick up this work is not reinventing a wheel.

Introduction

The Barrier Proteins of the Intestinal Epithelia

The intestinal barrier, with a surface area averaging about 32 square meters[196], defines the interface between the external and internal environments and it is the front line of defense against pathogens. Polarized epithelial cells are essential to establishing the boundaries, traffic patterns, and communication pathways between the outside and the inside of the gut. Polarized epithelia are characterized by having apical and basolateral plasma membrane domains, which are separated and constrained by cell-cell junctions including tight junctions (TJ) and adherens junctions (AJ). Together TJs and AJs compose the apical junctional complex (AJC). AJCs are essential to establishing polarity, maintaining cell-cell contacts, and protecting paracellular pathways between epithelial cells, and they are connected to the actomyosin and microtubule cytoskeletons, providing direct routes for maintenance and communication. Recent reviews of the structure of the gut mucosa and its many roles are included in this reference list.[197–201]

TJs form a barrier that aids in establishing polarity by blocking both paracellular diffusion of larger molecules and the movement of lipids and transmembrane proteins between the apical and basolateral borders. TJ proteins include: occludin, the claudin family, which includes over 20 proteins in mammals, zonula occludens (ZO1, ZO2, and ZO3) adaptor proteins which connect occludin and claudins to the actin cytoskeleton, junctional adhesional molecules (JAMs), and tricellulin. Each of these has been extensively reviewed, and recent reviews are included in this reference list.[202–204] Of particular interest to our group are the claudin proteins. Claudins form selectively permeable channels between epithelial cells and therefore largely define paracellular

permeability. Claudins are tightly controlled but can be dynamically up- or down-regulated as needed. Claudin-2 in particular is expressed in leaky epithelia and is often dysregulated in pathologies like cancer, inflammation, and fibrosis, though the molecular basis for its dysregulation and the downstream effects of this dysregulation is still poorly understood.[205]

Adherens junctions are (usually) located on the basal side of tight junctions in polarized epithelial cells. They provide mechanical adhesion between cells and are also directly linked to the cytoskeleton. Adherens junction proteins include: cadherins, catenins, and vinculin. Vinculin is a regulatory protein that allows indirect interaction with the actin cytoskeleton. Reviews of AJ proteins are also included in this reference list.[206]

Rab/Rap Proteins and Vesicular Trafficking of Proteins Involved in Barrier Integrity

Junctional proteins are dynamically regulated by intracellular trafficking via delivery of loaded vesicles to the plasma membrane or removal of membrane-bound junctional proteins by endocytosis. Recent reviews of barrier regulation are included in this reference list.[207] Rab proteins, which help to target and localize endosomes carrying junctional proteins, and to recycle those same proteins when junctions must be disassembled, are integral to maintaining and regulating epithelial barrier function. Specifically, Rab5, Rab11, and Rab13 are involved in stimuli-dependent transient endocytosis of tight junction molecules.[208,209]

Rab proteins perform the first step in tethering and docking a transport vesicle loaded with cargo. Rab-mediated tethering of vesicles to organelles or membranes is an important regulatory step in protein trafficking within a cell and the molecular

mechanisms of their actions have been described in reviews.[210–212] Briefly, activated (GTP-bound) Rabs inserted into the membrane of cargo-loaded vesicles can interact with motor proteins and/or with tethering factors that bring the membrane of the vesicle and its target membrane close enough to fuse together. They are then inactivated (GTP is hydrolyzed leaving the Rab GDP-bound) and removed from the membrane. This cycle is tightly regulated.

Rab/Rap activity depends on their ability to switch between GTP- and GDP-bound conformations, which is mediated by guanine nucleotide exchange factors, or GEFs.[213] The GEF known as "exchange protein directly activated by cAMP", or Epac, is know to be dependent on cAMP levels.[214] Epac regulates the GTPases Rap1 and Rap2, which have been linked to regulation of adherens junction formation and endothelial permeability.[215,216]

Another regulatory factor is the post-translational modification of phosphorylation at Ser/Thr and tyrosine residues by serine/threonine kinases, a mechanism that has been shown to be used by intracellular pathogens to disrupt host intracellular protein trafficking. A single Rab can be modulated by multiple different kinases. For example, Rab11A, which has been shown to be associated with recycling endosomes and also to be involved in maintenance of endothelial and epithelial barriers[217], can be phosphorylated by both PKC and PKG.[218] As described in the Waschbüsch review (2020), although many phosphorylated Rabs have been identified, their roles in trafficking and the specific protein kinases that phosphorylate them remain poorly defined. To further complicate the discussion, some Rabs can actually regulate TJ formation by modifying PKA signalling, as in the case of Rab13.[219]

Previous Studies on ADP-Ribosylating AB$_5$-Type Toxins and Barrier Function

Bacterial and viral pathogens frequently target cell-cell junctions, not only in the intestinal epithelia but throughout the body.[197,220–222] Many bacterial ADP-ribosylating toxins are known to directly target cell-cell junctions and cytoskeletal proteins. Catara et. al. (2019) provide an excellent review of these activities.[223] To summarize, C3-like ADP-ribosylating toxins specifically modify Rho-GTPases, impairing actin polymerization. *Pseudomonas aeruginosa* exoenzyme S and T modify Rab GTPases, impairing endocytic pathways. C2-like toxins modify actin directly, resulting in actin depolymerization. ADP-ribosylating AB$_5$-type toxins like cholera toxin (CT) and pertussis toxin (PT) target Gα proteins and do not directly affect junctional proteins or cytoskeletal elements, yet these toxins have been shown to affect cellular morphology and paracellular permeability, indicating the involvement of more complex signaling pathways after the initial ADP-ribosylation modification. These downstream signaling pathways have yet to be defined. Here we summarize some of the work that has been done in examining the effects of CT and PT modifications on epithelial barrier function.

Studies in the 1980's showed that CT induced increased small intestinal epithelial permeability to dyes[224–226] but did not produce histomorphological changes in rat, mouse, and rabbit models.[225,226] In the early 1990's it was shown that changes in transepithelial resistance (TER) upon cAMP stimulation, including stimulation by CT, are accounted for by activation of ion channels within apical and basolateral membranes and are not attributed to changes in tight junction permeability.[227,228]

Guichard et al. (2013)[36] found that CT treatment did disrupt trafficking of E-cadherin and junctional localization of Rab11 to adherens junctions in CACO-2 cells.

Additionally, the normal alignment of TJs stacked closely upon AJs was disrupted. Claudin-2 (Cld2) and ZO1 levels were increased in treated cells, and their normal patterns of staining throughout the cell were altered, although their localization at TJs was not affected. Co-localization of Rab11 and ZO1 was abolished. They also showed that PKA activity mediates the junction-disrupting effects of CT. CT treatment reduces the levels of Rab11/Sec15 and induces the formation of apical gaps between epithelial cells accompanied by leakage of serum albumin into the intestinal lumen in murine ligated loop models.

Markov et. al. (2019) recently showed that CT induced a decrease in TER and an increase in paracellular permeability for fluorescein in rat jejunal epithelial tissue (from ligated loops), and further study demonstrated an increase in the intracellular spaces between cells as well as an increase in Cld2 and a decrease in tricellulin, but no change in other tight junction proteins.[229] Contrary to previous studies, this group did show a reduction in the number of microvilli in the jejunal epithelial tissue. The results of this study were in contrast to a previously published study on rat colon tissues which showed that CT induced an increase in TER as well as an increase of claudin-3 and claudin-4, accompanied by no morphological changes in tight junctions but increased intercellular spacing.[230]

While PT has some genetic homology, similar structure, and similar ADP-ribosylation activity to that of CT, and while it inactivates $G_{\alpha i}$ proteins which primarily inhibit the cAMP pathway, PT's main activity is not suspected to be increasing intracellular cAMP.[180] It does cause a characteristic clustering effect on Chinese Hamster

Ovary (CHO) cells. This points to PT having an alternative cellular activity that has yet to be defined.

Little research has been done on pertussis toxin's (PT) effects on paracellular epithelial barriers. The research that does exist has been done largely in brain microvascular endothelial cells. The reason for this is that *Bordetella pertussis* infection and pertussis toxin-based vaccinations have occasionally been linked to febrile seizures in children. One theory is that PT loosens endothelial cell barriers and allows the traversal of immune cells and/or bacteria through the blood-brain barrier. Patterson et. al. (1995) demonstrated that PT caused a dose-dependent increase in permeability to albumin and suggested that this was related to PKC activation.[231] Similarly, and more recently, it was shown that PT did not affect barrier function in epithelial cells but did increase paracellular permeability to HRP in endothelial cells.[232] This was accompanied by a decrease in TER, and the endothelial cell changes were shown to be affected by PKC inhibitors and activators. Kügler et. al. (2007) showed that PT reduced TER and increased paracellular permeability to HRP in addition to allowing increased transmigration of monocytes in HBMECs,[37] and Seidel et. al. (2011) corroborated this finding and showed that macrophage as well as bacterial translocation across human brain microvascular endothelial cells (HBMECs) were increased after PT treatment.[233] Even more recently, Starost et. al. (2016) found that THP-1 human monocytic cells exhibited increased adherence to human cerebral endothelial TY10 cells after treatment with PT.[234] Kügler et. al. (2007) suggested that PT could be compromising the vesicular transport pathways needed for maintenance of AJCs. Similar results were produced in 2015, and these authors found that PT induced changes in the localization of VE-cadherin

and β-catenin (this work was also done in HBMECs).[235] Importantly, several of these studies showed that none of the described effects were observed when cells were treated with only the binding subunit of the toxin, indicating that the effects are a result of the catalytic subunit's ADP-ribosylating activity. Finally, in contrast to these described studies, Yin et. al. (2014) showed that PT had a protective effect and reduced clinical deficits in EAE animal models of MS.[236]

ArtAB shares genetic and structural homology with both CT and PT. While its A subunit is supposed to be more similar to that of PT, its binding subunits are more similar to CT's and have been shown to be interchangeable with other similar bacterial toxins.[24] To date, we have not identified any work probing the effects of ArtA, ArtB, or ArtAB holotoxin on epithelial or endothelial barriers.

Hypothesis and Goals for These Experiments

We hypothesize that ADP-ribosylating AB$_5$ toxins affect the trafficking of junctional proteins to and from the membrane at paracellular junctions via Rab/Rap GTPase phosphorylation by toxin-mediated protein kinase activity. In addition, since adherens junctions interact directly with the actin cytoskeleton, we intend to investigate a potential AJ-mediated connection between the ADP-ribosylation events and the downstream actin cytoskeletal rearrangements.

Because CT and PT appear to have differing effects on cellular barriers, and because these effects have not been directly compared in the past, investigating overall epithelial barrier effects by multiple ADP-ribosylating AB$_5$-type toxins could contribute greatly to our understanding of this class of toxins as a whole, and would provide insight into the less-well-characterized ArtAB toxin. In addition, we recently published data on

the morphological changes induced by all three toxins. In that work we failed to characterize changes in the cytoskeleton after toxin treatment. Since others have suggested that cytoskeletal rearrangements may be associated with barrier changes, and because tight junctions are inherently dependent on arrangements of the actin cytoskeleton, we intend to further investigate those effects here. Finally, we are interested in defining the intracellular interactions that occur downstream of the initial ADP-ribosylation event. In an effort to further connect the ADP-ribosylation post-translational modification to the observed effects of morphological changes, disruption of AJC molecule transport, and paracellular permeability. We intend to do this by probing the downstream targets of PKA/PKC phosphorylations. Based on the introductory material above it is clear that there are a lot of unknowns and much work to be done to fill in the gaps in knowledge. The list of questions is very long. For the purpose of this study, we narrowed them down to include:

- A study of toxin-induced changes in TEER of monolayers using ECIS

- A study of toxin-induced changes in permeability of monolayers and the ability of immune cells to transmigrate using variable size exclusion permeability and immune cell transmigration assays in transwells

- A study of toxin-induced changes in the intracellular localization and/or quantities of the following tight junction, adherens junction, and endocytic recycling vesicular trafficking proteins using fluorescence imaging and in-cell western blotting

    o ZO-1, ZO-2, ZO-3

    o Occludin

- Claudin-2, Claudin-3, Claudin-4

- Tricellulin

- E-cadherin

- Rab5, Rab11, Rab13, and the Epac-regulated GTPases Rap1 and Rap2

- A study of toxin-induced up and/or downregulation of those same proteins using qPCR on cell lysates

- A study to identify the specific targets of toxin-activated PKA and/or PKC phosphorylation using antibodies that detect PKA-phosphorylated or PKC-phosphorylated intracellular targets

- An *in vivo* study of toxin-induced changes to mouse small intestinal function using an ileal ligated loop model. The specific goals of this study were to determine:

  - Paracellular barrier integrity as determined by fluid accumulation in loops (measured quantitatively using a loop volume/length ratio), leakage of albumin into the lumenal fluid, and leakage of co-administered fluorescent ovalbumin from the loop into the surrounding tissues and blood stream

  - Toxin effects on the proteins mentioned above based on immunohistological staining and qPCR

- Studies with F-actin stains on toxin-treated cells to further define the morphological changes induced by AB_5-type ARTs.

This subject is complex and only a topical preliminary literature review ahas been conducted and considered at this point. A deeper literature review and extensive experiment planning would be required to devise a thorough investigation into the mechanisms of barrier effects of these toxins. The following is a preliminary attempt at this project and it is by no means complete; rather, it is intended as a starting point for a future graduate student.

Materials and Methods

<u>Review of Potential Methods</u>

Below we provide a brief overview of methods we considered using to explore

barrier function. This is largely a collection and review of methods described in the

papers referred to above. We also provide a rationale for choosing the methods we did.

The goal of documenting this is to lay a foundation for someone in Boise State

University's Biomolecular Sciences program to pick up where we left off without

reinventing the wheel.

<u>Cell lines/intestinal barrier models</u>

Previous relevant barrier studies have been conducted using Caco-2 and T84 cells.

[36,227,237] Caco-2 (ATCC HTB-37) are epithelial cells from colon tissue of a patient with

colorectal adenocarcinoma. T84 cells (ATCC CCL-248) are another human colorectal

carcinoma cell line. While both cell lines form monolayers that can be used as model

systems of gut epithelial barriers, and while both are frequently used interchangeably,

Caco-2 cells tend to differentiate into cells with biochemical and morphological

characteristics more like small intestinal epithelia, which is useful for our studies. In

addition, we already have access to Caco-2 cells through the Biomolecular Research

Center. In the future we would like to explore the development of co-culture or triple-co-

culture small intestinal models that incorporate immune cells and/or mucus-producing

cells in addition to the Caco-2 monolayer. Others have had success developing such

models recently and they offer a more realistic and robust model for studying host-toxin

interactions.[238–240]

For the experiments described below, we used Caco-2 cells cultured in Eagle's Minimum Essential Medium (MEM, Corning Ref. No. 10-010-CV) supplemented with 20% FBS (ATCC Prod. No. 30-2021 or Cytiva Cat. No. SH30071.01/29181802 or HyClone Cat. No. SH30071) and penicillin/streptomycin (Cytiva Cat. No. SV30010/29131438) at 37C with 5% CO2.

Due to our experimental struggles, also described below, we also attempted to conduct studies using mouse-derived primary small intestinal cells from Cell Biologics. The choice was made to use mouse cells instead of human cells because resources such as tight junction antibodies etc. for probing mouse cells were more readily available. With luck, we would be able to reproduce experiments on both the cancer cell line and the primary cell line. While CT and ArtAB primarily work in the gut, making the mouse small intestinal primary cells a good choice, pertussis toxin acts primarily in the respiratory tract and, apparently, in the brain microvasculature. If we have success with the gut model, we may be able to investigate other models in the future. Unfortunately, our cells became contaminated before we collected any usable data and we did not have time to try again. The remaining primary cells, as described below, are owned and stored by the Beard lab for possible future experiments.

Measurements of short-circuit current (I_{SC}) and TER/TEER

Previous relevant barrier studies have been conducted using various methods to measure transmembrane epithelial resistance (TEER). Volt-ohm meters,[237] calomel/Ag-AgCl electrodes with 5% agar bridge and with resistance measured with dual voltage clamp device with 100 or 25 μA current pulses,[227] and Ussing chambers[227] have been used to examine the effects of ADP-ribosylating AB_5-type toxins on epithelial barriers.

To our knowledge, at the time of writing this, no studies on the effects of CT, PT, or ArtAB on epithelial barrier TEER as measured using electric cell-substrate impedance sensing (ECIS) have been reported. We have ECIS equipment available and therefore chose to utilize these resources for our studies.

<div align="center">Measurements of permeability</div>

Several different methods of investigating paracellular permability have been reported. [^{3}H]inulin can be administered on apical side of transwell filter and the percent traversing hte monolayer can be quantified with a β-scintillation counter measuring counts/min of radioactivity.[237] Using an animal model, [^{3}H]mannitol can be administered to an animal after treatment in ileal ligated loops, and permeability can be measured by assaying the fluid within the loops for radioactivity.[226]

Radioactivity assays are not realistic for our group. Other ways of approaching this include administering FITC- or other fluorophore-labelled sugars such as dextrans, sodium fluorescein, albumin, etc. to cultured monolayers in transwell assays or, in animal models, to animals after or along with treatment in ileal ligated loops.[224,225]

Ileal ligated loops can provide information via immunohistological staining for proteins of interest (e.g. albumin)[36] and/or by quantifying the extravasation of albumin into luminal fluid.[225]

We planned to examine permeability using sodium fluorescein, albumin, and potentially another fluorophore-conjugated sugar on cultured Caco-2 and/or primary mouse small intestinal cells in transwells. We planned to use fluorescein isothiocyanate-conjugated ovalbumin (FITC-OVA) in the ligated loop model. FITC-OVA would be

injected along with toxin into the loop. Fluorescence would be measured in the tissue collected as well as in the blood and lumenal fluids.

<div align="center">Measurements of Distribution</div>

Ileal ligated loops also allow for examination of protein localization via immunohistological staining for proteins of interest (e.g. (Rab11, Sec15, Ecad).[36] For *in vitro* methods, confocal microscopy or SEM/TEM microscopy can be used to examine localization of proteins of interest.[36] One study mentioned above performed Western blots of TX-100 soluble/insoluble fractions from treated cells and compared these to a control.[237]

We planned to measure the up/down regulation of tight junction proteins and Rabs of interest using in-cell Western blots and rtPCR, and to examine distribution using confocal microscopy on treated cultured Caco-2 and/or mouse small intestinal primary cells and also with immunohistochemistry staining on tissue samples from ileal ligated loops.

Confirmation of CT Activity

CT (plasmid pJKT46) and CTB (plasmid JKT49) were purified as described in Chapter 3 of this dissertation using D-galactose affinity purification. Lab-purified proteins or commercially purified protein controls were run out on 12% SDS-PAGE gels. Gels were transferred onto nitrocellulose membranes (Invitrogen Ref. No. IB23001) using the iBlot2 dry blotting system with the P0 setting. After transfer, membranes were trimmed and stored in a plastic Western blot box in blocking buffer (10 g skim milk powder + 100 μL Tween-20 + 200 mL 1X PBS) overnight at 4°C. Blocked membranes were rinsed 2 times with 10 ML 1X PBS + 0.05% Tween-20 (PBS-T), then incubated at RT on a shaker

with 10 mL PBS-T for 15 minutes, 5 minutes, and 5 minutes with rinses in between each

incubation and a final rinse of 1X PBS. Primary antibody at 1:5000 in blocking buffer

was added and membranes were incubated at RT on a shaker for 1 hour. Membranes

were rinsed as described above, then secondary antibody at 1:10,000 in blocking buffer

was added and membranes were incubated at RT on a shaker for 1 hour. Membranes

were rinsed as described above. 2 mL each of luminol enhancer solution and stable

peroxide solution from the SuperSignal West Pico Plus Chemiluminescent Substate kit

(ThermoScientific Cat. No. 34577) were combined in a 50 mL conical, and 2 mL of the

mixed substrate was added directly to each membrane. Boxes were wrapped in foil and

incubated at RT for 5 min, then removed from boxes, covered in plastic wrap and

smoothed using the iBlot roller, and imaged on the BioRad imager in the shared

equipment room. Additional SDS-PAGE gels were loaded exactly the same but were

stained with Coomassie blue, destained, and imaged for comparison. Note: Fallon

Cassidy ran a similar experiment on 07/01/2021 to see if the CT antibodies would bind to

ArtAB. No results were obtained for this study.

Antibodies used for CT

- Primary: Rabbit anti-CT (Sigma Ref. No. C3062-1ML)
- Secondary: Goat anti-rabbit-HRP (ThermoScientific Ref. No. 31460)

Antibodies used for CTB

- Primary: Goat-anti CTB (CalBioChem Cat. No. 227040)
- Secondary: Rabbit anti-goat HRP (Bethyl Prod. No. A50-100P)

Controls:

- CT (List Labs 2 mg/mL #100B/#9100B)
- CT (Sigma 100 ug/mL C8052/085m4100v)
- CTB (Sigma 1 mg/mL C9903/082m4008)
- BSA (ThermoScientific Ref. No. 23209)

Morphological assays were performed by seeding CHO cells (ATCC CCL-61) cultured in Ham's F-12 media (Gibco Ref. No. 11765-047) supplemented with 10% FBS (ATCC Prod. No. 30-2021 or Cytiva Cat. No. SH30071.01/29181802 or HyClone Cat. No. SH30071) and penicillin/streptomycin (Cytiva Cat. No. SV30010/29131438) in a black-walled, clear-bottomed 96-well plate. CHO cells were incubated overnight, then starved in serum-free media for 4 hours before treatment with 25 ug/mL CT, *E. coli* control, or media only. Treated cells were incubated overnight and imaged with a brightfield microscope at 24 hours.

LAL assays were performed per manufacturer's instructions.

Electric Cell-Substrate Impedance Sensing

For a preliminary study, 8-well ECIS arrays (8W10E+) were coated with 200 μL/well of gelatin. Caco-2 cells (ATCC HTB-37) in EMEM + 20% FBS were seeded at $2*10^5$ cells/mL, 400 μL /well with 200 μL media added first, then 200 μL cells, except for one cell-free well which was filled with 400 μL media. Media was changed every other day. On day 8, 30 minutes of baseline data were collected prior to treatment, then cells were treated with ArtAB-His at 10, 5, 2.5, 1.25, 0.5, or 0.3 ug/well. No effect was noted after 24 hours so wells were rinsed and treated with the same amount of CT. The CT used was old, and upon running out the CT on an SDS-PAGE gel it was discovered that the CTA subunit had broken down and was no longer present, so the cells had really been treated with CTB alone.

For ECM studies, 8-well ECIS arrays (8W10E+) were coated with 200 μL 100 ug/mL rat tail collagen type I (Advanced Biomatrix Cat. No. 5056-20 mL), mouse laminin, (Millipore, Cat. No. CC095), or fibronectin (Advanced Biomatrix Cat. No.

5050) prior to L-cysteine reduction and incubated at RT for 20 minutes. ECM proteins were removed, and wells were rinsed with filter sterilized nanopure water. For all studies, arrays were reduced with 200 μL /well 10 mM L-cysteine solution (Applied BioPhysics, Electrode-stabilizing Solution) incubated at RT for 20 minutes. L-cysteine solution was removed, and wells were rinsed with filter sterilized nanopure water. Caco-2 cells (ATCC HTB-37) in EMEM + 20% FBS were seeded at $2*10^5$ cells/mL, 400 μL /well with 200 μL media added first, then 200 μL cells, except for one cell-free well which was filled with 400 μL media. Cells were continuously agitated to ensure dispersion and an even/monodisperse cell solution. Arrays were allowed to sit covered in the biosafety cabinet at RT for 20 min after seeding to allow for cell adhesion and to avoid convective currents caused by dramatic and rapid temperature changes in moving the array to the 37C incubator. After RT incubation, arrays were moved to incubator set to 37C and 5% CO2. Media (EMEM + 20% FBS) was changed daily or every other day as needed.

For Experiment 1 – One array was coated with Collagen I and incubated for 7 days prior to starting on ECIS equipment. Single frequency/time settings were selected for this experiment (monitors wells at single frequency of 4000 Hz at 0.5 s/well, updates every 4 seconds after collecting data from each well). Cells were monitored on ECIS for 2 days, then treated with 20 μL CTB at a final concentration of 40, 20, 10, 6, 3, or 0 ug/mL (1 well media only, 1 well *E. coli* control). Treated cells were monitored for 1 day but no response was observed.

For Experiment 2 – Two arrays with 2 wells each coated in collagen I, laminin, and fibronectin, and 2 uncoated wells (for media control and cell-free control) were prepared and directly started on ECIS equipment. Growth was monitored for 10 days

with daily media changes. After day 10, cells were allowed to continue growing with daily media changes but were not monitored on ECIS equipment. Literature states that Caco-2 cells require 2-3 weeks for maturation. We had intended to re-start these on ECIS at the three-week mark, however, cells became contaminated during the long incubation time in a shared incubator and could not be used for experiments.

For experiment 3 – Two arrays were prepared as described for Experiment 2 and directly started on ECIS equipment. After the first 24 hours, the media was changed with EMEM containing 10% FBS (instead of 20%) and this was continued for subsequent media changes. Growth was monitored for 13 days. A consistent and stable monolayer was never achieved, and cells could not be used for experiments.

As a note, other references used Caco-2 cells when they reached a baseline TEER of 800-1500 Ω/cm^2 (albeit this reference had no mention of how many days post-confluency this was)[237] or a baseline TEER of >1000 Ω/cm^2 after 7 days (assumed to be post-seeding, not post-confluency).[227] The highest semi-stable TEER we ever achieved was between 900-1000 Ω/cm^2.

alamarBlue™ and crystal violet assays as well as brightfield microscopy were performed exactly as described in Chapter 2 of this dissertation document. In one experiment, cells were seeded at 5000 cells/well as we have done for similar experiments with other cell lines. In a second experiment, cells were seeded at confluency so that we could compare the effects of the toxin on growing cells to the effects on an established monolayer.

Mouse Intestinal Ligated Loops

Experiments were performed on three separate occasions. The methods here describe what was done for the final, and most thorough, set of experiments, performed in May of 2022. Procedures were performed as described by Boerner, Luissint, and Parkos (2021)[241] using the BRV's surgical suite and murine anesthesia equipment. A summary of the experimental groups is included in Table 1. Treatments were prepared so that 10 ug in 50 μL (final concentration 0.2 ug/μL) of toxin or control would be administered along with 0.25 ug in 50 μL (final concentration 1.25 mg/mL) of FITC-OVA would be administered in each loop.

For anesthesia, the machine was warmed up on low flow (100 mL/min and 1.2-1.5%) for > 5 minutes. After warming up, the chamber was filled on high flow (100 mL/min and 3-4%) before animals were subjected to anesthesia treatments. Once animals were under anesthesia they were moved (by holding the animal near the base of the tail) to a scale for weighing, then to a pre-heated surgical board and immediately fitted with a nose cone connected to the flowing isofluorane. Animals were maintained at a flow rate of 100 mL/min at 1.2-5% isofluorane. Animals were monitored throughout the surgery for signs of consciousness and/or agonal breathing, either symptom indicating a need to adjust the anesthesia. Animals were secured and maintained in supine position by the four limbs using small binder clips and magnets on the two front paws and one rear paw and a rodent pulse oximeter/heart rate monitor on the other rear paw.

A physical exam was performed to check heart rate (between 400-700 beats/min) and rhythm, mucous membrane color (pink), and respiratory rate (not lower than 40 - 60 breaths/min). When animals were stable, anesthetic depth was assessed by pedal

withdrawal reflex (pinching of the skin between the toes). If mouse did not respond, we proceeded with the surgery. Vitals and pedal reflex were monitored throughout the surgery according to IACUC guidelines.

Although ligated loops are non-survival surgeries, we attempted to use aseptic/sterile technique where possible. Surgical instruments were scrubbed with soap and rinsed with water and then 70% ethanol before use. Fur of the abdominal midline was shaved and the area was scrubbed with Betadine antiseptic solution. A midline laparotomy was performed by making a vertical incision in the middle of the abdomen with sharp surgical scissors and peritoneum was exposed. Care was taken to not injure intra-abdominal organs. A cotton gauze pad with a hole cut in the center was placed over the incision, and cotton swabs soaked in 1X PBS were used to mobilize and exteriorize the caecum, followed by the ileum, onto the cotton gauze pad (Figure 2a). Great care was taken not to injure the blood supply, and exposed tissues were kept moist with 1X PBS dripped from a 10 mL syringe every 2-3 minutes. Major arteries and blood vessels in the mesentery were identified and ligation sites were chosen (Figure 2a,b). Mesentery was fenestrated using the needle attached to a silk suture (Perma Hand Silk 18" 683G) held with needle drivers. Surgical knots were tied at each of the two initial ligation sites, avoiding blood vessels as much as possible, then sharp scissors were used to cut the intestine inside of the ligations keeping the major blood supplies and mesenteric membranes intact. Luminal contents and fecal matter were rinsed out of the open-ended segment using a transfer pipette fitted with a gel-loading pipette tip. The tip was inserted as far into the intestinal segment as possible without disrupting the blood supplies with movement, then 1X PBS was flushed. This was repeated from both ends until segment

was cleared of fecal matter. If segments were too large for fecal matter to clear with this method, additional cuts were made internally and smaller segments were flushed. The cut ends were ligated and additional internal ligations and cuts were made so that two loops with independent blood supplies were formed and sealed at both ends (Figure 2c). Finally, a 1 mL insulin needle was used to draw up 100 μL of toxin + 100 μL FITC-OVA at the final concentrations listed above. 100 μL of the mixed fluid was injected into each loop according to the experimental groups listed in Table 1.

Intestines were gently replaced within the surgical incision using cotton swabs soaked in 1X PBS, and the incision was sealed with a small binder clip. Animals were placed on heating pads in anesthesia chambers for a 90 minute incubation period. Breathing rate and coloring were monitored throughout the incubation period. At the end of the incubation period, pedal reflex was checked to ensure animal was still under anesthesia, then animal was euthanized by bilateral thoracotomy and cardiac puncture with a 25-gauge needle. Blood was collected and allowed to clot at room temperature prior to centrifugation and isolation of serum. Serum was aliquoted into RNA later for future qPCR test for 16s bacterial DNA or into a clear-bottomed 96-well plate for measurement of fluorescence. Loops were then removed from the abdomen, length and weight were measured, and photos were collected. Loops were opened on one end and contents were released into a centrifuge tube. Loops were flushed with 100 uL of 1X PBS in an insulin needle injected into the tied end of the loop. Volume of fluid was measured and aliquoted into RNAlater (Invitrogen RNAlater Solution Ref AM7020) for future cytokine analysis or into a black-walled, clear-bottomed 96-well plate for measurement of fluorescence. Loop tissue was cut into sections and stored in either RNAlater for future

cytokine analysis or into 4% paraformaldehyde (Thermo Scientific Paraformaldehyde Solution J19943-K2) for histology. Loops for histology were submitted to the histology core lab at the Biomolecular Research Center for H&E staining and preparation and freezing of slides for future immunohistological staining. Immunohistological staining has not yet been performed.

Table 4.1.   Experimental groups for mouse ileal ligated loops in May 2022

	Group	Sample (loop1)	Control(loop2)	Inoculum	#mice
1	ArtAB	Purified ArtAB	1 X PBS E.coli vehicle	10 ug	4 (2 male/2 female)
2	CT	Purified CT	1 X PBS E.coli vehicle	10 ug	4(2male/2 female)
3	CTB	Purified CTB	1 X PBS E.coli vehicle	equimolar	4(2male/2 female)
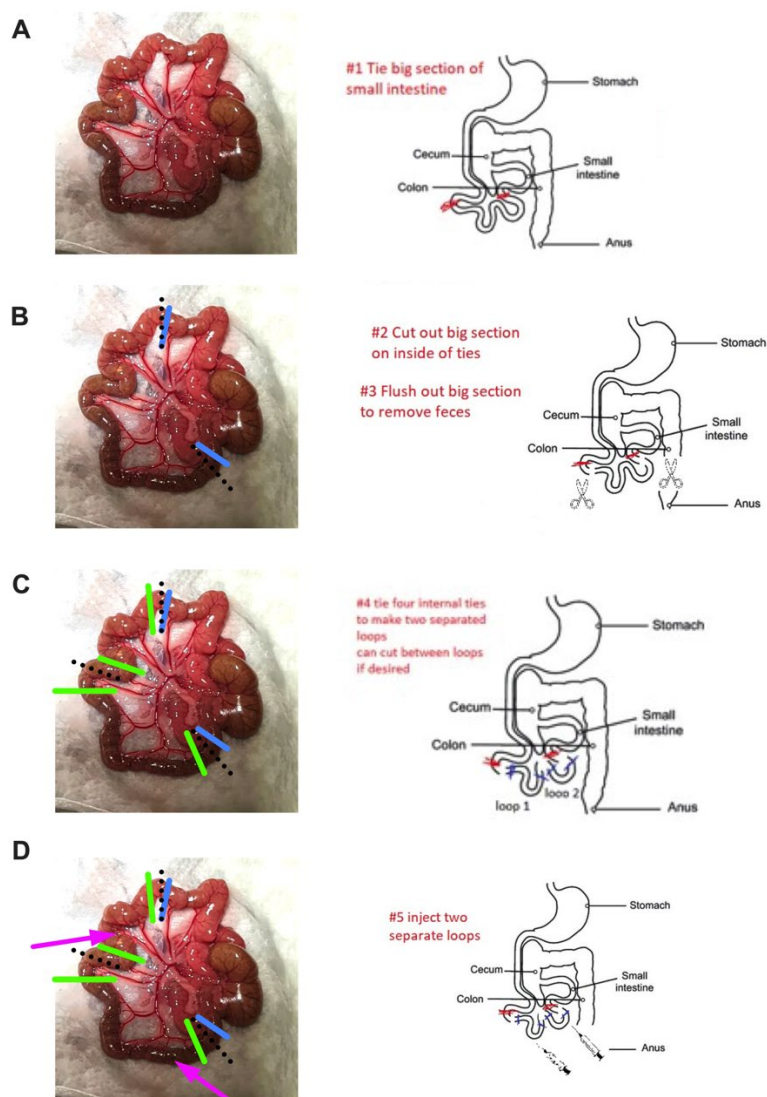
Figure 4.3.   Mouse intestinal ligated loop method

Example of initial ligation sites (blue), cut sites (black dotted line), Loop tie-off ligation sites (green), and injection sites (pink arrows) are included in the left-hand image of each panel. Descriptions of each step are included in the right hand image of each panel.

Mouse Primary Cell Assays

Cells purchased from Cell Biologics were seeded in a T75 flask immediately upon arrival, then split 1:3 after 3 days of incubation with daily media change. Two of the flasks were split the next day 1:2 and incubated for one more day before stocking down for future use. The third flask was split into cultureware coated with collagen I for

experiments: one 6-well culture plate for RNA/protein harvesting, one 24-well plate for coverslips for staining/imaging, one 96-well plate for PKA/PKC experiments, and two 8-well ECIS arrays (8W10E+). The plan was to treat with 25 ug/mL holotoxin or equimolar pentamer, and toxins were purified and prepared for use. Unfortunately, the cells in cultureware were contaminated with yeast and could not be used for experiments. The remaining primary cells are owned and stored by the Beard lab for possible future experiments.

Results

<u>Confirmation of CT Activity</u>

We intended to treat both cultured monolayers and mice (via ileal ligated loops) with ArtAB and CT purified by our own lab to remove variables of differing production methods. We have previously used commercial CT in our lab, therefore we wanted to ensure that our purified toxin was active, acted the same as the commercial toxin, and could be bound by the antibodies we currently owned. We had recently purified CTB pentamer as well, and had considered using the pentamer as a control in our planned experiments, therefore we conducted similar experiments on both CT and CTB.

All unboiled CT/CTB samples, both commercial and lab-purified, produced a prominent but unexpected band between 35 and 55 kDa, which is lighter than the expected band for the pentamer (~58.2 kDa). This band was recognized by both the anti-CT and anti-CTB antibodies (Figure 4.1 a2, a4, a6, b2, b4). Only the List Labs CT sample produced a band at the expected weight for the CTB pentamer, and this was also recognized by the anti-CT antibody (Figure 4.1 a4). CTA monomers appeared to be weakly recognized by the anti-CT antibody (Figure 4.1 a1, a2, a3, a4). Neither primary antibody recognized the BSA negative control (Figure 4.1 a7, b5) and both secondary antibodies did bind the primary antibody positive controls (Figure 4.1 a8, b6).

For future reference, the left panels of Figure 1 are highly representative of the often-repeated SDS-PAGE gels of CT and CTB. The unexpected band between 35 and - 55 kDa is always present, and a band where holotoxin is expected, around 85.4 kDa, is rarely, if ever, observed.

Morphological assays with CHO cells treated with lab-purified CT showed that CT did, in fact, produce the expected elongation as observed with treatment with commercial CT (data not shown).

We also attempted to perform an endotoxin assay because, despite being purified from ClearColi® which contain modified LPS, we wanted to ensure that endotoxin levels in lab-purified protein were low enough to use the purified toxin in cell and animal experiments. We tried to conduct LAL assays using two separate commercial LAL-based endotoxin detection and quantification kits, however results were inconclusive with both kits. Despite the failure to confirm endotoxin levels, we have used proteins purified from ClearColi® in the past for cell and animal experiments with no problems. To create an *E. coli* protein/LPS control that contains everything that in the purified CT sample except the CT itself, we grew, induced, and purified an empty pBAD18 vector transformed into ClearColi® using the exact same purification scheme.

In summary, we showed that our lab-purified CT runs similarly to commercial CT on an SDS-PAGE gel in both the native and heat-denatured states, indicating that it likely folds similarly, and that the antibodies we currently use to detect commercial CT will work on our lab-purified CT. We also showed that the lab-purified CT produces the same effects on CHO cells as commercial CT. We conclude that our lab-purified CT can be used in cell and animal experiments, provided that an *E. coli* protein/LPS control (empty pBAD18 vector transformed into ClearColi® and grown, induced, and purified using the exact same purification scheme) is used as a control in all studies.
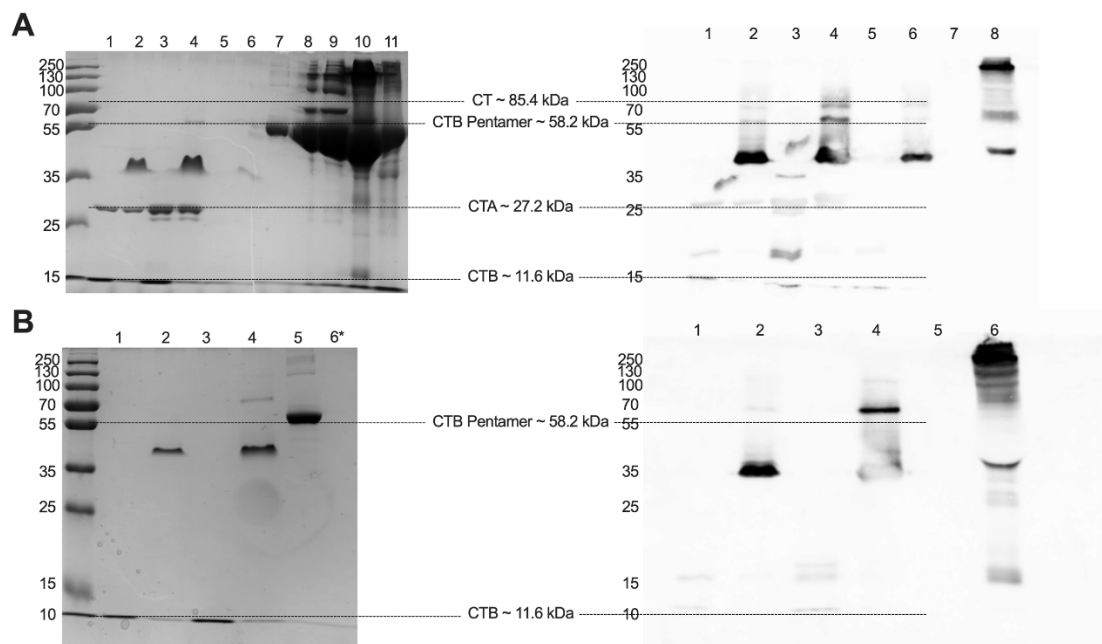
Figure 4.1.   Western blot analysis of CT and CTB purified in our lab compared to commercial CT and CTB

(A) 12% SDS-PAGE gel (left) and Western blot (right) of commercial and lab-purified CT (plasmid pJKT46) using rabbit anti-CT antibody. 1: Our CT Boiled, 2: Our CT Unboiled, 3: List Labs CT Boiled, 4: List Labs CT Unboiled, 5: Sigma CT Boiled, 6: Sigma CT Unboiled, 7: BSA Negative Control, 8: Rabbit Anti-C, 9: Goat Anti-CTB, 10: HRP-conjugated Goat Anti-Rabbit, 11: HRP-conjugated Rabbit Anti-Goat. Lane 8 was included to confirm expected activity of secondary antibody. Lanes 9-11 were included to confirm expected presence of antibodies. (B) 12% SDS-PAGE gel (left) and Western blot (right) of commercial and lab-purified CTB (plasmid pJKT49) using goat anti-CTB primary antibody. 1: Our CT Boiled, 2: Our CT Unboiled, 3: Sigma CT Boiled, 4: Sigma CT Unboiled, 5: BSA Negative Control, 6*/6: Goat Anti-CTB was included on the gel for the Western blot but was not loaded onto the SDS-PAGE gel for Coomassie staining as it had already been confirmed on the gel featured in panel a. Lane 6 was included to confirm expected activity of secondary antibody.

Electric Cell-Substrate Impedance Sensing

The preliminary study described in the methods section was the only study that produced any usable data, however the study design and methods were flawed in that cells were treated with multiple treatments and the toxin used to treat cells was unreliable as described. This data should not be used to draw any conclusions.

We were unable to obtain results in additional ECIS studies due to contamination issues and also failure to obtain a coherent monolayer that produced a consistent TEER reading. We attempted to define a toxin concentration that would produce an effect on a

Caco-2 monolayer using alamarBlue™ metabolic activity and crystal violet cell viability assays in conjunction with brightfield microscopy, however data from these assays were also inconclusive. No toxin concentration produced a marked and definitive or measurable phenotype. For these reasons we tabled the ECIS experiments, however details are provided below for future use.

Mouse Intestinal Ligated Loops

We performed ileal ligated loops on mice on three separate occasions (October 2019, June 2021, and May 2022). Surgeries were performed per the protocols approved by the Boise State University institutional animal care and use committee (IACUC, IACUC number AC20-018). Mice were housed and maintained and all surgeries were performed in the Boise State University Biomedical Research Vivarium (BRV) core facilities. During the October 2019 and June 2021 ileal ligated loop experiments, the mice were fasted for 4 hours prior to surgery with the goal of reducing the excrement in the bowel. Unfortunately, this procedure was not sufficient to eliminate waste in the bowel. No statistically significant data could be determined from the fluid accumulation or length/width data. The H & E stain allowed us to establish a villi-to-crypt ratio that identifies damage to the intestine. This is a debated method because the villi-to-crypt ratio varies between species, individuals, and portions of the gut.[242] In June 2021 however, we collected control sections just outside of each loop. This allowed us to compare loop villi-to-crypt ratios to a non-treated control. With a sample size of n=6 (n=2 per treatment), the data is not conclusive. Further studies are required to obtain a clear result.

Many procedural errors were corrected in the May 2022 experiments. First of all, the sample size was increased to n=12 (n=3 per treatment) To deal with the excrement issue, we adapted a flushing method using a transfer pipette connected to a gel loading tip that dispensed 1X PBS, similar to the method described by Boerner, Luissint, and Parkos (2021)[241] Flushing the loops before treatment allowed for more accurate fluid accumulation data. Fluid accumulation was noted in both the ArtAB and CT treatments (Figure 4.2a). The second improvement in the May 2022 experiments was that FITC-Ova was delivered at the time of treatment. The presence of FITC-Ova in the serum suggested that the integrity of the gut may be compromised as seen in CT and CTB treatments (Figure 4.2b). This data may not be conclusive because some of the damage to the gut could be caused by the surgery or flushing. The introduction of FITC-Ova also allowed for fluorescent microscopy images to be taken that show the profusion of the FITC-Ova and likely the treatment protein into the gut tissue (Figure 4.2e. The final improvement made in May 2022 was that slices were fixed and H&E stained (Figure 4.2f and slices were preserved for future immunohistochemistry (IHC) with antibodies specific for immune cells. IHC will support the villi-to-crypt ratio in indicating inflammation and infiltration of immune cells. This data will be collected by Tinker Lab students in the fall semester of 2022. Overall, the ileal ligated loops experiments give us insight into how the integrity, inflammation and immune response in the gut compares between ArtAB and CT. Additionally, CT was compared to the subunit CTB response to support the use of CTB as a non-toxic vaccine adjuvant. Future research into the impact of ArtAB, ArtAB mutants, and ArtAB subunits on the mouse gut is currently being discussed.

158
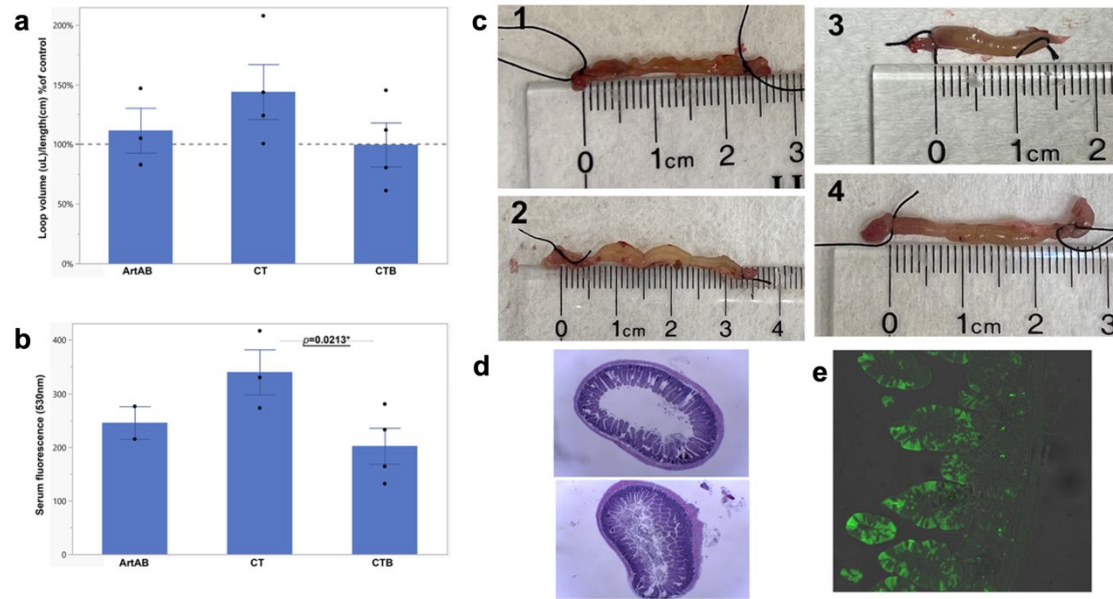
Figure 4.2.   Mouse ligated loop experiment, spring 2022, toxin effects on fluid accumulation and barrier function

Each mouse had two loops, experimental (ArtAB, CT or CTB) and control (vehicle). (a) ratio of loop fluid volume (μL) over loop length (cm) as percentage of control (n=3-4), (b) GFP fluorescence in serum for mice with loops containing ArtAB, CT or CTB (n=2-4), (c) control (1), CTB (2), ArtAB(3) and CT (4) loop examples, (d) example histological sections from ligated loops, (e) example loop treated with FITC-Ova from untreated mouse.

Mouse Primary Cell Assays

Mouse small intestinal primary cells were purchased with the intention of conducting experiments to investigate how ArtAB, CT, and PT holotoxins and ArtB and CTB pentamers affect intestinal epithelial barriers, however no data was collected from these assays. A description of the work performed in provided in the methods section for future reference.

Discussion

The literature review indicates that AB_5 toxins have effects on epithelial barrier integrity and that these effects may be distinct depending on the pathway. Epithelial barrier disruption is important from both a pathogenesis and vaccine perspective.

We hypothesized that ADP-ribosylating AB_5 toxins affect the trafficking of junctional proteins to and from the membrane at paracellular junctions via Rab/Rap GTPase phosphorylation by toxin-mediated protein kinase activity. In addition, since adherens junctions interact directly with the actin cytoskeleton, we sought to investigate a potential AJ-mediated connection between the ADP-ribosylation events and the downstream actin cytoskeletal rearrangements. To pursue these questions, future students will pursue this list of experiments outlined in the introduction of this section.

160

CHAPTER FIVE: EVALUATION OF THE EFFICACY OF A CHOLERA-TOXIN-

BASED *STAPHYLOCOCCUS AUREUS* VACCINE AGAINST BOVINE

INTRAMAMMARY CHALLENGE

Hussain A. Alabdullah[1,†], Elise Overgaard[2,†], Danielle Scarbrough[2], Janet E. Williams[1], Omid Mohammad Mousa[3], Gary Dunn[3], Laura Bond[4], Mark A. McGuire[1], and Juliette K. Tinker[2,3,*]

[1]   Department of Animal and Veterinary Science, University of Idaho, Moscow, ID 83844, USA
[2]   Biomolecular Sciences Graduate Program, Boise State University, Boise, ID 83725, USA
[3]   Department of Biological Sciences, Boise State University, Boise, ID 83725, USA
[4]   Biomolecular Research Center, Boise State University, Boise, ID 83725, USA
[*]   Correspondence: juliettetinker@boisestate.edu
[†]   These authors contributed equally to this work

Authorship statement: My direct contributions to this manuscript included the work of blood and milk sample processing, protein expression and purification, and immunogenicity ELISA assays; data curation and formal analysis of vaccine-specific antibody response data; writing the manuscript, and preparing it for submission with Dr. Tinker's help.

Abstract

Staphylococcus aureus (*S. aureus*) is a primary agent of bovine mastitis and a source of significant economic loss for the dairy industry. We previously reported antigen-specific immune induction in the milk and serum of dairy cows following vaccination with a cholera toxin A_2 and B subunit (CTA_2/B) -based vaccine containing the iron-regulated surface determinant A (IsdA) and clumping factor A (ClfA) antigens of *S. aureus* (IsdA + ClfA-CTA_2/B). The goal of the current study was to assess the efficacy of this vaccine to protect against *S. aureus* infection after intramammary challenge. Six mid-lactation heifers were randomized to vaccinated and control groups. On days 1 and 14, animals were inoculated intranasally with vaccine or vehicle control, and on day 20, animals were challenged with *S. aureus*. Clinical outcome, milk quality, bacterial shedding, and somatic cell count (SCC) were followed for ten days post-challenge. Vaccinated animals did not show signs of clinical *S. aureus* mastitis and had lower SCCs compared to control animals during the challenge period. Reductions in bacterial shedding were observed but were not significant between groups. Antibody analysis of milk and serum indicated that, upon challenge, vaccinated animals produced enhanced IsdA- and ClfA-CTA_2/B specific immunoglobulin G (IgG) responses, while responses to CTA_2/B alone were not different between groups. Responses after challenge were largely IgG1 against the IsdA antigen and mixed IgG1/IgG2 against the ClfA antigen. In addition, there was a significant increase in interferon gamma (IFN-γ) expression from blood cells in vaccinated animals on day 20. While preliminary, these findings support evidence of the induction of active immunity by IsdA + ClfA-CTA_2/B, and further assessment of this vaccine is warranted.

162

Introduction

Mastitis, or inflammation of the udder, is one of the most economically significant diseases affecting dairy cattle worldwide and is most often the result of a bacterial infection. *Staphylococcus aureus* (*S. aureus*), a main etiological agent, is highly contagious and can spread rapidly among herds. It is estimated that up to 70% of U.S. herds are positive for *S. aureus*, and this bacterium caused the highest overall annual yield losses among other mastitis pathogens in a recent Finnish study.[243,244] *S. aureus* infections are most commonly transmitted during the milking process and can impact animal welfare as well as milk yield and quality.[245] The ability of this bacterium to form biofilms and replicate intracellularly can promote subclinical colonization of the mammary gland, often leading to chronic infection, which is difficult to detect and is frequently the source of herd reinfection.[246–248] *S. aureus* is also commonly resistant to antimicrobial treatment and has a low expected cure rate during lactation.[249] While the impact of *S. aureus* infection is difficult to quantify, clinical mastitis caused by Gram-positive pathogens is reported to cost between $133 and $444 per case, or as much as USD 2 billion annually.[250,251] These costs include many factors such as milk loss, veterinary expenses, diagnostic testing, and loss of animals. Prevention of *S. aureus* mastitis with a cost-effective vaccine would improve animal welfare, reduce antibiotic use, and positively impact the economics and efficiency of milk production.

Previous approaches to *S. aureus* vaccination in cattle include whole-cell live and killed vaccines as well as purified antigens. Currently, two whole-cell inactivated vaccines are licensed for protection against *S. aureus* mastitis—Lysigin® (Boehringer Ingelheim, Duluth, GA, USA) and Startvac® (Hipra, Girona, Spain). While efficacy

studies are somewhat conflicting, these vaccines have reported moderate decreases in the incidence of new *S. aureus* intramammary infection but are not in widespread use.[252–257] Recent studies have focused on the use of multiple purified surface adhesins and secreted virulence factors to develop a vaccine that offers more strain-to-strain cross-protection. Iron-regulated surface determinant A (IsdA) is a fibrinogen- and fibronectin-binding adhesin that contributes to iron sequestration and is a well-studied *S. aureus* vaccine candidate.[258–261] The presence of *isdA* is conserved among bovine *S. aureus*, and IsdA is expressed from these strains in milk.[260,262–265] The clumping factor A (ClfA) fibrinogen adhesin is also highly conserved, expressed from bovine clinical isolates, and a recognized vaccine candidate against mastitis.[266–272] The conservation, surface exposure, and importance in multiple mechanisms of pathogenesis supports the inclusion of the IsdA and ClfA antigens in a multivalent bovine vaccine. However, a number of additional antigens have been characterized and may be necessary to protect against multiple *S. aureus* serotypes.

While immune correlates of protection are not known, an understanding of immune responses is needed to inform antigen selection. The induction of both humoral and cellular immunity is essential to combating intracellular *S. aureus* infection.[273–275] Cellular subpopulations that play a central role in defense against *S. aureus* include neutrophils, CD8+ T lymphocytes, and CD4+ Th17 lymphocytes.[276,277] Cholera toxin (CT), produced by the bacterium *Vibrio cholerae*, and the homologous heat-labile toxin I (LTI), produced by the bacterium *Escherichia coli*, are gold standard vaccine adjuvants that can stimulate systemic immunity from mucosal and dermal sites (previously reviewed [278]). The mechanism of adjuvanticity of these toxins depends upon active

binding subunit targeting of dendritic cells and neutrophils, and has been attributed to enhanced antigen presentation, upregulation of surface molecules, and promotion of B-cell isotype switching to antigen-specific immunoglobulin A (IgA) and immunoglobulin G (IgG).[279–283] CT and its non-toxic binding subunit (CTB) can also induce Th1, Th2, and Th17 responses.[2,284,285]

The toxic active subunit of CT (CTA) is subdivided into an enzymatically active domain (CTA$_1$) and a linker domain (CTA$_2$), which is non-covalently associated with the B subunit. CTA$_2$/B chimeras were first described as a mechanism to make stable human vaccine with antigens coupled to the CTB subunit via the A$_2$ linker domain.[286,287] These non-toxic molecules retain the adjuvanticity of CTB and possess additional advantages including ease of purification, direct association of antigen to adjuvant, and a holotoxin-like structure that retains binding and internalization motifs.[288,289] As reported previously, we have incorporated *S. aureus* IsdA and ClfA into a CTA$_2$/B vaccine platform (IsdA + ClfA CTA$_2$/B). After two intranasal doses this vaccine was found to stimulate significant *S. aureus* antigen-specific humoral and cellular immunity in bovine blood and milk.[290]

For this study we hypothesized that intranasal IsdA + ClfA-CTA$_2$/B would be effective in reducing or eliminating *S. aureus* shedding and disease after intramammary challenge in cattle. We describe a preliminary trial to determine the efficacy of this mucosal enterotoxin-based vaccine to protect against acute *S. aureus* mastitis. While the vaccine did not prevent bacterial shedding after challenge, results indicate that IsdA + ClfA-CTA$_2$/B induces antigen-specific immune responses that may contribute to a reduction in clinical severity and infiltration of leukocytes, or somatic cell count (SCC), in infected animals.

Materials and Methods

<u>Bacterial Strains, Plasmids, and Growth Conditions</u>

S. aureus Newbould 305 was used for the cloning of *isdA* and *clfA* to construct

IsdA + ClfA-CTA2/B and was also used for bacterial challenge.[264,291] *E. coli* ClearColi®

(Lucigen, Madison, WI, USA) was used for protein expression (Table 4.1). The vector

pARLDR19 expressing CTA$_2$/B and containing a multiple cloning site was used to

construct the plasmids pLR001 for IsdA-CTA$_2$/B expression and pLR003 for ClfA-

CTA$_2$/B expression (Figure 4.1A) as described previously.[292] For bacterial challenge, *S.*

aureus Newbould 305 was prepared as described.[252] Briefly, Newbould 305 was grown at

37 °C with shaking to mid-log phase in brain–heart infusion and harvested by

centrifugation at $3000 \times g$ for 15 minutes at 4 °C. The cell pellet was washed with

phosphate-buffered saline (1X PBS, pH 7.2) and adjusted to an optical density (O.D.) of

0.2 at 600 nm. Serial dilutions were performed in 1X PBS to reach a bacterial

concentration of 400 CFU/mL, as determined by plating on blood agar (BA).
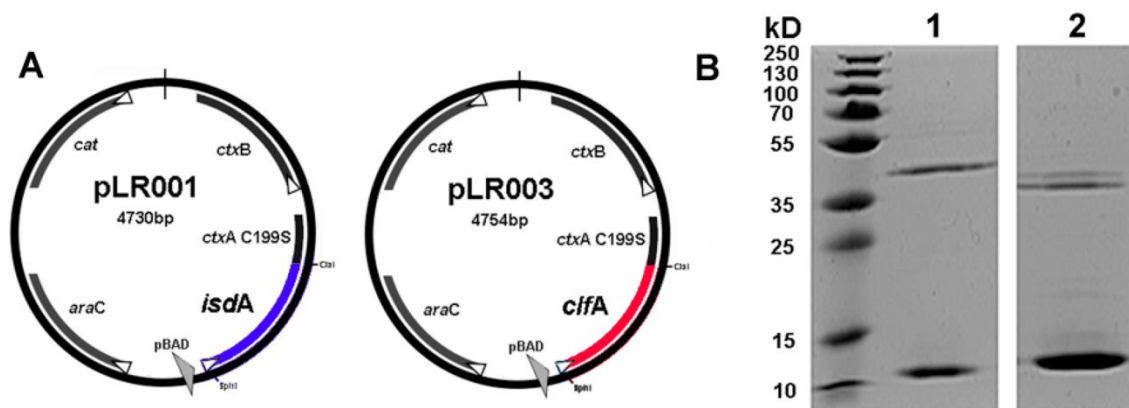
Figure 5.1. *S. aureus* **cholera toxin A$_2$/B (CTA$_2$/B) chimeric mucosal vaccines**

(A) pLR001 for expression of IsdA-CTA$_2$/B, and pLR003 for expression of ClfA-CTA$_2$/B, and (B) SDS-PAGE of purified IsdA-CTA$_2$/B (1, IsdA-CTA$_2$~38 kDa, CTB~11 kDa) and ClfA-CTA$_2$/B (2, ClfA-CTA$_2$~37 kDa, CTB~11 kDa).

Table 5.1.   **Bacterial strains, plasmids, and primers used in vaccine trial study**

Bacterial Strains	Genotype/Characteristics		Source
E. coli ClearColi®	BL21(DE3)		Lucigen, Madison, WI
S. aureus Newbould 305	Bovine clinical isolate		[291]

Plasmids	Gene	Vector	Source
pLR001	*isdA* (Newbould)	pARLDR19	[290]
pLR003	*clfA* (Newbould)	pARLDR19	[290]

Bovine Cytokine qPCR Primers	Gene	Amplicon (bp)	Source
FW 5′-GCATCGTGGAGGGACTTATGA-3′ RV 5′-GGGCCATCCACAGTCTTCTG-3′	GAPDH	67	[293]
FW 5′-CTTGTCGGAAATGATCCAGTTTT-3′ RV 5′-TCAGGCCCGTGGTTCTCA-3′	IL-10	66	[294]
FW 5′-CAGAAAGCGGAAGAGAAGTCAGA-3′ RV 5′-TGCAGGCAGGAGGACCAT-3′	IFN-γ	72	[293]
FW 5′-GGCTCCCATGATTGTGGTAGTT-3′ RV 5′-GCCCAGTGGACAGGTTTCTG-3′	IL-6	64	[294]

<u>Protein Expression and Purification</u>

Chimeras were purified as previously described.[290,292] Briefly, to express IsdA-CTA$_2$/B and ClfA-CTA$_2$/B, ClearColi® with pLR001 or pLR003 were grown at 37 °C to an O.D. of 0.9 at 600 nm and induced for 24 hours with 0.2% L-arabinose. Proteins were isolated from the periplasmic extract with 1 mg/mL polymyxin B and purified by affinity chromatography on immobilized D-galactose (Pierce™ D-Galactose Agarose, Thermo Fisher, Waltham, MA, USA). Vaccine proteins were dialyzed into sterile 5% glycerol + 1X PBS and concentrations were determined by bicinchoninic acid assay (BCA) (Pierce™ BCA, Thermo Fisher, Waltham, MA, USA). Sizes and purities of the vaccine chimeras were confirmed by sodium dodecyl sulphate-polyacrylamide gel electrophoresis (SDS-PAGE) prior to mixing at a final protein concentration of 600 µg/5 mL for vaccination (Figure 4.1B). Vaccines were tested to ensure endotoxin levels were below

0.05 EU/mL (LAL Endpoint Chromogenic, Lonza, Allendale, NJ, USA), plated for

sterility on tryptic soy agar, and stored at −80 °C until use.

Animals, Vaccination, Challenge, and Clinical Assessment

All animal protocols were pre-approved by the University of Idaho Animal Care

and Use Committee. Lactating healthy Holstein cows in the third or fourth lactation were

pre-screened for inclusion as being those with two consecutive SCC readings below 200

$\times 10^3$ cells/mL and no clinical evidence of mastitis. Further enrollment criteria were

followed as described previously[290] and included: (1) no growth of *S. aureus* culture from

milk as determined by plating on mannitol salt agar (MSA) and PCR with *S. aureus nuc*

and *isdA* primers, (2) low baseline anti-IsdA responses as determined by enzyme-linked

immunosorbent assay (ELISA) of milk and serum, and (3) no evidence of bovine

leukemia virus infection (Washington Animal Disease Diagnostic Lab, WADDL,

Pullman, WA, USA). Seven selected cows were ultimately randomized into vaccinated

and control groups. Figure 4.2 shows the summary of trial design. Four vaccinated

animals received a 600 µg intranasal dose of IsdA + ClfA-CTA$_2$/B in 1X PBS + 5%

glycerol on days 1 and 14 (orange arrows, blue bar), and a control group of three animals

of similar age and lactation period received vehicle control (1X PBS + 5% glycerol)

mock vaccination on days 1 and 14 (orange arrows, grey bar). The vaccine was delivered

in 2.5 mL volumes into each nare using a nasal cannula (Merck & Co., Kenilworth, NJ,

USA). On day 20, all animals were challenged in two quarters with 400 CFU in 1 mL of

S. aureus Newbould 305 (yellow arrow). Quarters were identified as left front (LF), left

rear (LR), right front (RF), and right rear (RR). The bacterial challenge was inoculated

into two diagonal quarters of each vaccinated cow using teat cannulae (Valley Vet

Supply, Marysville, KS, USA). Animals were monitored closely during the challenge

period (days 20 to 30) and evaluated for the presence of clinical mastitis by assessment of

rectal temperature (Figure 4.3), milk quality (Figure 4.S2), and udder consistency

(examination for edema, hardening, and/or swelling, Table 4.S1) on days of milk

sampling during the trial (Figure 4.2).[295,296] Enrolled animals that developed pain and/or

fever that exceeded 103 °F were administered painkillers (Banamine® and aspirin) as

recommended by the attending veterinarian. Shortly after challenge (day 21), one

vaccinated animal developed a severe *Escherichia coli* mastitis case in an unchallenged

quarter (2779 LF) with systemic illness including septicemia. Thereafter, the other three

quarters were involved, and the animal developed clinical mastitis due to *Staphylococcus*

aureus. The animal was euthanized on day 5 post-challenge. Results from this animal are

not included in the data in this report and resulting sample size was n = 3 per group, as

represented in Figure 4.2. On day 30 all other animals began treatment with Spectramast

(Zoetis, Parsippany, NJ, USA) until consecutive negative cultures were indicative of safe

release to herd as determined by the attending veterinarian.
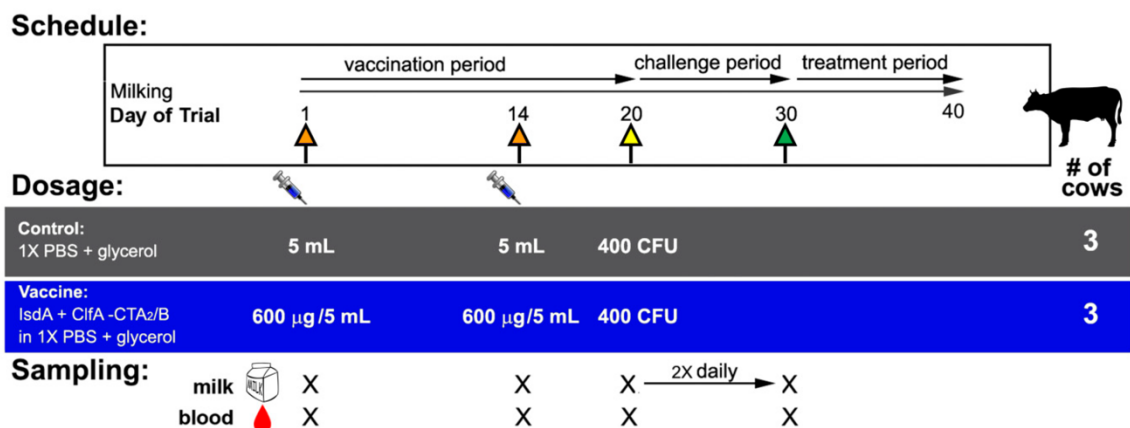
Figure 5.2.   Vaccine trial design summary

Animals (n = 3 per group, #) were vaccinated intranasally on day 1 and boosted on day 14 with 5 mL of either phosphate-buffered saline (PBS) + 5% glycerol vehicle control or 600 μg IsdA + ClfA-CTA2/B vaccine (orange arrows). On day 20 animals were challenged once with 400 colony-forming units (CFU) of S. aureus Newbould 305 in two quarters (yellow arrow) and on day 30, animals were treated (end of challenge period, green arrow). Samples of blood were taken on days 1, 14, 20, and 30 (X). Samples of milk were taken on days 1 and 14 (X), and every day for ten days over the challenge period (days 20–30, X→X).

Sample Collection and Milk Culture

Blood and milk were sampled on day −2 for screening and then on days 1, 14, 20, and 30, and milk was sampled twice daily during the challenge period (Figure 4.2). Blood was collected from the tail vein and allowed to coagulate at room temperature (RT) for 1 hour prior to centrifugation and resuspension into 1:10 inhibitor solution (IS, 1X HALT™ protease inhibitor and 5% glycerol in 1X PBS). On day 20, whole blood was also collected in vacutainer tubes for peripheral blood mononuclear cell (PBMC) isolation (Becton Dickinson, Franklin Lakes, NJ, USA). Milk was collected aseptically as 50 mL quarter samples after washing teat ends with 70% ethanol and was aliquoted into three equal tubes for culture, SCC, and ELISA. For SCC, milk was fixed prior to shipping and analysis was performed using the California Mastitis Test (WADDL, Pullman, WA, USA). For ELISA, milk was centrifuged at $700 \times g$ for 20 minutes at 4 °C to remove fat. Skim milk was collected and centrifuged at $20,000 \times g$ for 30 minutes at 4 °C. Whey was collected and stored in 1:10 IS. Equal volumes of diluted whey from each

quarter were pooled and stored at −20 °C prior to analysis. For milk culture, 100 µL and 10 µL of tenfold serially diluted quarter milk was plated on MSA, BA, and MP2 agar (Udder Health Systems, Inc., Meridian, ID, USA) to determine the number of colony-forming units per mL (CFU/mL). The presence of larger yellow colonies with yellow zones on MSA, beta-hemolysis on BA, or small, white, esculin-negative colonies on MP2 was considered presumptive *S. aureus*. These colonies were isolated and confirmed by a positive coagulase test or a PCR test using *nuc* or *isdA* primers.[264] CFU by quarter data, based upon final quantitation on MSA, was determined once daily on days −2, 1, 14, and 20 prior to challenge and twice daily (AM/PM) during the challenge period. Quarter data were combined and total CFU/mL by cow was reported for six animals (n = 3 per group).

IgG, IgG1, IgG2, and IgA Enzyme-Linked Immunosorbent Assay (ELISA)

IsdA- and ClfA-specific immune responses in serum and milk were detected using ELISA as described.[292] Briefly, 96-well microtiter plates (Nunc, Thermo Fisher, Waltham, MA, USA) were coated with 10 µg of either IsdA-CTA$_2$/B, ClfA-CTA$_2$/B, or CTA$_2$/B in 1X PBS and incubated overnight at 4 °C. Coated plates were blocked for 2 hours at 37 °C in 1% goat milk + 1X PBS. After washing, plates were incubated with two-fold dilutions of either bovine serum (dilutions initiated at 1:200 concentration) or pooled quarter milk (dilutions initiated at a 1:10 concentration). Plates were incubated at 4 °C overnight. After washing, plates were incubated with horseradish peroxidase (HRP)-conjugated anti-bovine IgG, IgG1, IgG2, or IgA (1:10,000 Bethyl Laboratories, Montgomery, TX, USA) at 37 °C for 1 hour. Plates were developed with tetramethylbenzidine (PromegaTM TMB One, Thermo Fisher, Waltham, MA, USA) and read at 370 nm per TMB manufacturer's instruction. ELISA results from serum or pooled

quarter milk were reported by cow (n = 3) and presented as the ratio of results (day X/day 1) of the O.D. (370 nm) from a representative antibody dilution in the linear part of the curve (1:1600 serum, 1:160 milk). Results are the average of three independent assays.

Peripheral Blood Mononuclear Cell (PBMC) Isolation and Cytokine qRT-PCR

PBMCs were isolated from whole bovine blood on day 20 for cytokine analysis. PBMCs were isolated using a density gradient established by layering whole blood diluted 1:2 with 1X PBS on Histopaque®-1077 (Sigma-Aldrich, St. Louis, MO, USA). Blood samples were centrifuged at $800 \times g$ for 30 minutes at RT. The buffy coat was removed and washed three times by centrifugation with Hank's Balanced Salt Solution for 10 minutes at $400 \times g$ at RT, and cells were counted with 0.2% trypan blue. For cytokine assays, total RNA from PBMCs from each cow (n = 3 per group) was extracted (RNeasy, Qiagen, Germantown, MD, USA) with an additional Dnase I (Promega, Madison, WI, USA) digestion. cDNA was reverse transcribed per manufacturer's instructions (High-Capacity RNA-to-cDNA™ Kit, Thermo Fisher, Waltham, MA, USA). qRT-PCR was conducted using SYBR fast (Kapa Biosystems, Thermo Fisher, Waltham, MA, USA) on interferon gamma (IFN-γ), interleukin-6 (IL-6), and interleukin-10 (IL-10) primers, using bovine glyceraldehyde 3-phosphate dehydrogenase (GAPDH) as a reference gene (primers, Table 4.1). Results are presented as relative gene expression $2^{-\Delta\Delta Ct}$.[297] All qRT-PCR experiments were performed in triplicate per cow PBMC sample.

Sample Size, Statistical Methods, and Analysis

Sample size was estimated prior to study by power analysis based upon predicted SCC and CFU/mL in milk and using the assumption that quarters are independent, as has been reported.[298,299] A sample size of 13 quarters per group was predicted to provide, at a

95% level of confidence, 80% power to detect a difference in logged SCC. Resulting quarter bacterial counts and SCC data from this study were analyzed by (1) assuming independent quarters and (2) as the combined average of quarters by cow. Outcomes were not different, thus results are reported as the average by cow and assuming quarters are not independent. The log-base 10 values of CFU, SCC, temperature, and serum and milk anti-IsdA, ClfA, and CTB antibodies were analyzed using repeated measures analysis of variance (ANOVA) with time as the within-subjects variable and group as the between-subjects variable. Within-subjects correlation was modeled with either first-order autoregressive or compound symmetric structure, depending on Akaike's Information Criterion.[300] Comparisons of interest were identified prior to modeling and were examined regardless of the significance of main effects or interaction. First, we explicitly compared the outcome at each study time point. Second, we examined the change in outcome within group, comparing days and adjusting the paired comparisons using false discovery rate.[301] Cytokine analysis was performed using a two-group t-test between vaccinated and control animals. Statistical analyses were conducted using JMP and SAS software (Cary, NC). *p*-values are reported as $p \leq 0.05(*)$, $p \leq 0.01(**)$, or $p \leq 0.0001(****)$ and reflect two-sided tests.

Results

Bacterial Culture and Clinical Assessment

Quantification of *S. aureus* was determined after plating milk that had been

sampled once daily on days −2, 1, 14, and 20 prior to challenge and twice daily during

the challenge period (Figure 4.2). Prior to challenge no animals were found to be

shedding *S. aureus*, and immediately after challenge all animals shed high levels of *S.*

aureus from infected quarters (Figure 4.3A). Results revealed a rapid decline in bacterial

shedding from all animals within 24 hours and then a slow decline beginning in the

middle of the challenge period. Between days 2 and 10 of the challenge period (days 22

and 30 of trial) control animals shed a total of 1.08×10^6 CFU/mL and vaccinated

animals shed 7.53×10^5 CFU/mL. Differences between treatment groups were observed

on days 21, 29, and 30 during the challenge period ($p = 0.029$, 0.011, and 0.018,

respectively), however, after adjusting for multiple comparisons, these results are not

significant. *S. aureus* was isolated from all challenged quarters in both treatment groups,

and all animals continued to shed *S. aureus* throughout the trial. Animals did not shed

from uninfected quarters. While one vaccinated animal was culture negative at two time

points late in the challenge period (day 29 AM and day 30 AM), no animals were

consistently sterile of *S. aureus* by the end of the challenge period. Analysis of positive

quarters indicated that there were more days showing a lower percentage of infected

quarters for vaccinated animals (Supplementary Figure 4.S1)
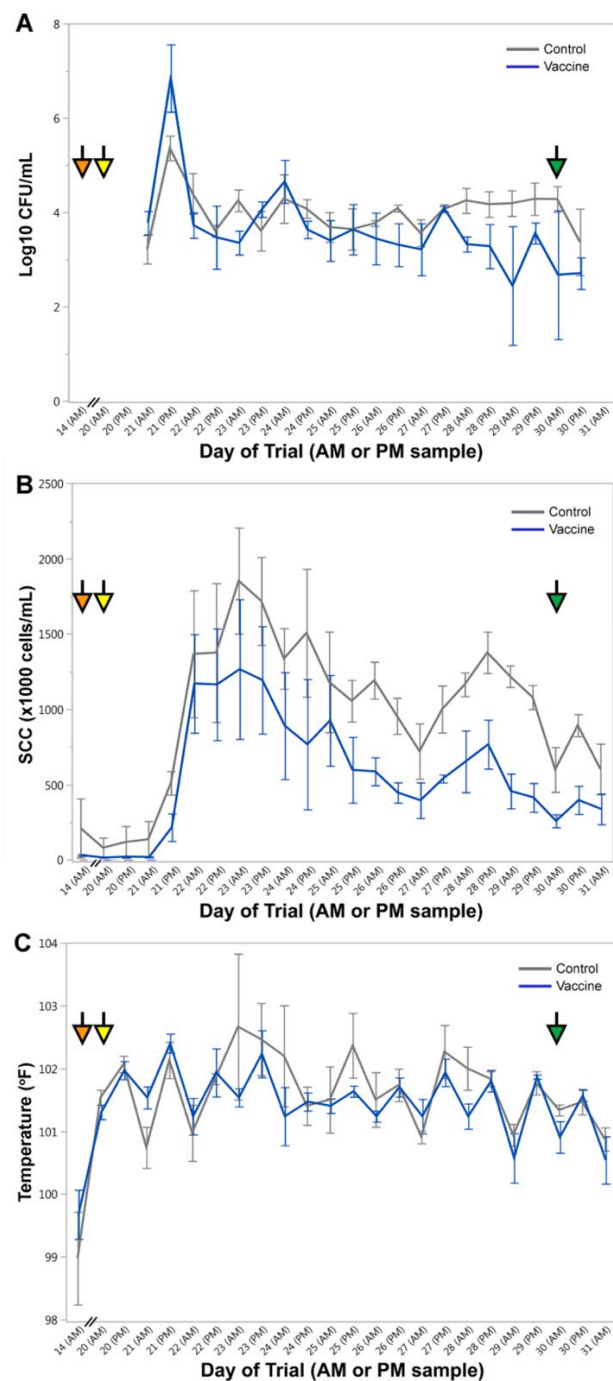
Figure 5.3.   Vaccination outcomes during the trial period

(A) Quantification of bacterial shedding by cows during the challenge period. Log10 of CFU/mL of Staphylococcus aureus on mannitol salt agar (MSA). Mean ± standard error, n = 3 per group, and analyzed using repeated measures analysis of variance (ANOVA). No significance after false discovery rate adjustment for multiple comparisons. (B) Somatic cell count (SCC) (×1000 cells/mL) by cow. Mean ± standard error, n = 3 per group, and analyzed using repeated measures ANOVA. During the challenge period, control cows uniformly had higher SCC than vaccinated cows (main model effect p = 0.002). (C) Rectal temperature in degrees Fahrenheit (°F). Mean ± standard error, n = 3 per group, and analyzed using repeated measures ANOVA showing no significance between groups. Orange arrows indicate day of booster vaccination (14), yellow arrows indicate day of bacterial challenge (20) and green arrows indicates the last day of challenge (30).

SCC taken once daily before the challenge period and twice daily during challenge is shown in Figure 4.3B. Results show a consistently reduced SCC from vaccinated animals beginning 48 hours post-challenge (day 22). While individual days were not significant after adjustment, across and after the challenge period (days 21 to 39) unvaccinated animals had significantly higher SCC than vaccinated animals (model main effect of treatment group, $p = 0.002$). SCCs of individual cows throughout the trial are shown in Supplementary Figure 4.S3B.

The average rectal temperature per group during the challenge period is shown in Figure 4.3C. Temperatures at 72 hours post-challenge (day 23 AM) showed an average of 102.7 °F for control and 101.5 °F for vaccinated animals, however there was no statistically significant difference in temperature between groups on any day during this period. In addition, no differences in temperature between groups occurred within 24 hours after vaccination (days 1 and 14).

Clinical assessments indicated that animals did not show signs of systemic illness, loss of appetite, or adverse local reactions due to the vaccine, and no animals had clinical evidence of mastitis prior to challenge (day 20). Clinical results are summarized in Supplementary Table 4.S1. Clinical mastitis due to *S. aureus* was observed in challenged quarters of control cows 2767 (LF and RF) and 2830 (LR) throughout the evaluation period. The latter cow developed a persistent mastitis starting on day 23 with apparent milk changes that included clots and flakes in the LR quarter. Clinical mastitis in this animal included persistent udder swelling in addition to pain, heat, and sensation of the affected teat until the end of the challenge period. Temporary enlargement of the

supramammary lymph node was noted in one of the vaccinated cows (2823) on day 24, and persistent enlargement observed in one control animal (2830).

Milk quality assessments indicated that while the fat, protein, lactose, and solids-not-fat (SNF) percentages were frequently higher in vaccinated animals, these differences were not statistically significant (Supplementary Figure 4.S2).

Vaccine-Specific Antibody Responses in Blood and Milk

Antigen-specific humoral responses were quantified by ELISA from blood and milk. Anti-IgG responses in serum on days 14, 20 and 30, relative to day 1, are shown in Figure 4.4A–C and E. Vaccinated animals (blue bars) showed a significant IsdA-CTA_2/B-specific IgG response in serum after challenge on day 30 relative to days 14 and 20 (p_{adj} = 0.008 for both) and on day 30 relative to control animals (p = 0.030 *) (Figure 4.4A). Vaccinated animals showed a similar, but non-significant, anti-ClfA-CTA_2/B-specific IgG responses in serum on day 30 relative to days 14 and 20 (p_{adj} = 0.120) as well as on day 30 relative to control animals (p = 0.079) (Figure 4.4C). Anti-CTA_2/B-specific IgG responses in serum remained low and non-significant between groups throughout and after challenge (day 30) (Figure 4.4E).
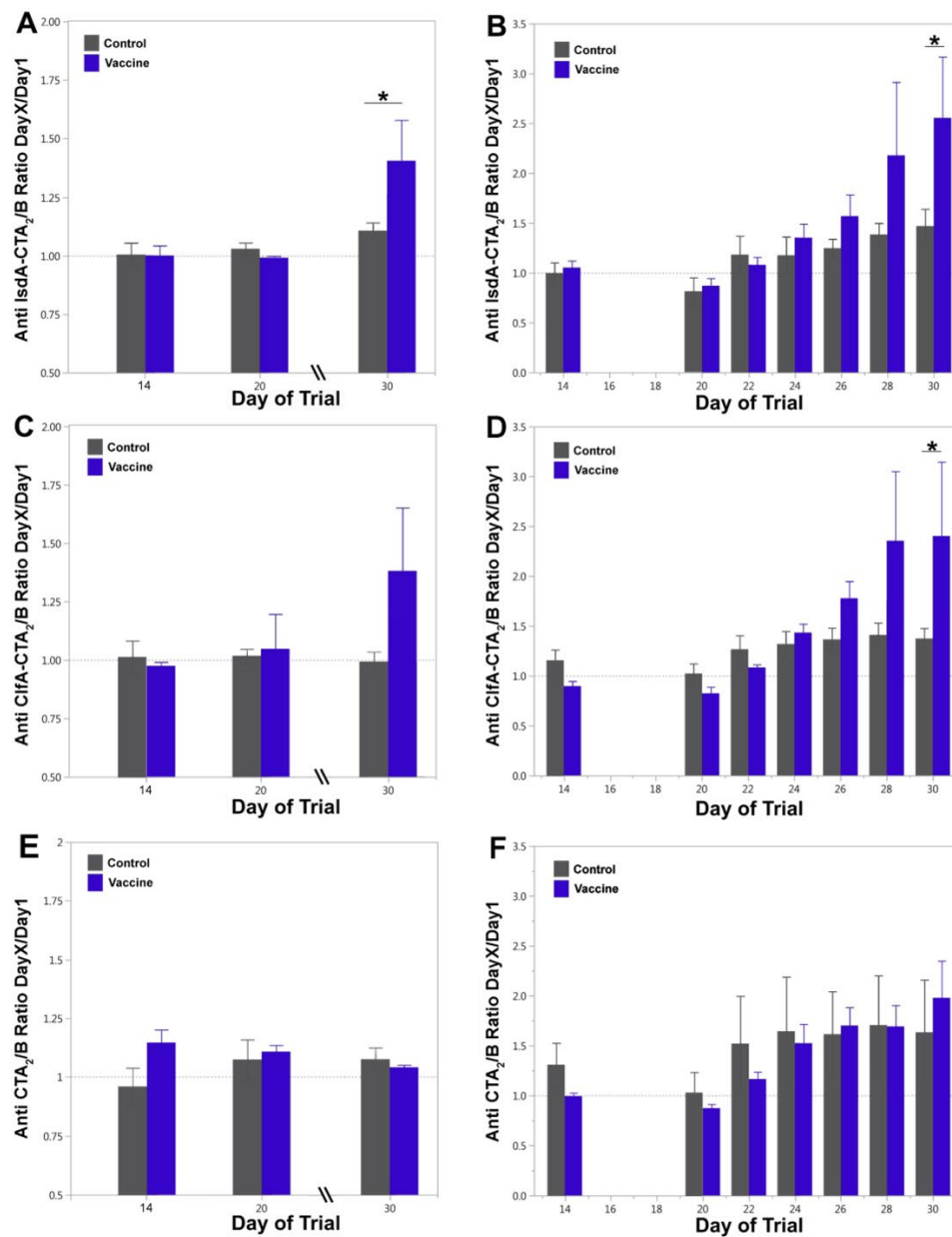
Figure 5.4.   Immunoglobulin G (IgG) antibody responses in serum and milk as determined by enzyme-linked immunosorbent assay (ELISA)

Anti-IsdA-CTA2/B IgG responses in (A) serum and (B) milk, anti-ClfA-CTA2/B IgG responses in (C) serum and (D) milk, and anti-CTA2/B IgG responses in (E) serum and (F) milk. Serum was analyzed on days 14, 20, and 30 and milk on days 14, 20, 22, 24, 26, 28, and 30 during the trial period. Results are reported as ELISA ratios of day X/day 1 at O.D. 370 at serum dilutions of 1:1600 and milk dilutions of 1:160. Shown are mean and standard error by treatment with control (gray) and vaccinated (blue) (n = 3 per group). Significant differences between groups are represented as $p \leq 0.05$ (*). The log10 of the values were analyzed using repeated measures analysis of variance (ANOVA) with a compound symmetric covariance structure for cows across days. Model-based estimates were compared between groups within days and adjusted for multiple comparisons.

Anti-IgG responses in milk on days 14, 22, 24, 26, 28, and 30, relative to day 1, are shown in Figure 4.4B,D–F. IsdA-CTA$_2$/B-specific IgG responses in milk increased over the challenge period in vaccinated animals, with values significantly higher on day 30 relative to days 20 to 26 (adjusted p-values all <0.05) and on day 30 relative to control cows (p = 0.030 *) (Figure 4.4B). The anti-IsdA-CTA$_2$/B differences between days for control cows were non-significant after day 20. Anti-ClfA-CTA$_2$/B-specific IgG responses in milk were significant on day 30 relative to days 20–24 (adjusted p-values all <0.05) for the vaccinated group and on day 30 relative to unvaccinated cows (p = 0.043 *) (Figure 4.4D). Milk anti-CTA$_2$/B-specific IgG responses increased moderately during the challenge period in both vaccinated and control animals with significant increases on day 30 relative to days 14 and 20 in the vaccinated group and no change in the control group (adjusted p-values all <0.05). The differences in anti-CTA$_2$B responses between vaccine and control groups were non-significant on all days tested (Figure 4.4F).

Serum IgG subtype (IgG1 and IgG2) responses were evaluated to further define the T helper immune response (Figure 4.5A–D). Vaccinated animals exhibited increases in IgG1 and IgG2 responses on day 30 for both the IsdA- and ClfA-CTA$_2$/B antigens. The serum anti-IsdA-CTA$_2$/B IgG1 response on day 30 relative to days 14 and 20 was significant for vaccinated animals (blue bars, p_{adj} = 0.004 and p_{adj} = 0.007, respectively), and the difference between groups was significant on day 30 (p = 0.033 *) (Figure 4.5A). For anti-IsdA-CTA$_2$/B IgG2 responses, day 30 was higher than days 14 and 20 for both vaccinated and control groups (p_{adj} = 0.045 for both comparisons) with no significant differences between groups on day 30 (Figure 4.5B). For serum anti-ClfA-CTA$_2$/B IgG1, vaccinated animals showed an increase on day 30 compared to day 14 (p_{adj} = 0.023) and

day 20 (p_{adj} = 0.029), and the difference between groups was significant on day 30 (p = 0.029 *) (Figure 4.5C). For anti-ClfA-CTA$_2$/B IgG2 responses, day 30 was higher than days 14 and 20 for both groups as well (p_{adj} = 0.015 for both comparisons), however the difference between vaccinated and control groups on day 30 was non-significant after adjustment (p = 0.050) (Figure 4.5D). Assessment of milk anti-IsdA-CTA$_2$/B and anti-ClfA-CTA$_2$/B IgG1, IgG2 and IgA responses was also performed, and while results indicated an increase on day 30 for both IgG1 and IgA, they were non-significant between vaccine and control groups on the days (14, 20, and 30) tested (data not shown).

Combined, ELISA analysis shows an induction of antigen-specific humoral responses in the milk and serum after intranasal IsdA + ClfA-CTA$_2$/B vaccination, as evidenced by a significant booster effect upon bacterial challenge. Antibody subtyping indicated that both antigens stimulated a Th2-type response, with ClfA potentially inducing a mixed Th1/Th2 response. Lastly, there was no significant antibody response to the CTA$_2$/B adjuvant vector alone.

Cytokine Assay

The stimulation of cellular cytokine responses was assessed by quantitative RT-PCR using PBMCs isolated from vaccinated and control cows on day 20 (Figure 4.5E). interleukin-12 (IL-12), tumor necrosis factor alpha (TNF-α), and interleukin-4 (IL-4) levels were not significantly different between vaccinated and control animals (data not shown). Vaccinated cows showed a slight but significant increase in IFN-γ expression (p = 0.048 *) but no significant difference in IL-10 or IL-6 expression (Figure 4.5E).

180
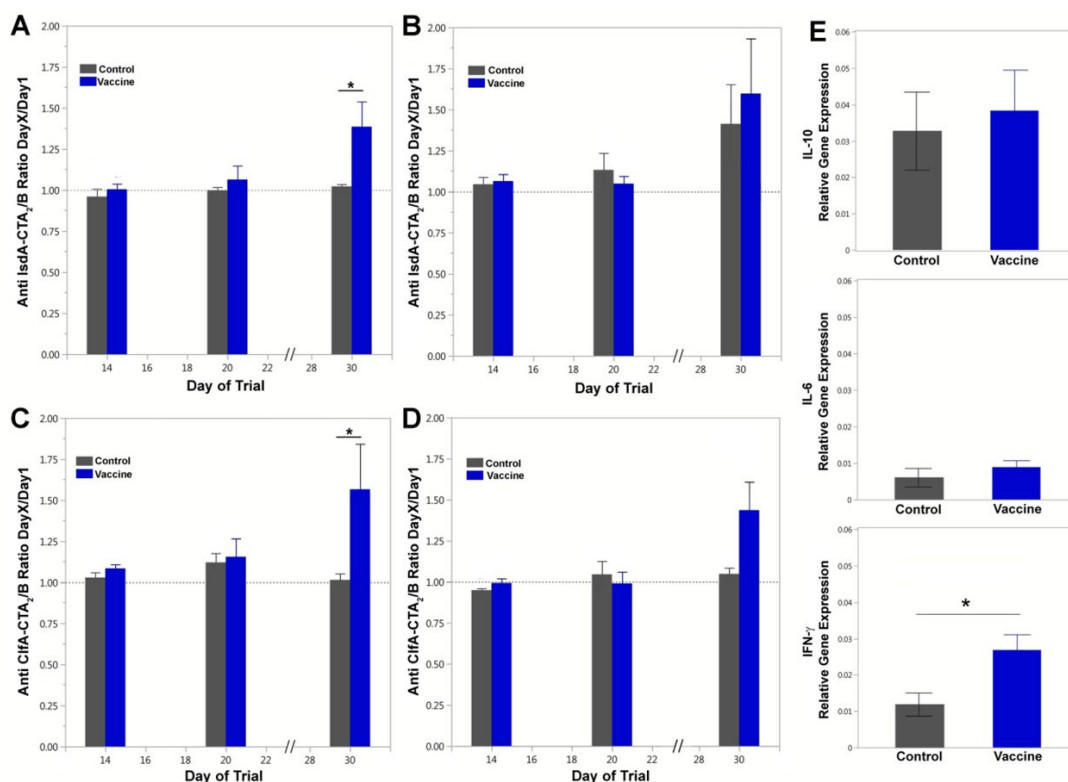
Figure 5.5.   Serum IgG1, IgG2, and cytokine expression analysis

(A) Anti-IsdA-CTA₂/B IgG1, *(B)* anti-IsdA-CTA2/B IgG2, *(C)* anti-ClfA-CTA2/B IgG1, and *(D)* anti-ClfA-CTA2/B IgG2 responses in serum on days 14, 20, and 30. Results are reported as ELISA ratios of day X/day 1 at O.D. 370 at serum dilutions of 1:1600. Shown are mean and standard error by treatment with control (gray) and vaccinated (blue) (n = 3 per group). The log10 of the values were analyzed using analysis of variance (ANOVA), with a compound symmetric covariance structure for cows across days. Model-based estimates were compared between groups within days and adjusted for multiple comparisons. *(E)* IL-10, IL-6, and IFN-γ expression as determined by quantitative RT-PCR of peripheral blood mononuclear cells (PBMCs) isolated from whole blood after boost on day 20. Results are shown as relative gene expression to GAPDH ($2^{-\Delta\Delta Ct}$). Data are presented as mean and standard error of control (gray) and vaccinated (blue) showing median and range (n = 3 per group). Data were analyzed using a two-group t-test between vaccinated and control. Significant differences between groups are represented as $p \leq 0.05$ (*).

Discussion

This report describes the outcomes of a small bovine challenge trial to assess the efficacy of the IsdA + ClfA-CTA$_2$/B mucosal *S. aureus* mastitis vaccine. We hypothesized that vaccination would prevent or reduce bacterial shedding from the udder after intramammary challenge and reduce disease outcomes. Animals were vaccinated intranasally during milking and challenged in two quarters with the homologous *S. aureus* Newbould 305 vaccine strain. An averaged reduction in CFU/mL from combined quarters of vaccinated compared to unvaccinated animals was observed beginning 24 hours after challenge to the end of the challenge period, however, this difference was not significant on specific days during the challenge period. Analysis of bacteriology using independent quarters did not change data interpretations, however, a lower percentage of infected quarters was observed on multiple days after challenge. Analysis of SCC revealed that vaccinated animals had lower numbers of cells on the majority of days during the challenge period of the trial, and this decrease was significant between vaccinated and control animals during the whole of the period. These results were also consistent with the evidence of reduced clinical mastitis in vaccinated animals.

The assessment of humoral immune responses in milk and serum in this report showed induction of IsdA- and ClfA-CTA$_2$/B specific IgG antibodies in vaccinated animals after *S. aureus* challenge indicating that vaccination induced antigen-specific responses that were amplified by bacterial challenge. In contrast to previous studies, no significant increase in antigen-specific humoral responses was detected in the serum directly after vaccination and boost, despite the same vaccine dose and schedule.[290] The lower sample size in this trial compared to previous trials with IsdA + ClfA-CTA$_2$/B may

have contributed to this outcome, and larger trials will be essential to advance this vaccine candidate. In addition, animals were vaccinated during milking for this study instead of during dry-off, which is a period of higher susceptibility to mastitis and changes in immune function that may explain observed differences in immunogenicity. As with previous trials, antibody analysis revealed that not all vaccinated animals responded well to the same vaccine preparation and dosage. Variations in host genetics or inconsistencies in administration can cause these disparities, and larger trials will help to exclude them. Other vaccination routes, or alternate prime-boost strategies, may also promote vaccination consistency and efficacy. These routes were not explored in this early study to enable a narrow focus on mucosal delivery, but intramuscular, subcutaneous, and transdermal routes are all effective for CT-adjuvanted vaccines and could be explored. Lastly, in this study we maintained a short dosage interval of only 14 days to align with previous trials, however, a longer interval between doses may improve responses and will be explored in the future.

Animals were vaccinated during milking to permit bacterial quantification and limit the potential for systemic or chronic infection. Despite this, one vaccinated animal was euthanized shortly after challenge due to an *E. coli* infection that rapidly became systemic. While little has been reported about the effects of co-infection on the severity of *E. coli* mastitis, the cow immune status is a key factor, and *S. aureus* is known for the production of virulence factors that modulate the immune response.[302] Specifically the *S. aureus* superantigens (SAgs) can activate specific T-cell subsets, resulting in inflammation, tissue damage, and potential T-cell anergy.[303–305] *S. aureus* Newbould 305 strain was chosen for these studies because it induces mild and chronic mastitis, has been

utilized before in vaccine challenge trials, and contains a limited repertoire of SAgs.[291,306,307] It is recognized, however, that immune dysregulation likely occurred upon challenge and, despite vaccination, contributed to the enhanced spread and systemic infection in this animal. The potential for co-infection and the ability of the vaccine to protect against heterologous *S. aureus* isolates that may induce more severe disease will both need to be addressed in future studies.

As described above, CT and its non-toxic B subunit can induce humoral and cellular immune responses to co-delivered antigens. CTA_2/B molecules retain much of the well-characterized adjuvanticity of CTB to induce both humoral and cellular responses. The IgG1 and IgG2 profiles we observed in the serum of vaccinated animals on day 30 were consistent with our previous studies indicating that CTA_2/B chimeras promote a largely Th2-type cellular response.[290,292] In the current study, however, the responses to IsdA were more clearly polarized toward Th2, while the anti-ClfA responses are supportive of a potential mixed Th1/Th2 response. Cytokine expression analysis in the current study, performed on day 20 prior to challenge, showed no effect on IL-10 and IL-6, but an increase in IFN-γ in vaccinated animals. Cytokine analysis from previous immunogenicity studies using the IsdA + ClfA-CTA_2/B vaccine largely supported a Th2-type response and did not indicate IFN-γ upregulation.[290,292] This apparent contradiction may be due to differences in the timing of analysis (6 days after vaccination in the current study versus 45 days after vaccination in previous studies) and the methods used (unstimulated versus stimulated PBMCs). Reports indicate that while CTB more commonly induces Th2-type responses, it can induce a mixed Th2/Th1 response with enhanced IFN-γ secretion, depending upon the antigen and route of delivery.[2,308–312]

Similar to CTB, vaccination with CTA$_2$/B chimeras may promote early macrophage or dendritic cell activation and antigen presentation through IFN-γ upregulation. In this study there was not a clear early effect on the inflammatory and pro-inflammatory balance of serum IL-6 and IL-10, however, others have reported anti-inflammatory properties in CT and its derivatives. These properties may be advantageous for the prevention of *S. aureus* udder colonization and are consistent with our observed reduction in SCC after challenge.[313–315]

Lastly, in this study we determined if animals responded to the vaccine adjuvant alone by producing anti-CTA$_2$/B humoral responses. Results showed no significant differences between vaccinated and control groups. While *S. aureus* challenge was not expected to induce anti-CT antibodies, previous studies have reported the undesirable effect of significant anti-CT antibodies after use of this adjuvant for mucosal vaccination.[316] The low adjuvant-specific antibody response observed here, combined with the reduced recruitment of somatic cells, provides support for the utility of CTA$_2$/B-based vaccines.

These studies indicate that IsdA + ClfA-CTA$_2$/B may be effective in the reduction of *S. aureus* colonization and clinical outcome, as evidenced by reduced SCC, but do not provide evidence of complete protection or elimination. Both vaccinated and unvaccinated animals shed high levels of *S. aureus* Newbould 305 immediately after challenge, and all animals in the study were found to shed the challenge strain during the entire 10-day challenge period. This outcome may be the result of a high bacterial dose and the artificial nature of intramammary challenge. The use of a lower challenge dose, a different method of challenge, and/or focus on natural transmission in a larger field trial

will better determine efficacy to prevent infection. In addition, studies are needed that utilize heterologous isolates, compare outcomes with current vaccines, and assess alternate routes of immunization. IsdA and ClfA are established and highly-conserved antigens from bovine *S. aureus*, however, the incorporation of additional antigens, including toxins and anti-immune factors, may also be necessary to promote strain cross-protection and control immune modulation.

Conclusions

Results indicate vaccine efficacy in reducing SCC and improving clinical outcome and support further exploration of the IsdA + ClfA-CTA$_2$/B vaccine to prevent bovine mastitis. The development of an effective vaccine to prevent mastitis caused by *S. aureus* would have many positive impacts on animal health and food production and may decrease overall antibiotic use in the industry. Needle-free vaccination of cattle would also be beneficial by reducing the transmission of disease, inducing mucosal immunity, and promoting vaccine distribution and use. This study provides important preliminary results of a cholera-toxin-based intranasal vaccine in a mastitis challenge model and supports the continued exploration of this antigen-adjuvant platform to prevent bovine disease.

Supplementary Materials
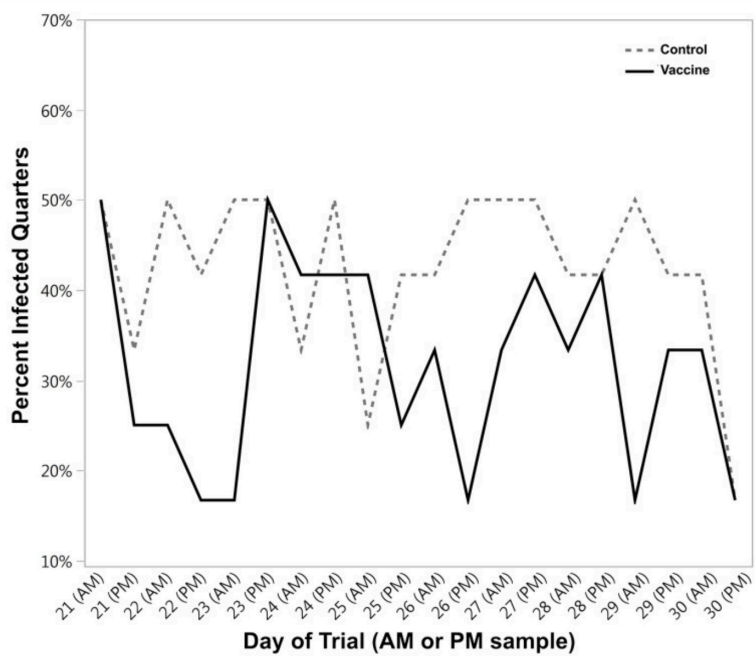
Figure 5.S1.   Percent *S. aureus* Newbould 305 infected quarters from vaccinated and control groups during the challenge period (n=12 per group)

188
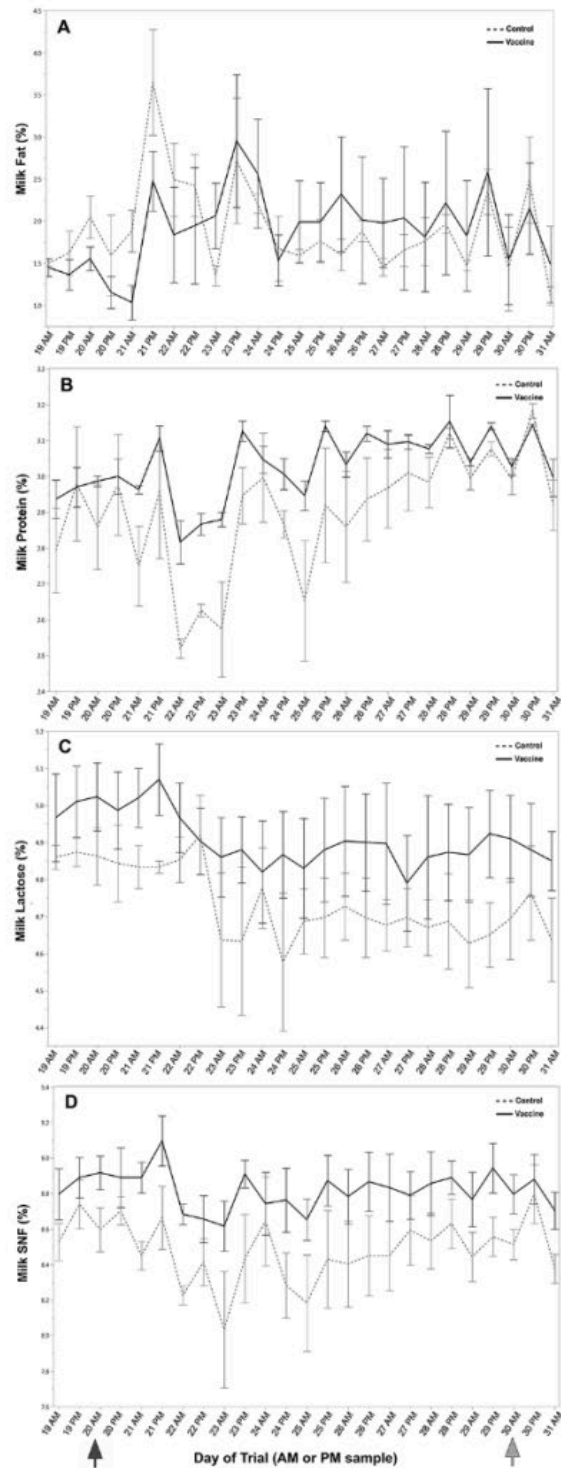
Figure 5.S2.　Milk quality assessment during the trial period

(A) Percent milk fat, (B) milk protein, (C) milk lactose, and (D) solids-not-fat (SNF). Vaccination occurred on days 1 and 14 (not shown), challenge occurred on day 20 (AM, black arrow) and the end of the challenge period was day 30 (AM, gray arrow).
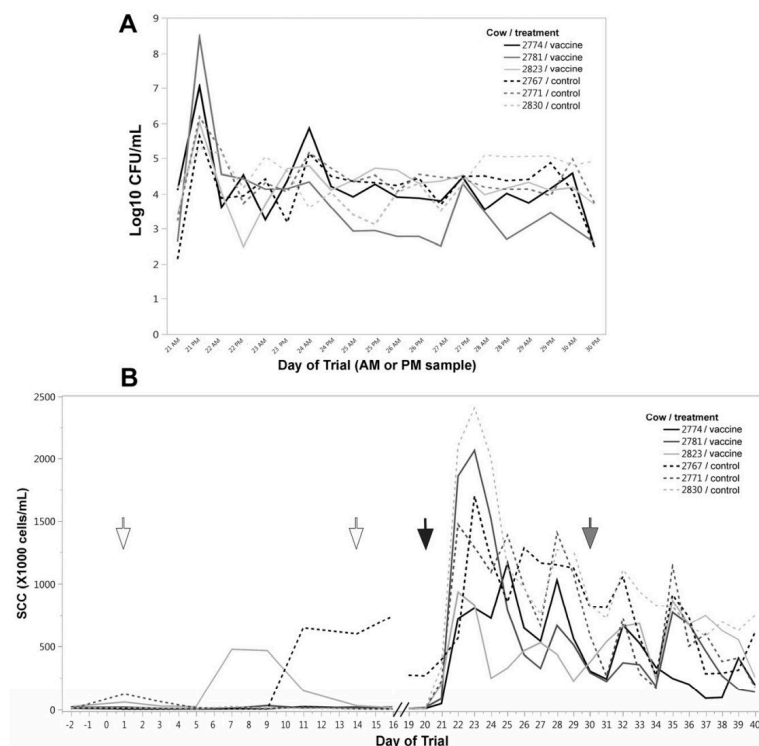
Figure 5.S3.   Individual cow bacterial shedding and SCC during trial

(A) Quantification of bacterial shedding by cow during the challenge period. Log 10 of CFU/mL of Staphylococcus aureus on mannitol salt agar (MSA). (B) SCC by cow during entire trial. Dashed lines are control animals and solid lines are vaccinated animals. White arrows indicate vaccination days (1 and 14), dark gray arrow indicates challenge day (20) and light grey arrow indicates the last day of challenge (30).

Table 5.S1.   Clinical outcomes after challenge on day 20

Cow	Group	Clinical Outcome
2774	Vaccine	No evidence of clinical mastitis
2779	Vaccine	Day 20; severe *Escherichia coli* mastitis in unchallenged quarter (2779 LF) with systemic illness including septicemia. Thereafter, the other three quarters were involved and developed clinical mastitis due to *Staphylococcus aureus* and the animal was euthanized on day 5 post-challenge (day 25)
2781	Vaccine	No evidence of clinical mastitis
2823	Vaccine	No evidence of clinical mastitis, temporary enlargement of supramammary lymph node
2767	Control	Day 24 and day 25; evidence of clinical mastitis in challenged quarters LF and RF
2771	Control	No evidence of clinical mastitis
2830	Control	Persistent clinical mastitis in challenged quarter LR starting on day 23, persistent swelling of supramammary lymph node

Funding, Acknowledgements, and Conflicts of Interest

Conflicts of Interest

J.K.T. holds an unlicensed patent for the use of cholera toxin chimera as a staphylococcal vaccine (Tinker, U.S. Pat. No. 8,834,898).

CHAPTER SIX: FINAL DISCUSSION

The results of these studies provide a foundation for future work in characterizing the structures and functions of AB_5-type ARTs.

In chapter two, we established a simple and efficient purification scheme for purifying tag-free native ArtAB holotoxin. We used that purified toxin to establish a phenotype for ArtAB and compared it to the well-characterized cellular phenotypes of CT- and PT-treated mammalian cells. We also provided preliminary evidence for the distinct cellular activity of ArtB and began to characterize that activity.

In chapter three, we produced a predicted structural model for ArtAB and determined its structural relationship to other ARTs. We used the model to identify important residues in the predicted active site, as determined by structural homology to PT, and we characterized ArtAB's potential NAD+ binding pocket. We created a set of mutants with mutations in the predicted important residues, and we conducted preliminary work to test their effects on ArtAB activity. We found that all three mutants had distinct effects on cellular morphology and intracellular cAMP. We encountered difficulty with many important assays, but the methods we attempted have been described in detail so that the next graduate student will not start from scratch. We also characterized ArtAB's molecular weight, general shape, and Stokes radius, and we determined that it is stable as a holotoxin and does not form aggregates in solution under normal physiological conditions.

In chapter four, we produced a topical literature review and proposed the hypothesis that ARTs affect paracellular barriers through mediation of adhesion molecule transport via Rab/Rap GTPases. We conducted mouse ligated loop surgeries and, despite the small sample size, produced data that will direct future studies of ART activity on mouse small intestine tissue. Finally, we documented our attempted experiments and laid the groundwork for future investigations of barrier effects of ArtAB.

In chapter five, we tested an A_2/B_5-based vaccine against *S. aureus* to prevent bovine mastitis in a bovine clinical trial. We observed a mixed Th1/Th2-type immunogenic response to the CTB-based vaccine and significant reduction in SCC in vaccinated animals. We also conducted a preliminary study (Appendix A) on caprine clinical isolates and determined that there are likely distinct antigenic differences between goat and bovine isolates.

There are many questions left unanswered. A sampling of work that can be done in the future includes:

- Working to develop a theory about the evolutionary benefits of carrying phage-derived A subunits, B_5 subunits, or both, including discussions of the interchangeability and even flexibility in arrangements of the distinct subunits.

- Tracing the evolutionary history of the ART fold.

- Defining the internalization and intracellular trafficking patterns and mechanisms of ArtAB and comparing them to those of well-defined AB_5-type ARTs like CT and PT.

- Determining the location of the proteolytic cut site, if any, for the ArtA subunit and confirming that the C38 and C198 residues do form the characteristic disulfide bond connecting the A_1 and A_2 subunits after proteolytic cleavage.

- Defining the residues that are important in ArtAB, CT, PT, and other ARTs for selecting and binding their ADP-ribosylation targets, and comparing the target-binding sites across different groups of ARTs.

- Characterizing the distinctive ArtB cellular response and elucidating the specific mechanisms of B_5 immunogenic effects.

- Elucidating the downstream molecular interactions that occur after the initial ADP-ribosylation event and further differentiating the cAMP and morphological responses to ART treatment.

- Establishing repeatable assays that can be used to directly assess ART activity.

- Establishing repeatable assays that can be used to explore the effects of ARTs on paracellular barriers.

- Defining the role of ArtAB in *Salmonella* pathogenicity and determining whether an ArtAB mutant would have utility either as a vaccine candidate itself or as part of a multivalent *Salmonella* vaccine. This would involve defining the prevalence of ArtAB among clinical, pathogenic *Salmonella* strains as well as defining the prevalence of those strains in severe disease.

- Developing an ArtAB double mutant genetically detoxified vaccine candidate with R6/E115 mutations similar to that of PT, which has shown promise in clinical trials.

- Conducting larger animal studies with the A_2/B_5-based vaccine against *S. aureus* to prevent bovine mastitis to further characterize its immunogenic effects and to establish its ability to protect against clinical or sub-clinical infection.

- Considering alternative routes of administration for A_2/B_5-based vaccines. Their activity at mucosal membranes opens up options for oral, intranasal, or even transdermal routes of administration.

- Surveying a wider range of caprine clinical isolates to inform antigen selection for a caprine A_2/B_5-based vaccine against *S. aureus* to prevent mastitis.

- Conducting user experience-style studies to characterize the need for vaccines against mastitis and to determine routes of administration, packaging, and dosing schedules that would be beneficial and feasible for producers.

Finally, the work done to characterize ArtAB's structure will be immediately put to use in determining ArtAB's three-dimensional structure. A proposal we submitted to the Pacific Northwest Cryo-EM Center (PNCC - https://pncc.labworks.org/), an NIH-funded national core facility with cryo-electron microscopy equipment that does not exist in the state of Idaho, has been accepted. I attended a two-week microscope operation training workshop that included training on protein sample preparation, grid vitrification

using plunge freezer equipment, and microscope operation including electron beam setup and tuning protocols, grid screening, data collection setup, and practice using the microscope user interface and SerialEM software package. Protein samples have been prepared and shipped to PNCC where they are currently being stored. This is an incredible opportunity that has been made possible by NIH funding for PNCC and also by travel support from the BMOL program and the Biomolecular Research Center. The next steps are to return to PNCC to prepare and screen grids and to determine the grid types, buffer conditions, and other parameters that are conducive to collecting data on the ArtAB holotoxin.

A high-resolution atomic structure of ArtAB would immediately enable studies of the biochemistry of ArtAB's active site and of its common core structure. In addition, Dr. Tinker's lab is focused on identifying, cloning, and purifying novel AB_5-type ARTs. If cryo-EM data collection for ArtAB is successful and a structure is obtained, the defined protein buffer and grid vitrification conditions would provide an immediate starting point for obtaining structures of new AB_5 ARTs, ArtAB mutants, and ArtAB interacting with binding partners like NAD+ or sialylated glycans.

I want to close with a short discussion of the truly global and collaborative nature of this work. In their 2018 review paper titled *Insights into the biogenesis, function, and regulation of ADP-ribosylation,* Michael Cohen and Paul Chang wrote, "…one oddity about the field of ADP-ribosylation is the intellectual and, in fact, physical divide between bacterial ART scientists and those that study eukaryotic ARTs. Despite the common interest and expertise, there is currently very little interaction between these scientists, as we do not share reagents, we do not attend each other's meetings, and we

are essentially considered separate fields of biology. This makes little sense and is a major obstacle for progression in a field of biology that is already technically challenging and difficult. Bacterial and eukaryotic ARTs clearly share common mechanistic features, and the tools and knowledge necessary to study them and the modifications they make have significant overlap. It's time for the two sides to get together." I would encourage anyone reading this dissertation to respond to that call and engage in collaborations with scientists in any field of research related to ARTs. There is much to uncover about the evolutionary history of the ART fold, and, though we have a grasp of some of the targets of ARTs and even some understanding of the downstream effects of ADP-ribosylation, the questions that remain unanswered are many.

REFERENCES

1. Beddoe T, Paton AW, Le Nours J, Rossjohn J, Paton JC. Structure, Biological Functions and Applications of the AB5 Toxins. *Trends Biochem Sci*. 2010;35(7):411. doi:10.1016/J.TIBS.2010.02.003

2. Eriksson K, Fredriksson M, Nordström I, Holmgren J. Cholera toxin and its B subunit promote dendritic cell vaccination with different influences on Th1 and Th2 development. *Infect Immun*. 2003;71(4):1740-1747. doi:10.1128/IAI.71.4.1740-1747.2003

3. Fan E, Merritt EA, Verlinde CLMJ, Hol WGJ. AB5 toxins: structures and inhibitor design. *Curr Opin Struct Biol*. 2000;10(6):680-686. doi:10.1016/S0959-440X(00)00152-4

4. Mukhopadhyay S, Linstedt AD. Retrograde trafficking of AB5 toxins: Mechanisms to therapeutics. *J Mol Med*. 2013;91(10):1131-1141. doi:10.1007/S00109-013-1048-7/FIGURES/5

5. Cho JA, Chinnapen DJF, Aamar E, te Welscher YM, Lencer WI, Massol R. Insights on the trafficking and retro-translocation of glycosphingolipid-binding bacterial toxins. *Front Cell Infect Microbiol*. 2012;2:51. doi:10.3389/FCIMB.2012.00051/BIBTEX

6. Saitoh M, Tanaka K, Nishimori K, et al. The artAB genes encode a putative ADP-ribosyltransferase toxin homologue associated with Salmonella enterica serovar Typhimurium DT104. *Microbiology*. 2005;151(9):3089-3096. doi:https://doi.org/10.1099/mic.0.27933-0

7. Hottiger MO, Hassa PO, Lüscher B, Schüler H, Koch-Nolte F. Toward a unified nomenclature for mammalian ADP-ribosyltransferases. *Trends Biochem Sci*. 2010;35(4):208-219. doi:10.1016/J.TIBS.2009.12.003

8.   Cohen MS, Chang P. Insights into the biogenesis, function, and regulation of ADP-ribosylation. *Nat Chem Biol*. 2018;14(3):236-243. doi:10.1038/NCHEMBIO.2568

9.   Lüscher B, Ahel I, Altmeyer M, et al. ADP-ribosyltransferases, an update on function and nomenclature. *FEBS J*. 2021. doi:10.1111/FEBS.16142

10.   Lingwood C. Therapeutic Uses of Bacterial Subunit Toxins. *Toxins (Basel)*. 2021;13(6). doi:10.3390/TOXINS13060378

11.   Song KR, Lim JK, Park SE, et al. Oral Cholera Vaccine Efficacy and Effectiveness. *Vaccines*. 2021;9(12). doi:10.3390/VACCINES9121482

12.   Gregg KA, Merkel TJ. Pertussis Toxin: A Key Component in Pertussis Vaccines? *Toxins 2019, Vol 11, Page 557*. 2019;11(10):557. doi:10.3390/TOXINS11100557

13.   Seo H, Garcia C, Ruan X, Duan Q, Sack DA, Zhang W. Preclinical Characterization of Immunogenicity and Efficacy against Diarrhea from MecVax, a Multivalent Enterotoxigenic E. coli Vaccine Candidate. *Infect Immun*. 2021;89(7). doi:10.1128/IAI.00106-21

14.   Lichtenstein BR, Höcker B. Engineering an AB5 Protein Carrier. *Sci Rep*. 2018;8(1):12643. doi:10.1038/S41598-018-30910-Y

15.   Pan C, Wu J, Qing S, et al. Biosynthesis of Self-Assembled Proteinaceous Nanoparticles for Vaccination. *Adv Mater*. 2020;32(42):2002940. doi:10.1002/ADMA.202002940

16.   Cheng RA, Wiedmann M. The ADP-Ribosylating Toxins of Salmonella. *Toxins (Basel)*. 2019;11(7). doi:10.3390/TOXINS11070416

17.   Hiley L, Fang NX, Micalizzi GR, Bates J. Distribution of Gifsy-3 and of Variants of ST64B and Gifsy-1 Prophages amongst Salmonella enterica Serovar Typhimurium Isolates: Evidence that Combinations of Prophages Promote Clonality. *PLoS One*. 2014;9(1):e86203. doi:10.1371/JOURNAL.PONE.0086203

18.   Moreno Switt AI, den Bakker HC, Cummings CA, et al. Identification and Characterization of Novel Salmonella Mobile Elements Involved in the Dissemination of Genes Linked to Virulence and Transmission. *PLoS One*. 2012;7(7):e41247. doi:10.1371/JOURNAL.PONE.0041247

19. Boyd EF, Carpenter MR, Chowdhury N. Mobile effector proteins on phage genomes. *http://dx.doi.org/104161/bact21658*. 2012;2(3):139-148. doi:10.4161/BACT.21658

20. Boyd EF. Bacteriophage-Encoded Bacterial Virulence Factors and Phage–Pathogenicity Island Interactions. *Adv Virus Res*. 2012;82:91-118. doi:10.1016/B978-0-12-394621-8.00014-5

21. Jobling MG, Holmes RK. Type II heat-labile enterotoxins from 50 diverse Escherichia coli isolates belong almost exclusively to the LT-IIc family and may be prophage encoded. *PLoS One*. 2012;7(1). doi:10.1371/journal.pone.0029898

22. MG J. The Chromosomal Nature of LT-II Enterotoxins Solved: A Lambdoid Prophage Encodes Both LT-II and One of Two Novel Pertussis-Toxin-Like Toxin Family Members in Type II Enterotoxigenic Escherichia Coli. *Pathog Dis*. 2016;74(3). doi:10.1093/FEMSPD/FTW001

23. Tyler JS, Livny J, Friedman DI. Lambdoid Phages and Shiga Toxin. *Phages*. April 2014:129-164. doi:10.1128/9781555816506.CH7

24. Gao X, Deng L, Stack G, et al. Evolution of host adaptation in the Salmonella typhoid toxin. 2017;2(12):1592-1599. doi:10.1038/s41564-017-0033-2

25. Song J, Gao X, Galán JE. Structure and function of the Salmonella Typhi chimaeric A2B5 typhoid toxin. *Nat 2013 4997458*. 2013;499(7458):350-354. doi:10.1038/nature12377

26. Wang H, Paton JC, Herdman BP, Rogers TJ, Beddoe T, Paton AW. The b subunit of an AB5 toxin produced by salmonella enterica serovar typhi up-regulates chemokines, cytokines, and adhesion molecules in human macrophage, colonic epithelial, and brain microvascular endothelial cell lines. *Infect Immun*. 2013;81(3):673-683. doi:10.1128/IAI.01043-12/SUPPL_FILE/ZII999090009SO1.PDF

27. Tack DM, Ray L, Griffin PM, et al. Preliminary Incidence and Trends of Infections with Pathogens Transmitted Commonly Through Food — Foodborne Diseases Active Surveillance Network, 10 U.S. Sites, 2016–2019. *MMWR Morb Mortal Wkly Rep*. 2020;69(17):509-514. doi:10.15585/mmwr.mm6917a1

28.   WHO. *Interventions for the Control of Non-TyphoidalSalmonella Spp. in Beef and Pork: Meeting Report and Systematic Review*. World Health Organization: Geneva, Switzerland,; 2016.

29.   CDC. Antibiotic resistance threats in the United States. *Centers Dis Control Prev*. 2019:1-150.

30.   Knodler LA, Elfenbein JR. Salmonella enterica. *Trends Microbiol*. 2019;27(11):964-965. doi:10.1016/j.tim.2019.05.002

31.   Morningstar-Shaw BR, Mackie BSA, Barker DK, Palmer EA. *Salmonella Serotypes Isolated from Animals and Related Sources*. Atlanta, Georgia; 2016.

32.   Cheng RA, Eade CR, Wiedmann M. Embracing diversity: Differences in virulence mechanisms, disease severity, and host adaptations contribute to the success of nontyphoidal salmonellaas a foodborne pathogen. *Front Microbiol*. 2019;10(JUN):1368. doi:10.3389/fmicb.2019.01368

33.   Leekitcharoenphon P, Hendriksen RS, Le Hello S, et al. Global genomic epidemiology of Salmonella enterica serovar Typhimurium DT104. *Appl Environ Microbiol*. 2016;82(8):2516-2526. doi:10.1128/AEM.03821-15

34.   Allen CA, Fedorka-Cray PJ, Vazquez-Torres A, et al. In vitro and in vivo assessment of Salmonella enterica serovar typhimurium DT104 virulence. *Infect Immun*. 2001;69(7):4673-4677. doi:10.1128/IAI.69.7.4673-4677.2001

35.   Poppe C, Smart N, Khakhria R, Johnson W, Spika J, Prescott J. Salmonella typhimurium DT104: A virulent and drug-resistant pathogen. *Can Vet J*. 1998;39(9):559-565.

36.   Guichard A, Cruz-Moreno BC, Aguilar B, et al. Cholera Toxin Disrupts Barrier Function by Inhibiting Exocyst-Mediated Trafficking of Host Proteins to Intestinal Cell Junctions. *Cell Host Microbe*. 2013;14(3):294-305. doi:10.1016/J.CHOM.2013.08.001

37.   Kügler S, Böcker K, Heusipp G, Greune L, Kim KS, Schmidt MA. Pertussis toxin transiently affects barrier integrity, organelle organization and transmigration of monocytes in a human brain microvascular endothelial cell barrier model. *Cell Microbiol*. 2007;9(3):619-632. doi:10.1111/J.1462-5822.2006.00813.X

38. Tamamura Y, Tanaka K, Uchida I. Characterization of pertussis-like toxin from Salmonella spp.That catalyzes ADP-ribosylation of G proteins. *Sci Rep*. 2017;7(1):1-13. doi:10.1038/s41598-017-02517-2

39. Uchida I, Ishihara R, Tanaka K, et al. Salmonella enterica serotype Typhimurium DT104 ArtA-dependent modification of pertussis toxin-sensitive G proteins in the presence of [32P]NAD. *Microbiology*. 2009;155(11):3710-3718. doi:10.1099/mic.0.028399-0

40. Lencer WI, Constable C, Moe S, et al. Proteolytic activation of cholera toxin and Escherichia coli labile toxin by entry into host epithelial cells: Signal transduction by a protease- resistant toxin variant. *J Biol Chem*. 1997;272(24):15562-15568. doi:10.1074/jbc.272.24.15562

41. Millen SH, Lewallen DM, Herr AB, Iyer SS, Weiss AA. Identification and characterization of the carbohydrate ligands recognized by pertussis toxin via a glycan microarray and surface plasmon resonance. *Biochemistry*. 2010;49(28):5954-5967. doi:10.1021/bi100474z

42. Cabrera A, Lepage JE, Sullivan KM, Seed SM. Vaxchora: A Single-Dose Oral Cholera Vaccine. *Ann Pharmacother*. 2017;51(7):584-589. doi:10.1177/1060028017698162

43. Czerkinsky C, Sun J Bin, Lebens M, et al. Cholera Toxin B Subunit as Transmucosal Carrier-Delivery and Immunomodulating System for Induction of Antiinfectious and Antipathological Immunitya. *Ann N Y Acad Sci*. 1996;778(1):185-193. doi:10.1111/J.1749-6632.1996.TB21127.X

44. Adkins I, Holubova J, Kosova M, Sadilkova L. Bacteria and their Toxins Tamed for Immunotherapy. *Curr Pharm Biotechnol*. 2012;13(8):1446-1473. doi:10.2174/138920112800784835

45. Goletz TJ, Klimpel KR, Leppla SH, Keith JM, Berzofsky JA. Delivery of Antigens to the MHC Class I Pathway Using Bacterial Toxins. *Hum Immunol*. 1997;54(2):129-136. doi:10.1016/S0198-8859(97)00081-5

46. Morón G, Dadaglio G, Leclerc C. New tools for antigen delivery to the MHC class I pathway. *Trends Immunol*. 2004;25(2):92-97. doi:10.1016/J.IT.2003.11.008

47. Jobling MG, Holmes RK. Identification of motifs in cholera toxin A1 polypeptide that are required for its interaction with human ADP-ribosylation factor 6 in a bacterial two-hybrid system. *Proc Natl Acad Sci U S A*. 2000;97(26):14662-14667. doi:10.1073/pnas.011442598

48. Kumar S, Stecher G, Tamura K. MEGA7: Molecular Evolutionary Genetics Analysis Version 7.0 for Bigger Datasets. *Mol Biol Evol*. 2016;33(7):1870-1874. doi:10.1093/MOLBEV/MSW054

49. Jones DT, Taylor WR, Thornton JM. The rapid generation of mutation data matrices from protein sequences. *Bioinformatics*. 1992;8(3):275-282. doi:10.1093/bioinformatics/8.3.275

50. Byres E, Paton AW, Paton JC, et al. Incorporation of a non-human glycan mediates human susceptibility to a bacterial toxin. *Nature*. 2008;456(7222):648-652. doi:10.1038/nature07428

51. Littler DR, Ang SY, Moriel DG, et al. Structure-function analyses of a pertussis-like toxin from pathogenic Escherichia coli reveal a distinct mechanism of inhibition of trimeric G-proteins. *J Biol Chem*. 2017;292(36):15143-15158. doi:10.1074/JBC.M117.796094/ATTACHMENT/A888E899-E5DA-4556-985B-7A27173034D7/MMC2.PDF

52. Deng L, Song J, Gao X, et al. Host adaptation of a bacterial toxin from the human pathogen salmonella typhi. *Cell*. 2014;159(6):1290-1299. doi:10.1016/j.cell.2014.10.057

53. Waterhouse A, Bertoni M, Bienert S, et al. SWISS-MODEL: Homology modelling of protein structures and complexes. *Nucleic Acids Res*. 2018;46(W1):W296-W303. doi:10.1093/nar/gky427

54. Tinker JK, Davis CT, Arlian BM. Purification and characterization of Yersinia enterocolitica and Yersinia pestis LcrV-cholera toxin A2/B chimeras. *Protein Expr Purif*. 2010;74(1):16-23. doi:10.1016/j.pep.2010.04.021

55. Feoktistova M, Geserick P, Leverkus M. Crystal violet assay for determining viability of cultured cells. *Cold Spring Harb Protoc*. 2016;2016(4):343-346. doi:10.1101/pdb.prot087379

56. Souvorov A, Agarwala R, Lipman DJ. SKESA: Strategic k-mer extension for scrupulous assemblies. *Genome Biol*. 2018;19(1):1-13. doi:10.1186/S13059-018-1540-Z/TABLES/6

57. Song J, Gao X, Galán JE. Structure and function of the Salmonella Typhi chimaeric A 2 B 5 typhoid toxin. *Nature*. 2013;499(7458):350-354. doi:10.1038/nature12377

58. Gaballa A, Cheng RA, Harrand AS, Cohn AR, Wiedmann M. The Majority of Typhoid Toxin-Positive Salmonella Serovars Encode ArtB, an Alternate Binding Subunit. *mSphere*. 2021;6(1). doi:10.1128/msphere.01255-20

59. Zhang Y. I-TASSER server for protein 3D structure prediction. *BMC Bioinformatics*. 2008;9(1):1-8. doi:10.1186/1471-2105-9-40

60. Kuziemko GM, Stroh M, Stevens RC. Cholera toxin binding affinity and specificity for gangliosides determined by surface plasmon resonance. *Biochemistry*. 1996;35(20):6375-6384. doi:10.1021/bi952314i

61. Holmgren J, Lonnroth I, Mansson JE, Svennerholm L. Interaction of cholera toxin and membrane Gm1 ganglioside of small intestine. *Proc Natl Acad Sci U S A*. 1975;72(7):2520-2524. doi:10.1073/pnas.72.7.2520

62. Chong P, Klein M. Single-step purification of pertussis toxin and its subunits by heat-treated fetuin-Sepharose affinity chromatography. *Biochem Cell Biol*. 1989;67(7):387-391. doi:10.1139/o89-061

63. Pande AH, Moe D, Jamnadas M, Tatulian SA, Teter K. The pertussis toxin S1 subunit is a thermally unstable protein susceptible to degradation by the 20S proteasome. *Biochemistry*. 2006;45(46):13734-13740. doi:10.1021/bi061175+

64. Gillenius P, Jäätmaa E, Askelöf P, Granström M, Tiru M. The standardization of an assay for pertussis toxin and antitoxin in microplate culture of Chinese hamster ovary cells. *J Biol Stand*. 1985;13(1):61-66. doi:10.1016/S0092-1157(85)80034-2

65. Stavric S, Speirs JI, Konowalchuk J, Jeffrey D. Stimulation of cyclic AMP secretion in Vero cells by enterotoxins of Escherichia coli and Vibrio cholerae. *Infect Immun*. 1978;21(2):514-517. doi:10.1128/iai.21.2.514-517.1978

66. Krueger KM, Mende-Mueller LM, Barbieri JT. Protease treatment of pertussis toxin identifies the preferential cleavage of the S1 subunit. *J Biol Chem*. 1991;266(13):8122-8128. doi:10.1016/s0021-9258(18)92950-9

67. Gill DM, Rappaport RS. Origin of the enzymatically active a, fragment of cholera toxin. *J Infect Dis*. 1979;139(6):674-680. doi:10.1093/infdis/139.6.674

68. Stein PE, Boodhoo A, Armstrong GD, Cockle SA, Klein MH, Read RJ. The crystal structure of pertussis toxin. *Structure*. 1994;2(1):45-57. doi:10.1016/S0969-2126(00)00007-1

69. Carbonetti NH, Mays RM, Artamonova G V., Plaut RD, Worthington ZEV. Proteolytic cleavage of pertussis toxin S1 subunit is not essential for its activity in mammalian cells. *BMC Microbiol*. 2005;5(1):1-14. doi:10.1186/1471-2180-5-7

70. Plaut RD, Scanlon KM, Taylor M, Teter K, Carbonetti NH. Intracellular disassembly and activity of pertussis toxin require interaction with ATP. *Pathog Dis*. 2016;74(6):65. doi:10.1093/femspd/ftw065

71. Cherubin P, Fidler D, Quiñones B, Teter K. Bimodal response to Shiga toxin 2 subtypes results from relatively weak binding to the target cell. *Infect Immun*. 2019;87(12). doi:10.1128/IAI.00428-19

72. Cherubin P, Quiñones B, Teter K. Cellular recovery from exposure to sub-optimal concentrations of AB toxins that inhibit protein synthesis. *Sci Rep*. 2018;8(1):1-10. doi:10.1038/s41598-018-20861-9

73. Glineur C, Locht C. Importance of ADP-ribosylation in the morphological changes of PC12 cells induced by cholera toxin. *Infect Immun*. 1994;62(10):4176-4185. doi:10.1128/iai.62.10.4176-4185.1994

74. Fishman PH, Atikkan EE. Mechanism of action of cholera toxin: Effect of receptor density and multivalent binding on activation of adenylate cyclase. *J Membr Biol*. 1980;54(1):51-60. doi:10.1007/BF01875376

75. Maneval DR, Colwell RR, Joseph SW, Grays R, Donta ST. A tissue culture method for the detection of bacterial enterotoxins. *J Tissue Cult Methods*. 1980;6(2):85-90. doi:10.1007/BF01666023

76. Guerrant RL, Brunton LL. Characterization of the Chinese hamster ovary cell assay for the enterotoxins of Vibrio cholerae and Escherichia coli and for antitoxin: Differential inhibition by gangliosides, specific antisera, and toxoid. *J Infect Dis*. 1977;135(5):720-728. doi:10.1093/infdis/135.5.720

77. Nozawa RT, Yokota T, Kuwahara S. Assay method for Vibrio cholerae and Escherichia coli enterotoxins by automated counting of floating Chinese hamster ovary cells in culture medium. *J Clin Microbiol*. 1978;7(5):479-485. doi:10.1128/jcm.7.5.479-485.1978

78. Terrinoni M, Holmgren J, Lebens M, Larena M. Proteomic analysis of cholera toxin adjuvant-stimulated human monocytes identifies Thrombospondin-1 and Integrin-β1 as strongly upregulated molecules involved in adjuvant activity. *Sci Rep*. 2019;9(1):1-13. doi:10.1038/s41598-019-38726-0

79. Hewlett EL, Sauer KT, Myers GA, Cowell JL, Guerrant RL. Induction of a novel morphological response in Chinese hamster ovary cells by pertussis toxin. *Infect Immun*. 1983;40(3):1198-1203. doi:10.1128/iai.40.3.1198-1203.1983

80. Burns DL, Kenimer JG, Manclark CR. Role of the A subunit of pertussis toxin in alteration of Chinese hamster ovary cell morphology. *Infect Immun*. 1987;55(1).

81. Creydt VP, Silberstein C, Zotta E, Ibarra C. Cytotoxic effect of Shiga toxin-2 holotoxin and its B subunit on human renal tubular epithelial cells. *Microbes Infect*. 2006;8(2):410-419. doi:10.1016/j.micinf.2005.07.005

82. Yasuda Y, Matano K, Asai T, Tochikubo K. Affinity purification of recombinant cholera toxin B subunit oligomer expressed in Bacillus brevis for potential human use as a mucosal adjuvant. *FEMS Immunol Med Microbiol*. 1998;20(4):311-318. doi:10.1111/j.1574-695x.1998.tb01141.x

83. Dugas B, Paul-Eugène N, Génot E, Mencia-Huerta JM, Braquet P, Kolb JP. Effect of bacterial toxins on human B cell activation. II. Mitogenic activity of the B subunit of cholera toxin. *Eur J Immunol*. 1991;21(2):495-500. doi:10.1002/eji.1830210236

84. Smets LA, Van Rooy H. Mitogenic and antimitogenic effects of cholera toxin-mediated cyclic AMP levels in 3T3 cells. *J Cell Physiol*. 1987;133(2):395-399. doi:10.1002/jcp.1041330227

85. Okada N, Kitano Y. Effects of Cholera Toxin on Proliferation of Cultured Human Keratinocytes in Relation to Intracellular Cyclic AMP Level~. *J Invest Dermatol.* 1982;79(1):42-47. doi:10.1111/1523-1747.ep12510580

86. Allam M, Bertrand R, Zhang-Sun G, Pappas J, Viallet J. Cholera toxin triggers apoptosis in human lung cancer cell lines. *Cancer Res.* 1997;57(13):2615-2618.

87. Nashar TO, Williams NA, Hirst TR. Cross-linking of cell surface ganglioside GM1 induces the selective apoptosis of mature CD8+ T lymphocytes. *Int Immunol.* 1996;8(5):731-736. doi:10.1093/intimm/8.5.731

88. Keller MD, Ching KL, Liang FX, et al. Decoy exosomes provide protection against bacterial toxins. *Nature.* 2020;579(7798):260-264. doi:10.1038/S41586-020-2066-6

89. Cohen MS, Chang P. Insights into the biogenesis, function, and regulation of ADP-ribosylation. *Nat Chem Biol.* 2018;14(3):236-243. doi:10.1038/NCHEMBIO.2568

90. Barth H, Stiles B. Binary Actin-ADP-Ribosylating Toxins and their Use as Molecular Trojan Horses for Drug Delivery into Eukaryotic Cells. *Curr Med Chem.* 2008;15(5):459-469. doi:10.2174/092986708783503195

91. Holbourn KP, Shone CC, Acharya KR. A family of killer toxins. Exploring the mechanism of ADP-ribosylating toxins. *FEBS J.* 2006;273(20):4579-4593. doi:10.1111/J.1742-4658.2006.05442.X

92. Han SS, Tainer JA. The ARTT motif and a unified structural understanding of substrate recognition in ADP-ribosylating bacterial toxins and eukaryotic ADP-ribosyltransferases. *Int J Med Microbiol.* 2002;291(6/7):523-529. doi:10.1078/1438-4221-00162

93. Deng Q, Barbieri JT. Molecular mechanisms of the cytotoxicity of ADP-ribosylating toxins. *Annu Rev Microbiol.* 2008;62:271-288. doi:10.1146/ANNUREV.MICRO.62.081307.162848

94. Palazzo L, Mikoč A, Ahel I. ADP-ribosylation: new facets of an ancient modification. *FEBS J.* 2017;284(18):2932-2946. doi:10.1111/FEBS.14078

95.   Bazan JF, Koch-Nolte F. Sequence and structural links between distant ADP-ribosyltransferase families. *Adv Exp Med Biol*. 1997;419:99-107. doi:10.1007/978-1-4419-8632-0_12/COVER

96.   Aravind L, Zhang D, De Souza RF, Anand S, Iyer LM. The Natural History of ADP-Ribosyltransferases and the ADP-Ribosylation System. *Curr Top Microbiol Immunol*. 2015;384:3. doi:10.1007/82_2014_414

97.   Han S, Tainer JA. The ARTT motif and a unified structural understanding of substrate recognition in ADP-ribosylating bacterial toxins and eukaryotic ADP-ribosyltransferases. *Int J Med Microbiol*. 2001;291(6-7):523-529. doi:10.1078/1438-4221-00162

98.   Rack JGM, Palazzo L, Ahel I. (ADP-ribosyl)hydrolases: structure, function, and biology. *Genes Dev*. 2020;34(5-6):263. doi:10.1101/GAD.334631.119

99.   Doxey AC, Mansfield MJ, Montecucco C. Discovery of novel bacterial toxins by genomics and computational biology. *Toxicon*. 2018;147:2-12. doi:10.1016/J.TOXICON.2018.02.002

100.   Tremblay O, Thow Z, Geddes-McAlister J, Rod Merrill A. Several New Putative Bacterial ADP-Ribosyltransferase Toxins Are Revealed from In Silico DataMining, Including the Novel Toxin Vorin, Encoded by the Fire Blight Pathogen Erwinia amylovora. *Toxins (Basel)*. 2020;12(12):792. doi:10.3390/toxins12120792

101.   Lyons B, Ravulapalli R, Lanoue J, et al. Scabin, a Novel DNA-acting ADP-ribosyltransferase from Streptomyces scabies. *J Biol Chem*. 2016;291(21):11198. doi:10.1074/JBC.M115.707653

102.   Thanabalu T, Hindley J, Jackson-Yap J, Berry C. Cloning, sequencing, and expression of a gene encoding a 100-kilodalton mosquitocidal toxin from Bacillus sphaericus SSII-1. *J Bacteriol*. 1991;173(9):2776. doi:10.1128/JB.173.9.2776-2785.1991

103.   Fünfhaus A, Poppinga L, Genersch E. Identification and characterization of two novel toxins expressed by the lethal honey bee pathogen Paenibacillus larvae, the causative agent of American foulbrood. *Environ Microbiol*. 2013;15(11):2951-2965. doi:10.1111/1462-2920.12229

104. Turner M, Tremblay O, Heney KA, et al. Characterization of C3larvinA, a novel RhoA-targeting ADP-ribosyltransferase toxin produced by the honey bee pathogen, Paenibacillus larvae. *Biosci Rep*. 2020;40(1). doi:10.1042/BSR20193405

105. Ebeling J, Fünfhaus A, Genersch E. The Buzz about ADP-Ribosylation Toxins from Paenibacillus larvae, the Causative Agent of American Foulbrood in Honey Bees. *Toxins 2021, Vol 13, Page 151*. 2021;13(2):151. doi:10.3390/TOXINS13020151

106. Domenighini M, Magagnoli C, Pizza M, Rappuoli R. Common features of the NAD-binding and catalytic site of ADP-ribosylating toxins. *Mol Microbiol*. 1994;14(1):41-50. doi:10.1111/J.1365-2958.1994.TB01265.X

107. Hanukoglu I, Library WO. Proteopedia: Rossmann fold: A beta-alpha-beta fold at dinucleotide binding sites. *Biochem Mol Biol Educ*. 2015;43(3):206-209. doi:10.1002/BMB.20849

108. Paton AW, Srimanote P, Talbot UM, Wang H, Paton JC. A New Family of Potent AB5 Cytotoxins Produced by Shiga Toxigenic Escherichia coli. *J Exp Med*. 2004;200(1):35-46. doi:10.1084/JEM.20040392

109. Ng NM, Littler DR, Paton AW, et al. EcxAB Is a Founding Member of a New Family of Metalloprotease AB5 Toxins with a Hybrid Cholera-like B Subunit. *Structure*. 2013;21(11):2003-2013. doi:10.1016/J.STR.2013.08.024

110. Simon NC, Aktories K, Barbieri JT. Novel bacterial ADP-ribosylating toxins: structure and function. *Nat Rev Microbiol*. 2014;12(9):599. doi:10.1038/NRMICRO3310

111. Watanabe M, Enomoto S, Takamura-Enya T, et al. Enzymatic properties of pierisin-1 and its N-terminal domain, a guanine-specific ADP-ribosyltransferase from the cabbage butterfly. *J Biochem*. 2004;135(4):471-477. doi:10.1093/JB/MVH062

112. Totsuka Y, Kawanishi M, Nishigaki R, et al. Analysis of HPRT and supF mutations caused by pierisin-1, a guanine specific ADP-ribosylating toxin derived from the cabbage butterfly. *Chem Res Toxicol*. 2003;16(8):945-952. doi:10.1021/TX034052O/SUPPL_FILE/TX034052OSI20030318_123041.PDF

113. Spanò S, Ugalde JE, Galán JE. Delivery of a Salmonella Typhi exotoxin from a host intracellular compartment. *Cell Host Microbe*. 2008;3(1):30-38. doi:10.1016/J.CHOM.2007.11.001

114. Schirmer J, Wieden HJ, Rodnina M V., Aktories K. Inactivation of the elongation factor Tu by mosquitocidal toxin-catalyzed mono-ADP-ribosylation. *Appl Environ Microbiol*. 2002;68(10):4894-4899. doi:10.1128/AEM.68.10.4894-4899.2002/ASSET/D322B34C-D5EC-4222-936F-1241FADD053E/ASSETS/GRAPHIC/AM1020620005.JPEG

115. Treiber N, Reinert DJ, Carpusca I, Aktories K, Schulz GE. Structure and Mode of Action of a Mosquitocidal Holotoxin. *J Mol Biol*. 2008;381(1):150-159. doi:10.1016/J.JMB.2008.05.067

116. Fünfhaus A, Genersch E. Proteome analysis of Paenibacillus larvae reveals the existence of a putative S-layer protein. *Environ Microbiol Rep*. 2012;4(2):194-202. doi:10.1111/J.1758-2229.2011.00320.X

117. Lyons B, Lugo MR, Carlin S, Lidster T, Rod Merrill A. Characterization of the catalytic signature of Scabin toxin, a DNA-targeting ADP-ribosyltransferase. *Biochem J*. 2018;475(1):225-245. doi:10.1042/BCJ20170818

118. Lugo MR, Lyons B, Lento C, Wilson DJ, Rod Merrill A. Dynamics of Scabin toxin. A proposal for the binding mode of the DNA substrate. *PLoS One*. 2018;13(3):e0194425. doi:10.1371/JOURNAL.PONE.0194425

119. Rubin EJ, Gill DM, Boquet P, Popoff MR. Functional modification of a 21-kilodalton G protein when ADP-ribosylated by exoenzyme C3 of Clostridium botulinum. *Mol Cell Biol*. 1988;8(1):418-426. doi:10.1128/MCB.8.1.418-426.1988

120. Braun U, Habermann B, Just I, Aktories K, Vandekerckhove J. Purification of the 22 kDa protein substrate of botulinum ADP-ribosyltransferase C3 from porcine brain cytosol and its characterization as a GTP-binding protein highly homologous to the rho gene product. *FEBS Lett*. 1989;243(1):70-76. doi:10.1016/0014-5793(89)81220-7

121. Just I, Mohr C, Schallehn G, et al. Purification and characterization of an ADP-ribosyltransferase produced by Clostridium limosum. *J Biol Chem*. 1992;267(15):10274-10280. doi:10.1016/S0021-9258(19)50014-X

122. Ganesan AK, Frank DW, Misra RP, Schmidt G, Barbieri JT. Pseudomonas aeruginosa Exoenzyme S ADP-ribosylates Ras at Multiple Sites *. *J Biol Chem*. 1998;273(13):7332-7337. doi:10.1074/JBC.273.13.7332

123. Aktories K, Bärmann M, Ohishi I, Tsuyama S, Jakobs KH, Habermann E. Botulinum C2 toxin ADP-ribosylates actin. *Nature*. 1986;322(6077):390-392. doi:10.1038/322390A0

124. Vandekerckhove J, Schering B, Bärmann M, Aktories K. Clostridium perfringens iota toxin ADP-ribosylates skeletal muscle actin in Arg-177. *FEBS Lett*. 1987;225(1-2):48-52. doi:10.1016/0014-5793(87)81129-8

125. Popoff MR, Boquet P. Clostridium spiroforme toxin is a binary toxin which ADP-ribosylates cellular actin. *Biochem Biophys Res Commun*. 1988;152(3):1361-1368. doi:10.1016/S0006-291X(88)80435-2

126. Threlfall EJ. Epidemic Salmonella typhimurium DT 104—a truly international multiresistant clone. *J Antimicrob Chemother*. 2000;46(1):7-10. doi:10.1093/JAC/46.1.7

127. Miura S, Tamamura Y, Takayasu M, et al. Influence of sos-inducing agents on the expression of artab toxin gene in salmonella enterica and salmonella bongori. *Microbiol (United Kingdom)*. 2020;166(8):785-793. doi:10.1099/MIC.0.000939/CITE/REFWORKS

128. Overgaard E, Morris B, Mohammad Mousa O, et al. *Cellular Activity of Salmonella Typhimurium ArtAB Toxin and Its Receptor-Binding Subunit*. Vol 13. MDPI; 2021:In Progress. doi:10.3390/TOXINS13090599/S1

129. Mirdita M, Schütze K, Moriwaki Y, Heo L, Ovchinnikov S, Steinegger M. ColabFold: making protein folding accessible to all. *Nat Methods 2022 196*. 2022;19(6):679-682. doi:10.1038/s41592-022-01488-1

130. Dong R, Peng Z, Zhang Y, Yang J. mTM-align: an algorithm for fast and accurate multiple protein structure alignment. *Bioinformatics*. 2018;34(10):1719-1725. doi:10.1093/BIOINFORMATICS/BTX828

131. Dong R, Pan S, Peng Z, Zhang Y, Yang J. mTM-align: a server for fast protein structure database search and multiple protein structure alignment. *Nucleic Acids Res*. 2018;46(W1):W380-W386. doi:10.1093/NAR/GKY430

132. Altschul SF, Madden TL, Schäffer AA, et al. Gapped BLAST and PSI-BLAST: a new generation of protein database search programs. *Nucleic Acids Res*. 1997;25(17):3389. doi:10.1093/NAR/25.17.3389

133. Zhang Y, Skolnick J. Scoring function for automated assessment of protein structure template quality. *Proteins*. 2004;57(4):702-710. doi:10.1002/PROT.20264

134. Jobling MG, Palmer LM, Erbe JL, Holmes RK. Construction and characterization of versatile cloning vectors for efficient delivery of native foreign proteins to the periplasm of Escherichia coli. *Plasmid*. 1997;38(3):158-173. doi:10.1006/PLAS.1997.1309

135. Philo JS. Improved methods for fitting sedimentation coefficient distributions derived by time-derivative techniques. *Anal Biochem*. 2006;354(2):238-246. doi:10.1016/J.AB.2006.04.053

136. Stafford WF. Boundary analysis in sedimentation transport experiments: A procedure for obtaining sedimentation coefficient distributions using the time derivative of the concentration profile. *Anal Biochem*. 1992;203(2):295-301. doi:10.1016/0003-2697(92)90316-Y

137. Miles AJ, Wallace BA. Synchrotron radiation circular dichroism spectroscopy of proteins and applications in structural and functional genomics. *Chem Soc Rev*. 2006;35(1):39-51. doi:10.1039/B316168B

138. Whitmore L, Wallace BA. Protein secondary structure analyses from circular dichroism spectroscopy: methods and reference databases. *Biopolymers*. 2008;89(5):392-400. doi:10.1002/BIP.20853

139. Miles AJ, Ramalli SG, Wallace BA. DichroWeb, a website for calculating protein secondary structure from circular dichroism spectroscopic data. *Protein Sci*. 2022;31(1):37-46. doi:10.1002/PRO.4153

140. Miles AJ, Janes RW, Wallace BA. Tools and methods for circular dichroism spectroscopy of proteins: a tutorial review. *Chem Soc Rev*. 2021;50(15):8400-8413. doi:10.1039/D0CS00558D

141. Compton LA, Johnson WC. Analysis of protein circular dichroism spectra for secondary structure using a simple matrix multiplication. *Anal Biochem*. 1986;155(1):155-167. doi:10.1016/0003-2697(86)90241-1

142. Sreerama N, Woody RW. Estimation of protein secondary structure from circular dichroism spectra: comparison of CONTIN, SELCON, and CDSSTR methods with an expanded reference set. *Anal Biochem*. 2000;287(2):252-260. doi:10.1006/ABIO.2000.4880

143. Sreerama N, Venyaminov SY, Woody RW. Estimation of protein secondary structure from circular dichroism spectra: inclusion of denatured proteins with native proteins in the analysis. *Anal Biochem*. 2000;287(2):243-251. doi:10.1006/ABIO.2000.4879

144. Gasteiger E, Hoogland C, Gattiker A, et al. The Proteomics Protocols Handbook - Chapter 52: Protein Identification and Analysis Tools on the ExPASy Server. *Proteomics Protoc Handb*. 2005:571-607. http://www.springerlink.com/content/v25w251748632172. Accessed July 13, 2022.

145. Miles AJ, Wallace BA. CDtoolX, a downloadable software package for processing and analyses of circular dichroism spectroscopic data. *Protein Sci*. 2018;27(9):1717-1722. doi:10.1002/PRO.3474

146. Drew ED, Janes RW. PDBMD2CD: providing predicted protein circular dichroism spectra from multiple molecular dynamics-generated protein structures. *Nucleic Acids Res*. 2020;48(W1):W17-W24. doi:10.1093/NAR/GKAA296

147. O'Neal CJ, Amaya EI, Jobling MG, Holmes RK, Hol WGJ. Crystal structures of an intrinsically active cholera toxin mutant yield insight into the toxin activation mechanism. *Biochemistry*. 2004;43(13):3772-3782. doi:10.1021/BI0360152

148. Stein PE, Boodhoo A, Armstrong GD, Cockle SA, Klein MH, Read RJ. The crystal structure of pertussis toxin. *Structure*. 1994;2(1):45-57. doi:10.1016/S0969-2126(00)00007-1

149. Pu X, Oxford JT. Proteomic analysis of engineered cartilage. *Methods Mol Biol*. 2015;1340:263. doi:10.1007/978-1-4939-2938-2_19

150. Xu Y, Barbieri JT. Pertussis toxin-catalyzed ADP-ribosylation of Gi-2 and Gi-3 in CHO cells is modulated by inhibitors of intracellular trafficking. *Infect Immun*. 1996;64(2):593-599. doi:10.1128/IAI.64.2.593-599.1996

151. García-Saura AG, Herzog LK, Dantuma NP, Schüler H. MacroGreen, a simple tool for detection of ADP-ribosylated proteins. *Commun Biol 2021 41*. 2021;4(1):1-8. doi:10.1038/s42003-021-02439-w

152. Jumper J, Evans R, Pritzel A, et al. Highly accurate protein structure prediction with AlphaFold. *Nat 2021 5967873*. 2021;596(7873):583-589. doi:10.1038/s41586-021-03819-2

153. Akdel M, Pires DE V, Pardo EP, et al. A structural biology community assessment of AlphaFold 2 applications. *bioRxiv*. September 2021:2021.09.26.461876. doi:10.1101/2021.09.26.461876

154. Bryant P, Pozzati G, Elofsson A. Improved prediction of protein-protein interactions using AlphaFold2. *Nat Commun 2022 131*. 2022;13(1):1-11. doi:10.1038/s41467-022-28865-w

155. Skolnick J, Gao M, Zhou H, Singh S. AlphaFold 2: Why It Works and Its Implications for Understanding the Relationships of Protein Sequence, Structure, and Function. *J Chem Inf Model*. 2021;61(10):4827. doi:10.1021/ACS.JCIM.1C01114

156. Evans R, O'Neill M, Pritzel A, et al. Protein complex prediction with AlphaFold-Multimer. *bioRxiv*. March 2022:2021.10.04.463034. doi:10.1101/2021.10.04.463034

157. Mariani V, Biasini M, Barbato A, Schwede T. lDDT: a local superposition-free score for comparing protein structures and models using distance difference tests. *Bioinformatics*. 2013;29(21):2722. doi:10.1093/BIOINFORMATICS/BTT473

158. UCSF ChimeraX User Guide. https://www.rbvi.ucsf.edu/chimerax/docs/user/index.html. Accessed August 7, 2022.

159. Kelley LA, Mezulis S, Yates CM, Wass MN, Sternberg MJE. The Phyre2 web portal for protein modeling, prediction and analysis. *Nat Protoc 2015 106*. 2015;10(6):845-858. doi:10.1038/nprot.2015.053

160. Okajima Y, Shimamura T, Ozawa A, Sasaki S. Molecular Properties of Cholera Enterotoxin. *Tokai J Exp Clin Med*. 1981;6(2):193-201.

161. Branson TR, McAllister TE, Garcia-Hartjes J, et al. A Protein-Based Pentavalent Inhibitor of the Cholera Toxin B-Subunit. *Angew Chemie*. 2014;126(32):8463-8467. doi:10.1002/ANGE.201404397

162. Fu O, Pukin A V., Vanufford HCQ, et al. Tetra- versus Pentavalent Inhibitors of Cholera Toxin. *ChemistryOpen*. 2015;4(4):471-477. doi:10.1002/OPEN.201500006

163. Zuilhof H. Fighting Cholera One-on-One: The Development and Efficacy of Multivalent Cholera-Toxin-Binding Molecules. *Acc Chem Res*. 2016;49(2):274-285. doi:10.1021/ACS.ACCOUNTS.5B00480/ASSET/IMAGES/LARGE/AR-2015-004804_0010.JPEG

164. Ohtomo N, Muraoka T, Tashiro A, Zinnaka Y, Amako K. Size and Structure of the Cholera Toxin Molecule and Its Subunits. *J Infect Dis*. 1976;133(Supplement_1):S31-S40. doi:10.1093/INFDIS/133.SUPPLEMENT_1.S31

165. Kurosky A, Markel DE, Touchstone B, Peterson JW. Chemical characterization of the structure of cholera toxin and its natural toxoid. *J Infect Dis*. 1976;133(March):S14-S22. doi:10.1093/infdis/133.supplement_1.s14

166. Lönnroth I, Holmgren J. Subunit structure of cholera toxin. *J Gen Microbiol*. 1973;76(2):417-427. doi:10.1099/00221287-76-2-417/CITE/REFWORKS

167. Ramalli SG, Miles AJ, Janes RW, Wallace BA. The PCDDB (Protein Circular Dichroism Data Bank): A Bioinformatics Resource for Protein Characterisations and Methods Development. *J Mol Biol*. 2022;434(11):167441. doi:10.1016/J.JMB.2022.167441

168. Klose DP, Wallace BA, Janes RW. DichroMatch: a website for similarity searching of circular dichroism spectra. *Nucleic Acids Res*. 2012;40(W1):W547-W552. doi:10.1093/NAR/GKS449

169. Barbieri JT, Cortina G. ADP-ribosyltransferase mutations in the catalytic S-1 subunit of pertussis toxin. *Infect Immun*. 1988;56(8):1934-1941. doi:10.1128/IAI.56.8.1934-1941.1988

170. Kaslow HR, Schlotterbeck JD, Mar VL, Burnette WN. Alkylation of Cysteine 41, but Not Cysteine 200, Decreases the ADP-ribosytransferase Activity of the S1 Subunit of Pertussis Toxin. *J Biol Chem*. 1989;264(11):6386-6390. doi:10.1016/S0021-9258(18)83361-0

171. Sakari M, Tran MT, Rossjohn J, Pulliainen AT, Beddoe T, Littler DR. Crystal structures of pertussis toxin with NAD+ and analogs provide structural insights into the mechanism of its cytosolic ADP-ribosylation activity. *J Biol Chem*. 2022;298(5):101892. doi:10.1016/J.JBC.2022.101892

172. Loosmore SM, Zealey GR, Boux HA, et al. Engineering of genetically detoxified pertussis toxin analogs for development of a recombinant whooping cough vaccine. *Infect Immun*. 1990;58(11):3653-3662. doi:10.1128/IAI.58.11.3653-3662.1990

173. Burnette WN, Cieplak W, Mar VL, Kaljot KT, Sato H, Keith JM. Pertussis Toxin S1 Mutant with Reduced Enzyme Activity and a Conserved Protective Epitope. *Science (80-)*. 1988;242(4875):72-74. doi:10.1126/SCIENCE.2459776

174. Pizza M, Bartoloni A, Prugnola A, Silvestri S, Rappuoli R. Subunit S1 of pertussis toxin: mapping of the regions essential for ADP-ribosyltransferase activity. *Proc Natl Acad Sci*. 1988;85(20):7521-7525. doi:10.1073/PNAS.85.20.7521

175. Sakari M, Tran MT, Rossjohn J, Pulliainen AT, Beddoe T, Littler DR. Crystal structures of pertussis toxin with NAD+ and analogs provide structural insights into the mechanism of its cytosolic ADP-ribosylation activity. *J Biol Chem*. 2022;298(5):101892. doi:10.1016/j.jbc.2022.101892

176. Zamith HP da S, Godinho RO, da Costa Junior VL, Corrado AP. The quantitative analysis of the mechanism involved in pertussis toxin-mediated cell clustering and its implications in the in vitro quality control of diphtheria tetanus and whole cell pertussis vaccines. *Toxicol Vitr*. 2021;70:105029. doi:10.1016/J.TIV.2020.105029

177.   Hazeki O, Ui M. Modification by islet-activating protein of receptor-mediated regulation of cyclic AMP accumulation in isolated rat heart cells. *J Biol Chem*. 1981;256(6):2856-2862. doi:10.1016/S0021-9258(19)69693-6

178.   Hoonakker ME, Ruiterkamp N, Hendriksen CFM. The cAMP assay: A functional in vitro alternative to the in vivo Histamine Sensitization test. *Vaccine*. 2010;28(5):1347-1352. doi:10.1016/J.VACCINE.2009.11.009

179.   Douglas-Bardsley A, Asokanathan C, Tierney S, Hockley J, Markey K. Collaborative study for the calibration of the replacement International Standard for pertussis toxin for use in histamine sensitisation and CHO cell clustering assays. *Biologicals*. 2019;62:85-92. doi:10.1016/J.BIOLOGICALS.2019.09.001

180.   Gray MC, Guerrant RL, Hewlett EL. The CHO Cell Clustering Response to Pertussis Toxin: History of Its Discovery and Recent Developments in Its Use. *Toxins 2021, Vol 13, Page 815*. 2021;13(11):815. doi:10.3390/TOXINS13110815

181.   Tinker JK, Erbe JL, Hol WGJ, Holmes RK. Cholera Holotoxin Assembly Requires a Hydrophobic Domain at the A-B5 Interface: Mutational Analysis and Development of an In Vitro Assembly System. *Infect Immun*. 2003;71(7):4093. doi:10.1128/IAI.71.7.4093-4101.2003

182.   Le Nours J, Paton AW, Byres E, et al. Structural Basis of Subtilase Cytotoxin SubAB Assembly. *J Biol Chem*. 2013;288(38):27505. doi:10.1074/JBC.M113.462622

183.   O'Neal CJ, Jobling MG, Holmes RK, Hol WGJ. Structural basis for the activation of cholera toxin by human ARF6-GTP. *Science (80-)*. 2005;309(5737):1093-1096. doi:10.1126/SCIENCE.1113398/SUPPL_FILE/ONEAL_SOM.PDF

184.   Reinert DJ, Carpusca I, Aktories K, Schulz GE. Structure of the Mosquitocidal Toxin from Bacillus sphaericus. *J Mol Biol*. 2006;357(4):1226-1236. doi:10.1016/J.JMB.2006.01.025

185.   Vaccines Licensed for Use in the United States | FDA. https://www.fda.gov/vaccines-blood-biologics/vaccines/vaccines-licensed-use-united-states. Accessed August 15, 2022.

186.   M P, MR F, V S, R R. Genetic detoxification of bacterial toxins. *Methods Mol Med*. 1996;4:361-378. doi:10.1385/0-89603-334-1:91

187. Lebens M, Terrinoni M, Karlsson SL, et al. Construction and preclinical evaluation of mmCT, a novel mutant cholera toxin adjuvant that can be efficiently produced in genetically manipulated Vibrio cholerae. *Vaccine*. 2016;34(18):2121-2128. doi:10.1016/J.VACCINE.2016.03.002

188. Clements JD, Norton EB. The Mucosal Vaccine Adjuvant LT(R192G/L211A) or dmLT. *mSphere*. 2018;3(4). doi:10.1128/MSPHERE.00215-18/ASSET/CD49F70A-069B-4E25-B29B-ECA92BCCB9BB/ASSETS/GRAPHIC/SPH0041825950002.JPEG

189. Seubert A, D'Oro U, Scarselli M, Pizza M. Genetically detoxified pertussis toxin (PT-9K/129G): implications for immunization and vaccines. *https://doi.org/101586/147605842014942641*. 2014;13(10):1191-1204. doi:10.1586/14760584.2014.942641

190. Sánchez J, Holmgren J. Virulence factors, pathogenesis and vaccine protection in cholera and ETEC diarrhea. *Curr Opin Immunol*. 2005;17(4):388-398. doi:10.1016/J.COI.2005.06.007

191. Hopp A-K, Hottiger MO, Hopp A-K;, Hottiger MO. Uncovering the Invisible: Mono-ADP-ribosylation Moved into the Spotlight. *Cells 2021, Vol 10, Page 680*. 2021;10(3):680. doi:10.3390/CELLS10030680

192. Kraus WL. PARPs and ADP-Ribosylation: 50 Years … and Counting. *Mol Cell*. 2015;58(6):902-910. doi:10.1016/J.MOLCEL.2015.06.006

193. Bütepage M, Eckei L, Verheugd P, Lüscher B. Intracellular Mono-ADP-Ribosylation in Signaling and Disease. *Cells 2015, Vol 4, Pages 569-595*. 2015;4(4):569-595. doi:10.3390/CELLS4040569

194. Corda D, Di Girolamo M. Functional aspects of protein mono-ADP-ribosylation. *EMBO J*. 2003;22(9):1953-1958. doi:10.1093/EMBOJ/CDG209

195. Feng B, Liu C, Shan L, He P. Protein ADP-Ribosylation Takes Control in Plant–Bacterium Interactions. *PLOS Pathog*. 2016;12(12):e1005941. doi:10.1371/JOURNAL.PPAT.1005941

196. Helander HF, Fändriks L. Surface area of the digestive tract – revisited. *http://dx.doi.org/103109/003655212014898326*. 2014;49(6):681-689. doi:10.3109/00365521.2014.898326

218

197. Paradis T, Bègue H, Basmaciyan L, Dalle F, Bon F. Tight Junctions as a Key for Pathogens Invasion in Intestinal Epithelial Cells. *Int J Mol Sci 2021, Vol 22, Page 2506*. 2021;22(5):2506. doi:10.3390/IJMS22052506

198. Alizadeh A, Akbari P, Garssen J, Fink-Gremmels J, Braber S. Epithelial integrity, junctional complexes, and biomarkers associated with intestinal functions. *https://doi.org/101080/2168837020211996830*. 2021. doi:10.1080/21688370.2021.1996830

199. Citi S. The mechanobiology of tight junctions. *Biophys Rev 2019 115*. 2019;11(5):783-793. doi:10.1007/S12551-019-00582-7

200. Monaco A, Ovryn B, Axis J, Amsler K. The Epithelial Cell Leak Pathway. *Int J Mol Sci 2021, Vol 22, Page 7677*. 2021;22(14):7677. doi:10.3390/IJMS22147677

201. Adil MS, Narayanan SP, Somanath PR. Cell-cell junctions: structure and regulation in physiology and pathology. *https://doi.org/101080/2168837020201848212*. 2020;9(1):1848212. doi:10.1080/21688370.2020.1848212

202. Kuo W-T, Odenwald MA, Turner JR, Zuo L, Li Zuo C. Tight junction proteins occludin and ZO-1 as regulators of epithelial proliferation and survival. *Ann N Y Acad Sci*. May 2022. doi:10.1111/NYAS.14798

203. Tsukita S, Tanaka H, Tamura A. The Claudins: From Tight Junctions to Biological Systems. *Trends Biochem Sci*. 2019;44(2):141-152. doi:10.1016/J.TIBS.2018.09.008

204. Garrido-Urbani S, Bradfield PF, Imhof BA. Tight junction dynamics: the role of junctional adhesion molecules (JAMs). *Cell Tissue Res*. 2014;355(3):701-715. doi:10.1007/S00441-014-1820-1

205. Venugopal S, Anwer S, Szászi K. Claudin-2: Roles beyond Permeability Functions. *Int J Mol Sci 2019, Vol 20, Page 5655*. 2019;20(22):5655. doi:10.3390/IJMS20225655

206. Pinheiro D, Bellaïche Y. Mechanical Force-Driven Adherens Junction Remodeling and Epithelial Dynamics. *Dev Cell*. 2018;47(1):3-19. doi:10.1016/J.DEVCEL.2018.09.014

207. Nighot P, Ma T. Endocytosis of Intestinal Tight Junction Proteins: In Time and Space. *Inflamm Bowel Dis*. 2021;27(2):283-290. doi:10.1093/IBD/IZAA141

208. Lock JG, Stow JL. Rab11 in Recycling Endosomes Regulates the Sorting and Basolateral Transport of E-Cadherin. *https://doi.org/101091/mbc.e04-10-0867*. 2005;16(4):1744-1755. doi:10.1091/MBC.E04-10-0867

209. Marzesco AM, Dunia I, Pandjaitan R, et al. The Small GTPase Rab13 Regulates Assembly of Functional Tight Junctions in Epithelial Cells. *Mol Biol Cell*. 2002;13(6):1819. doi:10.1091/MBC.02-02-0029

210. Zerial M, McBride H. Rab proteins as membrane organizers. *Nat Rev Mol Cell Biol 2001 22*. 2001;2(2):107-117. doi:10.1038/35052055

211. RS G, MP M, YW W. Mechanisms of action of Rab proteins, key regulators of intracellular vesicular transport. *Biol Chem*. 2017;398(5-6):565-575. doi:10.1515/HSZ-2016-0274

212. Waschbüsch D, Khan AR. Phosphorylation of Rab GTPases in the regulation of membrane trafficking. *Traffic*. 2020;21(11):712-719. doi:10.1111/TRA.12765

213. Müller MP, Goody RS. Molecular control of Rab activity by GEFs, GAPs and GDI. *https://doi.org/101080/2154124820161276999*. 2017;9(1-2):5-21. doi:10.1080/21541248.2016.1276999

214. Cheng X, Ji Z, Tsalkova T, Mei F. Epac and PKA: a tale of two intracellular cAMP receptors. *Acta Biochim Biophys Sin (Shanghai)*. 2008;40(7):651. doi:10.1111/J.1745-7270.2008.00438.X

215. Pannekoek WJ, Kooistra MRH, Zwartkruis FJT, Bos JL. Cell–cell junction formation: The role of Rap1 and Rap1 guanine nucleotide exchange factors. *Biochim Biophys Acta - Biomembr*. 2009;1788(4):790-796. doi:10.1016/J.BBAMEM.2008.12.010

216. Pannekoek WJ, Linnemann JR, Brouwer PM, Bos JL, Rehmann H. Rap1 and Rap2 Antagonistically Control Endothelial Barrier Resistance. *PLoS One*. 2013;8(2):e57903. doi:10.1371/JOURNAL.PONE.0057903

217. Guichard A, Nizet V, Bier E. Rab11-mediated trafficking in host-pathogen interactions. *Nat Rev Microbiol*. 2014;12(9):624. doi:10.1038/NRMICRO3325

218. Zhai X, Leo MD, Jaggar JH. Endothelin-1 Stimulates Vasoconstriction Through Rab11A Serine 177 Phosphorylation. *Circ Res*. 2017;121(6):650. doi:10.1161/CIRCRESAHA.117.311102

219. Köhler K, Zahraoui A. Tight junction: a co-ordinator of cell signalling and membrane trafficking. *Biol Cell*. 2005;97(8):659-665. doi:10.1042/BC20040147

220. Zheng M, Sun S, Zhou J, Liu M. Virulence factors impair epithelial junctions during bacterial infection. *J Clin Lab Anal*. 2021;35(2):e23627. doi:10.1002/JCLA.23627

221. Le Guennec L, Coureuil M, Nassif X, Bourdoulous S. Strategies used by bacterial pathogens to cross the blood–brain barrier. *Cell Microbiol*. 2020;22(1):e13132. doi:10.1111/CMI.13132

222. Linfield DT, Raduka A, Aghapour M, Rezaee F. Airway tight junctions as targets of viral infections. *https://doi.org/101080/2168837020211883965*. 2021;9(2). doi:10.1080/21688370.2021.1883965

223. Catara G, Corteggio A, Valente C, Grimaldi G, Palazzo L. Targeting ADP-ribosylation as an antimicrobial strategy. *Biochem Pharmacol*. 2019;167:13. doi:10.1016/J.BCP.2019.06.001

224. Magnusson K-E, Kihlström E, Sundqvist T. Effect of cholera toxin on rat intestinal permeability assessed with fluorescent dextran 3000. *FEMS Microbiol Lett*. 1985;29(1-2):15-18. doi:10.1111/J.1574-6968.1985.TB00827.X

225. Ohishi I, Odagiri Y. Histopathological effect of botulinum C2 toxin on mouse intestines. *Infect Immun*. 1984;43(1):54-58. doi:10.1128/iai.43.1.54-58.1984

226. Triadafilopoulos G, Pothoulakis C, Weiss R, Giampaolo C, LaMont JT. Comparative study of Clostridium difficile toxin a and cholera toxin in rabbit ileum. *Gastroenterology*. 1989;97(5):1186-1192. doi:10.1016/0016-5085(89)91689-2

227. Lencer W, Delp C, Neutra M, Madara J. Mechanism of cholera toxin action on a polarized human intestinal epithelial cell line: role of vesicular traffic. *J Cell Biol*. 1992;117(6):1197-1209. doi:10.1083/JCB.117.6.1197

228. Shapiro M, Matthews J, Hecht G, Delp C, Madara JL. Stabilization of F-actin prevents cAMP-elicited Cl- secretion in T84 cells. *J Clin Invest*. 1991;87(6):1903-1909. doi:10.1172/JCI115215

229. Markov AG, Vishnevskaya ON, Okorokova LS, et al. Cholera toxin perturbs the paracellular barrier in the small intestinal epithelium of rats by affecting claudin-2 and tricellulin. *Pflügers Arch - Eur J Physiol 2019 4719*. 2019;471(9):1183-1189. doi:10.1007/S00424-019-02294-Z

230. Markov AG, Falchuk EL, Kruglova NM, Rybalchenko O V., Fromm M, Amasheh S. Comparative analysis of theophylline and cholera toxin in rat colon reveals an induction of sealing tight junction proteins. *Pflügers Arch - Eur J Physiol 2014 46611*. 2014;466(11):2059-2065. doi:10.1007/S00424-014-1460-Z

231. Patterson CE, Stasek JE, Schaphorst KL, Davis HW, Garcia JGN. Mechanisms of pertussis toxin-induced barrier dysfunction in bovine pulmonary artery endothelial cell monolayers. *Am J Physiol - Lung Cell Mol Physiol*. 1995;268(6 12-6). doi:10.1152/ajplung.1995.268.6.l926

232. Brückener KE, el Bayâ A, Galla H-J, Schmidt MA. Permeabilization in a cerebral endothelial barrier model by pertussis toxin involves the PKC effector pathway and is abolished by elevated levels of cAMP. *J Cell Sci*. 2003;116(9):1837-1846. doi:10.1242/JCS.00378

233. Seidel G, Böcker K, Schulte J, et al. Pertussis toxin permeabilization enhances the traversal of Escherichia coli K1, macrophages, and monocytes in a cerebral endothelial barrier model in vitro. *Int J Med Microbiol*. 2011;301(3):204-212. doi:10.1016/J.IJMM.2010.08.018

234. Starost LJ, Karassek S, Sano Y, et al. Pertussis Toxin Exploits Host Cell Signaling Pathways Induced by Meningitis-Causing E. coli K1-RS218 and Enhances Adherence of Monocytic THP-1 Cells to Human Cerebral Endothelial Cells. *Toxins 2016, Vol 8, Page 291*. 2016;8(10):291. doi:10.3390/TOXINS8100291

235. Karassek S, Starost L, Solbach J, et al. Pertussis Toxin Exploits Specific Host Cell Signaling Pathways for Promoting Invasion and Translocation of Escherichia coli K1 RS218 in Human Brain-derived Microvascular Endothelial Cells *. *J Biol Chem*. 2015;290(41):24835-24843. doi:10.1074/JBC.M115.650101

236. JX Y, Z T, Y G, et al. Pertussis toxin modulates microglia and T cell profile to protect experimental autoimmune encephalomyelitis. *Neuropharmacology*. 2014;81:1-5. doi:10.1016/J.NEUROPHARM.2014.01.027

237. Köhler H, Sakaguchi T, Hurley BP, Kase BJ, Reinecker H-C, McCormick BA. Salmonella enterica serovar Typhimurium regulates intercellular junction proteins and facilitates transepithelial neutrophil and bacterial passage. *https://doi.org/101152/ajpgi005352006*. 2007;293(1). doi:10.1152/AJPGI.00535.2006

238. Calatayud M, Dezutter O, Hernandez-Sanabria E, Hidalgo-Martinez S, Meysman FJR, Van De Wiele T. Development of a host-microbiome model of the small intestine. *FASEB J*. 2019;33(3):3985-3996. doi:10.1096/FJ.201801414R

239. Darling NJ, Mobbs CL, González-Hau AL, Freer M, Przyborski S. Bioengineering Novel in vitro Co-culture Models That Represent the Human Intestinal Mucosa With Improved Caco-2 Structure and Barrier Function. *Front Bioeng Biotechnol*. 2020;8:992. doi:10.3389/FBIOE.2020.00992/BIBTEX

240. Hoffmann P, Burmester M, Langeheine M, et al. Caco-2/HT29-MTX co-cultured cells as a model for studying physiological properties and toxin-induced effects on intestinal cells. *PLoS One*. 2021;16(10):e0257824. doi:10.1371/JOURNAL.PONE.0257824

241. Boerner K, Luissint AC, Parkos CA. Functional Assessment of Intestinal Permeability and Neutrophil Transepithelial Migration in Mice using a Standardized Intestinal Loop Model. *JoVE (Journal Vis Exp*. 2021;2021(168):e62093. doi:10.3791/62093

242. Dickson BC, Streutker CJ, Chetty R. Coeliac disease: an update for pathologists. *J Clin Pathol*. 2006;59(10):1008. doi:10.1136/JCP.2005.035345

243. Heikkilä AM, Liski E, Pyörälä S, Taponen S. Pathogen-specific production losses in bovine mastitis. *J Dairy Sci*. 2018;101(10):9493-9504. doi:10.3168/jds.2018-14824

244. *Dairy 2014: Milk Quality, Milking Procedures, and Mastitis on U.S. Dairies*. Washington, DC, USA; 2016. https://www.aphis.usda.gov/animal_health/nahms/dairy/downloads/dairy14/Dairy 14_dr_Mastitis.pdf.

245. Roberson JR, Fox LK, Hancock DD, Gay JM, Besser TE. Sources of Intramammary Infections from Staphylococcus aureus in Dairy Heifers at First Parturition. *J Dairy Sci*. 1998;81(3):687-693. doi:10.3168/jds.S0022-0302(98)75624-3

246. Hébert A, Sayasith K, Sénéchal S, Dubreuil P, Lagacé J. Demonstration of intracellular Staphylococcus aureus in bovine mastitis alveolar cells and macrophages isolated from naturally infected cow milk. *FEMS Microbiol Lett*. 2000;193(1):57-62. doi:10.1111/j.1574-6968.2000.tb09402.x

247. Sacco SC, Velázquez NS, Renna MS, et al. Capacity of two Staphylococcus aureus strains with different adaptation genotypes to persist and induce damage in bovine mammary epithelial cells and to activate macrophages. *Microb Pathog*. 2020;142:104017. doi:10.1016/j.micpath.2020.104017

248. Zaatout N, Ayachi A, Kecha M. Staphylococcus aureus persistence properties associated with bovine mastitis and alternative therapeutic modalities. *J Appl Microbiol*. 2020;129(5):1102-1119. doi:10.1111/jam.14706

249. Sol J, Sampimon OC, Snoep JJ, Schukken YH. Factors Associated with Bacteriological Cure during Lactation after Therapy for Subclinical Mastitis Caused by Staphylococcus aureus. *J Dairy Sci*. 1997;80(11):2803-2808. doi:10.3168/jds.S0022-0302(97)76243-X

250. Rollin E, Dhuyvetter KC, Overton MW. The cost of clinical mastitis in the first 30 days of lactation: An economic modeling tool. *Prev Vet Med*. 2015;122(3):257-264. doi:10.1016/j.prevetmed.2015.11.006

251. Cha E, Bar D, Hertl JA, et al. The cost and management of different types of clinical mastitis in dairy cows estimated by dynamic programming. *J Dairy Sci*. 2011;94(9):4476-4487. https://pubmed.ncbi.nlm.nih.gov/21854920/. Accessed September 15, 2020.

252. Middleton JR, Ma J, Rinehart CL, Taylor VN, Luby CD, Steevens BJ. Efficacy of different Lysigin[TM] formulations in the prevention of Staphylococcus aureus intramammary infection in dairy heifers. *J Dairy Res*. 2006;73(1):10-19. doi:10.1017/S0022029905001354

253. Schukken YH, Bronzo V, Locatelli C, et al. Efficacy of vaccination on Staphylococcus aureus and coagulase-negative staphylococci intramammary infection dynamics in 2 dairy herds. *J Dairy Sci*. 2014;97(8):5250-5264. doi:10.3168/jds.2014-8008

254. Bradley AJ, Breen JE, Payne B, White V, Green MJ. An investigation of the efficacy of a polyvalent mastitis vaccine using different vaccination regimens under field conditions in the United Kingdom. *J Dairy Sci*. 2015;98(3):1706-1720. doi:10.3168/jds.2014-8332

255. Piepers S, Prenafeta A, Verbeke J, De Visscher A, March R, De Vliegher S. Immune response after an experimental intramammary challenge with killed Staphylococcus aureus in cows and heifers vaccinated and not vaccinated with Startvac, a polyvalent mastitis vaccine. *J Dairy Sci*. 2017;100(1):769-782. doi:10.3168/JDS.2016-11269

256. Landin H, Mörk MJ, Larsson M, Waller KP. Vaccination against Staphylococcus aureus mastitis in two Swedish dairy herds. *Acta Vet Scand*. 2015;57(1). doi:10.1186/s13028-015-0171-6

257. Freick M, Frank Y, Steinert K, Hamedy A, Passarge O, Sobiraj A. Mastitis vaccination using a commercial polyvalent vaccine or a herd-specific Staphylococcus aureus vaccine: Results of a controlled field trial on a dairy farm. *Tierarztl Prax Ausgabe G Grosstiere - Nutztiere*. 2016;44(4):219-229. doi:10.15653/TPG-150912

258. Kim HK, DeDent A, Cheng AG, et al. IsdA and IsdB antibodies protect mice against Staphylococcus aureus abscess formation and lethal challenge. *Vaccine*. 2010;28(38):6382-6392. doi:10.1016/j.vaccine.2010.02.097

259. Clarke SR, Andre G, Walsh EJ, Dufrêne YF, Foster TJ, Foster SJ. Iron-regulated surface determinant protein A mediates adhesion of Staphylococcus aureus to human corneocyte envelope proteins. *Infect Immun*. 2009;77(6):2408-2416. doi:10.1128/IAI.01304-08

260. Stapleton MR, Wright L, Clarke SR, et al. Identification of conserved antigens from staphylococcal and streptococcal pathogens. *J Med Microbiol*. 2012;61(6):766-779. doi:10.1099/jmm.0.040915-0

261. Clarke SR, Brummell KJ, Horsburgh MJ, et al. Identification of in vivo-expressed antigens of Staphylococcus aureus and their use in vaccinations for protection against nasal carriage. *J Infect Dis*. 2006;193(8):1098-1108. doi:10.1086/501471

262. Wolf C, Kusch H, Monecke S, et al. Genomic and proteomic characterization of Staphylococcus aureus mastitis isolates of bovine origin. *Proteomics*. 2011;11(12):2491-2502. doi:10.1002/pmic.201000698

263. Herron-Olson L, Fitzgerald JR, Musser JM, Kapur V. Molecular Correlates of Host Specialization in Staphylococcus aureus. *PLoS One*. 2007;2(10):e1120. doi:10.1371/JOURNAL.PONE.0001120

264. Bouchard D, Peton V, Almeida S, et al. Genome sequence of staphylococcus aureus newbould 305, a strain associated with mild bovine mastitis. *J Bacteriol*. 2012;194(22):6292-6293. doi:10.1128/JB.01188-12

265. Misra N, Wines TF, Knopp CL, McGuire MA, Tinker JK. Expression, immunogenicity and variation of iron-regulated surface protein A from bovine isolates of Staphylococcus aureus. *FEMS Microbiol Lett*. 2017;364(9):82. doi:10.1093/femsle/fnx082

266. Xu H, Hu C, Gong R, et al. Evaluation of a novel chimeric B cell epitope-based vaccine against mastitis induced by either Streptococcus agalactiae or Staphylococcus aureus in mice. *Clin Vaccine Immunol*. 2011;18(6):893-900. doi:10.1128/CVI.00066-11

267. Castagliuolo I, Piccinini R, Beggiao E, et al. Mucosal genetic immunization against four adhesins protects against Staphylococcus aureus-induced mastitis in mice. *Vaccine*. 2006;24(20):4393-4402. doi:10.1016/j.vaccine.2006.02.055

268. Gong R, Hu C, Xu H, et al. Evaluation of clumping factor a binding region a in a subunit vaccine against Staphylococcus aureus-induced mastitis in mice. *Clin Vaccine Immunol*. 2010;17(11):1746-1752. doi:10.1128/CVI.00162-10

269. Maira-Litrán T, Bentancor L V., Bozkurt-Guzel C, O'Malley JM, Cywes-Bentley C, Pier GB. Synthesis and Evaluation of a Conjugate Vaccine Composed of Staphylococcus aureus Poly-N-Acetyl-Glucosamine and Clumping Factor A. *PLoS One*. 2012;7(9):e43813. doi:10.1371/JOURNAL.PONE.0043813

270. Hawkins J, Kodali S, Matsuka Y V., et al. A recombinant clumping factor A-containing vaccine induces functional antibodies to Staphylococcus aureus that are not observed after natural exposure. *Clin Vaccine Immunol*. 2012;19(10):1641-1650. doi:10.1128/CVI.00354-12

271. Creech CB, Frenck RW, Fiquet A, et al. Persistence of immune responses through 36 months in healthy adults after vaccination with a novel Staphylococcus aureus 4-Antigen Vaccine (SA4Ag). *Open Forum Infect Dis*. 2020;7(1). doi:10.1093/ofid/ofz532

272. Fluit AC, Terlingen AM, Andriessen L, et al. Evaluation of the DiversiLab system for detection of hospital outbreaks of infections by different bacterial species. *J Clin Microbiol*. 2010;48(11):3979-3989. doi:10.1128/JCM.01191-10

273. Gómez MI, Sordelli DO, Buzzola FR, García VE. Induction of cell-mediated immunity to Staphylococcus aureus in the mouse mammary gland by local immunization with a live attenuated mutant. *Infect Immun*. 2002;70(8):4254-4260. doi:10.1128/IAI.70.8.4254-4260.2002

274. Lee JW, O'Brien CN, Guidry AJ, Paape MJ, Shafer-Weaver KA, Zhao X. Effect of a trivalent vaccine against Staphylococcus aureus mastitis lymphocyte subpopulations, antibody production, and neutrophil phagocytosis. *Can J Vet Res*. 2005;69(1):11-18. /pmc/articles/PMC1142164/. Accessed June 7, 2022.

275. Camussone CM, Veaute CM, Porporatto C, Morein B, Marcipar IS, Calvinho LF. Immune response of heifers against a Staphylococcus aureus CP5 whole cell vaccine formulated with ISCOMATRIX^{TM} adjuvant. *J Dairy Res*. 2013;80(1):72-80. doi:10.1017/S0022029912000593

276. Riollet C, Rainard P, Poutrel B. Cell subpopulations and cytokine expression in cow milk in response to chronic Staphylococcus aureus infection. *J Dairy Sci*. 2001;84(5):1077-1084. doi:10.3168/jds.S0022-0302(01)74568-7

277. Lin L, Ibrahim AS, Xu X, et al. Th1-Th17 cells mediate protective adaptive immunity against Staphylococcus aureus and Candida albicans infection in mice. *PLoS Pathog*. 2009;5(12):e1000703. doi:10.1371/journal.ppat.1000703

278. Snider DP. The mucosal adjuvant activities of ADP-ribosylating bacterial enterotoxins. *Crit Rev Immunol*. 2017;37(2-6):499-530. doi:10.1615/CritRevImmunol.v37.i2-6.150

279. George-Chandy A, Eriksson K, Lebens M, Nordström I, Schön E, Holmgren J. Cholera toxin B subunit as a carrier molecule promotes antigen presentation and increases CD40 and CD86 expression on antigen-presenting cells. *Infect Immun*. 2001;69(9):5716-5725. doi:10.1128/IAI.69.9.5716-5725.2001

280. Schnitzler AC, Burke JM, Wetzler LM. Induction of cell signaling events by the cholera toxin B subunit in antigen-presenting cells. *Infect Immun*. 2007;75(6):3150-3159. doi:10.1128/IAI.00581-06

281. Nashar TO, Hirst TR, Williams NA. Modulation of B-cell activation by the B subunit of Escherichia coli enterotoxin: Receptor interaction up-regulates MHC class II, B7, CD40, CD25 and ICAM-1. *Immunology*. 1997;91(4):572-578. doi:10.1046/j.1365-2567.1997.00291.x

282. Bromander AK, Kjerrulf M, Holmgren J, Lycke N. *Cholera Toxin Enhances Antigen Presentation*. Vol 371.; 1995:1501-1506. https://europepmc.org/article/med/7502845. Accessed September 15, 2020.

283. Cong Y, Weaver CT, Elson CO. The mucosal adjuvanticity of cholera toxin involves enhancement of costimulatory activity by selective up-regulation of B7.2 expression. 1997;159(11):5301-5308. http://www.ncbi.nlm.nih.gov/pubmed/9548469. Accessed September 15, 2020.

284. Xu-Amano J, Jackson RJ, Fujihashi K, Kiyono H, Staats HF, McGhee JR. Helper Th1 and Th2 cell responses following mucosal or systemic immunization with cholera toxin. *Vaccine*. 1994;12(10):903-911. doi:10.1016/0264-410X(94)90033-7

285. Mattsson J, Schön K, Ekman L, Fahlén-Yrlid L, Yrlid U, Lycke NY. Cholera toxin adjuvant promotes a balanced Th1/Th2/Th17 response independently of IL-12 and IL-17 by acting on Gsα in CD11b+ DCs. *Mucosal Immunol 2015 84*. 2014;8(4):815-827. doi:10.1038/mi.2014.111

286. Jobling MG, Holmes RK. Fusion proteins containing the A2 domain of cholera toxin assemble with B polypeptides of cholera toxin to form immunoreactive and functional holotoxin-like chimeras. *Infect Immun*. March . https://journals.asm.org/doi/abs/10.1128/iai.60.11.4915-4924.1992. Accessed June 7, 2022.

287. Hajishengallis G, Hollingshead SK, Koga T, Russell MW. Mucosal immunization with a bacterial protein antigen genetically coupled to cholera toxin A2/B subunits. *J Immunol*. 1995;154(9):4322-4332.

288. Martin M, Hajishengallis G, Metzger DJ, Michalek SM, Connell TD, Russell MW. Recombinant antigen-enterotoxin A2/B chimeric mucosal immunogens differentially enhance antibody responses and B7-dependent costimulation of CD4+ T cells. *Infect Immun*. 2001;69(1):252-261. doi:10.1128/IAI.69.1.252-261.2001

289. Sultan F, Jin LL, Jobling MG, Holmes RK, Stanley SL. Mucosal immunogenicity of a holotoxin-like molecule containing the serine-rich Entamoeba histolytica protein (SREHP) fused to the A2 domain of cholera toxin. *Infect Immun*. 1998;66(2):462-468. https://journals.asm.org/doi/full/10.1128/IAI.66.2.462-468.1998. Accessed June 7, 2022.

290. Misra N, Wines TF, Knopp CL, et al. Immunogenicity of a Staphylococcus aureus-cholera toxin A2/B vaccine for bovine mastitis. *Vaccine*. 2018;36(24):3513-3521. doi:10.1016/J.VACCINE.2018.04.067

291. Prasad LB, Newbould FH. Inoculation of the bovine teat duct with Staph. Aureus: the relationship of teat duct length, milk yield and milking rate to development of intramammary infection. *Can Vet J*. 1968;9(5):107. https://www.ncbi.nlm.nih.gov/pmc/articles/PMC1697182/. Accessed June 7, 2022.

292. Arlian BM, Tinker JK. Mucosal immunization with a Staphylococcus aureus IsdA-cholera toxin A 2/B chimera induces antigen-specific Th2-type responses in mice. *Clin Vaccine Immunol*. 2011;18(9):1543-1551. https://pubmed.ncbi.nlm.nih.gov/21734065/. Accessed September 15, 2020.

293. Gonzales VK, De Mulder ELW, De Boer T, et al. Platelet-rich plasma can replace fetal bovine serum in human meniscus cell cultures. *Tissue Eng - Part C Methods*. 2013;19(11):892-899. doi:10.1089/ten.tec.2013.0009

294. Coussens PM, Verman N, Coussens MA, Elftman MD, McNulty AM. Cytokine Gene Expression in Peripheral Blood Mononuclear Cells and Tissues of Cattle Infected with Mycobacterium avium subsp. paratuberculosis: Evidence for An Inherent Proinflammatory Gene Expression Pattern. *Infect Immun*. 2004;72(3):1409-1422. doi:10.1128/IAI.72.3.1409-1422.2004/ASSET/8397B14C-BC08-454F-8A15-4441E20B2FA3/ASSETS/GRAPHIC/ZII0030412060005.JPEG

295. Wenz JR, Garry FB, Barrington GM. Comparison of disease severity scoring systems for dairy cattle with acute coliform mastitis. *J Am Vet Med Assoc*. 2006;229(2):259-262. doi:10.2460/javma.229.2.259

296. Atalla H, Gyles C, Wilkie B, Leslie K, Mallard B. Somatic cell scores and clinical signs following experimental intramammary infection of dairy cows with a Staphylococcus aureus small colony variant (S. aureus SCV) in comparison to other bovine strains. *Vet Microbiol*. 2009;137(3-4):326-334. doi:10.1016/j.vetmic.2009.01.027

297. Livak KJ, Schmittgen TD. Analysis of relative gene expression data using real-time quantitative PCR and the 2-ΔΔCT method. *Methods*. 2001;25(4):402-408. doi:10.1006/meth.2001.1262

298. Shkreta L, Talbot BG, Diarra MS, Lacasse P. Immune responses to a DNA/protein vaccination strategy against Staphylococcus aureus induced mastitis in dairy cows. *Vaccine*. 2004;23(1):114-126. doi:10.1016/j.vaccine.2004.05.002

299. Leitner G, Lubashevsky E, Glickman A, Winkler M, Saran A, Trainin Z. Development of a Staphylococcus aureus vaccine against mastitis in dairy cows: I. Challenge trials. *Vet Immunol Immunopathol*. 2003;93(1-2):31-38. doi:10.1016/S0165-2427(03)00051-5

300. Anderson D, Burnham K. *Model Selection and Multi-Model Inference: A Practical Information-Theoretic Approach*. 2nd ed. New York, NY, USA: Springer; 2002.

301. Benjamini Y, Hochberg Y. *Controlling the False Discovery Rate: A Practical and Powerful Approach to Multiple Testing*. Vol 57. John Wiley & Sons, Ltd; 1995:289-300. doi:10.1111/J.2517-6161.1995.TB02031.X

302. Burvenich C, Van Merris V, Mehrzad J, Diez-Fraile A, Duchateau L. *Severity of E. Coli Mastitis Is Mainly Determined by Cow Factors*. Vol 34. EDP Sciences; 2003:521-564. http://dx.doi.org/10.1051/vetres:2003023. Accessed September 15, 2020.

303. Proctor RA. Immunity to Staphylococcus aureus : Implications for Vaccine Development. *Microbiol Spectr*. 2019;7(4). doi:10.1128/microbiolspec.gpp3-0037-2018

304. Wilson GJ, Tuffs SW, Wee BA, et al. Bovine Staphylococcus aureus superantigens stimulate the entire T cell repertoire of cattle. *Infect Immun*. 2018;86(11). doi:10.1128/IAI.00505-18/SUPPL_FILE/ZII999092591S1.PDF

305. Günther J, Petzl W, Bauer I, et al. Differentiating Staphylococcus aureus from Escherichia coli mastitis: S. aureus triggers unbalanced immune-dampening and host cell invasion immediately after udder infection. *Sci Rep*. 2017;7(1):1-14. doi:10.1038/s41598-017-05107-4

306. Schukken YH, Mallard BA, Dekkers JCM, Leslie KE, Stear MJ. Genetic Impact on the Risk of Intramammary Infection Following Staphylococcus aureus Challenge. *J Dairy Sci*. 1994;77(2):639-647. doi:10.3168/jds.S0022-0302(94)76994-0

307. Kim Y, Atalla H, Mallard B, Robert C, Karrow N. Changes in Holstein cow milk and serum proteins during intramammary infection with three different strains of Staphylococcus aureus. *BMC Vet Res*. 2011;7(1):1-13. doi:10.1186/1746-6148-7-51

308. Liu T, Wei Y, Liu G, et al. A mutated cholera toxin without the ADP-ribosyltransferase activity induces cytokine production and inhibits apoptosis of splenocytes in mice possibly via toll-like receptor-4 signaling. *Mol Immunol*. 2016;75:21-27. doi:10.1016/j.molimm.2016.05.005

309. Wiedinger K, Pinho D, Bitsaktsis C. Utilization of cholera toxin B as a mucosal adjuvant elicits antibody-mediated protection against S. pneumoniae infection in mice. *Ther Adv Vaccines*. 2017;5(1):15-24. doi:10.1177/2051013617691041

310. Anjuère F, George-Chandy A, Audant F, Rousseau D, Holmgren J, Czerkinsky C. Transcutaneous Immunization with Cholera Toxin B Subunit Adjuvant Suppresses IgE Antibody Responses Via Selective Induction of Th1 Immune Responses. *J Immunol*. 2003;170(3):1586-1592. doi:10.4049/jimmunol.170.3.1586

311. Albu DI, Jones-Trower A, Woron AM, Stellrecht K, Broder CC, Metzger DW. Intranasal Vaccination Using Interleukin-12 and Cholera Toxin Subunit B as Adjuvants To Enhance Mucosal and Systemic Immunity to Human Immunodeficiency Virus Type 1 Glycoproteins. *J Virol*. 2003;77(10):5589-5597. doi:10.1128/jvi.77.10.5589-5597.2003

312. Baldauf KJ, Royal JM, Hamorsky KT, Matoba N. Cholera Toxin B: One Subunit with Many Pharmaceutical Applications. *Toxins 2015, Vol 7, Pages 974-996*. 2015;7(3):974-996. doi:10.3390/TOXINS7030974

313. Holmgren J, Harandi AM, Czerkinsky C. Mucosal adjuvants and anti-infection and anti-immunopathology vaccines based on cholera toxin, cholera toxin B subunit and CpG DNA. *Expert Rev Vaccines*. 2003;2(2):205-217. doi:10.1586/14760584.2.2.205

314. Royal JM, Matoba N. Therapeutic potential of cholera toxin b subunit for the treatment of inflammatory diseases of the Mucosa. *Toxins (Basel)*. 2017;9(12):379. doi:10.3390/toxins9120379

315. Zhang L, Huang Y, Lin Y, et al. Anti-inflammatory effect of cholera toxin B subunit in experimental stroke. *J Neuroinflammation*. 2016;13(1):1-14. doi:10.1186/s12974-016-0610-y

316. Russell MW, Moldoveanu Z, White PL, Sibert GJ, Mestecky J, Michalek SM. Salivary, nasal, genital, and systemic antibody responses in monkeys immunized intranasally with a bacterial protein antigen and the Cholera toxin B subunit. *Infect Immun*. 1996;64(4):1272-1283. doi:10.1128/IAI.64.4.1272-1283.1996

317. Alabdullah HA, Overgaard E, Scarbrough D, et al. Evaluation of the efficacy of a cholera-toxin-based staphylococcus aureus vaccine against bovine intramammary challenge. *Vaccines*. 2021;9(1):1-17. doi:10.3390/vaccines9010006

318. Misra N, Wines TF, Knopp CL, McGuire MA, Tinker JK. Expression, immunogenicity and variation of iron-regulated surface protein A from bovine isolates of Staphylococcus aureus. *FEMS Microbiol Lett*. 2017;364(9):82. doi:10.1093/FEMSLE/FNX082

319. Mazinani M, Rude B. Population, World Production and Quality of Sheep and Goat Products. 2020. doi:10.3844/ajavsp.2020.291.299

320. Lu CD, Miller BA. Current status, challenges and prospects for dairy goat production in the Americas. *Asian-Australasian J Anim Sci*. 2019;32(8):1244. doi:10.5713/AJAS.19.0256

321. Miller BA, Lu CD. Current status of global dairy goat production: an overview. *Asian-Australasian J Anim Sci*. 2019;32(8):1219. doi:10.5713/AJAS.19.0253

322. Mahlangu P, Maina N, Kagira J. and Antibiogram of Bacteria Isolated from Milk of Goats with Subclinical Mastitis in Thika East Subcounty, Kenya. *Res Artic Preval*. 2018. doi:10.1155/2018/3801479

323. Akter S, Rahman MM, Sayeed MA, et al. Prevalence, aetiology and risk factors of subclinical mastitis in goats in Bangladesh. *Small Rumin Res*. 2020;184:106046. doi:10.1016/J.SMALLRUMRES.2020.106046

324. Donmez E, Kirkan S. Virulence Properties of Staphylococcus Species from Goats Investigation of Virulence Properties of Staphylococcus Species Isolated from Goats with Subclinical Mastitis. *Isr J Vet Med* □. 2022;77(2).

325. Mishra AK, Sharma N, Singh DD, et al. Prevalence and bacterial etiology of subclinical mastitis in goats reared in organized farms. *Vet World*. 2018;11(1):20. doi:10.14202/VETWORLD.2018.20-24

326. Balemi A, Gumi B, Amenu K, et al. Prevalence of Mastitis and Antibiotic Resistance of Bacterial Isolates from CMT Positive Milk Samples Obtained from Dairy Cows, Camels, and Goats in Two Pastoral Districts in Southern Ethiopia. *Anim 2021, Vol 11, Page 1530*. 2021;11(6):1530. doi:10.3390/ANI11061530

327. Hussein HA, Fouad MT, Abd El-Razik KA, et al. Study on prevalence and bacterial etiology of mastitis, and effects of subclinical mastitis and stage of lactation on SCC in dairy goats in Egypt. *Trop Anim Health Prod*. 2020;52(6):3091-3097. doi:10.1007/S11250-020-02331-5/TABLES/7

328. Gabli Z, Djerrou Z, Gabli AE, Bensalem M. Prevalence of mastitis in dairy goat farms in Eastern Algeria. *Vet World*. 2019;12(10):1563. doi:10.14202/VETWORLD.2019.1563-1572

329. Danmallam FA, Pimenov NV. Study on prevalence, clinical presentation, and associated bacterial pathogens of goat mastitis in Bauchi, Plateau, and Edo states, Nigeria. *Vet World*. 2019;12(5):638. doi:10.14202/VETWORLD.2019.638-645

330. Mcc S, Pacc M, Lima MC, et al. Mastitis in dairy goats from the state of Minas Gerais, Brazil: profiles of farms, risk factors and characterization of bactéria. *Pesqui Veterinária Bras*. 2018;38(9):1742-1751. doi:10.1590/1678-5150-PVB-5698

331. Altaf M, Ijaz M, Kashif Iqbal M, et al. Pakistan Veterinary Journal Molecular Characterization of Methicillin Resistant Staphylococcus aureus (MRSA) and Associated Risk Factors with the Occurrence of Goat Mastitis. doi:10.29261/pakvetj/2019.079

332. Harvey KL, Jarocki VM, Charles IG, Djordjevic SP. The diverse functional roles of elongation factor tu (Ef-tu) in microbial pathogenesis. *Front Microbiol*. 2019;10(OCT):2351. doi:10.3389/FMICB.2019.02351/BIBTEX

333. Skaar EP, Schneewind O. Iron-regulated surface determinants (Isd) of Staphylococcus aureus: Stealing iron from heme. *Microbes Infect*. 2004;6(4):390-397. doi:10.1016/j.micinf.2003.12.008

234

334. Horsburgh MJ, Ingham E, Foster SJ. In Staphylococcus aureus, Fur Is an Interactive Regulator with PerR, Contributes to Virulence, and Is Necessary for Oxidative Stress Resistance through Positive Regulation of Catalase and Iron Homeostasis. *J Bacteriol*. 2001;183(2):468. doi:10.1128/JB.183.2.468-475.2001

335. Cosgrove K, Coutts G, Jonsson IM, et al. Catalase (KatA) and Alkyl Hydroperoxide Reductase (AhpC) Have Compensatory Roles in Peroxide Stress Resistance and Are Required for Survival, Persistence, and Nasal Colonization in Staphylococcus aureus. *J Bacteriol*. 2007;189(3):1025. doi:10.1128/JB.01524-06

336. Speziale P, Pietrocola G, Rindi S, et al. Structural and functional role of Staphylococcus aureus surface components recognizing adhesive matrix molecules of the host. *Future Microbiol*. 2009;4(10):1337-1352. doi:10.2217/FMB.09.102

337. Clarke SR, Harris LG, Richards RG, Foster SJ. Analysis of Ebh, a 1.1-Megadalton Cell Wall-Associated Fibronectin-Binding Protein of Staphylococcus aureus. *Infect Immun*. 2002;70(12):6680. doi:10.1128/IAI.70.12.6680-6687.2002

338. Berube BJ, Wardenburg JB. Staphylococcus aureus α-Toxin: Nearly a Century of Intrigue. *Toxins 2013, Vol 5, Pages 1140-1166*. 2013;5(6):1140-1166. doi:10.3390/TOXINS5061140

339. Heins JN, Suriano JR, Taniuchi H, And $, Anfinsen CB. Characterization of a Nuclease Produced by Staphylococcus aureus. *J Biol Chem*. 1967;242(5):1016-1020. doi:10.1016/S0021-9258(18)96225-3

340. Jonsson K, McDevitt D, McGavin MH, Patti JM, Hook M. Staphylococcus aureus Expresses a Major Histocompatibility Complex Class II Analog (∗). *J Biol Chem*. 1995;270(37):21457-21460. doi:10.1074/JBC.270.37.21457

341. Lee LY, Miyamoto YJ, McIntyre BW, et al. The Staphylococcus aureus Map protein is an immunomodulator that interferes with T cell–mediated responses. *J Clin Invest*. 2002;110(10):1461-1471. doi:10.1172/JCI16318

342. Korea CG, Balsamo G, Pezzicoli A, et al. Staphylococcal Esx proteins modulate apoptosis and release of intracellular Staphylococcus aureus during infection in epithelial cells. *Infect Immun*. 2014;82(10):4144-4153. doi:10.1128/IAI.01576-14/SUPPL_FILE/ZII999090878SO3.PDF

343. Ubukata K, Nonoguchi R, Matsuhashi M, Konno M. Expression and inducibility in Staphylococcus aureus of the mecA gene, which encodes a methicillin-resistant S. aureus-specific penicillin-binding protein. *J Bacteriol*. 1989;171(5):2882. doi:10.1128/JB.171.5.2882-2885.1989

344. Traber KE, Lee E, Benon S, et al. agr function in clinical Staphylococcus aureus isolates. *Microbiology*. 2008;154(Pt 8):2265. doi:10.1099/MIC.0.2007/011874-0

345. Nossa CW, Oberdorf WE, Yang L, et al. Design of 16S rRNA gene primers for 454 pyrosequencing of the human foregut microbiome. *World J Gastroenterol*. 2010;16(33):4135-4144. doi:10.3748/WJG.V16.I33.4135

346. Morot-Bizot SC, Talon R, Leroy S. Development of a multiplex PCR for the identification of Staphylococcus genus and four staphylococcal species isolated from food. *J Appl Microbiol*. 2004;97(5):1087-1094. doi:10.1111/J.1365-2672.2004.02399.X

347. Pati R, Mehta RK, Mohanty S, et al. Topical application of zinc oxide nanoparticles reduces bacterial skin infection in mice and exhibits antibacterial activity by inducing oxidative stress response and cell membrane disintegration in macrophages. *Nanomedicine Nanotechnology, Biol Med*. 2014;10(6):1195-1208. doi:10.1016/J.NANO.2014.02.012

348. Loughman A, Sweeney T, Keane FM, Pietrocola G, Speziale P, Foster TJ. Sequence diversity in the A domain of Staphylococcus aureus fibronectin-binding protein A. *BMC Microbiol*. 2008;8(1):1-14. doi:10.1186/1471-2180-8-74/FIGURES/6

349. Paniagua-Contreras G, Sáinz-Espuñes T, Monroy-Pérez E, et al. Virulence Markers in Staphylococcus aureus Strains Isolated from Hemodialysis Catheters of Mexican Patients. *Adv Microbiol*. 2012;2(4):476-487. doi:10.4236/AIM.2012.24061

350. Donnio PY, Février F, Bifani P, et al. Molecular and Epidemiological Evidence for Spread of Multiresistant Methicillin-Susceptible Staphylococcus aureus Strains in Hospitals. *Antimicrob Agents Chemother*. 2007;51(12):4342. doi:10.1128/AAC.01414-06

351. Jarraud S, Mougel C, Thioulouse J, et al. Relationships between Staphylococcus aureus Genetic Background, Virulence Factors, agr Groups (Alleles), and Human Disease. *Infect Immun*. 2002;70(2):631. doi:10.1128/IAI.70.2.631-641.2002

352. Brakstad OG, Aasbakk K, Maeland JA. Detection of Staphylococcus aureus by polymerase chain reaction amplification of the nuc gene. *J Clin Microbiol*. 1992;30(7):1654. doi:10.1128/JCM.30.7.1654-1660.1992

353. Technical University of Denmark National Food Institute. Multiplex PCR for the detection of the mecA gene. 2008;06.02.2008.

354. Zadoks RN, Schukken YH, Wiedmann M. Multilocus sequence typing of Streptococcus uberis provides sensitive and epidemiologically relevant subtype information and reveals positive selection in the virulence gene pauA. *J Clin Microbiol*. 2005;43(5):2407-2417. doi:10.1128/JCM.43.5.2407-2417.2005

355. Wicher KB, Fries E. Haptoglobin, a hemoglobin-binding plasma protein, is present in bony fish and mammals but not in frog and chicken. *Proc Natl Acad Sci U S A*. 2006;103(11):4168-4173. doi:10.1073/PNAS.0508723103/SUPPL_FILE/08723DATA_SET1.PDF

356. Schaffer AC, Lee JC. Vaccination and passive immunisation against Staphylococcus aureus. *Int J Antimicrob Agents*. 2008;32 Suppl 1(SUPPL. 1). doi:10.1016/J.IJANTIMICAG.2008.06.009

357. Crosby HA, Kwiecinski J, Horswill AR. Staphylococcus aureus Aggregation and Coagulation Mechanisms, and Their Function in Host-Pathogen Interactions. *Adv Appl Microbiol*. 2016;96:1-41. doi:10.1016/BS.AAMBS.2016.07.018

APPENDIX A: PRESENCE OF *STAPHYLOCOCCUS AUREUS* VIRULENCE

FACTORS IN CAPRINE CLINICAL ISOLATES

Introduction

Our group has developed and tested a cholera toxin-based *Staphylococcus aureus* vaccine to prevent mastitis in dairy cows.[290,317,318] While our goal thus far has been to target the bovine dairy market, masitits also affects other animal species, including goats. In many parts of the world, especially in developing countries, smaller animals like goats are preferred over cows for simplified management, reproduction, and processing after slaughter. Although the global caprine dairy market is much smaller than the bovine dairy market(1.3-1.9% of total global milk production and 20.8% of global dairy products come from sheep and goats[319]), the market for goat milk is expanding in developed countries, as many people with allergies to cow's milk and cow dairy products can safely consume goat milk, and undeveloped countries alike.

While most of the world dairy goat production and consumption occurs in Asia and Africa[320], there are organized markets for goat milk in Europe that are specialized for industrial cheesemaking, and consumer demand in countries like China, the U.S., and New Zealand is driving dairy operation expansion where it has not historically been a priority. Because the demands of regional markets are varied, there is an accompanying level of variation in the rules, restrictions, and oversight of the industry across countries.[320,321] In addition, the prevalence of *S. aureus* in clinical and/or subclinical isolates from goats varies widely across the globe. Recent studies in Kenya[322], Bangladesh[323], Turkey[324], and India[325] found a low prevalence of *S. aureus* in clinical or subclinical mastitis with *S. aureus* accounting for 10.7%, 10%, 12.2%, and 6.6% (respectively) of the bacterial/microbial isolates from mastitis in each study. Studies in Ethiopia[326], Egypt[327], Algeria[328], a second group in Turkey[326], and Nigeria[329] found

higher prevalence with *S. aureus* accounting for 17.2%, 24.4%, 40.5%, and 20% (respectively) of bacterial/microbial isolates. Studies in Brazil[330] and Pakistan[331] found that *S. aureus* accounted for 60% and 80.8% (repsectively) of bacterial/microbial isolates. Despite wide regional variation in the prevalence of *S. aureus* in clinical isolates, most studies made note of the fact that *S. aureus* is a top priority pathogen globally. A vaccine to prevent *S. aureus* colonization could have great impacts on the global caprine dairy industry.

We could potentially redevelop our bovine mastitis vaccine into a caprine mastitis vaccine to address the challenge of preventing clinical and/or subclinical mastitis in a globally expanding caprine dairy market. To do so we must evaluate our current vaccine strategy to ensure that appropriate virulence factors are included as antigens. A list of priority *S. aureus* virulence factors, identified from bovine and human studies, is included in Table A.A1. We conducted a small study on three clinical isolates obtained from infected goats (samples obtained from University of Idaho), testing for the presence of each of these virulence factors with PCR.

Table A.A1. *Staphylococcus aureus* **virulence factors and potential antigens for incorporation into a vaccine**

Gene	Protein Name	Function
16SrRNA	small ribosomal RNA subunit	Protein synthesis – interacts with Shine-Dalgarno sequence, positive control for PCR
tuf	translation elongation factor tu	Protein synthesis – transports aminoacylated tRNA to ribosome Host interaction – moonlights on cell surface – interacts with immune system regulators, fibronectin and other ECM proteins, molecular decoys to evade immune detection[332]
IsdA	iron-regulated surface protein A	Iron sequestration – interacts with fibronectin, fibrinogen, haem, hemin, transferrin, fetuin[333]
IsdB	iron-regulated surface protein B	Iron sequestration – interacts with haemoglobin and haem[333]
IsdC	iron-regulated surface protein C	Iron sequestration and haem transport to cytoplasm – interacts with hemin[333]
IsdH	iron-regulated surface protein H	Iron sequestration – binds haptoglobin[333]
fur	ferric uptake repressor	Iron homeostasis – detects iron, responds with genetic regulation, regulates *katA*[334,335]
clfA	clumping factor A	Clumping of blood plasma – interacts with fibrinogen, carried by most clinical isolates[336]
fnbpA	fibronectin binding protein A	Adhesin – interacts with fibronectin, fibrinogen, and elastin, platelet-activating factor[336]
cnA	collagen adhesin	Adhesin – interacts with collagen I and IV, carried by strains in bone/joint infections[336]
ebhB	extracelluar matrix-binding protein	Adhesin – interacts with fibronectin[337]
SpA	Staphylococcal protein A	Blocking of phagocytosis – interacts with Fc domain of Ig[336]
perR	peroxide regulator	Oxidative stress resistance – controls iron storage proteins, regulates *fur, katA* expression[334,335]
katA	catalase	Oxidative stress resistance – catalyzes reduction of H_2O_2[335]
hla	alpha hemolysin	Host injury – pore-forming toxin[338]
nuc	thermonuclease	Host injury - DNA/RNA endo-exonuclease[339]
map	MHC class II analogous protein	Host immunomodulation [340,341]
esxA	EsxA (of Ess secretion pathway)	Release from host – interferes with host apopototic pathways[342]
mecA	penicillin binding protein 2A	β-lactam resistance[343]
agr	accessory gene regulator	Global regulator of *S. aureus* virulence factors and surface proteins[344]
flbA	NFACT family protein	Likely adhesin – contains Fnbp-like domain (NCBI reference sequence WP_000312768.1)

Materials and Methods

Clinical samples collected from infected goats (University of Idaho) were
streaked on mannitol salt agar (MSA) plates to confirm the presence of and to isolate *S.
aureus* in each sample. DNA was isolated from colonies on MSA plates using a DNA
extraction kit (EZBioResearch) per manufacturer's instructions but using a lysis buffer
composed of 20 mM Tric Cl, 2 nM EDTA, 1.2% TX-100, 20 mg/mL lysozyme pH 8.01.
Concentrations were confirmed with nano-drop. Isolated DNA was used to detect
presence or absence of antigens by PCR. Bovine *S. aureus* Newbold 305 genomic DNA
and methicilin-resistant *S. aureus* (MRSA) were used as controls as these genes have
been well characterized in these strains. No template (no DNA) was used as a negative
control. IsdA, Spa, and 16s rRNA gene products were cleaned and prepared for
sequencing following manufacturer's instructions. Primers used are listed in Table A.A2.

Table A.A2.   Primers for caprine antigen screening study.

Gene	Forward Primer		Amplicon (bp)	Source
	Name	Sequence		
16SrRNA	16SrRNA8F	FW: AGAGTTTGATCCTGGCTCAG	526	[345]
	16SrRNA534R	RV: ATTACCGCGGCTGCTGGC		
tuf	TstaG422	FW: GGCCGTGTTGAACGTGGTCAAATCA	370	[346]
	TstaG765	RV: TIACCATTTCAGTACCTTCTGGTAA		
IsdA	isdA FW Tyler	FW: CGGTTCAACCAAAACCTGCT	380	[265]
	isdA RV Tyler	RV: GCGAAGGCAACTGTGCTAAT		
IsdB	137pr	FW: CAAATGGCGAAGCACAAGCAG	347	[265]
	138pr	RV: ACGAGAGTTTGGTGCGCTATG		
IsdC	isdC PCR FW	FW: GAGTATCGAAGGACATAAAG	384	*
	isdC PCR RV	RV: GCTAAGGATGCAACTGG		
IsdH	IsdHForward	FW: AGCAGCACTGCAACAAATCC	545	[265]
	IsdHReverse	RV: CCCCACCATGATTGGCTTG		
fur	furFW	FW: AGAAAAGAAGGCGCAAAACA	178	[347]
	furRV	RV: TAGCTTGGCACGTTTCACAC		
clfA	127pr	FW: GCACCAAGCAGGTTATGTC	318	[265]
	128pr	RV: CCTATGCCAGTAGCCAATGTC		
fnbpA	pfnbAAdomF	FW: GTGAAAAACAATCTTAGGTAC	1750	[348]
	pfnbAAdomR	RV: TATCAATAGCTGATGAATCCG		
cna	cnaFW	FW: TTCACAAGCTTGGTATCAAGAGCATGG	452	[349]
	cnaRV	RV: GAGTGCCTTCCCAAACCTTTTGAGC		
ebhB	ebhBFW	FW: CGCGTTCTGTTGAGTCTAGAGC	1059	*
	ebhBRV	RV: CTTGAACGCCCCCCGGTC		
spa	spa1113F	FW: TAA AGA CGA TCC TTC GGT GAG	401	[350]
	spa1514R	RV: CAG CAG TAG TGC CGT TTG CTT		
perR	perR FW	FW: CACCGCAAAGACAAGCAATA	191	[347]
	perR RV	RV: GAATCGACTTGATGAGTCTCCA		
katA	katA FW	FW: AAAGGTTCTGGTGCATTTGG	173	[347]
	katA RV	RV: AACGCAAATCCTCGAATGTC		
hla	hlaFW	FW: CTGATTACTATCCAAGAAATTCGATTG	211	[351]
	hlaRV	RV: CTTTCCAGCCTACTTTTTTATCAGT		
nuc	129pr	FW: GCGATTGATGGTGATACGGTT	270	[352]
	130pr	RV: AGCCAAGCCTTGACGAACTAAAGC		
map	map441F	FW: CAGGCATTCACACAGCTGAC	578	*
	map1019R	RV: CACTAACGCCTCTGTCAG		
	170pr	FW: CAGCTAACTTAGTTCATGCG	747	*
	171pr	RV: GGAAACTTCACTTTAGTCGC		
esxA	esxAFW	FW: GGCAATGATTAAGATGAGTCC	287	*
	esxARV	RV: GCAAACCGAAATTATTAG		
mecA	135pr	FW: GGGATCATAGCGTCATTATTC	527	[353]
	136pr	RV: AACGATTGTGACACGATAGCC		
agr	agrFW	FW: CTACAAAGTTGCAGCGATGGA	226	[354]
	agrRV	RV: TGGGCAATGAGTCTGTGAGA		
flbA	flbA FW	FW: AAGCACCACCTAC	631	*
	flbA RV	RV: TGAGCATTTGCTG		

* Our group, unpublished

Results and Discussion

Results are presented in Figure A.A1. All three of the clinical goat isolates had the same results for each gene tested. This could possibly indicate that the isolates were all of the same strain. Future studies will include sequence analysis to confirm clonality. Data from this study could be combined with whole genome sequencing data to see if there are consistencies.
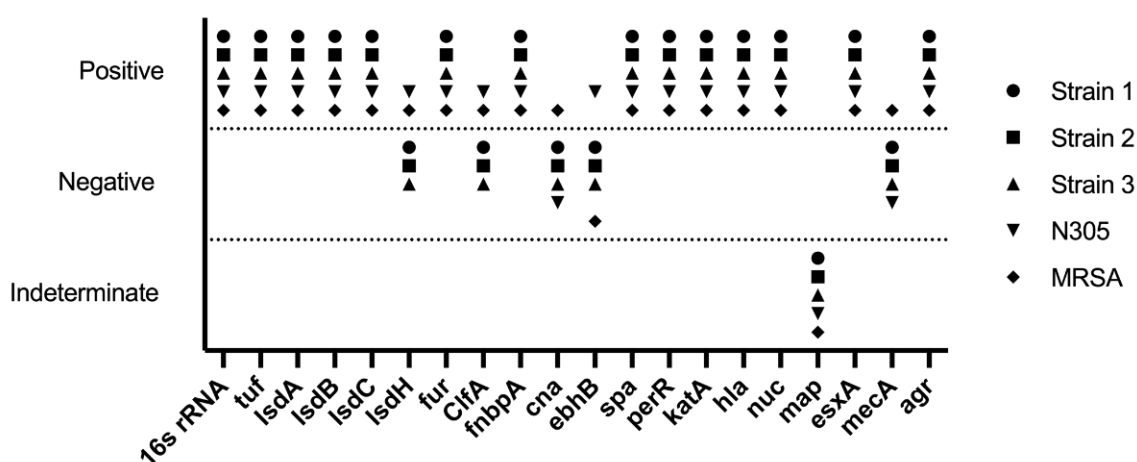

Figure A.A1. Potential antigens for a caprine *S. aureus* vaccine to protect against mastitis

Caprine clinical Staphylococcus aureus isolates were tested for the presence of genes of interest that could potentially be incorporated into a caprine version of our S. aureus vaccine. Bovine N305 and MRSA were included as controls.

We tested all strains for the presence of *map* using two distinct primer sets, however we were unable to produce conclusive results with either primer set for any strain, hence the result of "indeterminate" (Figure A.A1).

The goat isolates tested negative for the presence of *ClfA, IsdH, can, ebhB,* and *mecA* (Figure A.A1). IsdH participates in the iron sequestration process by binding haptoglobin, which binds to free hemoglobin that leaks into circulation under pathological conditions like infection. Haptoglobin is produced by all mammals[355] and can be used as a biomarker in cows to detect subclinical mastitis.[355] More research is

needed to determine whether the absence of IsdH on goat strains of *S. aureus* is common.

ClfA is a fibrinogen-binding adhesin and important *S. aureus* virulence factor, and has been studied as a vaccine candidate for human monoclonal therapies and vaccines (previously reviewed[356,357]).ClfA is carried by most clinical isolates so the fact that these isolates were negative is interesting.[336] We have previously incorporated ClfA into our bovine vaccine, however, based on these results, it appears that this would not be a likely candidate for a caprine vaccine.

The goat isolates tested positive for the presence of *IsdA, IsdB,* and *IsdC* as well as *fur, fnbpA, spa, perR, katA, hla, nuc, esxA,* and *agr.* We have previously incorporated IsdA in our bovine vaccine and this could be included in a caprine version.

Further testing with more clinical isolates collected from varied sources will be required to confirm consistencies in the presence and/or absence of priority antigens for caprine vaccine construction.